공학박사학위논문

# A multiscale modeling approach to predict the sequence-dependent shape and mechanical properties of DNA nanostructures

# DNA 나노구조체의 염기서열에 따른 형상 및 역학적 특성을 예측하는 멀티스케일 모델링 방법

2020년 8월

서울대학교 대학원

기계항공공학부

이 재 영

# Abstract

DNA nanotechnology is a rising field that designs, manufactures, and analyzes DNA nanostructures using the self-assembly principle, creating various related applications. DNA nanostructures are based on the connection between sequences (A, T, G, and C), and its mechanical properties are derived from interactions between atoms. Therefore, to completely understand the mechanical characteristics of DNA nanostructures, all-atomic simulation is required. However, in general, a DNA nanostructure is composed of connections between thousands of sequences in a salt solution, and in order to simulate it on an atomic scale, the atomic system containing billions of degrees of freedom should be solved numerically, which is almost impossible. Accordingly, coarse-grained models have been developed to analyze DNA nanostructures by reducing the degree of freedom, but there are still difficulties to achieve both high efficiency and accuracy of the analysis. Here, this study presents a method to rapidly predict DNA nanostructures at the nanoscale accuracy through multiscale modeling. First, the connections between sequences were classified, and molecular dynamics simulations of a reduced system including them were performed to quantify the sequence-dependent mechanical properties. Next, a finite element model was developed to embody the unique properties, and electrostatic repulsion inside the structure due to the negative charge of DNA in the solution. The assembled finite elements incorporate all the mechanical properties at the sequence-level. Through numerical procedure and normal mode analysis, the equilibrium shape and dynamic properties are rapidly and accurately predicted. The proposed approach can be applied to the analysis of nucleic-acid-based structures and extended to multiscale modeling methods of biomaterials.

Keywords: DNA nanotechnology, DNA nanostructure, Mechanical properties, Multiscale modeling, Molecular dynamics simulation, Finite element analysis

Student Number: 2014-21861

# Contents

# List of Figures

Figure 2-6. Rotational mechanical rigidity distributions in DNA oligomers. Rigidities were calculated for total 33 BP steps except for the four-terminal BPs in each oligomer: (a) tilt-bending, (b) roll-bending, and (c) torsional rigidities. Noting that each oligomer has different sequences at the center at 16 to 18th BP steps, corresponding rigidities deviated, whereas a repeating tendency of rigidities occurs at the other BP steps due to the repetition of the sequence of AGTC from the center to end. Black lines represent the mean and standard deviation of rigidity values of regular BP steps. Rigidities of 16-18th BP steps are illustrated as colored lines and marked with triangles for central nicked BP steps.

Figure 2-7. Translational mechanical rigidity distributions in DNA oligomers. Rigidities were calculated for total 33 BP steps except for the four-terminal BPs in each oligomer: (a) tilt-bending, (b) roll-bending, and (c) torsional rigidities. Noting that each oligomer has different sequences at the center at 16 to 18th BP steps, corresponding rigidities deviated, whereas a repeating tendency of rigidities occurs at the other BP steps due to the repetition of the sequence of AGTC from the center to end. Black lines represent the mean and standard deviation of rigidity values of regular BP steps. Rigidities of 16-18th BP steps are illustrated as colored lines and marked with triangles for central nicked BP steps.

Figure 2-8. Mechanical properties for the BP step. $B_\tau$ and $B_\rho$ represent the bending rigidities, $C$ indicates the torsional rigidity, $Y_{Dx}$ and $Y_{Dy}$ represent the shearing rigidities, and $S$ indicates the stretching rigidity.

Figure 2-9. Mechanical rigidities of regular and nicked BP steps. Six figures represent (a) tilt-bending, (b) roll-bending, (c) torsional, (d) shift-shearing, (e) slide-shearing, and (f) stretching rigidities, respectively using average mechanical rigidities. Blue represents the rigidities of regular BP steps (MN/PQ) while orange and green indicate the values of nicked BP steps (MN/PnQ or MnN/PQ).

Figure 2-10. Comparison of the BP step parameters in stiffened BP steps by a nick. GA/TnC, GC/GnC, and CG/CnG steps were stiffened by a nick for the stretching and bending rigidities with the decrease of the roll (ρ) and shift (Dx).

Figure 2-11. Pixel plot of mechanical coupling coefficients of regular and nicked BP steps. Overall mechanical coupling coefficients in off-diagonal squares are illustrated with a blue and red color gradient. Diagonal values for rigidities are not illustrated. Lower left and upper right squares divided by a slope represent coupling coefficients of regular and nicked BP steps, respectively. Four three by three plots also subdivide this pixel plot with different coupled modes: the upper left plots for rotation-rotation, the upper right and lower left plots for rotation-translation, and the lower right plots for translation-translation.

Figure 2-12. Correlation plots of four primary mechanical coupling coefficients for regular and nicked BP steps. These plots represent the correlation between (a) rise to twist, (b) tilt to rise, (c) slide to twist, and (d) slide to rise. Domains were divided into intervals of 0.2° and 0.002 nm for twist and rise where error bars were obtained as standard errors of the mean.

Figure 4-22. Opening angle estimation of the V-bricks. The central opening angle of the V-brick was controlled by the number of BPs in two short (N1) and long (N2) helices to connect the centers, and the prediction of variants (expressed as N1/N2) confirmed the previous study11.

Figure 4-23. Prediction of a tube assembly and twist-correction effect. A small torsional deformation was observed in the V brick. This produced a global distortion, which predicted about 2° per ring in the tube (red). The twist-corrected tube reduced the distortion through deliberately deleting BPs (green).

Figure 4-24. The twist-correction effect in tube assembly. The tube structures stacking ten twist-corrected and initial rings were represented as green and pink color (a). For the initial structure, the apparent angle (ϕ) and the twist angle per ring ($\theta$) have the relation as $Dsin(10\theta)/2 = 10H\tan(\phi)$, where $D$ and $H$ are the diameter and height of each ring structure. From the measured apparent angle (5.5°), diameter (195 nm), and height (34 nm), the twist per angle was calculated as around 2.0° in line with the previous result. Twist-correction effects were observed for the V bricks by introducing counter-twist through the BP deletion (b). The cross-section of the initial V brick (red) shows small right-handed twist deformation for the hinge axis, whereas the twist of the in twist-corrected V brick (green) showed straight cross-section.

Figure 4-25. Prediction of hierarchical DNA nanostructures. (a) Prediction of a three-fold assembly. Twist-corrected triangle brick, embossed V brick, and connector brick were assembled to the three-fold assembly. (b) Prediction of the polyhedrons. The three-dimensional self-limiting tetrahedrons (T), hexahedrons (H), and dodecahedrons (D).

Figure 4-26. Triangular brick prediction. Atomic representation (a) and density map (b) were constructed. The density map was generated using the plugin, volmap in VMD with a resolution of 4 Å.

Figure 4-34. Central plane in the pointer structure. The central plane for the cryo-EM structure was compared to the previous study. This comparison shows the general agreement at the core, such as the inter-helical distance due to the electrostatic repulsion, but indicates the mismatch in the outer helices.

Figure 4-35. Comparison of the CO angles. Three representative CO angles were calculated following the previous definition using the vectors connecting the six points, which were determined as two mean coordinates of two CO-nick BP steps and four coordinates of the two BPs away from the CO in each lag. The mean and standard deviation were calculated using the measured values for all CO steps.

Figure 4-36. DNA origami structures of honeycomb. In the structure, the distance and angles at crossover sites were measured and compared with the MD results. Three representative CO angles were determined from the vectors connecting the eight points, which were determined as coordinates of four BPs at the crossover sites and four coordinates of the three BPs away from the crossover in each lag.

Figure 4-37. Comparison of BP step parameters. The translational and rotational parameters of all BP steps in the structure were consistent with the previous results. The mean and standard deviation were calculated using the measured values for all BP steps.

Figure 5-12. The development figure of a twisting block. 2-BPs were inserted into all 14-BP-long strands resulting in 16-BP-long strands. Any BP was not inserted into the other strands. In six regions where nicks exist, the locations of the nicks were programmed to control the sequence-dependent rigidities with at least 4-BPs away from Holliday-junctions.

Figure 5-13. List of C/B ratio and an example design of a twisting block to design stiff and flexible structures. (a) C/B ratio of nicked BP steps was defined as the ratio of torsional rigidity to bending rigidity normalized by corresponding regular BP steps. The standard deviations of the C/B ratio were listed in Table 5-1. (b) White and colored strands represent scaffold and staple strands, respectively. The nicks were selected to induce the highest and lowest C/B ratio among possible nine positions of staple strands.

Figure 5-14. Experimental validation of twist control through controlling nick sequences. (a) Mechanical analysis of DNA nanostructures with BP-insertion. The twist angle is induced by the torsional energy due to the inserted BPs and controlled by C/B ratio. (b) AFM analysis of trans and cis monomers. (c) Results of trans ratio and twist angle from sequence design of nicks. Two pairs of stiff, moderate, and flexible structures are represented as descending order of mean C/B ratio in brackets. The trans ratio was calculated as dividing the number of trans monomers by the total number of monomers. The standard deviation of the trans ratio was calculated using the trans ratios of AFM images (Table 5-4 and Table 5-5).

Figure 6-1. Prediction of RMSF. (a) Helix index and the BP connectivity diagram of the 12HB structure. Helix index represents constituent helices, and the connection diagram indicates the BP connection. (b) Comparison of RMSF values. BP index (Green arrow) represents the nodal positions of BPs along the longitudinal direction for each helix in the structure. The predicted RMSF showed a good agreement with those from MD simulation.

Figure 6-2. Comparison of the root-mean-square-fluctuation (RMSF). The RMSF values with respect to the nodal points in helices were obtained using normal mode analysis, and they were compared with the previous results.

Figure 6-3. Prediction of correlation coefficients, and computation time. (a) The correlation coefficients indicate the correlated BPs according to the direction (Pearson correlation) and the probability (generalized correlation) of their molecular motions. The upper-left and lower-right triangles represent the correlation coefficients from MD simulations and the present framework, respectively. (b). CPU time for the analysis. The MD simulation required 16 days in a workstation with two Intel Xeon E5-2680 12-core CPUs and four Nvidia Tesla K80 GPUs, but in this framework, the analysis was completed in one minute using a PC with an Intel i7-4770 3.40 GHz CPU without a GPU.

# List of Tables

Table 5-1. Rigidity ratio of nicked BP steps compared to regular BP steps. Equivalent isotropic bending rigidity was used to calculate rigidity ratio values. The standard derivation (Std) of rigidity ratios in nicked BP steps compared to regular BP steps ($\sigma_{N/R}$) was approximated based on statistical theory as $\sigma_{\alpha/\beta} = \alpha/\beta\left(\sigma_\alpha^2/\alpha^2 + \sigma_\beta^2/\beta^2\right)^{1/2}$ where $\alpha$ and $\beta$ represent the mean values of two independent properties, and $\sigma_\alpha$ and $\sigma_\beta$ indicate their standard deviations, respectively.

Table 5-2. The number of nicked BP steps used in the experimental design and mean rigidity ratio. The mean rigidity ratio was used as a reference value to design DNA origami structures. The mean rigidity ratio of each structure was calculated by dividing the summation of multiplying each rigidity ratio and the corresponding number of nicked BP steps by sixty as the total number of nicked BP steps. A figure below the table shows the mean rigidity ratio values for each structure.

Table 5-3. Numerical solution of trans ratio for different structures.

Table 5-4. Summary of AFM analysis. The trans ratio of DNA origami structures was calculated as the ratio of trans monomers for the total number of monomers. Trans ratio values of AFM images were used to calculate the standard deviation in brackets.

Table 5-5. The number of monomers and trans-cis ratio from AFM images.

Table 5-6. MALDI-TOF results by Bio-RP and PAGE methods. For the comparison of Bio-RP and PAGE methods in oligonucleotides purification, representative ten staples were used to MALDI-TOF (Figure 5-10). The error is the difference in molecular weight divided by the reference value.

Table 7-1. The natural frequency of bundle structures.

Table 7-2. The persistence length of bundle structures.

# 1. Introduction

## 1.1. Background and objectives

Structural DNA nanotechnology opens a new era in programming artificial constructs through the self-assembling nature to create complex and delicate DNA assemblies with nanometer precision[1,2]. With the development of assembling principles[3-6], versatile design strategies to expand the structural diversity from monomers[7-10] to hierarchical assemblies[11,12] have been proposed. The demands for analysis of DNA nanostructures designs have, therefore, significantly increased, but the limitation in experimental characterization led to a need for computational methods. The representative atom-level approach is the molecular dynamics (MD) simulation, which provides a means of investigating the nanoscale mechanism to extract the intrinsic properties in DNA. Unfortunately, despite the extreme accuracy, MD simulation requires extensive computational cost inherent to inter-atomic calculations, severely limiting the analysis only for highly reduced DNA assembly in the month scale time.

To reduce the computational cost, the development of coarse-grained models has been fueled by modeling the essential properties of DNA motifs. Dynamic models[13-15] reduce the atomistic degrees of freedom into representative beads that interact via diversely parametrized potentials with the implicit ionic solution. Despite the advantage in describing the detailed characteristics such as inter-DNA repulsion and thermal dissociation, the dynamic model is inherently based on time integration, and thus especially for a largely deformable structure, it requires still weeks scale time to reach a reasonable equilibrium state. As an alternative approach, a continuum model[16,17] reduces a base-pair into the unit node, of which connection was regarded as a finite element described by empirical parameters. The numerical procedure provides an equilibrium configuration more rapidly in an hour level owing to the time-independent formulation. However, this model requires design-specific parameterization since its component element cannot include the unique properties

depending on the underlying sequence, and electrostatic repulsion by helical configuration.

To address these challenges, this study aims to present a rapid and precise analysis approach for DNA nanostructures through multiscale modeling. We developed a finite element framework directly embodying local intrinsic properties at sequence-level to overcome the parameterization in coarse-grained modeling. The unique elasticity of structural motifs, representing the connection between base-pairs, were completely characterized by MD simulations. Finite elements were rigorously developed to describe the distinctive mechanical properties, and the electrostatic interaction in the structural assembly. Consequently, the finite element assembly incorporates the structural nature of the component elements without the loss of resolution at the base-pair level, providing the global feature of DNA assemblies with minimized parameterization.

## 1.2. Research outline

In Chapter 1, the overall flow of the multiscale modeling method of a DNA nanostructure is introduced. In brief, the elements constituting the DNA nanostructure were classified, and their mechanical properties at the nanoscale were quantified through molecular dynamics simulation. By assembling the finite element that can embody the properties, an entire assembly was established reflecting their intrinsic characteristics. As a scale-up effect, the assembled structure has an electrostatic repulsion between inner helices, which was also modeled into finite elements. Through numerical procedures, equilibrium configuration was found, and further static and dynamic analyses were performed.

In Chapter 2, the mechanical properties between base-pairs constituting the DNA helix were investigated. DNA nanostructures are basically a set of DNA helices and each helix consists of a series of base-pairs, so understanding of the mechanical properties between base-pairs must be preceded by the analysis of the assembled DNA structures. In addition, DNA nanostructures are composed of numerous staple DNAs, and the DNA nicks occurring at their ends occur inevitably inside the structure, so it is also important to understand the mechanical characteristics of nick sites in the helix. The sequence-dependent mechanical properties of two successive base-pairs with and without a nick were characterized since the effects of the base sequence cannot be neglected in nanoscale.

In Chapter 3, we describe technical details for the multiscale modeling method of DNA nanostructures. Modeling of structural elements is introduced, which can incorporate the intrinsic characteristics of structural motifs as the elements constituting DNA nanostructures. The mechanical properties obtained from molecular dynamics simulation in Chapter 2, were converted to those suitable for structural elements. The modeling of electrostatic elements is described, which can apply the electrostatic repulsion between the helix inside the structure. Finally, the details of generating the initial configuration, and the numerical procedure to find the nonlinear solution is introduced.

In Chapter 4, the results of structural analysis using the proposed multiscale method are presented. The structural features of the previously reported DNA nanostructures were analyzed through the proposed method. It was confirmed that the results showed a good agreement with the ones through experiments and atomic simulations. The global shape was consistent with that observed for all tested designs of DNA nanostructure. Furthermore, structural details such as translational or rotational parameters between base-pairs inside the structure were captured as well.

In Chapter 5, to control the twist of the DNA nanostructures sequence design principle was proposed, and it was verified through experiments and the proposed multiscale approach. The sequence-dependent mechanical properties as identified in Chapter 2 were used to control the global twisted shape through only the design of the base sequence. In particular, focusing on the reduction of the torsional rigidity at the nick sites, the details of designing nick sequences in the DNA nanostructures to regulate its twist angle was described. This was also verified through the proposed multiscale analysis and experiments.

In Chapter 6, the analysis and results of the dynamic characteristics properties for the DNA nanostructures are presented. By performing the normal mode analysis, the eigenvalues and eigenmodes of the analyzed DNA nanostructures through the proposed multiscale approach finite element were obtained. The obtained eigensolution was used to derive the dynamic fluctuation of base-pairs in the structure and the coupling coefficients between two base-pairs. The results were in good agreement with the ones from the molecular dynamics simulation, showing the high computing efficiency.

In Chapter 7, the method of predicting the overall rigidity of the DNA nanostructures is introduced and its results were investigated. By employing the natural frequency and mode shape of the bundled DNA nanostructure analyzed through the proposed approach, the bending and torsional rigidities of the entire structure were derived. The obtained rigidities were converted into the corresponding bending and torsional persistence lengths, which were compared with the experimentally measured ones, showing the good agreement.

## 1.3. Overview of the multiscale modeling approach

We first defined three basic structural motifs of DNA nanostructures according to the topological connection between base-pairs: base-pair step (BP step), crossover step (CO step), and single-stranded DNA (ssDNA) part (Figure 1-1). A BP step represents two BPs connected successively within a helix, categorized into regular and nicked BP steps where one of the backbones is broken in nicked ones. A nicked BP step located at a crossover site is separately denoted as a CO-nick BP step. Two BPs connected across helices by the same backbone are referred to as a CO step. If another CO step exists next to it forming a Holliday junction, we call it as a double CO step, and as a single CO step otherwise. Antiparallel crossovers are only considered in this work. Sequence combinations for these structural motifs are denoted more specifically as MN/PQ for regular BP steps, MN/PnQ or MnN/PQ for nicked BP steps, MN-PnQ or MnN-PQ for CO-nick BP steps, and MN|PQ and MN||PQ for single and double CO steps, respectively. M, N, P, and Q represent a DNA base and n indicates the nick position. They are not specified for ssDNA as its mechanical role as an entropic spring is governed by its end-to-end distance and contour length while its sequence dependence is negligible.

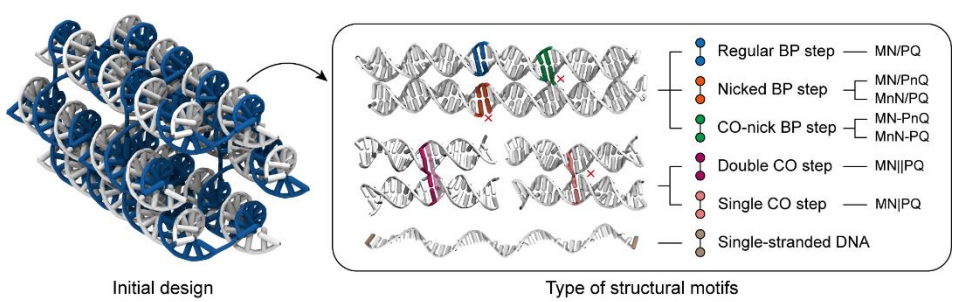


Figure 1-1. Type of structural motifs. Base-pair (BP) steps indicate the two successively connected BPs in a helix. The BP steps were subdivided into regular and nicked BP steps if one of the backbones was broken, and the nicked BP step at the crossover (CO) was denoted to the CO-nick BP step. CO steps represent two BPs connected across helices. If another CO step exists next to it, it was called as a double CO step, and as a single CO step otherwise.

The sequence-dependent relative geometry and mechanical properties of these motifs in equilibrium were quantified from the molecular trajectories obtained by MD simulations (Figure 1-2). Each BP of a step is approximated as a rigid block whose motion is described using a triad with three translational ($\Delta_x, \Delta_y, \Delta_z$) and three rotational ($\Theta_x, \Theta_y, \Theta_z$) DOFs. The relative three-dimensional motion between two triads representing constituent BPs of a step was recorded over time and converted to a covariance matrix providing its elastic properties under quasi-harmonic approximation[18,19].

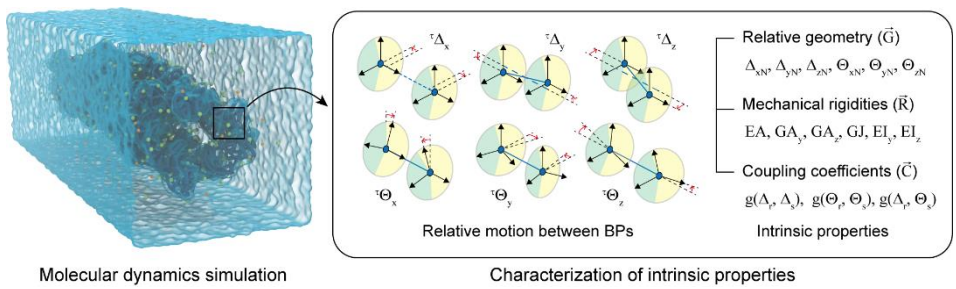


Figure 1-2. Characterization of intrinsic properties for each structural motif. Six relative motions between two BPs were obtained from the MD trajectory and converted into the intrinsic properties.

Accordingly, the relative geometry and mechanical properties of BP and CO steps were completely determined for all possible sequence combinations (Figure 1-3), including six relative geometry ($\vec{G}$), six mechanical rigidities ($\vec{R}$), and fifteen coupling coefficients ($\vec{C}$). The measured properties agree quantitatively well with known characteristics of DNA including the helical rise of 0.34 ± 0.01 nm, the interhelix distance at crossovers of 1.90 ± 0.02 nm, the helicity of 10.43 BP per turn, and the twist-stretch coupling coefficient of -277 ± 60 pNnm.

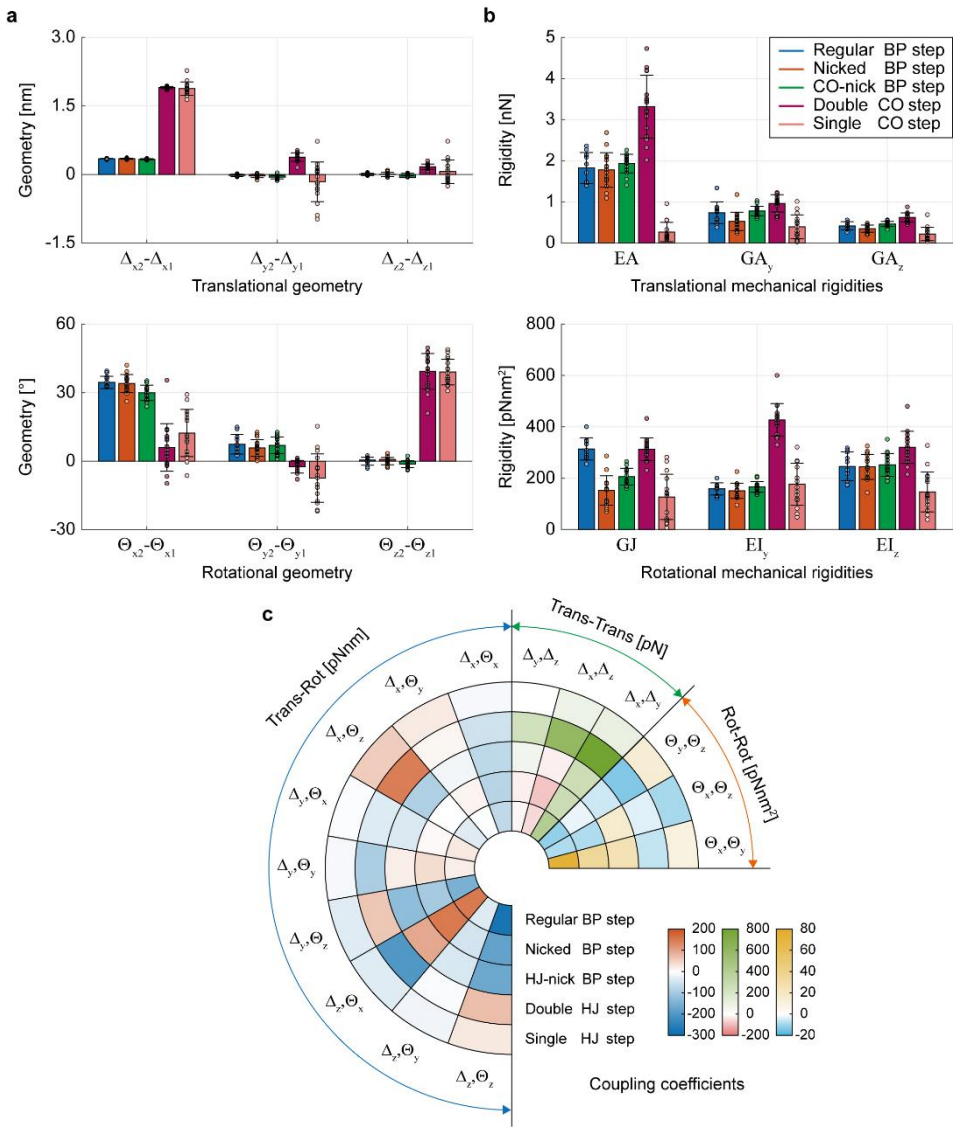


Figure 1-3. The relative geometry for the six relative motion between two BPs is expressed by the difference of nodal geometry values of BPs (**a**). The corresponding mechanical rigidities for the relative motion were calculated (**b**). Each point represents a sequence-dependent value, and bars and lines indicate mean and standard deviation values. (**c**) Coupling coefficients of structural motifs. Each segment indicates the mean values of the coupling coefficients for the two different directions among translation and rotation.

Structural models for BP and CO steps were then constructed by incorporating these intrinsic properties into beam finite elements (Figure 1-4) based on the co-rotational formulation[20] whose element stiffness matrix was given as $\mathbf{K}_{\mathrm{E}}^{\mathrm{ST}}(\vec{\mathrm{G}}, \vec{\mathrm{R}}, \vec{\mathrm{C}})$. Note that these models consider all the geometric and mechanical properties exactly without further approximation as well as their sequence dependence unlike simplified beam models used in CanDo[17]. For ssDNA, we employed the extensible freely-jointed-chain model with the characteristic values determined at divalent salt ($MgCl_2$) conditions[21] where the stretching rigidity was modified as a function of the ratio of end-to-end length to contour length in order to prevent the overestimation of tensional force for a short ssDNA by the original model.

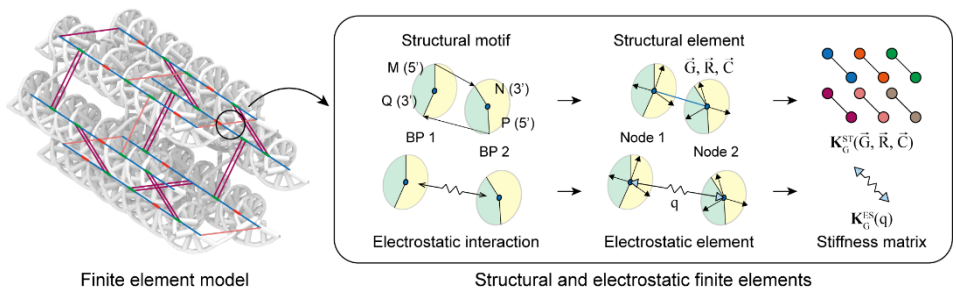


Figure 1-4. Finite element model. A structural element was developed to incorporate the intrinsic properties of a structural motif. An electrostatic element applied the electrostatic repulsion on two distant BPs. Each finite element provides a stiffness matrix to represent structural or electrostatic properties.

For the analysis of structured nucleic acids, it is important to model the electrostatic interaction between negatively charged BPs in an ionic solution to capture the deformation due to interhelix repulsion. We employed the Debye-Hückel theory from which the pairwise repulsive force between two BPs was derived as a nonlinear function of their distance. This nonlinear force was implemented using spring finite elements, referred to as electrostatic elements, whose element stiffness matrix was constructed as $\mathbf{K}_{\mathrm{E}}^{\mathrm{ES}}(q)$ for an effective charge $q$ of a BP. Following the previous studies[22,23] on the electrostatic force acting between two DNA double

helices, the effective charge was set to 0.7 for a 20 mM $MgCl_2$ condition. Electrostatic elements were created between two BPs within a cutoff distance of 2.5 nm, which is twice the Debye length approximately at that condition, considering the accuracy and computational efficiency.

The finite element model for an entire structure was built from its design information including the connectivity map and sequence of BPs from which structural motifs in the design could be identified (Figure 1-5). We assigned the corresponding structural element to each structural motif and placed the electrostatic elements between BPs across helices within the cutoff distance. The global stiffness matrix ($\mathbf{K}_G$) was constructed by assembling the element stiffness matrices from both structural and electrostatic elements. The three-dimensional shape of the structure in equilibrium was finally obtained by an automated nonlinear solution procedure that we developed to achieve fast convergence. Once the final shape was obtained, normal mode analysis was conducted to calculate the dynamic properties or overall stiffness values of the structure if necessary.

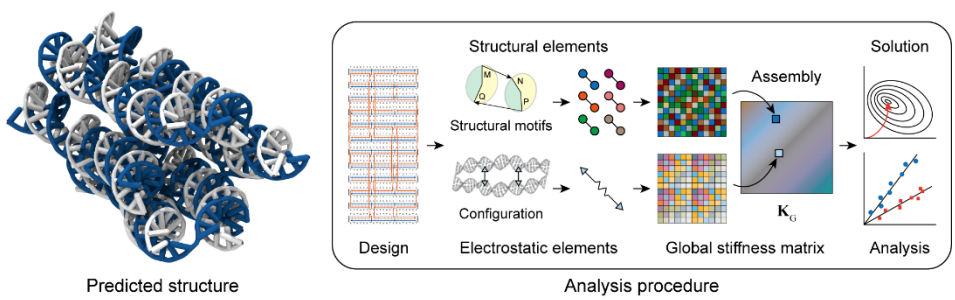


Figure 1-5. Analysis procedure. From the given design, the structural and electrostatic elements were generated, constructing the global stiffness matrix. Through the automated numerical procedure, equilibrium shape and structural features were predicted.

# 2. Investigation of the mechanical properties of DNA

## 2.1. Abstract

We quantified the sequence-dependent mechanical properties of base-pair steps with or without a nick in a DNA helix using molecular dynamics simulation. To extensively understand the mechanical characteristics of DNA nicks at single BP level and explore their utility in DNA nanostructure design, we first investigated the sequence-dependent mechanical properties of BP steps with a particular focus on the effect of nicks by performing MD simulation for a complete set of distinct double-stranded DNA oligomers constructed using all possible BP steps (ten without a nick and sixteen with a nick). Six primary mechanical rigidities and fifteen coupling coefficients were quantified extensively for all BP steps from MD trajectories, revealing the significant and highly sequence-dependent reduction (28 to 82%) of the torsional rigidity by nicks. No significant effect of a nick on mechanically coupled deformation such as the twist-stretch coupling was observed. These results suggest that the primary structural role of nick is the relaxation of torsional constraint by backbones known to be responsible for relatively high torsional rigidity of DNA. Our study illustrates the importance as well as the opportunities for considering sequence-dependent properties in structural DNA nanotechnology.

## 2.2. Methods

### 2.2.1. Generation of DNA oligomers

There exist ten distinct regular BP steps without a nick: AA/TT, AG/CT, GA/TC, GG/CC, AC/GT, AT/AT, GC/GC, TG/CA, TA/TA, and CG/CG steps. We used these regular BP steps to build ten 42-BP-long DNA double helices, each of which makes four complete turns about its helical axis. We chose this duplex length to prevent the behavior of the central BP step from being significantly affected by the highly flexible and localized motion of duplex ends[24,25]. A freely available program 3DNA was used for the construction of DNA oligomers with the default geometry of generic B-form DNA[26]. To investigate the effects of nicks, we constructed nicked DNA double helices as well by introducing a single-strand break in the middle of each BP step resulting in structures with sixteen unique nicked BP steps: AA/TnT, AG/CnT, GA/TnC, GG/CnC, AnA/TT, AnG/CT, GnA/TC, GnG/CC, AC/GnT, AnC/GT, AT/AnT, GC/GnC, TG/CnA, TnG/CA, TA/TnA, and CG/CnG steps (Table 2-1). The phosphorus atom and the attached oxygen atoms of the backbone at the nick site between the bases P and Q were removed in nicked BP steps[27,28]. Here, we represented a regular BP step as MN/PQ where M, N, P, and Q denote one of the canonical nucleobases (A, G, T, and C) and a nicked BP step as MN/PnQ or MnN/PQ where a nick existing between bases was indicated by ‘n’ (Figure 2-1).

Table 2-1. List of MD-simulated DNA oligomers. Each oligomer is 42-BP-long DNA double helix and has the same sequence pattern, 5'-$CTGA_5$-MN-$AGTC_5$-3' / 5'-$GACT_5$-PQ-$TCAG_5$-3'. MN/PQ represents one of the ten regular BP steps. Since MN/PQ or PQ/MN indicate identical one of ten BP steps, we selected notations by comparing M and P in order of A > G > T > C.

| Type | Base-pair (BP) step | | Oligomer sequence (5'→3') | |
|---|---|---|---|---|
| Regular | RR/YY | AA/TT | $CTGA_5$-TT-$AGTC_5$ | $GACT_5$-AA-$TCAG_5$ |
| | | AG/CT | $CTGA_5$-AG-$AGTC_5$ | $GACT_5$-CT-$TCAG_5$ |
| | | GA/TC | $CTGA_5$-TC-$AGTC_5$ | $GACT_5$-GA-$TCAG_5$ |
| | | GG/CC | $CTGA_5$-GG-$AGTC_5$ | $GACT_5$-CC-$TCAG_5$ |
| | RY/RY | AC/GT | $CTGA_5$-AC-$AGTC_5$ | $GACT_5$-GT-$TCAG_5$ |
| | | AT/AT | $CTGA_5$-AT-$AGTC_5$ | $GACT_5$-AT-$TCAG_5$ |
| | | GC/GC | $CTGA_5$-GC-$AGTC_5$ | $GACT_5$-GC-$TCAG_5$ |
| | YR/YR | TG/CA | $CTGA_5$-TG-$AGTC_5$ | $GACT_5$-CA-$TCAG_5$ |
| | | TA/TA | $CTGA_5$-TA-$AGTC_5$ | $GACT_5$-TA-$TCAG_5$ |
| | | CG/CG | $CTGA_5$-CG-$AGTC_5$ | $GACT_5$-CG-$TCAG_5$ |
| Nicked | RR/YnY | AA/TnT | $CTGA_5$-AA-$AGTC_5$ | $GACT_5$-TnT-$TCAG_5$ |
| | | AG/CnT | $CTGA_5$-AG-$AGTC_5$ | $GACT_5$-CnT -$TCAG_5$ |
| | | GA/TnC | $CTGA_5$-GA-$AGTC_5$ | $GACT_5$-TnC-$TCAG_5$ |
| | | GG/CnC | $CTGA_5$-GG-$AGTC_5$ | $GACT_5$-CnC-$TCAG_5$ |
| | RnR/YY | AnA/TT | $CTGA_5$-TT-$AGTC_5$ | $GACT_5$-AnA-$TCAG_5$ |
| | | AnG/CT | $CTGA_5$-CT-$AGTC_5$ | $GACT_5$-AnG-$TCAG_5$ |
| | | GnA/TC | $CTGA_5$-TC-$AGTC_5$ | $GACT_5$-GnA-$TCAG_5$ |
| | | GnG/CC | $CTGA_5$-CC-$AGTC_5$ | $GACT_5$-GnG-$TCAG_5$ |
| | RY/RnY | AC/GnT | $CTGA_5$-AC-$AGTC_5$ | $GACT_5$-GnT-$TCAG_5$ |
| | | AnC/GT | $CTGA_5$-GT-$AGTC_5$ | $GACT_5$-AnC-$TCAG_5$ |
| | | AT/AnT | $CTGA_5$-AT-$AGTC_5$ | $GACT_5$-AnT-$TCAG_5$ |
| | | GC/GnC | $CTGA_5$-GC-$AGTC_5$ | $GACT_5$-GnC-$TCAG_5$ |
| | YR/YnR | TG/CnA | $CTGA_5$-TG-$AGTC_5$ | $GACT_5$-CnA-$TCAG_5$ |
| | | TnG/CA | $CTGA_5$-CA-$AGTC_5$ | $GACT_5$-TnG-$TCAG_5$ |
| | | TA/TnA | $CTGA_5$-TA-$AGTC_5$ | $GACT_5$-TnA-$TCAG_5$ |
| | | CG/CnG | $CTGA_5$-CG-$AGTC_5$ | $GACT_5$-CnG-$TCAG_5$ |

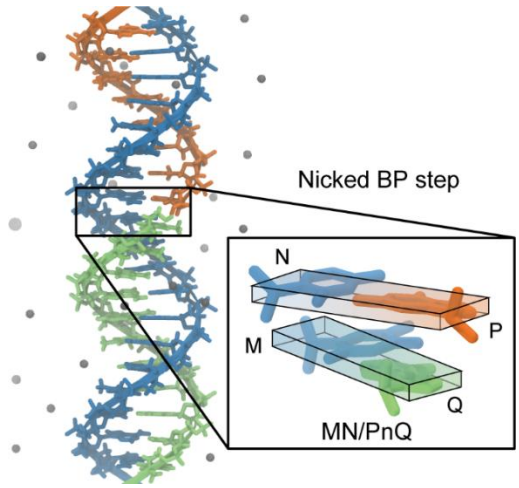


Figure 2-1. Schematic illustration of investigating the mechanical properties of the nicked base-pair (BP) step. A nicked BP step in a DNA double helix. Blue strand is well-connected, whereas the backbone is broken between the orange and green strands indicating a nick. The enlarged figure shows a nicked MN/PnQ step where M, N, P, and Q represent one of the canonical nucleobases (A, G, T, and C), and the nick exists between P and Q bases indicated by 'n'. The nicked BP step is illustrated with two successive BPs represented by thin and long plates.

### 2.2.2. Molecular dynamics simulations of DNA oligomers

We performed MD simulations to investigate the conformational dynamics of the DNA double helices using a freely available program, NAMD[29] with the CHARMM36 force field[30] for nucleic acids. The CHARMM36 force field was adopted since it showed general agreements with experiments from the previous MD studies of DNA nanostructures[10,31-34]. Each DNA oligomer was explicitly solvated in a 60 Å × 60 Å × 180 Å cubic TIP3P water box[35]. In this study, since the mechanical properties of nicked BP steps were expected to mainly contribute to the analysis and design of structural DNA nanotechnology where 10-20 mM $MgCl_2$ condition has generally been selected, MD simulation was performed under an $MgCl_2$ condition of 10 mM. The distance between the DNA oligomer and the cell boundary was approximately 20 Å, and periodic boundary conditions were applied. The short-range electrostatic and van der Walls potentials were smoothly reduced with the switching scheme active above 12 Å cut-off. We employed the Particle Mesh Ewald (PME) method[36] with a grid spacing of 1.0 Å to consider long-range electrostatic interactions efficiently. The static energy of each system was minimized for 20000 steps using the conjugate gradient algorithm. Trajectories of 100 ns were obtained under the isobaric-isothermal (NPT) ensemble after a pre-equilibrium process of 10 ns. We maintained the pressure at one bar using the Nosé-Hoover Langevin piston scheme[37] and the temperature at 298 K with Langevin thermostat[29] with a damping constant of 0.1 $ps^{-1}$. The equilibrated root-mean-square deviation (RMSD) values of DNA oligomers were obtained from their minimized coordinates during MD simulation (Figure 2-2).

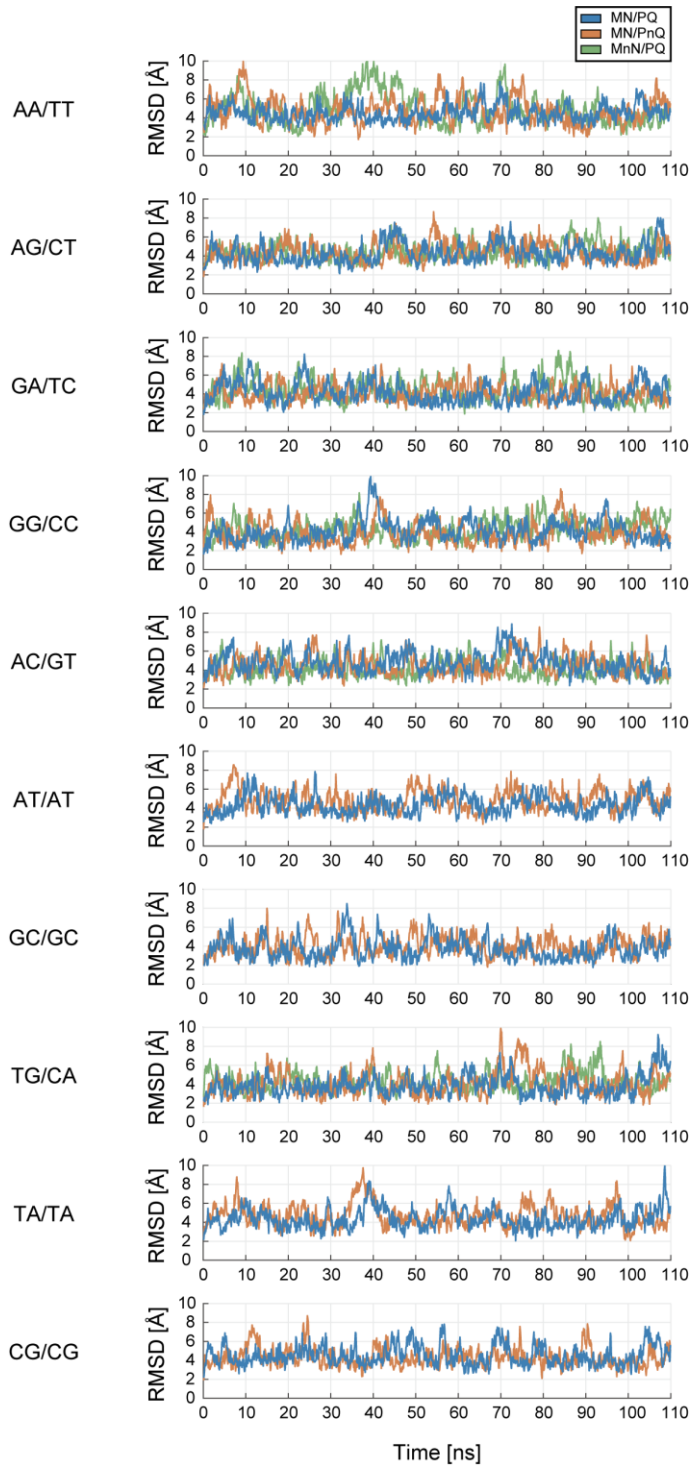


Figure 2-2. Root-mean-square deviation (RMSD) of DNA oligomers. Each RMSD value was calculated from the minimized structure.

### 2.2.3. Overview of characterizing mechanical properties

We analyzed and compared the conformational dynamics of regular and nicked BP steps using the obtained 100-ns-long MD trajectories for each of these twenty-six DNA oligomers in equilibrium. To measure the mechanical properties at BP level from MD trajectories, we employed six BP step parameters following the definition in 3DNA[26] and quantified the relative motion of two adjacent BPs in regular and nicked BP steps (Figure 2-3 and Figure 2-4).

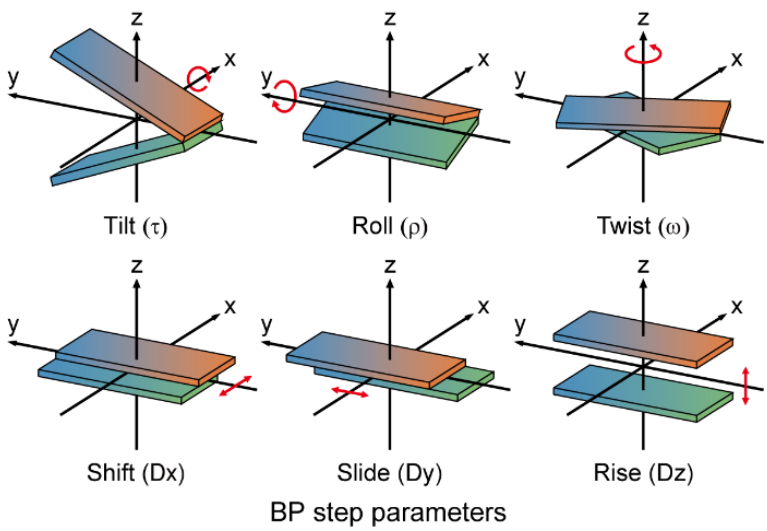


Figure 2-3. Six BP step parameters**.** These BP step parameters were defined in 3DNA and were determined as the relative rigid-body modes of the two BPs. The rigid-body rotations of a BP step were denoted by tilt (τ), roll (ρ), and twist (ω), and similarly, the rigid-body translations were denoted by shift (Dx), slide (Dy), and rise (Dz) for the x, y, and z-axes, respectively.

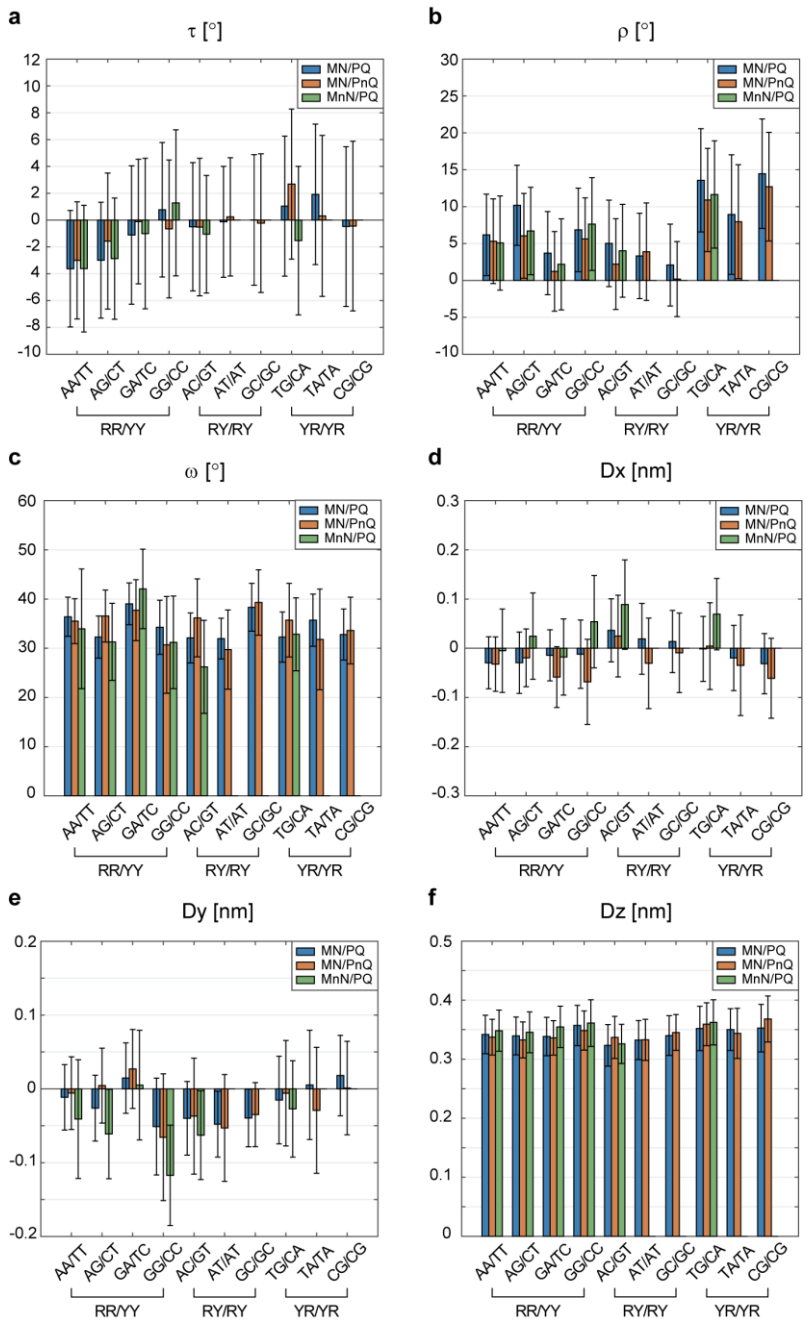


Figure 2-4. BP step parameters of the regular and nicked BP steps. Six figures represent overall BP step parameters: (**a**) tilt, (**b**) roll, (**c**) twist, (**d**) shift, (**e**) slide, and (**f**) rise. Blue represents the parameters of regular BP steps while red and green indicate the parameters of nicked BP steps.

The BP step parameters consist of three rotational and three translational rigid-body degrees of freedom defined as tilt (τ), roll (ρ), twist (ω), shift (Dx), slide (Dy), and rise (Dz), describing the stacked configuration of one BP relative to its neighbor (Table 2-2 and Table 2-3). Here, it was confirmed that the BP step parameters estimated from the MD trajectories were statistically different at the significance level of 0.01 according to the t-test comparing the regular and corresponding nicked BP steps. The mechanical rigidities ($B_\tau$, $B_\rho$, C, $Y_{Dx}$, $Y_{Dy}$, and S) and coupling coefficients ($g_{ij}$) of regular and nicked BP steps were then estimated using the covariance matrix[19,38-40] (Figure 2-5, Table 2-4, Table 2-5, Table 2-6, and Table 2-7).

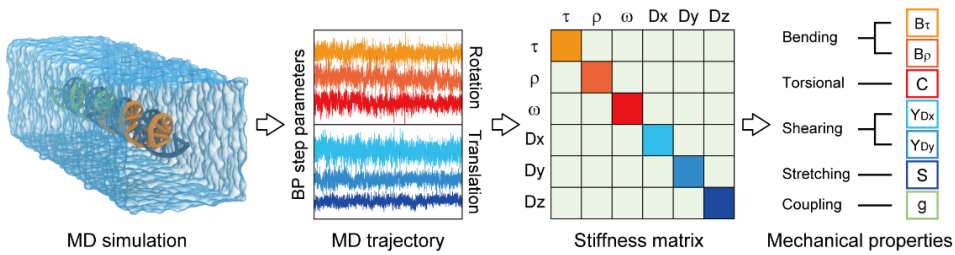


Figure 2-5. Derivation of mechanical properties. Mechanical rigidities and coupling coefficients were obtained from the MD trajectory of BP step parameters.

The stiffness matrix was calculated from the covariance matrix of the BP step parameters based on quasi-harmonic approximation as $\mathbf{K} = k_B T \mathbf{F}^{-1}$ where $\mathbf{K}$ and $\mathbf{F}$ are the stiffness matrix and the covariance matrix, $k_B$ is the Boltzmann constant, and T is the absolute temperature, respectively. We confirmed that the highly flexible motion of duplex ends did not affect the behavior of the central BP step since sequence-dependent mechanical rigidities were observed with the repeated pattern of sequence variation except for terminal BP steps (Figure 2-6 and Figure 2-7).

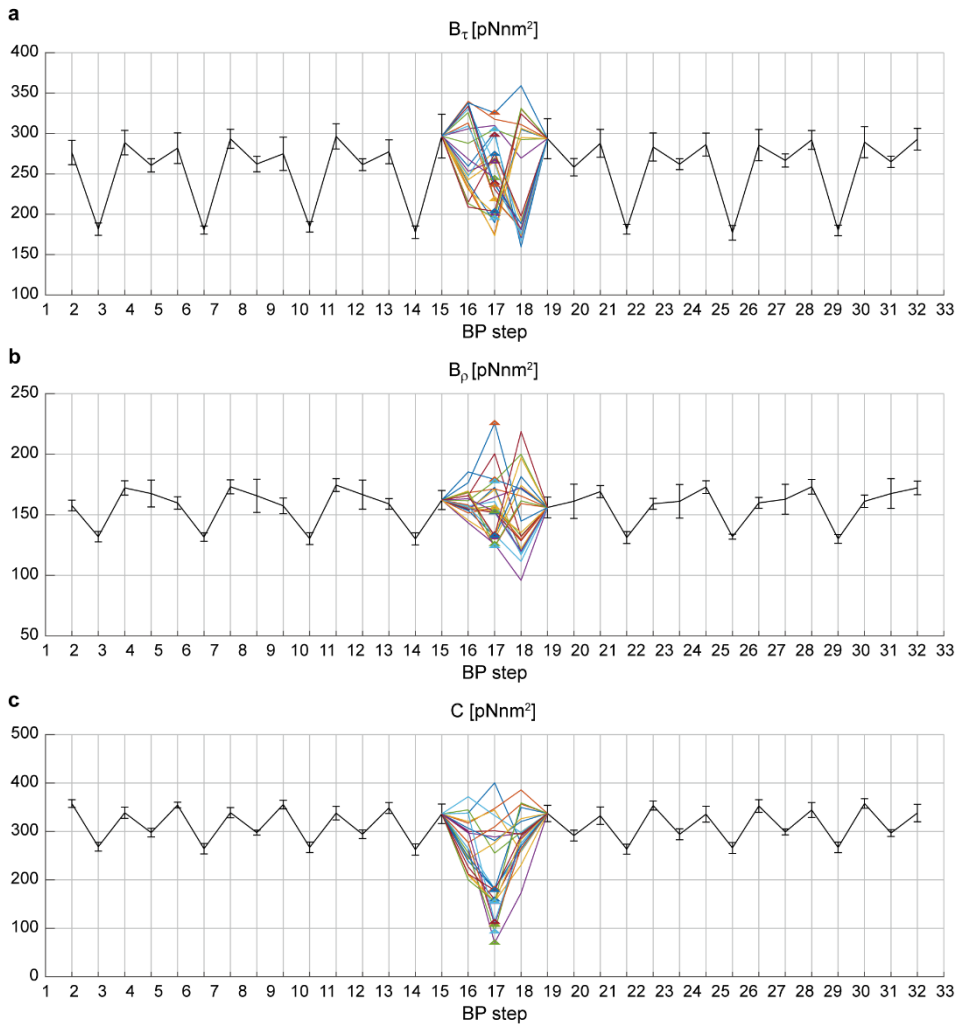


Figure 2-6. Rotational mechanical rigidity distributions in DNA oligomers. Rigidities were calculated for total 33 BP steps except for the four-terminal BPs in each oligomer: (**a**) tilt-bending, (**b**) roll-bending, and (**c**) torsional rigidities. Noting that each oligomer has different sequences at the center at 16 to 18th BP steps, corresponding rigidities deviated, whereas a repeating tendency of rigidities occurs at the other BP steps due to the repetition of the sequence of AGTC from the center to end. Black lines represent the mean and standard deviation of rigidity values of regular BP steps. Rigidities of 16-18th BP steps are illustrated as colored lines and marked with triangles for central nicked BP steps.

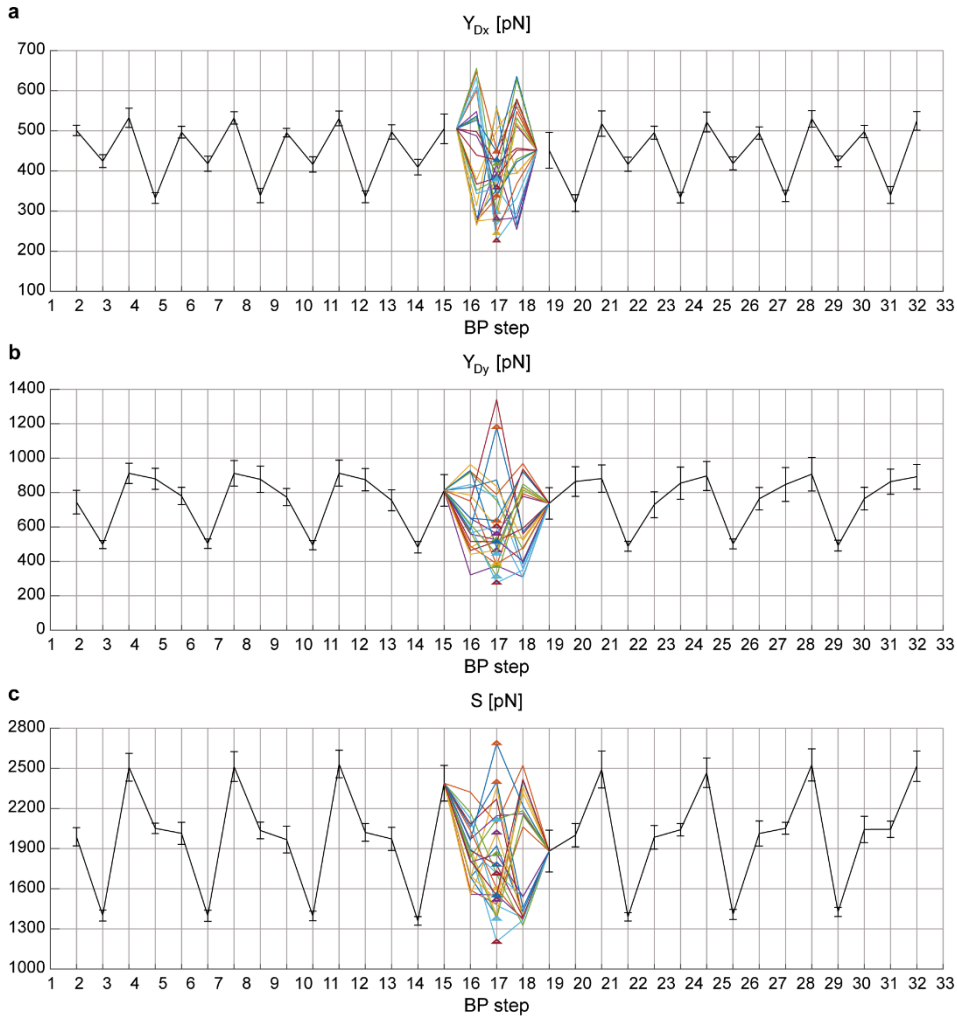


Figure 2-7. Translational mechanical rigidity distributions in DNA oligomers. Rigidities were calculated for total 33 BP steps except for the four-terminal BPs in each oligomer: (**a**) tilt-bending, (**b**) roll-bending, and (**c**) torsional rigidities. Noting that each oligomer has different sequences at the center at 16 to 18th BP steps, corresponding rigidities deviated, whereas a repeating tendency of rigidities occurs at the other BP steps due to the repetition of the sequence of AGTC from the center to end. Black lines represent the mean and standard deviation of rigidity values of regular BP steps. Rigidities of 16-18th BP steps are illustrated as colored lines and marked with triangles for central nicked BP steps.

Table 2-2. Sequence-dependent BP step parameters of regular BP steps. The mean and standard deviation are represented in the left and right column for each BP step parameter.

| Regular | τ [°] | | ρ [°] | | ω [°] | |
|---|---|---|---|---|---|---|
| AA/TT | -3.62 | 4.34 | 6.17 | 5.52 | 36.40 | 3.99 |
| AG/CT | -2.99 | 4.32 | 10.18 | 5.42 | 32.27 | 4.28 |
| GA/TC | -1.11 | 5.16 | 3.70 | 5.64 | 39.02 | 4.25 |
| GG/CC | 0.77 | 5.01 | 6.85 | 5.66 | 34.26 | 5.51 |
| AC/GT | -0.50 | 4.78 | 5.03 | 5.86 | 32.10 | 5.09 |
| AT/AT | -0.13 | 4.13 | 3.33 | 5.79 | 31.97 | 4.14 |
| GC/GC | 0.01 | 4.86 | 2.09 | 5.55 | 38.32 | 4.86 |
| TG/CA | 1.04 | 5.22 | 13.57 | 7.00 | 32.27 | 5.11 |
| TA/TA | 1.92 | 5.24 | 8.93 | 8.11 | 35.71 | 5.31 |
| CG/CG | -0.48 | 5.95 | 14.47 | 7.42 | 32.78 | 5.19 |
| Overall | -0.51 | 1.72 | 7.43 | 4.27 | 34.51 | 2.69 |

| Regular | **Dx** [nm] | | **Dy** [nm] | | **Dz** [nm] | |
|---|---|---|---|---|---|---|
| AA/TT | -0.03 | 0.05 | -0.01 | 0.04 | 0.34 | 0.03 |
| AG/CT | -0.03 | 0.06 | -0.03 | 0.04 | 0.34 | 0.03 |
| GA/TC | -0.01 | 0.05 | 0.01 | 0.05 | 0.34 | 0.03 |
| GG/CC | -0.01 | 0.07 | -0.05 | 0.07 | 0.36 | 0.03 |
| AC/GT | 0.04 | 0.06 | -0.04 | 0.05 | 0.32 | 0.04 |
| AT/AT | 0.02 | 0.07 | -0.05 | 0.04 | 0.33 | 0.03 |
| GC/GC | 0.01 | 0.06 | -0.04 | 0.04 | 0.34 | 0.03 |
| TG/CA | 0.00 | 0.07 | -0.02 | 0.06 | 0.35 | 0.04 |
| TA/TA | -0.02 | 0.07 | 0.01 | 0.07 | 0.35 | 0.04 |
| CG/CG | -0.03 | 0.06 | 0.02 | 0.05 | 0.35 | 0.04 |
| Overall | -0.01 | 0.02 | -0.02 | 0.03 | 0.34 | 0.01 |

Table 2-3. Sequence-dependent BP step parameters of nicked BP steps. The mean and standard deviation are represented in the left and right column for each BP step parameter.

| Nicked | **τ** [°] | | **ρ** [°] | | **ω** [°] | |
|---|---|---|---|---|---|---|
| AA/TnT | -3.01 | 4.37 | 5.32 | 5.73 | 35.50 | 4.56 |
| AnA/TT | -3.62 | 4.72 | 5.08 | 6.38 | 33.95 | 12.17 |
| AG/CnT | -1.57 | 5.07 | 6.05 | 5.75 | 36.55 | 5.30 |
| AnG/CT | -2.87 | 4.52 | 6.70 | 5.92 | 31.29 | 7.83 |
| GA/TnC | -0.11 | 4.64 | 1.23 | 5.40 | 37.73 | 6.20 |
| GnA/TC | -1.01 | 5.61 | 2.18 | 6.17 | 42.05 | 8.08 |
| GG/CnC | -0.66 | 5.14 | 5.62 | 5.57 | 30.69 | 9.83 |
| GnG/CC | 1.28 | 5.44 | 7.64 | 6.29 | 31.19 | 9.41 |
| AC/GnT | -0.52 | 5.12 | 2.21 | 6.15 | 36.17 | 7.91 |
| AnC/GT | -1.05 | 4.38 | 4.02 | 6.30 | 26.22 | 9.47 |
| AT/AnT | 0.24 | 4.41 | 3.90 | 6.61 | 29.72 | 8.05 |
| GC/GnC | -0.23 | 5.17 | 0.19 | 5.08 | 39.29 | 6.64 |
| TG/CnA | 2.68 | 5.59 | 10.90 | 7.00 | 35.70 | 7.49 |
| TnG/CA | -1.53 | 5.54 | 11.65 | 7.26 | 32.83 | 7.42 |
| TA/TnA | 0.32 | 6.00 | 7.96 | 7.72 | 31.80 | 10.24 |
| CG/CnG | -0.45 | 6.32 | 12.71 | 7.36 | 33.61 | 6.79 |
| Overall | -0.76 | 1.59 | 5.83 | 3.68 | 34.02 | 3.95 |

| Nicked | Dx [nm] | | Dy [nm] | | Dz [nm] | |
|---|---|---|---|---|---|---|
| AA/TnT | -0.03 | 0.06 | -0.01 | 0.05 | 0.34 | 0.03 |
| AnA/TT | -0.01 | 0.08 | -0.04 | 0.08 | 0.35 | 0.03 |
| AG/CnT | -0.02 | 0.06 | 0.00 | 0.05 | 0.33 | 0.03 |
| AnG/CT | 0.02 | 0.09 | -0.06 | 0.06 | 0.35 | 0.03 |
| GA/TnC | -0.06 | 0.06 | 0.03 | 0.05 | 0.34 | 0.03 |
| GnA/TC | -0.02 | 0.08 | 0.01 | 0.07 | 0.35 | 0.03 |
| GG/CnC | -0.07 | 0.09 | -0.07 | 0.09 | 0.35 | 0.03 |
| GnG/CC | 0.05 | 0.09 | -0.12 | 0.07 | 0.36 | 0.04 |
| AC/GnT | 0.02 | 0.08 | -0.04 | 0.08 | 0.34 | 0.04 |
| AnC/GT | 0.09 | 0.09 | -0.06 | 0.06 | 0.33 | 0.03 |
| AT/AnT | -0.03 | 0.09 | -0.05 | 0.07 | 0.33 | 0.03 |
| GC/GnC | -0.01 | 0.08 | -0.03 | 0.04 | 0.35 | 0.03 |
| TG/CnA | 0.00 | 0.09 | -0.01 | 0.07 | 0.36 | 0.04 |
| TnG/CA | 0.07 | 0.07 | -0.03 | 0.07 | 0.36 | 0.04 |
| TA/TnA | -0.03 | 0.10 | -0.03 | 0.09 | 0.34 | 0.04 |
| CG/CnG | -0.06 | 0.08 | 0.00 | 0.06 | 0.37 | 0.04 |
| Overall | 0.00 | 0.05 | -0.03 | 0.04 | 0.35 | 0.01 |

Table 2-4. Sequence-dependent mechanical rigidities of regular BP steps. The mean and standard deviation are represented in the left and right columns for each coefficient. The standard deviation is calculated by multiplying the diagonal value of the stiffness matrix by the standard deviation of the rise.

| Regular | $\mathbf{B_\tau}$ [pN nm$^2$] | | $\mathbf{B_\rho}$ [pN nm$^2$] | | $\mathbf{C}$ [pN nm$^2$] | |
|---|---|---|---|---|---|---|
| AA/TT | 301.53 | 28.76 | 172.67 | 16.47 | 400.39 | 38.18 |
| AG/CT | 317.62 | 29.97 | 171.36 | 16.17 | 347.47 | 32.78 |
| GA/TC | 277.69 | 26.64 | 170.73 | 16.38 | 344.19 | 33.02 |
| GG/CC | 309.91 | 29.72 | 164.48 | 15.77 | 288.76 | 27.69 |
| AC/GT | 218.91 | 23.85 | 157.40 | 17.15 | 255.39 | 27.82 |
| AT/AT | 263.28 | 26.20 | 161.00 | 16.02 | 332.80 | 33.12 |
| GC/GC | 230.96 | 22.86 | 200.35 | 19.83 | 301.64 | 29.86 |
| TG/CA | 189.65 | 20.22 | 132.03 | 14.08 | 281.44 | 30.01 |
| TA/TA | 174.92 | 17.75 | 123.80 | 12.56 | 309.72 | 31.42 |
| CG/CG | 173.43 | 19.80 | 129.45 | 14.78 | 276.46 | 31.57 |
| Overall | 245.79 | 55.83 | 158.33 | 23.71 | 313.83 | 42.90 |

| Regular | $\mathbf{Y_{Dx}}$ [pN] | | $\mathbf{Y_{Dy}}$ [pN] | | $\mathbf{S}$ [pN] | |
|---|---|---|---|---|---|---|
| AA/TT | 560.96 | 53.50 | 872.97 | 83.25 | 1920.88 | 183.18 |
| AG/CT | 452.93 | 42.73 | 789.85 | 74.52 | 2087.34 | 196.93 |
| GA/TC | 557.64 | 53.50 | 835.18 | 80.12 | 2361.15 | 226.52 |
| GG/CC | 391.30 | 37.52 | 560.77 | 53.77 | 2145.27 | 205.70 |
| AC/GT | 341.17 | 37.17 | 753.74 | 82.12 | 1711.07 | 186.42 |
| AT/AT | 266.11 | 26.48 | 773.42 | 76.97 | 1475.58 | 146.84 |
| GC/GC | 417.69 | 41.35 | 1340.78 | 132.73 | 2270.19 | 224.74 |
| TG/CA | 353.84 | 37.73 | 478.38 | 51.01 | 1396.03 | 148.85 |
| TA/TA | 333.37 | 33.82 | 380.62 | 38.62 | 1483.42 | 150.50 |
| CG/CG | 502.78 | 57.41 | 595.34 | 67.98 | 1401.16 | 160.00 |
| Overall | 417.78 | 99.62 | 738.11 | 267.10 | 1825.21 | 377.37 |

Table 2-5. Sequence-dependent mechanical rigidities of nicked BP steps. The mean and standard deviation are represented in the left and right columns for each coefficient. The standard deviation is calculated by multiplying the diagonal value of the stiffness matrix by the standard deviation of the rise.

| Nicked | $\mathbf{B_\tau}$ [pN nm$^2$] | | $\mathbf{B_\rho}$ [pN nm$^2$] | | $\mathbf{C}$ [pN nm$^2$] | |
|---|---|---|---|---|---|---|
| AA/TnT | 290.14 | 26.04 | 151.36 | 13.59 | 286.61 | 25.72 |
| AnA/TT | 266.41 | 26.66 | 125.85 | 12.59 | 70.31 | 7.04 |
| AG/CnT | 201.45 | 18.40 | 171.05 | 15.63 | 233.34 | 21.32 |
| AnG/CT | 298.20 | 29.83 | 151.99 | 15.21 | 181.74 | 18.18 |
| GA/TnC | 325.46 | 28.28 | 179.17 | 15.57 | 181.00 | 15.73 |
| GnA/TC | 264.98 | 26.14 | 152.94 | 15.09 | 155.48 | 15.34 |
| GG/CnC | 305.26 | 29.09 | 177.56 | 16.92 | 93.54 | 8.91 |
| GnG/CC | 274.88 | 30.13 | 152.00 | 16.66 | 159.88 | 17.52 |
| AC/GnT | 218.39 | 23.12 | 155.95 | 16.51 | 109.01 | 11.54 |
| AnC/GT | 244.64 | 24.90 | 152.75 | 15.55 | 107.29 | 10.92 |
| AT/AnT | 238.99 | 25.07 | 133.80 | 14.04 | 113.60 | 11.92 |
| GC/GnC | 236.59 | 20.83 | 225.72 | 19.87 | 181.73 | 16.00 |
| TG/CnA | 200.61 | 20.22 | 131.42 | 13.25 | 154.61 | 15.59 |
| TnG/CA | 195.50 | 20.62 | 124.14 | 13.10 | 155.75 | 16.43 |
| TA/TnA | 143.69 | 17.80 | 95.40 | 11.82 | 78.61 | 9.74 |
| CG/CnG | 203.66 | 21.56 | 132.67 | 14.04 | 178.67 | 18.91 |
| Overall | 244.30 | 48.87 | 150.86 | 29.41 | 152.57 | 57.12 |

| Nicked | $\mathbf{Y_{Dx}}$ [pN] | | $\mathbf{Y_{Dy}}$ [pN] | | $\mathbf{S}$ [pN] | |
|---|---|---|---|---|---|---|
| AA/TnT | 484.78 | 43.51 | 675.11 | 60.59 | 2090.21 | 187.60 |
| AnA/TT | 417.72 | 41.80 | 375.11 | 37.53 | 1554.08 | 155.50 |
| AG/CnT | 445.44 | 40.69 | 707.18 | 64.60 | 1869.10 | 170.74 |
| AnG/CT | 358.60 | 35.88 | 604.48 | 60.48 | 1715.58 | 171.64 |
| GA/TnC | 447.93 | 38.92 | 637.10 | 55.36 | 2687.06 | 233.49 |
| GnA/TC | 387.43 | 38.22 | 559.23 | 55.17 | 2019.50 | 199.23 |
| GG/CnC | 298.30 | 28.43 | 312.47 | 29.78 | 2119.06 | 201.95 |
| GnG/CC | 383.00 | 41.98 | 516.70 | 56.63 | 1779.80 | 195.06 |
| AC/GnT | 245.79 | 26.02 | 386.34 | 40.90 | 1604.89 | 169.89 |
| AnC/GT | 278.56 | 28.35 | 525.50 | 53.48 | 1858.67 | 189.17 |
| AT/AnT | 226.68 | 23.78 | 275.60 | 28.91 | 1204.57 | 126.36 |
| GC/GnC | 338.34 | 29.79 | 1179.81 | 103.87 | 2399.35 | 211.25 |
| TG/CnA | 280.91 | 28.32 | 465.77 | 46.95 | 1520.04 | 153.22 |
| TnG/CA | 379.03 | 39.98 | 443.81 | 46.82 | 1377.29 | 145.29 |
| TA/TnA | 201.02 | 24.90 | 245.38 | 30.39 | 1093.16 | 135.41 |
| CG/CnG | 427.12 | 45.21 | 513.39 | 54.35 | 1550.75 | 164.16 |
| Overall | 350.04 | 86.31 | 526.44 | 222.42 | 1777.69 | 421.11 |

Table 2-6. Sequence-dependent mechanical coupling coefficients of regular BP steps. The mean and standard deviation are represented in the left and right columns for each coefficient. The standard deviation is calculated by multiplying the off-diagonal value of the stiffness matrix by the standard deviation of the rise.

| Regular | $\mathbf{g}_{\tau\rho}$ [pN nm$^2$] | | $\mathbf{g}_{\tau\omega}$ [pN nm$^2$] | | $\mathbf{g}_{\rho\omega}$ [pN nm$^2$] | |
|---|---|---|---|---|---|---|
| AA/TT | 34.64 | 3.30 | 56.95 | 5.43 | 81.60 | 7.78 |
| AG/CT | 49.66 | 4.69 | 53.35 | 5.03 | 48.35 | 4.56 |
| GA/TC | -5.96 | -0.57 | -29.64 | -2.84 | 95.43 | 9.16 |
| GG/CC | 5.62 | 0.54 | 3.09 | 0.30 | 42.38 | 4.06 |
| AC/GT | 20.26 | 2.21 | 30.88 | 3.36 | 61.24 | 6.67 |
| AT/AT | 6.86 | 0.68 | 1.86 | 0.19 | 69.68 | 6.93 |
| GC/GC | 1.70 | 0.17 | 2.55 | 0.25 | 51.71 | 5.12 |
| TG/CA | -3.66 | -0.39 | -28.65 | -3.05 | 80.55 | 8.59 |
| TA/TA | 5.57 | 0.57 | -5.23 | -0.53 | 106.70 | 10.82 |
| CG/CG | 2.31 | 0.26 | 0.52 | 0.06 | 72.68 | 8.30 |
| Overall | 11.70 | 17.87 | 8.57 | 29.92 | 71.03 | 20.76 |

| Regular | $\mathbf{g}_{\mathbf{DxDy}}$ [pN] | | $\mathbf{g}_{\mathbf{DxDz}}$ [pN] | | $\mathbf{g}_{\mathbf{DyDz}}$ [pN] | |
|---|---|---|---|---|---|---|
| AA/TT | 106.75 | 10.18 | 209.90 | 20.02 | 373.70 | 35.64 |
| AG/CT | -18.85 | -1.78 | 190.45 | 17.97 | 369.88 | 34.90 |
| GA/TC | 74.01 | 7.10 | 102.12 | 9.80 | 509.49 | 48.88 |
| GG/CC | -7.39 | -0.71 | 46.05 | 4.42 | 454.48 | 43.58 |
| AC/GT | 16.90 | 1.84 | 45.34 | 4.94 | 522.58 | 56.93 |
| AT/AT | 4.80 | 0.48 | -15.49 | -1.54 | 281.05 | 27.97 |
| GC/GC | 8.83 | 0.87 | 20.41 | 2.02 | 939.72 | 93.03 |
| TG/CA | -46.57 | -4.96 | -48.68 | -5.19 | 174.33 | 18.59 |
| TA/TA | -0.79 | -0.08 | -5.55 | -0.56 | 262.03 | 26.58 |
| CG/CG | -21.70 | -2.48 | 14.87 | 1.70 | 100.67 | 11.50 |
| Overall | 11.60 | 45.90 | 55.94 | 86.23 | 398.79 | 234.89 |

Table 2-6 (Continued)

| Regular | $\mathbf{g}_{\tau Dx}$ [pN nm] | | $\mathbf{g}_{\tau Dy}$ [pN nm] | | $\mathbf{g}_{\tau Dz}$ [pN nm] | |
|---|---|---|---|---|---|---|
| AA/TT | -30.91 | -2.95 | -43.76 | -4.17 | -319.84 | -30.50 |
| AG/CT | -83.18 | -7.85 | -77.92 | -7.35 | -344.10 | -32.46 |
| GA/TC | -84.87 | -8.14 | 37.97 | 3.64 | -401.74 | -38.54 |
| GG/CC | -135.35 | -12.98 | -54.14 | -5.19 | -392.32 | -37.62 |
| AC/GT | -34.43 | -3.75 | -89.54 | -9.76 | 40.85 | 4.45 |
| AT/AT | -10.37 | -1.03 | 3.11 | 0.31 | 4.51 | 0.45 |
| GC/GC | -123.64 | -12.24 | -16.63 | -1.65 | -13.07 | -1.29 |
| TG/CA | -41.36 | -4.41 | -20.37 | -2.17 | -55.92 | -5.96 |
| TA/TA | -21.11 | -2.14 | 7.57 | 0.77 | -15.79 | -1.60 |
| CG/CG | -138.13 | -15.77 | 24.41 | 2.79 | -0.57 | -0.06 |
| Overall | -70.33 | 49.15 | -22.93 | 42.78 | -149.80 | 187.63 |

| Regular | $\mathbf{g}_{\rho Dx}$ [pN nm] | | $\mathbf{g}_{\rho Dy}$ [pN nm] | | $\mathbf{g}_{\rho Dz}$ [pN nm] | |
|---|---|---|---|---|---|---|
| AA/TT | -30.33 | -2.89 | -70.05 | -6.68 | -90.13 | -8.59 |
| AG/CT | 15.82 | 1.49 | 9.08 | 0.86 | -102.98 | -9.72 |
| GA/TC | -9.69 | -0.93 | -45.22 | -4.34 | -61.43 | -5.89 |
| GG/CC | 26.71 | 2.56 | 14.63 | 1.40 | -10.54 | -1.01 |
| AC/GT | -1.46 | -0.16 | 36.30 | 3.95 | 73.03 | 7.96 |
| AT/AT | 11.12 | 1.11 | 26.75 | 2.66 | 83.95 | 8.35 |
| GC/GC | 1.39 | 0.14 | 91.82 | 9.09 | 211.84 | 20.97 |
| TG/CA | -18.19 | -1.94 | 23.68 | 2.52 | -141.52 | -15.09 |
| TA/TA | 16.48 | 1.67 | 13.86 | 1.41 | -128.83 | -13.07 |
| CG/CG | 11.90 | 1.36 | 71.97 | 8.22 | -180.78 | -20.64 |
| Overall | 2.37 | 17.62 | 17.28 | 47.91 | -34.74 | 123.43 |

| Regular | $\mathbf{g}_{\omega Dx}$ [pN nm] | | $\mathbf{g}_{\omega Dy}$ [pN nm] | | $\mathbf{g}_{\omega Dz}$ [pN nm] | |
|---|---|---|---|---|---|---|
| AA/TT | 37.99 | 3.62 | -206.97 | -19.74 | -300.81 | -28.69 |
| AG/CT | 108.65 | 10.25 | -114.53 | -10.81 | -310.71 | -29.31 |
| GA/TC | 13.20 | 1.27 | -167.93 | -16.11 | -211.56 | -20.30 |
| GG/CC | 78.30 | 7.51 | -227.37 | -21.80 | -310.65 | -29.79 |
| AC/GT | 26.98 | 2.94 | -127.09 | -13.85 | -266.32 | -29.02 |
| AT/AT | -6.57 | -0.65 | -118.97 | -11.84 | -164.19 | -16.34 |
| GC/GC | 8.64 | 0.86 | -236.09 | -23.37 | -363.29 | -35.96 |
| TG/CA | 36.09 | 3.85 | -90.49 | -9.65 | -274.23 | -29.24 |
| TA/TA | 8.62 | 0.87 | -124.01 | -12.58 | -237.07 | -24.05 |
| CG/CG | 25.41 | 2.90 | -73.78 | -8.43 | -335.03 | -38.26 |
| Overall | 33.73 | 35.03 | -148.72 | 57.47 | -277.39 | 59.97 |

Table 2-7. Sequence-dependent mechanical coupling coefficients of nicked BP steps. The mean and standard deviation are represented in the left and right columns for each coefficient. The mean and standard deviation were calculated by multiplying the off-diagonal value of the stiffness matrix by the mean and standard deviation of the rise.

| Nicked | $\mathbf{g}_{\tau\rho}$ [pN nm$^2$] | | $\mathbf{g}_{\tau\omega}$ [pN nm$^2$] | | $\mathbf{g}_{\rho\omega}$ [pN nm$^2$] | |
|---|---|---|---|---|---|---|
| AA/TnT | 31.26 | 2.81 | 67.62 | 6.07 | 49.33 | 4.43 |
| AnA/TT | 22.05 | 2.21 | 13.95 | 1.40 | 8.67 | 0.87 |
| AG/CnT | 6.67 | 0.61 | -11.18 | -1.02 | 80.22 | 7.33 |
| AnG/CT | 39.99 | 4.00 | 32.73 | 3.27 | 42.16 | 4.22 |
| GA/TnC | -27.46 | -2.39 | 22.90 | 1.99 | 46.99 | 4.08 |
| GnA/TC | 0.74 | 0.07 | -13.49 | -1.33 | 37.70 | 3.72 |
| GG/CnC | -21.69 | -2.07 | 30.51 | 2.91 | 20.34 | 1.94 |
| GnG/CC | 1.41 | 0.15 | -42.54 | -4.66 | 24.92 | 2.73 |
| AC/GnT | 9.09 | 0.96 | 23.99 | 2.54 | 24.75 | 2.62 |
| AnC/GT | 43.41 | 4.42 | 4.89 | 0.50 | 40.29 | 4.10 |
| AT/AnT | -17.29 | -1.81 | -5.24 | -0.55 | 43.67 | 4.58 |
| GC/GnC | -16.50 | -1.45 | 11.82 | 1.04 | 6.80 | 0.60 |
| TG/CnA | -16.62 | -1.68 | -12.14 | -1.22 | 33.39 | 3.37 |
| TnG/CA | -6.46 | -0.68 | -25.80 | -2.72 | 43.16 | 4.55 |
| TA/TnA | -11.07 | -1.37 | 2.78 | 0.34 | 21.35 | 2.65 |
| CG/CnG | -4.91 | -0.52 | 26.97 | 2.85 | 35.91 | 3.80 |
| Overall | 2.04 | 22.02 | 7.99 | 26.71 | 34.98 | 17.74 |

| Nicked | $\mathbf{g}_{\mathbf{DxDy}}$ [pN] | | $\mathbf{g}_{\mathbf{DxDz}}$ [pN] | | $\mathbf{g}_{\mathbf{DyDz}}$ [pN] | |
|---|---|---|---|---|---|---|
| AA/TnT | 66.56 | 5.97 | 186.54 | 16.74 | 341.34 | 30.64 |
| AnA/TT | 113.27 | 11.33 | 74.07 | 7.41 | 130.68 | 13.08 |
| AG/CnT | 94.54 | 8.64 | 134.43 | 12.28 | 350.56 | 32.02 |
| AnG/CT | 81.75 | 8.18 | 116.62 | 11.67 | 226.87 | 22.70 |
| GA/TnC | 54.01 | 4.69 | 204.61 | 17.78 | 417.24 | 36.26 |
| GnA/TC | 55.18 | 5.44 | 95.38 | 9.41 | 347.20 | 34.25 |
| GG/CnC | 40.45 | 3.86 | 6.68 | 0.64 | 274.96 | 26.20 |
| GnG/CC | -103.97 | -11.39 | 222.78 | 24.42 | 79.20 | 8.68 |
| AC/GnT | 3.99 | 0.42 | 71.93 | 7.61 | 353.19 | 37.39 |
| AnC/GT | 75.21 | 7.65 | 88.65 | 9.02 | 444.22 | 45.21 |
| AT/AnT | -22.22 | -2.33 | -18.12 | -1.90 | 21.04 | 2.21 |
| GC/GnC | 19.33 | 1.70 | -10.07 | -0.89 | 816.80 | 71.91 |
| TG/CnA | -65.33 | -6.58 | -35.51 | -3.58 | 116.63 | 11.76 |
| TnG/CA | -31.10 | -3.28 | 80.50 | 8.49 | 69.81 | 7.36 |
| TA/TnA | 26.38 | 3.27 | 61.41 | 7.61 | 175.45 | 21.73 |
| CG/CnG | -59.11 | -6.26 | 8.66 | 0.92 | 95.11 | 10.07 |
| Overall | 21.81 | 63.06 | 80.54 | 79.11 | 266.27 | 199.68 |

Table 2-7 (Continued).

| Nicked | $\mathbf{g}_{\tau Dx}$ [pN nm] | | $\mathbf{g}_{\tau Dy}$ [pN nm] | | $\mathbf{g}_{\tau Dz}$ [pN nm] | |
|---|---|---|---|---|---|---|
| AA/TnT | -27.83 | -2.50 | -66.30 | -5.95 | -310.03 | -27.83 |
| AnA/TT | -27.26 | -2.73 | 38.30 | 3.83 | -237.65 | -23.78 |
| AG/CnT | -71.08 | -6.49 | 23.52 | 2.15 | -147.10 | -13.44 |
| AnG/CT | -59.02 | -5.91 | 12.91 | 1.29 | -286.55 | -28.67 |
| GA/TnC | -120.75 | -10.49 | 12.57 | 1.09 | -452.28 | -39.30 |
| GnA/TC | -89.55 | -8.83 | 79.29 | 7.82 | -328.75 | -32.43 |
| GG/CnC | -122.11 | -11.64 | -97.20 | -9.26 | -353.33 | -33.67 |
| GnG/CC | -147.25 | -16.14 | 93.38 | 10.23 | -339.50 | -37.21 |
| AC/GnT | -60.26 | -6.38 | -73.25 | -7.75 | 48.44 | 5.13 |
| AnC/GT | -31.40 | -3.20 | -6.71 | -0.68 | 5.82 | 0.59 |
| AT/AnT | -18.47 | -1.94 | 14.36 | 1.51 | 70.88 | 7.44 |
| GC/GnC | -138.14 | -12.16 | -19.00 | -1.67 | 41.64 | 3.67 |
| TG/CnA | -68.88 | -6.94 | -51.49 | -5.19 | -11.78 | -1.19 |
| TnG/CA | -98.71 | -10.41 | -4.98 | -0.52 | -105.70 | -11.15 |
| TA/TnA | -16.64 | -2.06 | -48.42 | -6.00 | -78.89 | -9.77 |
| CG/CnG | -175.43 | -18.57 | 9.41 | 1.00 | 93.84 | 9.93 |
| Overall | -79.55 | 50.05 | -5.23 | 52.82 | -149.43 | 180.24 |

| Nicked | $\mathbf{g}_{\rho Dx}$ [pN nm] | | $\mathbf{g}_{\rho Dy}$ [pN nm] | | $\mathbf{g}_{\rho Dz}$ [pN nm] | |
|---|---|---|---|---|---|---|
| AA/TnT | -32.85 | -2.95 | -7.03 | -0.63 | -59.67 | -5.36 |
| AnA/TT | -33.31 | -3.33 | -0.75 | -0.08 | -43.74 | -4.38 |
| AG/CnT | -21.85 | -2.00 | -4.34 | -0.40 | -107.53 | -9.82 |
| AnG/CT | 1.33 | 0.13 | -5.52 | -0.55 | -125.54 | -12.56 |
| GA/TnC | -7.43 | -0.65 | 28.29 | 2.46 | -5.81 | -0.50 |
| GnA/TC | 10.57 | 1.04 | 39.89 | 3.93 | -3.31 | -0.33 |
| GG/CnC | 25.32 | 2.41 | 39.97 | 3.81 | -59.60 | -5.68 |
| GnG/CC | -17.22 | -1.89 | 54.21 | 5.94 | -41.63 | -4.56 |
| AC/GnT | -15.20 | -1.61 | 82.57 | 8.74 | 78.52 | 8.31 |
| AnC/GT | -14.71 | -1.50 | 28.14 | 2.86 | 0.11 | 0.01 |
| AT/AnT | 20.77 | 2.18 | 8.39 | 0.88 | -26.42 | -2.77 |
| GC/GnC | -11.14 | -0.98 | 168.19 | 14.81 | 214.44 | 18.88 |
| TG/CnA | -27.78 | -2.80 | 51.82 | 5.22 | -157.29 | -15.86 |
| TnG/CA | -16.73 | -1.76 | 36.08 | 3.81 | -135.67 | -14.31 |
| TA/TnA | 4.29 | 0.53 | 22.01 | 2.73 | -78.58 | -9.73 |
| CG/CnG | -18.38 | -1.95 | 66.90 | 7.08 | -200.43 | -21.22 |
| Overall | -9.64 | 17.69 | 38.05 | 43.80 | -47.01 | 98.36 |

Table 2-7 (Continued).

| Nicked | $\mathbf{g}_{\omega Dx}$ [pN nm] | | $\mathbf{g}_{\omega Dy}$ [pN nm] | | $\mathbf{g}_{\omega Dz}$ [pN nm] | |
|---|---|---|---|---|---|---|
| AA/TnT | -3.00 | -0.27 | -143.15 | -12.85 | -274.44 | -24.63 |
| AnA/TT | 80.93 | 8.10 | -51.19 | -5.12 | -93.28 | -9.33 |
| AG/CnT | 3.54 | 0.32 | -147.34 | -13.46 | -181.10 | -16.54 |
| AnG/CT | 119.35 | 11.94 | -126.19 | -12.63 | -182.00 | -18.21 |
| GA/TnC | -92.72 | -8.06 | -124.40 | -10.81 | -257.20 | -22.35 |
| GnA/TC | 88.15 | 8.70 | -139.39 | -13.75 | -171.31 | -16.90 |
| GG/CnC | -56.45 | -5.38 | -84.93 | -8.09 | -176.98 | -16.87 |
| GnG/CC | 138.65 | 15.20 | -142.39 | -15.61 | -141.33 | -15.49 |
| AC/GnT | -53.18 | -5.63 | -63.98 | -6.77 | -155.16 | -16.42 |
| AnC/GT | 74.83 | 7.62 | -56.47 | -5.75 | -170.80 | -17.38 |
| AT/AnT | -65.71 | -6.89 | -18.30 | -1.92 | -70.62 | -7.41 |
| GC/GnC | -82.35 | -7.25 | -200.21 | -17.63 | -291.72 | -25.68 |
| TG/CnA | -50.58 | -5.10 | -103.10 | -10.39 | -178.02 | -17.94 |
| TnG/CA | 76.66 | 8.09 | -93.78 | -9.89 | -165.23 | -17.43 |
| TA/TnA | -67.53 | -8.36 | -27.52 | -3.41 | -112.30 | -13.91 |
| CG/CnG | -94.97 | -10.05 | -86.66 | -9.17 | -224.17 | -23.73 |
| Overall | 0.98 | 82.11 | -100.56 | 49.48 | -177.85 | 61.00 |

### 2.2.4. Mechanical properties of a base-pair step

MD trajectories of base-pair (BP) steps were analyzed based on a mechanical model with quasi-harmonic strain energy. Six BP step parameters describe bending (tilt and roll denoted by $\tau$ and $\rho$), torsional (twist denoted by $\omega$), shearing (shift and slide denoted by Dx and Dy), and stretching (rise denoted by Dz) modes. The strain energy for the six deformable modes in BP steps was assumed to the following form

$$\mathrm{E}(\mathbf{U}) = \frac{1}{2}\mathbf{U}^T\mathbf{K}\mathbf{U} = \frac{1}{2}(\mathbf{x} - \langle\mathbf{x}\rangle)^T\mathbf{K}(\mathbf{x} - \langle\mathbf{x}\rangle) \tag{2-1}$$

where $\mathbf{x}$ represents the coordinate vector of BP step parameters as $\mathbf{x} = [\tau\ \rho\ \omega\ \mathrm{Dx}\ \mathrm{Dy}\ \mathrm{Dz}]^T$, whose average is denoted as the angle bracket, $\mathbf{U}$ is displacement vector whose components indicate the displacement from the average configuration, and $\mathbf{K}$ is a positive definite stiffness matrix where the six diagonal and remaining symmetric off-diagonal terms represent mechanical stiffness (bending, torsion, shearing, and stretching) and coupling stiffness, respectively.

The probability distribution of BP step parameters can be approximated to an N-dimensional Gaussian function assuming moderate fluctuations under harmonic potential in contact with a heat bath of a certain temperature. The covariance matrix of the BP step parameters was used to induce the stiffness matrix of a BP step[38,39] as

$$\mathbf{K} = \mathrm{k_B}\mathrm{T}\mathbf{F}^{-1} \tag{2-2}$$

where $\mathrm{k_B}$ is the Boltzmann constant, $\mathrm{T}$ is the absolute temperature used in MD simulation, and $\mathbf{F}$ is the covariance matrix. Here, the covariance matrix was obtained using from the sampled MD trajectories of the BP step parameters[19] as

$$\mathrm{F_{ij}} = \langle(\mathrm{x_i} - \langle\mathrm{x_i}\rangle)(\mathrm{x_j} - \langle\mathrm{x_j}\rangle)\rangle \tag{2-3}$$

The strain energy is rewritten as diagonal and off-diagonal components as

$$E(\mathbf{U}) = \frac{1}{2}\sum_{i} K_{ii}U_i^2 + \sum_{i\neq j} K_{ij}U_iU_j \tag{2-4}$$

where $i$ and $j$ represent the BP step parameters as $\tau, \rho, \omega, Dx, Dy,$ and $Dz$. Diagonal terms contribute to mechanical rigidities corresponding to the six BP step parameters, and mechanical coupling coefficients are derived from off-diagonal terms between two BP step parameters. Mechanical rigidities of a BP step were then obtained by multiplying the diagonal stiffness components to the axial length of a BP step from linear elastic theory as

$$\begin{aligned} B_\tau &= K_{\tau\tau}\langle Dz\rangle \\ B_\rho &= K_{\rho\rho}\langle Dz\rangle \\ C &= K_{\omega\omega}\langle Dz\rangle \\ Y_{Dx} &= K_{DxDx}\langle Dz\rangle \\ Y_{Dy} &= K_{DyDy}\langle Dz\rangle \\ S &= K_{DzDz}\langle Dz\rangle \end{aligned} \tag{2-5}$$

where $B_\tau$ and $B_\rho$ represent bending rigidities corresponding to tilt and roll, $C$ is torsional rigidity, $Y_{Dx}$ and $Y_{Dy}$ indicate shear rigidities corresponding to shift and slide, $S$ is stretching rigidity, and $\langle Dz\rangle$ is the average of the rise, respectively. The equivalent isotropic bending or shearing rigidities ($B$ or $Y$) were obtained using the harmonic mean of anisotropic bending ($B_\tau$ and $B_\rho$) or shearing rigidities ($Y_{Dx}$ and $Y_{Dy}$), respectively as

$$B = \frac{2B_\tau B_\rho}{B_\tau + B_\rho} \tag{2-6}$$

$$Y = \frac{2Y_{Dx}Y_{Dy}}{Y_{Dx} + Y_{Dy}} \tag{2-7}$$

Likewise, mechanical coupling coefficients of a BP step were calculated by multiplying the off-diagonal stiffness to the axial length of the BP step as

$$g_{ij} = K_{ij}\langle Dz\rangle \tag{2-8}$$

where $g_{ij}$ is the mechanical coupling coefficients of two BP step parameters.

### 2.2.5. Elastic theory for the base-pair step

Mechanical rigidities were derived as assuming DNA structures of a homogeneous linear elastic material. The initial shape was assumed to have an area (A) and length (L) with axial z-direction. Then, the representative mechanical rigidities ($B_\tau$, $B_\rho$, C, $Y_{Dx}$, $Y_{Dy}$, and S) were derived by elastic theory (Figure 2-8).

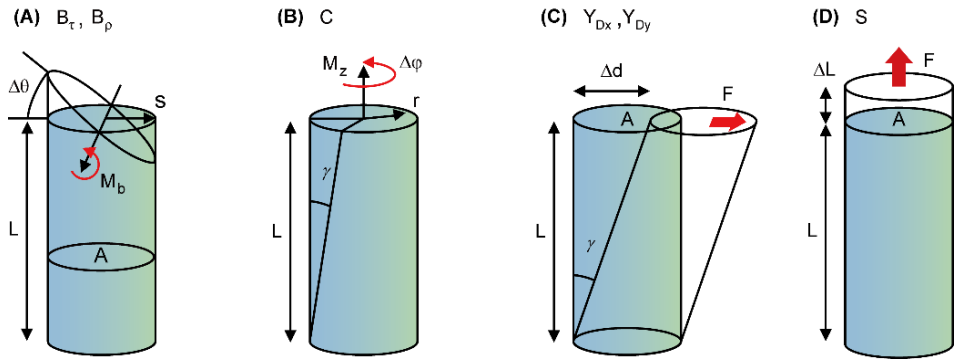


Figure 2-8. Mechanical properties for the BP step. $B_\tau$ and $B_\rho$ represent the bending rigidities, C indicates the torsional rigidity, $Y_{Dx}$ and $Y_{Dy}$ represent the shearing rigidities, and S indicates the stretching rigidity.

#### 2.2.5.1. Bending rigidities.

Bending moment ($M_b$) is obtained by integrating the axial stress ($\sigma_{zz}$) multiplied by the moment arm (s) perpendicular to the direction of bending moment over the cross-section area (A) as

$$M_b = \int_A \sigma_{zz} s dA = EI\frac{\Delta\theta}{L} \tag{2-9}$$

where axial stress, axial strain, and the second moment of area are defined as

$$\sigma_{zz} = E\varepsilon_{zz} = E\frac{\Delta\theta}{L} \tag{2-10}$$

$$\varepsilon_{zz} = \frac{\Delta\theta}{L} \tag{2-11}$$

$$I = \int_A s^2 dA \tag{2-12}$$

Bending rigidity (EI) is then evaluated as

$$EI = \frac{M_b}{\Delta\theta} L = k_{bending} L \tag{2-13}$$

where $k_{bending}$ is the stiffness defined by the ratio of applied bending moment and corresponding bending deformation. Bending rigidities of DNA, therefore, can be calculated in terms of components of stiffness matrix and BP step parameters as

$$B_\tau = (EI)_\tau = K_{\tau\tau}\langle Dz\rangle \tag{2-14}$$

$$B_\rho = (EI)_\rho = K_{\rho\rho}\langle Dz\rangle \tag{2-15}$$

where $B_\tau$ and $B_\rho$ represent tilt and roll bending rigidities, and $K_{\tau\tau}$ and $K_{\rho\rho}$ indicate the diagonal tilt and roll components in the stiffness matrix, respectively.

#### 2.2.5.2. Torsional rigidity.

Torsional moment ($M_z$) is obtained by integrating the shear stress ($\sigma_\tau$) multiplied by the moment arm (r) over the cross-section area (A) as

$$M_z = \int_A \sigma_\tau r dA = GJ\frac{\Delta\varphi}{L} \tag{2-16}$$

where shear stress ($\sigma_\tau$), shear strain ($\gamma$), and the second polar moment of area (J) are defined as

$$\sigma_\tau = G\gamma = G\frac{r\Delta\varphi}{L} \tag{2-17}$$

$$\gamma = \frac{r\Delta\varphi}{L} \tag{2-18}$$

$$J = \int_A r^2 dA \tag{2-19}$$

Then, the torsional rigidity (GJ) is evaluated as

$$GJ = \frac{M_t}{\Delta\varphi} L = k_{torsion} L \tag{2-20}$$

where $k_{torsion}$ is the stiffness defined by the ratio of applied torsional moment and corresponding torsional deformation. Therefore, we obtained the torsional rigidity of DNA corresponding to the twist parameter as

$$C = GJ = K_{\omega\omega}\langle Dz \rangle \tag{2-21}$$

where $C$ is generally referred to as torsional rigidity of DNA, and $K_{\omega\omega}$ is the diagonal twist component in the stiffness matrix.

**2.2.5.3. Shearing rigidities.**

Shearing rigidity is derived from the shear modulus (G) defined by the ratio of shear stress ($\sigma_\tau$) to the shear strain ($\gamma$) as

$$G = \frac{\sigma_\tau}{\gamma} = \frac{F/A}{\Delta d/L} = \frac{FL}{A\Delta d} \tag{2-22}$$

where $F$ and $\Delta L$ are the applied shear force and corresponding shear displacement. The shearing rigidity (GA) is then obtained as

$$GA = \frac{F}{\Delta L} L = k_{shearing} L \tag{2-23}$$

where $k_{shearing}$ is the stiffness defined by the ratio of applied shear force and corresponding displacement. We then obtained the shearing rigidities of DNA as

$$Y_{Dx} = (GA)_{Dx} = K_{DxDx}\langle Dz\rangle \tag{2-24}$$

$$Y_{Dy} = (GA)_{Dy} = K_{DyDy}\langle Dz\rangle \tag{2-25}$$

where $Y_{Dx}$ and $Y_{Dy}$ denote shearing rigidities corresponding to the shift and slide, and $K_{DxDx}$ and $K_{DyDy}$ are the diagonal shift and slide components in the stiffness matrix, respectively.

#### 2.2.5.4. Stretching rigidity.

Stretching rigidity is derived from Young's modulus (E) defined as the ratio of axial stress ($\sigma_{zz}$) to the axial strain ($\varepsilon_{zz}$) as

$$E = \frac{\sigma_{zz}}{\varepsilon_{zz}} = \frac{F/A}{\Delta L/L} = \frac{FL}{A\Delta L} \tag{2-26}$$

where $F$ and $\Delta L$ are the applied axial force and axial displacement. Stretching rigidity (EA) is evaluated as

$$EA = \frac{F}{\Delta L}L = k_{stretching}L \tag{2-27}$$

where $k_{stretching}$ is the stiffness defined by the ratio of applied axial force and corresponding displacement. Therefore, the stretching rigidity of DNA is obtained corresponding to the rise mode as

$$S = EA = K_{DzDz}\langle Dz\rangle \tag{2-28}$$

where $S$ is generally referred to the axial rigidity of DNA, and $K_{DzDz}$ is the diagonal component corresponding to the rise parameter in the stiffness matrix.

### 2.2.6. Equivalent isotropic rigidities in bending and shearing

Assuming a homogeneous linear elastic material, if a transverse load was applied to a beam, whose axis system coincides with the principal axes of bending, three-dimensional beam theory implies the following displacement field as

$$u_z = y\theta_x(z) - x\theta_y(z) \tag{2-29}$$

where z is the axial direction of the beam, x and y are the planar directions on the cross-section of the beam, and $\theta_x$ and $\theta_y$ are rigid-body rotations of the cross-section respectively. The strain field can be evaluated by the differentiation of the displacement field as

$$\varepsilon_{zz} = y\kappa_x(z) - x\kappa_y(z) \tag{2-30}$$

$$\varepsilon_{xx} = \varepsilon_{yy} = \gamma_{xy} = \gamma_{yz} = \gamma_{xz} = 0 \tag{2-31}$$

where the curvatures are defined as

$$\kappa_x = \frac{d\theta_x}{dz} \tag{2-32}$$

$$\kappa_y = \frac{d\theta_y}{dz} \tag{2-33}$$

The axial stress is described by Hooke's law as

$$\sigma_{zz} = E\varepsilon_{zz} = E[y\kappa_x(z) - x\kappa_y(z)] \tag{2-34}$$

The strain energy ($\pi$) stored in the beam with anisotropic bending rigidities is evaluated as

$$\pi = \int_z \int_A \frac{1}{2}\sigma_{zz}\varepsilon_{zz}\,dA\,dz = \int_z \frac{1}{2}(EI_y\kappa_x^2 + EI_x\kappa_y^2)\,dz \tag{2-35}$$

where $I_x$ and $I_y$ are the second moment of the area with respect to x- and y-directions on the cross-section.

When an equivalent isotropic beam is assumed, the force equation under a bending moment is found as

$$M_b = EI_y\kappa_x = EI_x\kappa_y = EI_{eqv}\kappa_{eqv} \tag{2-36}$$

If the strain energy stored in anisotropic and equivalent beams is the same, the following equation is satisfied

$$\begin{aligned}\pi &= \int_z \frac{1}{2}\left(EI_y\kappa_x^2 + EI_x\kappa_y^2\right)dz = \int_z \frac{1}{2}\left(\frac{M_b^2}{EI_x} + \frac{M_b^2}{EI_y}\right)dz \\ &= \int_z \frac{1}{2}\left(EI_{eqv}\kappa_{eqv}^2 + EI_{eqv}\kappa_{eqv}^2\right)dz = \int_z \frac{1}{2}\left(\frac{2M_b^2}{EI_{eqv}}\right)dz\end{aligned} \tag{2-37}$$

Equivalent bending rigidity ($B$ or $EI_{eqv}$) is then obtained by the harmonic mean of anisotropic bending rigidities as

$$B = \frac{2B_\tau B_\rho}{B_\tau + B_\rho} \tag{2-38}$$

or

$$EI_{eqv} = \frac{2EI_xEI_y}{EI_x + EI_y} \tag{2-39}$$

Likewise, equivalent shearing rigidity ($Y$ or $GA_{eqv}$) is obtained as

$$Y = \frac{2Y_{Dx}Y_{Dy}}{Y_{Dx} + Y_{Dy}} \tag{2-40}$$

or

$$GA_{eqv} = \frac{2GA_xGA_y}{GA_x + GA_y} \tag{2-41}$$

## 2.3. Mechanical rigidities of base-pair steps

We first examined the mechanical rigidities of regular BP steps (Figure 2-9). On the whole, the mechanical rigidities of regular BP steps were consistent with the ones determined in other experimental or computational studies. The calculated bending, torsional, shearing, and stretching rigidities were $B_{\tau}^{regular}$ = 246 ± 56 pN nm$^2$, $B_{\rho}^{regular}$ = 158 ± 24 pN nm$^2$, $C^{regular}$ = 314 ± 43 pN nm$^2$, $Y_{Dx}^{regular}$ = 418 ± 100 pN, $Y_{Dy}^{regular}$ = 738 ± 267 pN, and $S^{regular}$ = 1825 ± 377 pN, respectively (Table 2-4), which were comparable to the reference values in literature[24,25,39,41-54] ($B_{\tau}^{ref}$ = 236 ± 27 pN nm$^2$, $B_{\rho}^{ref}$ = 133 ± 34 pN nm$^2$, $C^{ref}$ = 317 ± 108 pN nm$^2$, $Y_{Dx}^{ref}$ = 323 ± 68 pN, $Y_{Dy}^{ref}$ = 526 ± 155 pN, and $S^{ref}$ = 1343 ± 631 pN). Here, $B_{\tau}$ and $B_{\rho}$ represent the bending rigidities corresponding to tilt and roll, $C$ is the torsional rigidity, $Y_{Dx}$ and $Y_{Dy}$ denote the shearing rigidities in shift and slide, and $S$ is the stretching rigidity. Our results confirmed the known fact that BP steps were more flexible to bend or shear toward the grooves than toward phosphate backbones because atoms are distributed wider in the direction of backbone sites, and more severe steric clashes occur when tilted or shifted than rolled or slid, respectively[55].

The obtained mechanical rigidities clearly show, as in the previous studies[24,25,52,53], the dependence on the sequence of a BP step including the effect of stacking order due to the chirality of DNA. For example, GC/GC and CG/CG steps exhibited the highest and lowest bending rigidities in roll, respectively, among all regular BP steps even though their constituent nucleobases were the same. A similar difference in the mechanical rigidities was observed for AT/AT and TA/TA steps as well. Further investigation of the results confirmed the dependence of DNA rigidities on the BP step group (Figure 2-9). The regular BP steps can be categorized into three BP step groups: purine-purine group denoted here as RR/YY (AA/TT, AG/CT, GA/TC, and GG/CC steps), the purine-pyrimidine group as RY/RY (AC/GT, AT/AT, and GC/GC steps), and the pyrimidine-purine group as YR/YR (TG/CA, TA/TA, and CG/CG steps) where R and Y represent purine and pyrimidine, respectively.

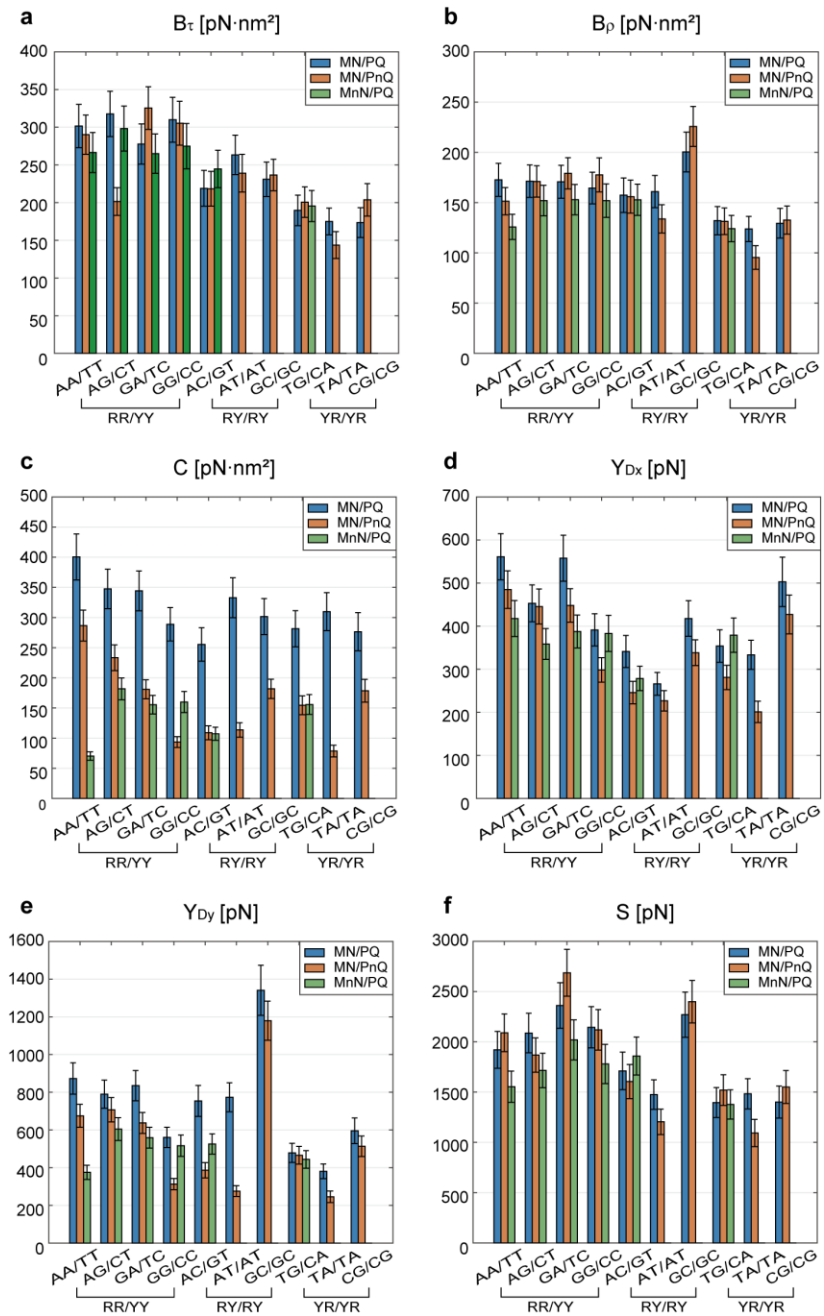


Figure 2-9. Mechanical rigidities of regular and nicked BP steps. Six figures represent (**a**) tilt-bending, (**b**) roll-bending, (**c**) torsional, (**d**) shift-shearing, (**e**) slide-shearing, and (**f**) stretching rigidities, respectively using average mechanical rigidities. Blue represents the rigidities of regular BP steps (MN/PQ) while orange and green indicate the values of nicked BP steps (MN/PnQ or MnN/PQ).

RR/YY group demonstrated relatively high rigidities, in general, whereas the YR/YR group exhibited low rigidities for all deformation modes. RY/RY group had intermediate rigidities, but GC/GC step was exceptionally stiffer in deformation modes of roll, slide, and rise than the other BP steps. It was reported that the structural difference among these BP step groups determined the stereochemical characteristics of a BP step affecting the BP step parameters and mechanical rigidities in equilibrium[55,56]. Also, these results were qualitatively parallel to those of earlier computational studies demonstrating that, for dinucleoside monophosphates, RR pair showed the strongest stacking force followed by RY pair while YR and YY pairs had relatively weaker stacking force similar to each other[57,58].

When introducing a nick to each regular BP step, we observed a considerable decrease in the torsional rigidity from $C^{regular} = 314 \pm 43$ pN nm$^2$ to $C^{nicked} = 153 \pm 57$ pN nm$^2$ on average amount approximately to 52% reduction (Figure 2-9C, Table 2-4, and Table 2-5). The softening effect of a nick in torsion was universal regardless of the location of the nick (MnN/PQ or MN/PnQ steps) as well as the sequence variation. Strikingly, we observed a drastic effect of nick location on the torsional rigidity for the AA/TT step. The maximum and minimum reductions were 82% of the AnA/TT step and 28% of the AA/TnT step, respectively. AA/TT step showed the highest torsional rigidity among all regular BP steps, and it was still the strongest in torsion when a nick was introduced at the TT site (AA/TnT step). However, when a nick was located at the AA site (AnA/TT step), the torsional rigidity was significantly reduced and became the most flexible nicked BP step. For the shearing rigidities, smaller softening effect of a nick was predicted where the reduction ratio ranged from 2% (AG/CnT step) to 40% (TA/TnA step) for the shift, and from 3% (TG/CnA step) to 64% (AT/AnT step) for slide leading to the mean reduction ratio of 22% (Figure 2-9D and E). Except for the case of TnG/CA whose shearing rigidity in the shift was slightly increased by 7%, all the other BP steps became flexible in both shift and slide with a nick. These results suggest that one of the primary structural roles of a nick could be the relaxation of torsional constraint by sugar-phosphate backbones known to be responsible for relatively high torsional

rigidity of DNA[59-61].

On the contrary, the bending and stretching rigidities of nicked BP steps ($B_\tau^{nicked}$ = 244 ± 49 pN nm$^2$, $B_\rho^{nicked}$ = 151 ± 29 pN nm$^2$, and $S^{nicked}$ = 1778 ± 421 pN) did not considerably deviate from the rigidities of regular BP steps on average with the maximum deviations of 22% for bending (AnA/TT step) and 26% for stretching (TA/TnA step), respectively (Figure 2-9). More interestingly, we could observe not only softening but also the stiffening effect of a nick depending on the sequence of BP steps. Six nicked BP steps (GA/TnC, AnC/GT, GC/GnC, TG/CnA, TnG/CA, and CG/CnG) showed the increased bending rigidity in tilt by 10% on average, four BP steps (GA/TnC, GG/CnC, GC/GnC, and CG/CnG) for the bending rigidity in roll by 7%, and six BP steps (AA/TnT, GA/TnC, AnC/GT, GC/GnC, TG/CnA, and CG/CnG) for the stretching rigidity by 9%. These results suggest that BP steps may adopt another equilibrium configuration where the base stacking force, a dominant factor to maintain the stability of BP steps without covalent bonds[27,28,62], becomes stronger. Perhaps, this stable equilibrium configuration is inaccessible for regular BP steps due to the constraints by backbones but becomes accessible for certain BP steps when one of the backbones was broken, and the backbone restrictions were released in consequence. To identify the stiffened conformation from MD traces, we looked more closely into GA/TnC, GC/GnC, and CG/CnG steps whose stretching and bending rigidities were increased by a nick. We found that these steps commonly exhibited the decrease in roll and shift parameters (Figure 2-4 and Figure 2-10), indicating that BP steps bend toward the minor groove. This result agrees with a previous study where the persistence length of DNA was found to be larger when BP steps bent toward the minor groove than when toward the major groove due to the difference in groove hydration[63].

We observed that a nick did not change the overall dependence of DNA rigidities on the BP step group. However, the location of a nick was a crucial factor in determining the mechanical rigidities of the purine-purine group (RR/YY). RR/YnY group was usually stiffer than RnR/YY group in every deformation mode and, on certain occasions, even stiffer than the regular RR/YY group. This was

probably because the RR pair exhibited much stronger stacking forces than YY pair and, therefore, dominated the mechanical rigidities of regular and nicked RR/YY group. As a result, RR/YnY group was naturally stiffer than RnR/YY group in general and could be even stiffer than regular RR/YY group in some instances if a nick induced a conformational transition of BP step to a more stable configuration.

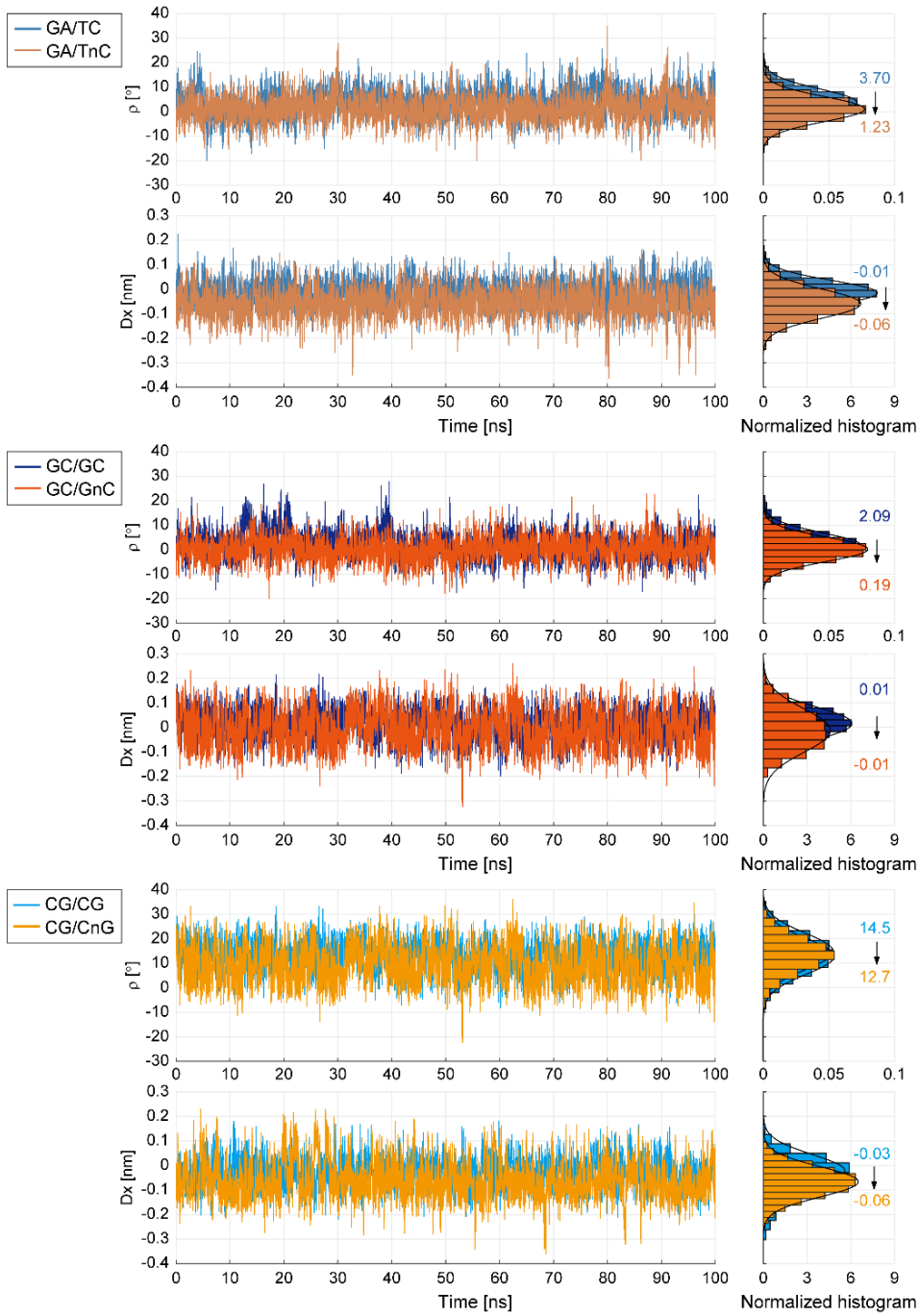


Figure 2-10. Comparison of the BP step parameters in stiffened BP steps by a nick. GA/TnC, GC/GnC, and CG/CnG steps were stiffened by a nick for the stretching and bending rigidities with the decrease of the roll (ρ) and shift (Dx).

## 2.4. Mechanical coupling coefficients of base-pair steps

The stiffness matrices obtained from MD trajectories of all regular and nicked BP steps also provide the mechanical coupling coefficients ($g_{ij}$), which are the off-diagonal terms of the stiffness matrix multiplied by the mean rise, indicating the correlation between two BP step parameters. Results indicated that nicks weakened, to some extent, the overall mechanical coupling of BP step parameters, but their effect was not strong enough to alter the overall pattern of the stiffness matrix or the correlation map (Figure 2-11, Table 2-6, and Table 2-7). Positively correlated BP step parameters in a regular BP step remained positively correlated in the corresponding nicked BP step as well. Similarly, highly correlated ones remained highly correlated with a nick. We could reproduce one of the well-known mechanical couplings, the twist-stretch coupling, which is the counterintuitive mechanical behavior of DNA revealed by recent experimental[41,42] and computational studies[39,40,54]. The negative mechanical coupling coefficient of twist and rise, which we obtained as $g_{\omega Dz}^{regular}$ = –277 ± 60 pN nm, was consistent with the reference value, $g_{\omega Dz}^{ref}$ = –222 ± 12 pN nm, reported in previous MD studies[39,54], which was predicted to reduce to $g_{\omega Dz}^{nicked}$ = –178 ± 61 pN nm for nicked BP steps on average in this study. We also obtained negative mechanical coupling coefficients for twist-slide as $g_{\omega Dy}^{regular}$ = –149 ± 57 pN nm and $g_{\omega Dy}^{nicked}$ = –101 ± 50 pN nm, respectively, in agreement with the reported value of $g_{\omega Dy}^{ref}$ = –222 ± 95 pN nm[39] demonstrating that, when DNA is over-twisted, it elongated with the reduction of the inter-strand distance corresponding to slide in our study as long as base-stacking and base-pairing were maintained without base separation (Figure 2-12).

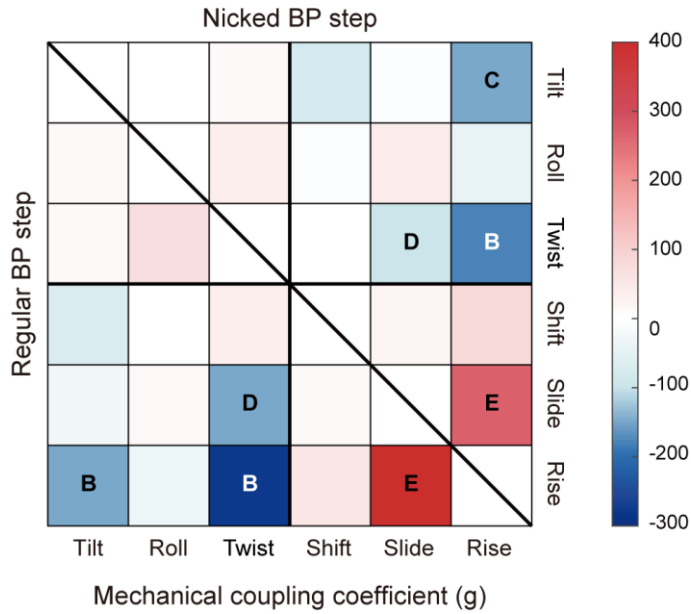


Figure 2-11. Pixel plot of mechanical coupling coefficients of regular and nicked BP steps. Overall mechanical coupling coefficients in off-diagonal squares are illustrated with a blue and red color gradient. Diagonal values for rigidities are not illustrated. Lower left and upper right squares divided by a slope represent coupling coefficients of regular and nicked BP steps, respectively. Four three by three plots also subdivide this pixel plot with different coupled modes: the upper left plots for rotation-rotation, the upper right and lower left plots for rotation-translation, and the lower right plots for translation-translation.

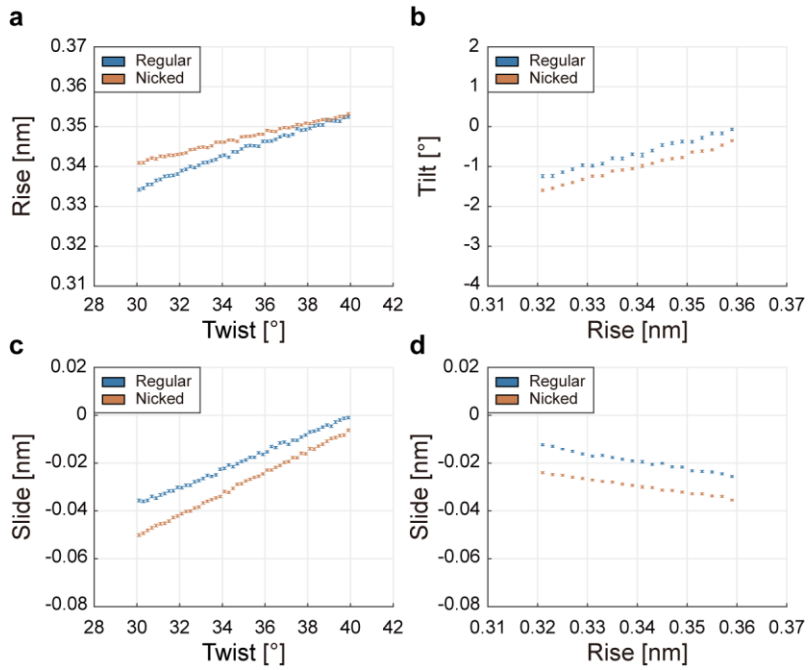


Figure 2-12. Correlation plots of four primary mechanical coupling coefficients for regular and nicked BP steps. These plots represent the correlation between (**a**) rise to twist, (**b**) tilt to rise, (**c**) slide to twist, and (**d**) slide to rise. Domains were divided into intervals of 0.2° and 0.002 nm for twist and rise where error bars were obtained as standard errors of the mean.

## 2.5. Effects of simulation parameters and neighboring sequence

In this study, we investigated the mechanical properties of nicked BP steps, suggesting that BP steps can have distinct C/B ratio. The twist angle of DNA structures can be, therefore, finely tuned continuously by choosing the sequences of a target C/B ratio based on the spectrum of C/B ratios established here. We employed CHARMM36 force field[30] for MD simulation since it showed a good agreement with experiments in previous MD studies for DNA nanostructures. It remains open, however, whether our results would stay if we use other force fields, ionic conditions, and neighboring sequences.

To verify, we simulated all the BP steps for 100 ns employing the parmbsc1 force field[64], another widely used force field in DNA oligomer simulations, to obtain the mechanical properties and the C/B ratios. As in the previous results obtained using the CHARMM36 force field, the parmbsc1 force field provided the sequence-dependent properties for regular and nicked BP steps (Figure 2-13, Table 2-8, Table 2-9, Table 2-10, Table 2-11, Table 2-12, and Table 2-13). It was also confirmed that nicks led to a significant reduction in torsional rigidity regardless of the force field used. On the whole, the geometry, mechanical rigidities, and coupling coefficients predicted by two force fields were comparable for both regular and nicked BP steps. While the parmbsc1 force field predicted relatively smaller torsional and shearing rigidities than the CHARMM36 as found in previous studies[30,64], the C/B ratios predicted by the parmbsc1 were not significantly deviated from those obtained using the CHARMM36 because the torsional rigidity decreases for both regular and nicked BP steps ($\mathrm{C/B\ ratio} = (\mathrm{C/B})^{\mathrm{nicked}}/(\mathrm{C/B})^{\mathrm{regular}}$) (Figure 2-13). Therefore, we could confirm that the trend of C/B ratio (and hence our design approach) is not sensitive to the choice of force field.

While limited, we increased the time duration from 100 to 300 ns for the GC/GnC step as a selected subset. We also performed additional simulations of 300 ns using the parmbsc1 force field with 100 mM of NaCl (Figure 2-14). It was

apparent that RMSD values were maintained within 2-8 Å, suggesting that oligomers stayed near an equilibrium state. Results indicated that the mechanical properties of BP steps did not considerably alter compared to original simulation either the simulation time was extended or salt concentration was changed from $MgCl_2$ to NaCl concentration.

Furthermore, to investigate the effect of the next-nearest-neighbor sequence variation, another additional MD simulations performed for nicked GG/CnC and AA/TnT steps as a limited subgroup in order to evaluate the effect of adjacent sequence variation of a BP step (Figure 2-15 and Figure 2-16). The dinucleotide GG/CnC step analyzed in this study is the same as the tetranucleotide AGGA/TCnCT step when considering neighboring sequences for the original DNA oligomer (Table 2-1). Likewise, the AA/TnT step was identical to the hexanucleotide GAAAAG/CTTnTTC step. We modified the sequence of the original oligomer for GG/CnC step from $GACT_4$-GAC-TCnCT-CAG-$TCAG_4$ to $GACT_4$-GAC-ACnCA-CAG-$TCAG_4$ to have the same dinucleotide GG/CnC step in the center but different tetranucleotide TGGT/ACnCA step. Likewise, the oligomer with the AA/TnT step was also modified from $GACT_4$-GA-CTTnTTC-AG-$TCAG_4$ to $GACT_4$-GA-GTTnTTG-AG-$TCAG_4$ with different hexanucleotide GTAATG/CATTAC step. We performed 100-ns-long MD simulations with the same protocol with the CHARMM36 force field and $MgCl_2$ condition. In both steps, RMSD values were maintained within 2-10 Å. The results indicate that the overall trend of the mechanical properties in sequence variation may be consistent with that of original steps, observing the less influence of sequence change as the farther from the central BP step. Nevertheless, since our MD simulation was limited in the nanosecond (ns) time-scale, it is promising that further investigations on mechanical properties of nicked BP steps remain under microsecond (μs) simulation and another testing environment.

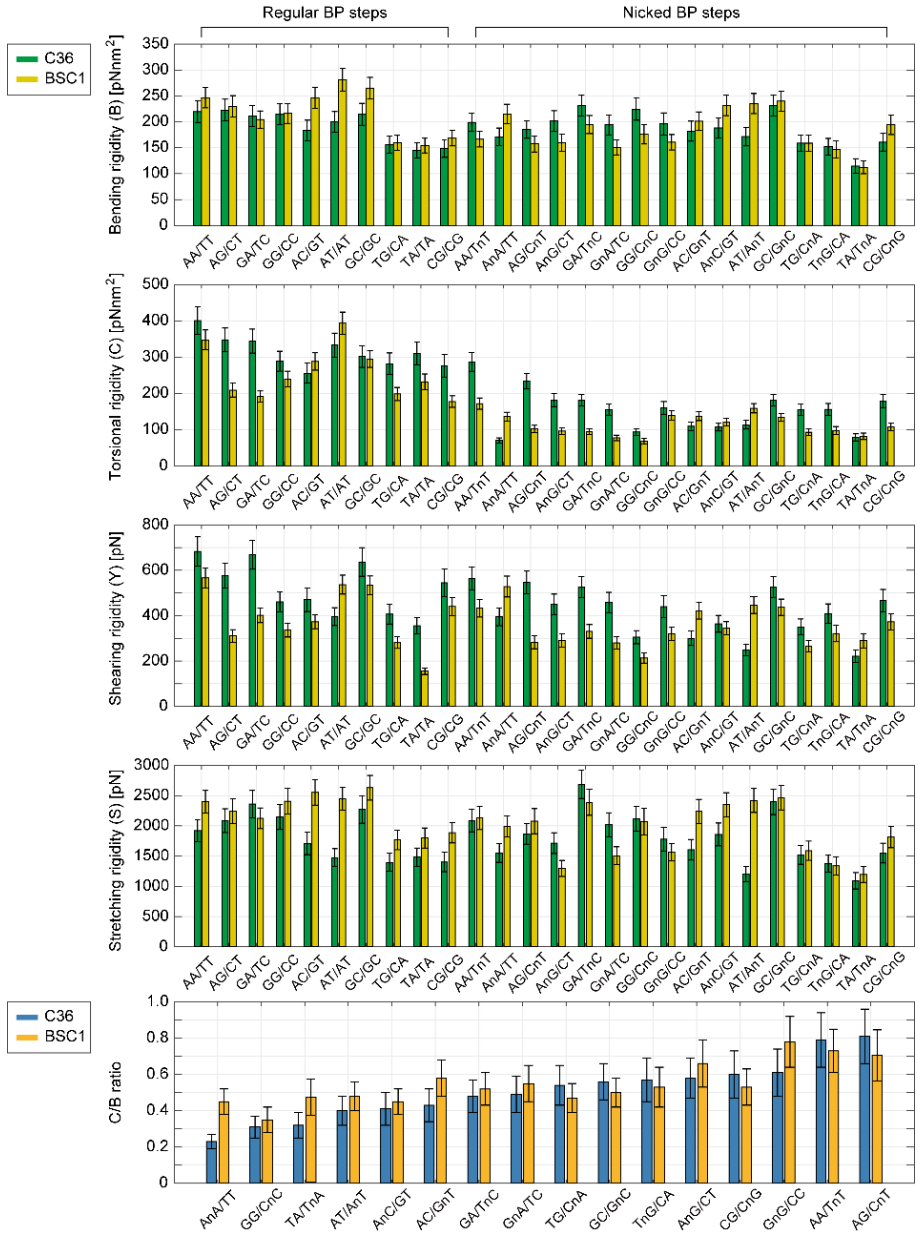


Figure 2-13. Comparison of mechanical rigidities and the C/B ratio in CHARMM36 and parmbsc1 force fields. Equivalent bending and shearing rigidities were described. Sequence-dependent mechanical properties were listed (Table 2-8, Table 2-9, Table 2-10, Table 2-11, Table 2-12, and Table 2-13). The C/B ratios of CHARMM36 were sorted in ascending order and the corresponding values of parmbsc1 were indicated.

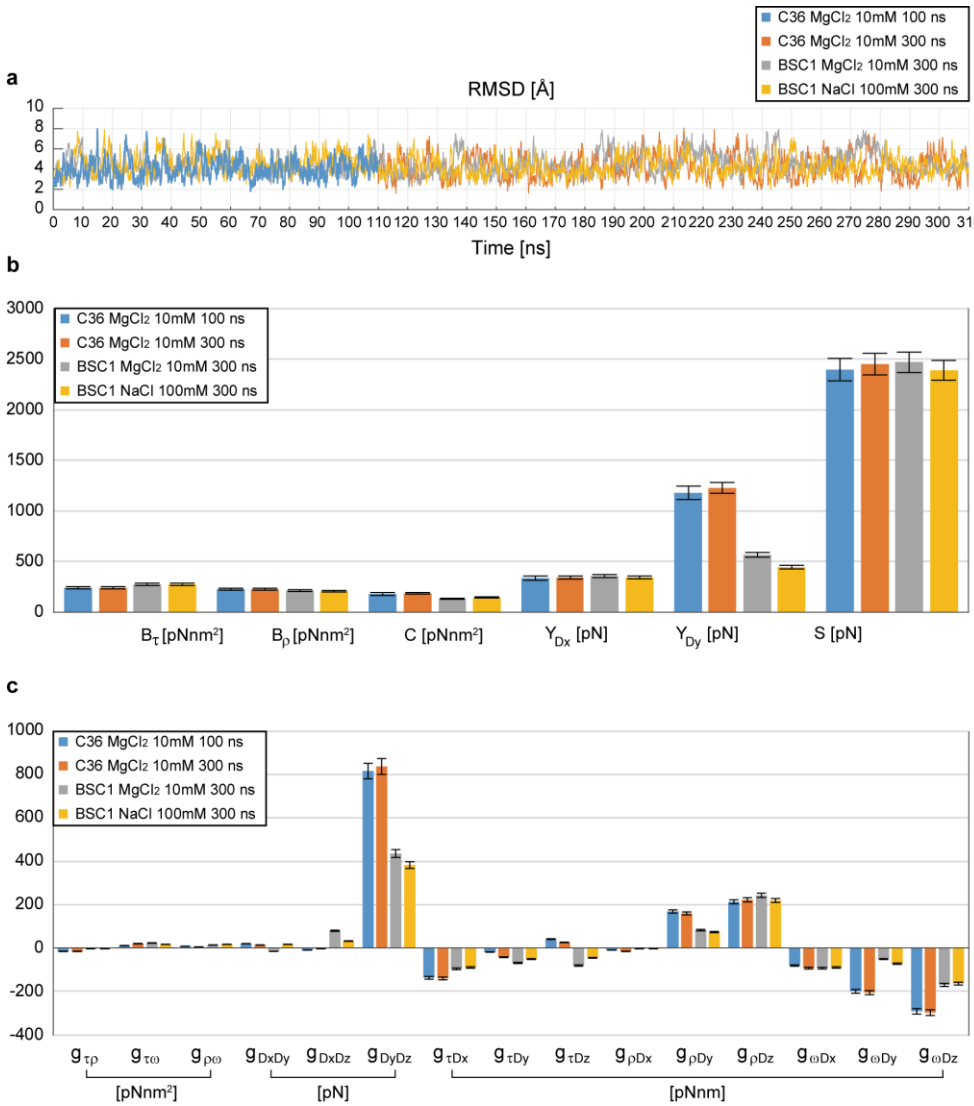


Figure 2-14. Effects of force field, simulation time, and salt condition on mechanical properties of nicked GC/GnC step. C36 and BSC1 represent the CHARMM36 and parmbsc1 force fields, respectively. (**a**) RMSD trajectories. Each RMSD value was calculated from the minimized structure omitting the four-terminal BPs on each end. (**b**, **c**) Mechanical rigidities and coupling coefficients. Each bar represents the overall value of the mechanical properties.

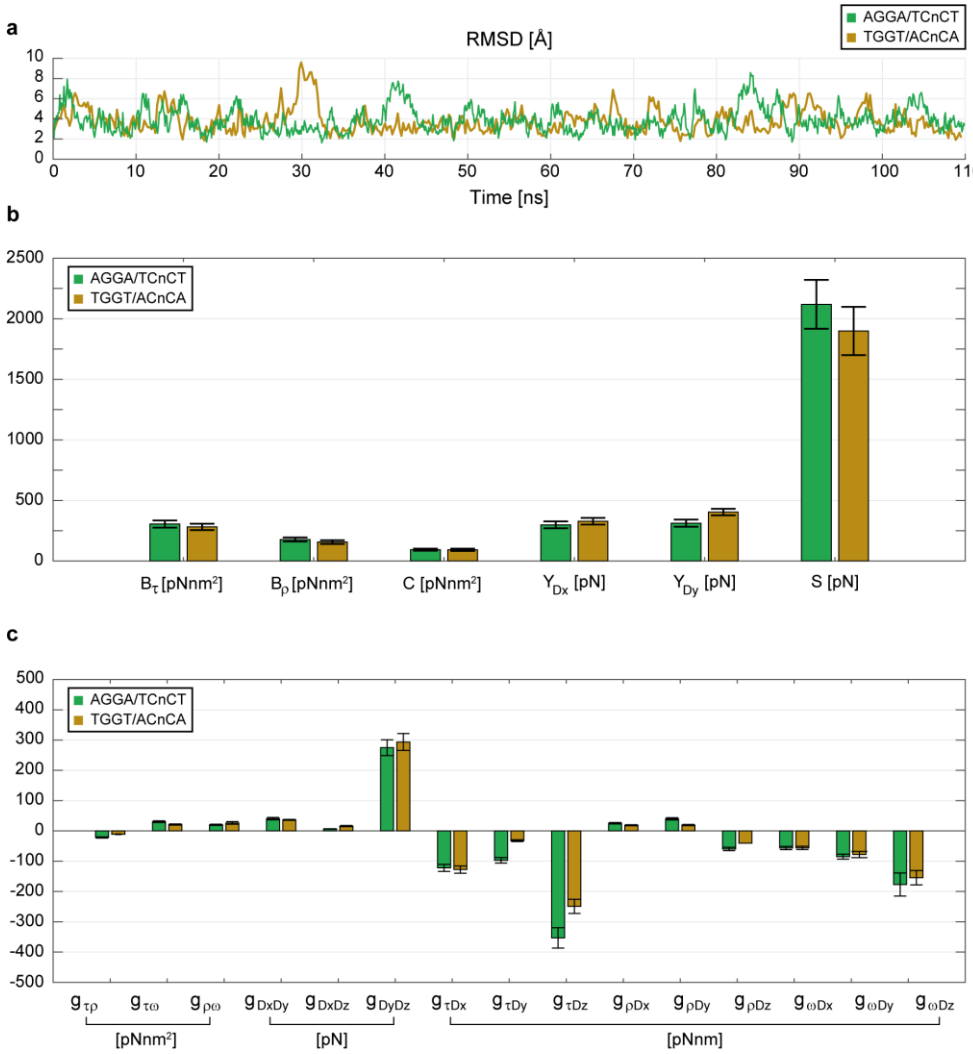


Figure 2-15. Effects of the-next-to-nearest-neighbor sequence on mechanical properties of nicked GG/CnC step. (**a**) RMSD trajectories. Each RMSD value was calculated from the minimized structure omitting the four-terminal BPs on each end. (**b**, **c**) Mechanical rigidities coupling coefficients. Each bar represents the overall value of the mechanical properties.

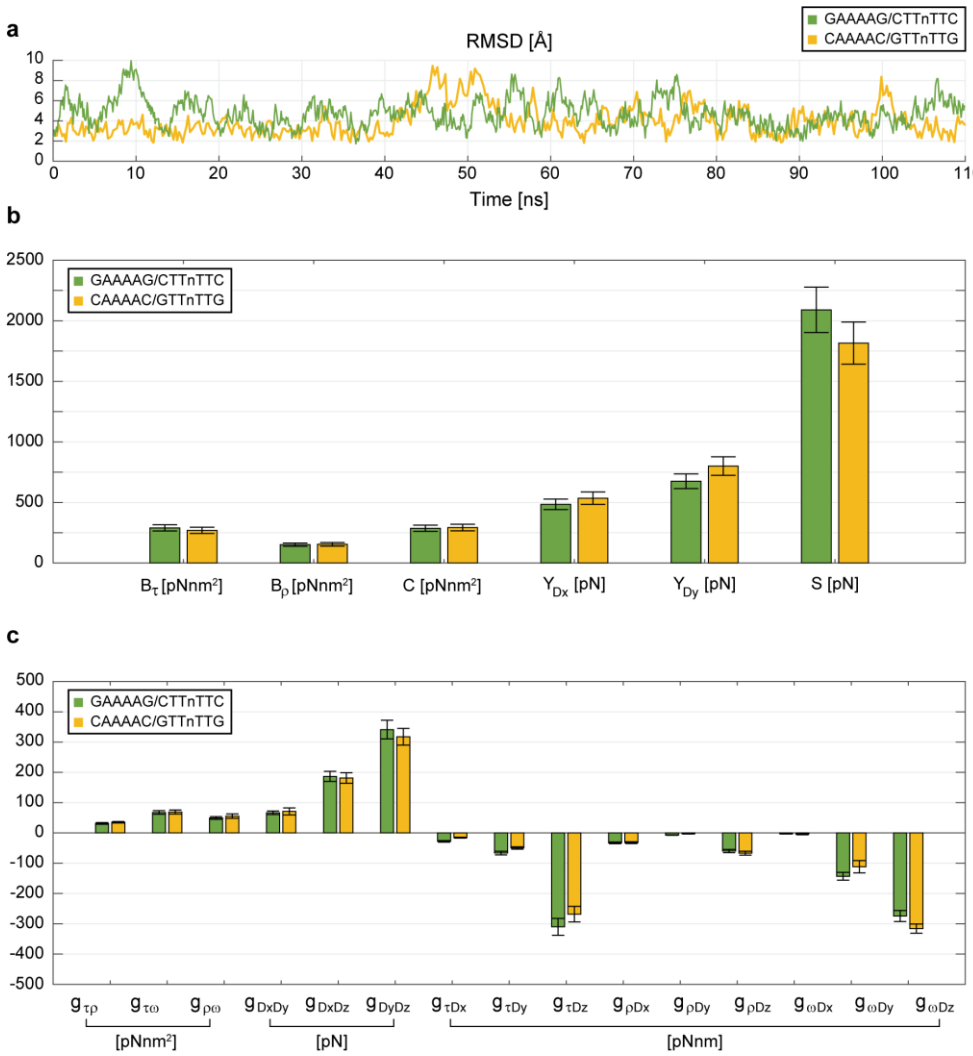


Figure 2-16. Effects of the-second-adjacent sequence on the mechanical properties of the nicked AA/TnT step. (**a**) RMSD trajectories. Each RMSD value was calculated from the minimized structure omitting the four-terminal BPs on each end. (**b**, **c**) Mechanical rigidities and coupling coefficients. Each bar represents the overall value of the mechanical properties.

Table 2-8. Sequence-dependent BP step parameters of regular BP steps using the parmbsc1 force field. The mean and standard deviation are represented in the left and right column for each BP step parameter.

| Regular | τ [°] | | ρ [°] | | ω [°] | |
|---|---|---|---|---|---|---|
| AA/TT | -2.79 | 3.86 | -0.50 | 4.98 | 37.37 | 3.97 |
| AG/CT | -1.95 | 4.44 | 2.26 | 5.52 | 33.00 | 5.76 |
| GA/TC | -0.74 | 4.72 | 1.03 | 5.10 | 36.65 | 6.40 |
| GG/CC | 2.04 | 4.85 | 3.24 | 6.31 | 35.38 | 5.31 |
| AC/GT | -0.92 | 3.93 | -1.53 | 5.23 | 34.44 | 4.49 |
| AT/AT | 0.58 | 3.64 | -1.28 | 4.54 | 32.75 | 3.52 |
| GC/GC | 1.34 | 4.07 | 0.67 | 4.95 | 39.12 | 4.28 |
| TG/CA | 2.61 | 5.34 | 6.40 | 6.81 | 32.19 | 6.03 |
| TA/TA | 0.06 | 5.36 | 8.19 | 6.90 | 34.80 | 6.49 |
| CG/CG | 3.33 | 5.14 | 10.95 | 6.39 | 33.75 | 6.21 |
| Overall | 0.36 | 2.00 | 2.94 | 4.25 | 34.95 | 2.22 |

| Regular | Dx [nm] | | Dy [nm] | | Dz [nm] | |
|---|---|---|---|---|---|---|
| AA/TT | -0.07 | 0.07 | -0.02 | 0.05 | 0.33 | 0.03 |
| AG/CT | -0.02 | 0.09 | -0.05 | 0.07 | 0.33 | 0.03 |
| GA/TC | -0.06 | 0.09 | -0.01 | 0.07 | 0.34 | 0.03 |
| GG/CC | -0.01 | 0.09 | -0.06 | 0.08 | 0.35 | 0.03 |
| AC/GT | 0.03 | 0.08 | -0.07 | 0.05 | 0.33 | 0.03 |
| AT/AT | 0.00 | 0.06 | -0.09 | 0.04 | 0.33 | 0.03 |
| GC/GC | 0.04 | 0.06 | -0.03 | 0.05 | 0.34 | 0.03 |
| TG/CA | 0.08 | 0.10 | 0.00 | 0.05 | 0.32 | 0.03 |
| TA/TA | -0.01 | 0.14 | 0.02 | 0.06 | 0.32 | 0.03 |
| CG/CG | -0.08 | 0.08 | 0.02 | 0.05 | 0.33 | 0.03 |
| Overall | -0.01 | 0.05 | -0.03 | 0.04 | 0.33 | 0.01 |

Table 2-9. Sequence-dependent BP step parameters of nicked BP steps using the parmbsc1 force field. The mean and standard deviation are represented in the left and right column for each BP step parameter.

| Nicked | τ [°] | | ρ [°] | | ω [°] | |
|---|---|---|---|---|---|---|
| AA/TnT | -3.52 | 4.19 | 2.29 | 6.40 | 35.87 | 6.07 |
| AnA/TT | -1.49 | 4.54 | -0.21 | 5.01 | 32.83 | 7.74 |
| AG/CnT | -3.00 | 5.16 | 4.01 | 6.32 | 29.35 | 8.08 |
| AnG/CT | 0.65 | 5.27 | 2.22 | 6.18 | 28.44 | 12.03 |
| GA/TnC | -0.93 | 4.75 | 1.01 | 6.29 | 33.16 | 10.16 |
| GnA/TC | 2.04 | 5.95 | 2.55 | 6.67 | 36.24 | 15.73 |
| GG/CnC | -2.57 | 4.92 | 8.10 | 6.36 | 30.06 | 9.27 |
| GnG/CC | 1.81 | 5.57 | 4.95 | 6.00 | 32.36 | 8.76 |
| AC/GnT | -2.89 | 4.54 | 0.14 | 5.56 | 36.34 | 6.92 |
| AnC/GT | -0.26 | 4.17 | -0.31 | 4.98 | 27.51 | 6.75 |
| AT/AnT | -0.62 | 4.02 | -0.48 | 4.80 | 30.16 | 5.64 |
| GC/GnC | 0.00 | 4.40 | 0.09 | 5.09 | 39.41 | 7.00 |
| TG/CnA | -0.65 | 5.30 | 10.43 | 6.51 | 31.51 | 8.35 |
| TnG/CA | 1.16 | 5.44 | 12.19 | 6.35 | 26.31 | 9.58 |
| TA/TnA | 2.66 | 7.99 | 8.63 | 8.54 | 32.73 | 17.63 |
| CG/CnG | 0.15 | 4.81 | 10.46 | 5.36 | 30.15 | 7.56 |
| Overall | -0.47 | 1.88 | 4.13 | 4.42 | 32.03 | 3.58 |

| Nicked | Dx [nm] | | Dy [nm] | | Dz [nm] | |
|---|---|---|---|---|---|---|
| AA/TnT | 0.00 | 0.06 | -0.04 | 0.06 | 0.32 | 0.03 |
| AnA/TT | 0.00 | 0.06 | -0.08 | 0.06 | 0.33 | 0.03 |
| AG/CnT | -0.01 | 0.07 | -0.08 | 0.08 | 0.32 | 0.03 |
| AnG/CT | -0.02 | 0.13 | -0.14 | 0.07 | 0.33 | 0.03 |
| GA/TnC | -0.03 | 0.08 | -0.03 | 0.07 | 0.32 | 0.03 |
| GnA/TC | 0.03 | 0.14 | -0.08 | 0.09 | 0.33 | 0.03 |
| GG/CnC | -0.11 | 0.10 | -0.03 | 0.08 | 0.31 | 0.03 |
| GnG/CC | 0.03 | 0.09 | -0.14 | 0.07 | 0.35 | 0.03 |
| AC/GnT | 0.09 | 0.07 | -0.09 | 0.06 | 0.33 | 0.03 |
| AnC/GT | -0.06 | 0.07 | -0.08 | 0.07 | 0.32 | 0.03 |
| AT/AnT | 0.00 | 0.07 | -0.09 | 0.05 | 0.32 | 0.03 |
| GC/GnC | 0.01 | 0.07 | -0.05 | 0.06 | 0.34 | 0.03 |
| TG/CnA | 0.05 | 0.09 | -0.03 | 0.07 | 0.33 | 0.03 |
| TnG/CA | -0.08 | 0.09 | -0.08 | 0.06 | 0.32 | 0.04 |
| TA/TnA | -0.05 | 0.16 | -0.01 | 0.10 | 0.33 | 0.04 |
| CG/CnG | -0.03 | 0.07 | -0.02 | 0.06 | 0.32 | 0.03 |
| Overall | -0.01 | 0.05 | -0.07 | 0.04 | 0.33 | 0.01 |

Table 2-10. Sequence-dependent mechanical rigidities of regular BP steps using the parmbsc1 force field. The mean and standard deviation are represented in the left and right columns for each rigidity. The standard deviation is calculated by multiplying the diagonal value of the stiffness matrix by the standard deviation of the rise.

| Regular | $\mathbf{B_\tau}$ [pN nm$^2$] | | $\mathbf{B_\rho}$ [pN nm$^2$] | | $\mathbf{C}$ [pN nm$^2$] | |
|---|---|---|---|---|---|---|
| AA/TT | 354.13 | 28.01 | 189.04 | 14.95 | 347.38 | 27.48 |
| AG/CT | 339.61 | 30.86 | 173.54 | 15.77 | 208.83 | 18.98 |
| GA/TC | 230.33 | 18.65 | 183.62 | 14.87 | 191.13 | 15.47 |
| GG/CC | 352.32 | 31.54 | 155.92 | 13.96 | 239.51 | 21.44 |
| AC/GT | 319.05 | 26.26 | 200.69 | 16.52 | 287.93 | 23.70 |
| AT/AT | 331.70 | 25.83 | 244.53 | 19.04 | 393.53 | 30.64 |
| GC/GC | 323.66 | 25.22 | 224.49 | 17.49 | 294.53 | 22.95 |
| TG/CA | 205.69 | 18.84 | 130.02 | 11.91 | 198.38 | 18.17 |
| TA/TA | 187.88 | 17.24 | 130.70 | 11.99 | 232.12 | 21.29 |
| CG/CG | 238.97 | 21.47 | 130.46 | 11.72 | 177.32 | 15.93 |
| Overall | 288.33 | 64.85 | 176.30 | 40.19 | 257.07 | 71.91 |

| Regular | $\mathbf{Y_{Dx}}$ [pN] | | $\mathbf{Y_{Dy}}$ [pN] | | $\mathbf{S}$ [pN] | |
|---|---|---|---|---|---|---|
| AA/TT | 457.74 | 36.21 | 743.95 | 58.85 | 2398.20 | 189.70 |
| AG/CT | 272.15 | 24.73 | 360.76 | 32.78 | 2247.31 | 204.20 |
| GA/TC | 291.92 | 23.63 | 644.33 | 52.16 | 2125.85 | 172.10 |
| GG/CC | 313.51 | 28.07 | 361.09 | 32.33 | 2407.37 | 215.52 |
| AC/GT | 252.15 | 20.75 | 718.94 | 59.17 | 2554.25 | 210.24 |
| AT/AT | 365.02 | 28.42 | 1012.94 | 78.87 | 2446.95 | 190.53 |
| GC/GC | 447.32 | 34.86 | 660.64 | 51.48 | 2631.09 | 205.03 |
| TG/CA | 180.30 | 16.51 | 639.19 | 58.53 | 1766.95 | 161.81 |
| TA/TA | 91.57 | 8.40 | 509.50 | 46.74 | 1800.52 | 165.17 |
| CG/CG | 317.64 | 28.53 | 718.86 | 64.58 | 1888.00 | 169.60 |
| Overall | 298.93 | 111.65 | 637.02 | 193.07 | 2226.65 | 316.17 |

Table 2-11. Sequence-dependent mechanical rigidities of nicked BP steps using the parmbsc1 force field. The mean and standard deviation are represented in the left and right columns for each rigidity. The standard deviation is calculated by multiplying the diagonal value of the stiffness matrix by the standard deviation of the rise.

| Regular | $\mathbf{B_\tau}$ [pN nm$^2$] | | $\mathbf{B_\rho}$ [pN nm$^2$] | | $\mathbf{C}$ [pN nm$^2$] | |
|---|---|---|---|---|---|---|
| AA/TnT | 322.67 | 29.18 | 112.16 | 10.14 | 171.76 | 15.53 |
| AnA/TT | 265.14 | 23.10 | 180.90 | 15.76 | 136.03 | 11.85 |
| AG/CnT | 225.68 | 22.50 | 120.85 | 12.05 | 101.69 | 10.14 |
| AnG/CT | 169.52 | 17.37 | 150.93 | 15.47 | 95.80 | 9.82 |
| GA/TnC | 286.92 | 25.83 | 147.30 | 13.26 | 94.51 | 8.51 |
| GnA/TC | 157.00 | 15.39 | 145.29 | 14.24 | 77.27 | 7.57 |
| GG/CnC | 288.84 | 30.74 | 126.59 | 13.47 | 68.24 | 7.26 |
| GnG/CC | 163.06 | 15.06 | 158.21 | 14.61 | 138.93 | 12.83 |
| AC/GnT | 242.32 | 21.58 | 171.80 | 15.30 | 137.10 | 12.21 |
| AnC/GT | 262.84 | 22.30 | 207.00 | 17.56 | 121.12 | 10.28 |
| AT/AnT | 274.58 | 22.49 | 205.69 | 16.85 | 158.86 | 13.01 |
| GC/GnC | 273.71 | 22.54 | 213.23 | 17.56 | 133.34 | 10.98 |
| TG/CnA | 198.08 | 19.68 | 132.30 | 13.14 | 92.87 | 9.23 |
| TnG/CA | 173.99 | 19.76 | 126.90 | 14.41 | 97.49 | 11.07 |
| TA/TnA | 120.94 | 13.25 | 104.35 | 11.43 | 81.66 | 8.94 |
| CG/CnG | 220.00 | 21.23 | 173.56 | 16.75 | 108.03 | 10.43 |
| Overall | 227.83 | 58.43 | 154.82 | 34.47 | 113.42 | 30.02 |

| Regular | $\mathbf{Y_{Dx}}$ [pN] | | $\mathbf{Y_{Dy}}$ [pN] | | $\mathbf{S}$ [pN] | |
|---|---|---|---|---|---|---|
| AA/TnT | 445.96 | 40.33 | 420.60 | 38.03 | 2131.16 | 192.72 |
| AnA/TT | 451.07 | 39.30 | 637.17 | 55.51 | 1989.50 | 173.32 |
| AG/CnT | 286.24 | 28.54 | 278.70 | 27.79 | 2078.69 | 207.27 |
| AnG/CT | 232.65 | 23.84 | 387.32 | 39.70 | 1296.95 | 132.93 |
| GA/TnC | 292.48 | 26.33 | 380.45 | 34.25 | 2390.54 | 215.19 |
| GnA/TC | 224.65 | 22.02 | 371.97 | 36.46 | 1507.45 | 147.77 |
| GG/CnC | 188.83 | 20.10 | 245.40 | 26.12 | 2070.96 | 220.40 |
| GnG/CC | 275.00 | 25.40 | 383.15 | 35.39 | 1565.90 | 144.64 |
| AC/GnT | 344.28 | 30.66 | 546.96 | 48.71 | 2238.17 | 199.32 |
| AnC/GT | 316.83 | 26.89 | 377.20 | 32.01 | 2349.27 | 199.35 |
| AT/AnT | 337.50 | 27.64 | 659.28 | 53.99 | 2420.47 | 198.22 |
| GC/GnC | 356.91 | 29.40 | 564.27 | 46.48 | 2468.90 | 203.36 |
| TG/CnA | 216.09 | 21.47 | 343.66 | 34.14 | 1590.12 | 157.99 |
| TnG/CA | 247.25 | 28.08 | 458.22 | 52.03 | 1339.69 | 152.13 |
| TA/TnA | 260.88 | 28.57 | 324.59 | 35.55 | 1196.90 | 131.09 |
| CG/CnG | 329.03 | 31.75 | 431.17 | 41.61 | 1814.63 | 175.13 |
| Overall | 300.35 | 76.01 | 425.63 | 119.98 | 1903.08 | 433.19 |

Table 2-12. Sequence-dependent mechanical coupling coefficients of regular BP steps using the parmbsc1 force field. The mean and standard deviation are represented in the left and right columns for each coefficient. The standard deviation is calculated by multiplying the off-diagonal value of the stiffness matrix by the standard deviation of the rise.

| Regular | $g_{\tau\rho}$ [pN nm$^2$] | | $g_{\tau\omega}$ [pN nm$^2$] | | $g_{\rho\omega}$ [pN nm$^2$] | |
|---|---|---|---|---|---|---|
| AA/TT | 18.82 | 1.49 | 60.82 | 4.81 | 40.55 | 3.21 |
| AG/CT | 28.49 | 2.59 | 52.31 | 4.75 | 47.68 | 4.33 |
| GA/TC | 0.66 | 0.05 | -3.69 | -0.30 | 38.27 | 3.10 |
| GG/CC | -21.07 | -1.89 | 7.73 | 0.69 | 37.57 | 3.36 |
| AC/GT | 33.72 | 2.78 | 41.41 | 3.41 | 51.33 | 4.22 |
| AT/AT | -1.43 | -0.11 | 2.00 | 0.16 | 59.20 | 4.61 |
| GC/GC | 4.38 | 0.34 | 8.69 | 0.68 | 27.33 | 2.13 |
| TG/CA | 6.82 | 0.62 | -29.11 | -2.67 | 58.59 | 5.37 |
| TA/TA | -3.57 | -0.33 | 5.08 | 0.47 | 79.96 | 7.34 |
| CG/CG | -13.74 | -1.23 | -12.60 | -1.13 | 47.39 | 4.26 |
| Overall | 5.31 | 17.43 | 13.26 | 29.01 | 48.79 | 14.72 |

| Regular | $g_{DxDy}$ [pN] | | $g_{DxDz}$ [pN] | | $g_{DyDz}$ [pN] | |
|---|---|---|---|---|---|---|
| AA/TT | -316.65 | -25.05 | -161.58 | -12.78 | 223.11 | 17.65 |
| AG/CT | 47.96 | 4.36 | 170.93 | 15.53 | 270.92 | 24.62 |
| GA/TC | -198.19 | -16.05 | -70.97 | -5.75 | 225.80 | 18.28 |
| GG/CC | -9.02 | -0.81 | 161.96 | 14.50 | 404.06 | 36.17 |
| AC/GT | -42.46 | -3.50 | 78.53 | 6.46 | 573.88 | 47.23 |
| AT/AT | -71.95 | -5.60 | -6.78 | -0.53 | 471.14 | 36.68 |
| GC/GC | -99.02 | -7.72 | 2.01 | 0.16 | 496.81 | 38.71 |
| TG/CA | -25.52 | -2.34 | -27.31 | -2.50 | 42.34 | 3.88 |
| TA/TA | -10.44 | -0.96 | -10.28 | -0.94 | 145.74 | 13.37 |
| CG/CG | -112.59 | -10.11 | -51.69 | -4.64 | 94.01 | 8.45 |
| Overall | -83.79 | 106.43 | 8.48 | 103.07 | 294.78 | 182.11 |

Table 2-12 (Continued).

| Regular | $\mathbf{g}_{\tau Dx}$ [pN nm] | | $\mathbf{g}_{\tau Dy}$ [pN nm] | | $\mathbf{g}_{\tau Dz}$ [pN nm] | |
|---|---|---|---|---|---|---|
| AA/TT | 24.56 | 1.94 | -6.28 | -0.50 | -329.44 | -26.06 |
| AG/CT | -81.54 | -7.41 | 7.23 | 0.66 | -389.80 | -35.42 |
| GA/TC | 34.49 | 2.79 | 20.60 | 1.67 | -181.36 | -14.68 |
| GG/CC | -169.38 | -15.16 | -35.06 | -3.14 | -435.37 | -38.98 |
| AC/GT | -41.87 | -3.45 | -10.97 | -0.90 | 62.29 | 5.13 |
| AT/AT | 0.16 | 0.01 | 1.24 | 0.10 | -12.40 | -0.97 |
| GC/GC | -129.99 | -10.13 | 0.88 | 0.07 | 43.79 | 3.41 |
| TG/CA | -91.95 | -8.42 | 15.00 | 1.37 | -74.61 | -6.83 |
| TA/TA | -57.03 | -5.23 | -8.29 | -0.76 | -28.67 | -2.63 |
| CG/CG | -140.86 | -12.65 | -13.12 | -1.18 | -59.56 | -5.35 |
| Overall | -65.34 | 70.42 | -2.88 | 15.82 | -140.51 | 182.99 |

| Regular | $\mathbf{g}_{\rho Dx}$ [pN nm] | | $\mathbf{g}_{\rho Dy}$ [pN nm] | | $\mathbf{g}_{\rho Dz}$ [pN nm] | |
|---|---|---|---|---|---|---|
| AA/TT | 29.59 | 2.34 | -21.04 | -1.66 | -6.48 | -0.51 |
| AG/CT | 65.96 | 5.99 | -11.02 | -1.00 | -40.44 | -3.67 |
| GA/TC | -20.43 | -1.65 | -32.65 | -2.64 | -15.82 | -1.28 |
| GG/CC | 81.53 | 7.30 | 54.14 | 4.85 | 43.77 | 3.92 |
| AC/GT | 22.85 | 1.88 | 88.99 | 7.32 | 194.57 | 16.01 |
| AT/AT | 54.15 | 4.22 | 2.18 | 0.17 | 162.63 | 12.66 |
| GC/GC | 10.36 | 0.81 | 99.89 | 7.78 | 229.88 | 17.91 |
| TG/CA | -2.63 | -0.24 | 56.92 | 5.21 | -110.11 | -10.08 |
| TA/TA | 17.36 | 1.59 | 31.78 | 2.92 | -113.96 | -10.45 |
| CG/CG | 36.48 | 3.28 | 27.93 | 2.51 | -82.54 | -7.41 |
| Overall | 29.52 | 31.23 | 29.71 | 45.54 | 26.15 | 127.40 |

| Regular | $\mathbf{g}_{\omega Dx}$ [pN nm] | | $\mathbf{g}_{\omega Dy}$ [pN nm] | | $\mathbf{g}_{\omega Dz}$ [pN nm] | |
|---|---|---|---|---|---|---|
| AA/TT | 6.07 | 0.48 | -144.83 | -11.46 | -194.10 | -15.35 |
| AG/CT | 87.85 | 7.98 | -58.24 | -5.29 | -195.47 | -17.76 |
| GA/TC | -25.16 | -2.04 | -176.73 | -14.31 | -123.35 | -9.99 |
| GG/CC | 93.18 | 8.34 | -99.60 | -8.92 | -202.01 | -18.09 |
| AC/GT | 74.49 | 6.13 | -77.57 | -6.38 | -172.19 | -14.17 |
| AT/AT | -6.47 | -0.50 | -127.31 | -9.91 | -132.87 | -10.35 |
| GC/GC | 60.64 | 4.73 | -81.95 | -6.39 | -221.24 | -17.24 |
| TG/CA | 35.84 | 3.28 | -131.77 | -12.07 | -171.15 | -15.67 |
| TA/TA | 27.87 | 2.56 | -150.22 | -13.78 | -241.17 | -22.12 |
| CG/CG | 54.62 | 4.91 | -130.57 | -11.73 | -225.20 | -20.23 |
| Overall | 40.89 | 40.36 | -117.88 | 37.25 | -187.88 | 38.53 |

Table 2-13. Sequence-dependent mechanical coupling coefficients of nicked BP steps using the parmbsc1 force field. The mean and standard deviation are represented in the left and right columns for each coefficient. The standard deviation is calculated by multiplying the off-diagonal value of the stiffness matrix by the standard deviation of the rise.

| Nicked | $\mathbf{g}_{\tau\rho}$ [pN nm$^2$] | | $\mathbf{g}_{\tau\omega}$ [pN nm$^2$] | | $\mathbf{g}_{\rho\omega}$ [pN nm$^2$] | |
|---|---|---|---|---|---|---|
| AA/TnT | 5.89 | 0.53 | 29.36 | 2.66 | 30.89 | 2.79 |
| AnA/TT | 18.05 | 1.57 | 19.15 | 1.67 | 18.69 | 1.63 |
| AG/CnT | 12.09 | 1.21 | 36.73 | 3.66 | 26.50 | 2.64 |
| AnG/CT | 14.44 | 1.48 | -0.74 | -0.08 | 19.03 | 1.95 |
| GA/TnC | -17.05 | -1.53 | 27.96 | 2.52 | 38.85 | 3.50 |
| GnA/TC | 1.22 | 0.12 | -23.89 | -2.34 | 32.39 | 3.18 |
| GG/CnC | -40.90 | -4.35 | -4.98 | -0.53 | 15.45 | 1.64 |
| GnG/CC | -0.12 | -0.01 | -17.66 | -1.63 | 26.59 | 2.46 |
| AC/GnT | 16.63 | 1.48 | 20.76 | 1.85 | 9.21 | 0.82 |
| AnC/GT | 45.74 | 3.88 | 16.46 | 1.40 | 34.74 | 2.95 |
| AT/AnT | -16.78 | -1.37 | -16.90 | -1.38 | 18.97 | 1.55 |
| GC/GnC | -2.61 | -0.22 | 22.64 | 1.86 | 14.30 | 1.18 |
| TG/CnA | -14.33 | -1.42 | 6.14 | 0.61 | 31.75 | 3.15 |
| TnG/CA | 5.25 | 0.60 | -38.59 | -4.38 | 28.37 | 3.22 |
| TA/TnA | 7.04 | 0.77 | 0.99 | 0.11 | 35.33 | 3.87 |
| CG/CnG | -17.44 | -1.68 | 23.70 | 2.29 | 32.32 | 3.12 |
| Overall | 1.07 | 19.84 | 6.32 | 21.94 | 25.84 | 8.77 |

| Nicked | $\mathbf{g}_{\mathbf{DxDy}}$ [pN] | | $\mathbf{g}_{\mathbf{DxDz}}$ [pN] | | $\mathbf{g}_{\mathbf{DyDz}}$ [pN] | |
|---|---|---|---|---|---|---|
| AA/TnT | -67.53 | -6.11 | 148.84 | 13.46 | 109.15 | 9.87 |
| AnA/TT | -83.73 | -7.29 | -59.51 | -5.18 | 61.42 | 5.35 |
| AG/CnT | -15.41 | -1.54 | 140.65 | 14.02 | 201.27 | 20.07 |
| AnG/CT | -27.01 | -2.77 | 76.54 | 7.84 | 144.85 | 14.85 |
| GA/TnC | 52.91 | 4.76 | 163.25 | 14.69 | 149.88 | 13.49 |
| GnA/TC | -29.30 | -2.87 | 24.20 | 2.37 | 97.91 | 9.60 |
| GG/CnC | -1.41 | -0.15 | 184.85 | 19.67 | 83.99 | 8.94 |
| GnG/CC | 41.42 | 3.83 | 35.48 | 3.28 | 122.71 | 11.33 |
| AC/GnT | 9.19 | 0.82 | 160.38 | 14.28 | 456.38 | 40.64 |
| AnC/GT | -58.90 | -5.00 | -51.30 | -4.35 | 340.76 | 28.91 |
| AT/AnT | -22.73 | -1.86 | 17.95 | 1.47 | 453.73 | 37.16 |
| GC/GnC | -15.28 | -1.26 | 80.55 | 6.63 | 437.12 | 36.00 |
| TG/CnA | -21.35 | -2.12 | -3.84 | -0.38 | 109.43 | 10.87 |
| TnG/CA | 25.89 | 2.94 | -6.46 | -0.73 | 58.38 | 6.63 |
| TA/TnA | -65.01 | -7.12 | 15.43 | 1.69 | 54.35 | 5.95 |
| CG/CnG | -32.54 | -3.14 | 22.46 | 2.17 | 45.87 | 4.43 |
| Overall | -19.42 | 38.81 | 59.34 | 79.00 | 182.95 | 150.02 |

Table 2-13 (Continued).

| Nicked | $\mathbf{g}_{\tau Dx}$ [pN nm] | | $\mathbf{g}_{\tau Dy}$ [pN nm] | | $\mathbf{g}_{\tau Dz}$ [pN nm] | |
|---|---|---|---|---|---|---|
| AA/TnT | -85.16 | -7.70 | -0.73 | -0.07 | -375.18 | -33.93 |
| AnA/TT | 2.51 | 0.22 | 91.58 | 7.98 | -229.99 | -20.04 |
| AG/CnT | -69.33 | -6.91 | -59.26 | -5.91 | -321.28 | -32.03 |
| AnG/CT | -12.45 | -1.28 | 50.52 | 5.18 | -6.68 | -0.68 |
| GA/TnC | -100.74 | -9.07 | -33.74 | -3.04 | -419.25 | -37.74 |
| GnA/TC | 20.02 | 1.96 | 87.91 | 8.62 | -66.35 | -6.50 |
| GG/CnC | -34.30 | -3.65 | -13.07 | -1.39 | -444.78 | -47.34 |
| GnG/CC | 34.36 | 3.17 | 37.57 | 3.47 | -59.30 | -5.48 |
| AC/GnT | -54.24 | -4.83 | -72.32 | -6.44 | -156.43 | -13.93 |
| AnC/GT | -17.66 | -1.50 | 46.41 | 3.94 | 91.70 | 7.78 |
| AT/AnT | 3.91 | 0.32 | -63.18 | -5.17 | -96.35 | -7.89 |
| GC/GnC | -96.96 | -7.99 | -69.11 | -5.69 | -82.54 | -6.80 |
| TG/CnA | -90.30 | -8.97 | -14.66 | -1.46 | -23.98 | -2.38 |
| TnG/CA | 51.51 | 5.85 | 73.73 | 8.37 | 13.17 | 1.50 |
| TA/TnA | -60.63 | -6.64 | -6.53 | -0.72 | -29.30 | -3.21 |
| CG/CnG | -93.89 | -9.06 | -25.91 | -2.50 | -18.32 | -1.77 |
| Overall | -37.71 | 50.56 | 1.82 | 56.19 | -139.05 | 167.33 |

| Nicked | $\mathbf{g}_{\rho Dx}$ [pN nm] | | $\mathbf{g}_{\rho Dy}$ [pN nm] | | $\mathbf{g}_{\rho Dz}$ [pN nm] | |
|---|---|---|---|---|---|---|
| AA/TnT | 17.04 | 1.54 | -15.18 | -1.37 | -50.09 | -4.53 |
| AnA/TT | 15.83 | 1.38 | -12.49 | -1.09 | -21.93 | -1.91 |
| AG/CnT | 29.21 | 2.91 | -13.60 | -1.36 | -59.84 | -5.97 |
| AnG/CT | 34.68 | 3.55 | -37.46 | -3.84 | -27.73 | -2.84 |
| GA/TnC | 38.47 | 3.46 | -6.85 | -0.62 | 15.72 | 1.41 |
| GnA/TC | -5.40 | -0.53 | 19.71 | 1.93 | -23.16 | -2.27 |
| GG/CnC | -30.74 | -3.27 | -34.99 | -3.72 | -17.46 | -1.86 |
| GnG/CC | -6.61 | -0.61 | 56.73 | 5.24 | 15.68 | 1.45 |
| AC/GnT | -19.20 | -1.71 | 61.36 | 5.46 | 201.67 | 17.96 |
| AnC/GT | -2.12 | -0.18 | 10.63 | 0.90 | 176.92 | 15.01 |
| AT/AnT | 37.73 | 3.09 | 2.15 | 0.18 | 140.38 | 11.50 |
| GC/GnC | -5.46 | -0.45 | 81.56 | 6.72 | 242.36 | 19.96 |
| TG/CnA | 2.24 | 0.22 | 50.05 | 4.97 | -95.21 | -9.46 |
| TnG/CA | 16.33 | 1.85 | 25.85 | 2.94 | -75.24 | -8.54 |
| TA/TnA | -23.40 | -2.56 | 24.79 | 2.72 | -44.83 | -4.91 |
| CG/CnG | 7.48 | 0.72 | 38.56 | 3.72 | -146.80 | -14.17 |
| Overall | 6.63 | 21.75 | 15.68 | 35.34 | 14.40 | 113.74 |

Table 2-13 (Continued).

| Nicked | $\mathbf{g}_{\omega Dx}$ [pN nm] | | $\mathbf{g}_{\omega Dy}$ [pN nm] | | $\mathbf{g}_{\omega Dz}$ [pN nm] | |
|---|---|---|---|---|---|---|
| AA/TnT | 55.01 | 4.97 | -123.43 | -11.16 | -163.41 | -14.78 |
| AnA/TT | -79.42 | -6.92 | -135.48 | -11.80 | -123.91 | -10.80 |
| AG/CnT | -31.61 | -3.15 | -58.06 | -5.79 | -227.55 | -22.69 |
| AnG/CT | -108.22 | -11.09 | -44.00 | -4.51 | -76.53 | -7.84 |
| GA/TnC | -47.67 | -4.29 | -109.25 | -9.83 | -163.68 | -14.73 |
| GnA/TC | -86.77 | -8.51 | -64.68 | -6.34 | -87.80 | -8.61 |
| GG/CnC | 30.14 | 3.21 | -46.59 | -4.96 | -59.28 | -6.31 |
| GnG/CC | -115.67 | -10.68 | -93.47 | -8.63 | -126.21 | -11.66 |
| AC/GnT | -107.97 | -9.62 | -71.83 | -6.40 | -133.23 | -11.86 |
| AnC/GT | -42.03 | -3.57 | -51.60 | -4.38 | -115.16 | -9.77 |
| AT/AnT | -69.16 | -5.66 | -23.08 | -1.89 | -98.61 | -8.08 |
| GC/GnC | -92.13 | -7.59 | -52.87 | -4.35 | -169.77 | -13.98 |
| TG/CnA | -3.56 | -0.35 | -51.51 | -5.12 | -166.34 | -16.53 |
| TnG/CA | -75.32 | -8.55 | -34.38 | -3.90 | -156.90 | -17.82 |
| TA/TnA | -93.52 | -10.24 | -45.93 | -5.03 | -73.86 | -8.09 |
| CG/CnG | -42.25 | -4.08 | -23.51 | -2.27 | -204.99 | -19.78 |
| Overall | -56.88 | 49.85 | -64.35 | 33.97 | -134.20 | 48.16 |

# 3. Multiscale modeling of DNA nanostructures

## 3.1. Abstract

We propose a multiscale modeling approach that precisely and rapidly predicts structured DNA assemblies, inherent in the complex and unique properties of each component. The intrinsic nature of structural motifs as the topological connection between base-pairs and electrostatic interactions were characterized by molecular dynamics and converted to finite elements directly embodying molecular-level characteristics. The finite element assembly, therefore, provides the prediction of its global shape and structural features of DNA nanostructure at the base-pair level The proposed approach shows the capability and efficiency by solving comprehensive designs consistent with the reported literature, revealing detailed and fundamental insights into structured DNA assemblies. It is possible to perform this framework for immediate analysis in a personal computing environment in minutes scales, to increase the accessibility of structural prediction.

## 3.2. Finite element framework for structural motifs

DNA nanostructures consist essentially of connectivity between base-pairs (BPs). Depending on how the base-pairs are connected, the structural motifs of DNA nanostructures can be divided into stacked BPs that form helices, which are called BP steps, and inter-connected BPs linking two helices (Crossover), which are denoted as CO steps. On the other hand, each BP consists of elementary base sequences (A, T, G, and C), whose local mechanical properties can affect the global properties of the structure. Here, we employed a finite element framework to model DNA nanostructures accurately and efficiently without the loss of information of local intrinsic properties.

We introduce one of the co-rotational (CR) beam finite element framework[20]. The concept is based on the decomposition of the rigid body motion and the deformation of the element in the local coordinate system. CR formulation is element independent and various local assumptions can be placed at the core of the formulation[20] to facilitate the construction of local beams. This CR framework is, therefore, not only suitable for describing the connection and motion of BPs as a beam element with their local properties but could be useful for the application of various structural motifs of nucleic acids. From the previous literature[20], the CR beam formulation is briefly described as below.

### 3.2.1. Operators

First, the useful operators are introduced. The capital bold letter represents a matrix or tensor, and the upper arrow indicates a column vector. The upper tilde operator for a 3-by-3 skew-symmetric matrix (**V**) provides a vector by

$$\tilde{\mathbf{V}} = \begin{bmatrix} -V_{23} & V_{13} & -V_{12} \end{bmatrix}^{T} \tag{3-1}$$

where $V_{ij}$ is the component of the matrix, **V**.

The under tilde operator of a vector ($\vec{v}$) generates a 3-by-3 skew-symmetric matrix as follows.

$$\underset{\sim}{\vec{v}} = \begin{bmatrix} 0 & -v_3 & v_2 \\ v_3 & 0 & -v_1 \\ -v_2 & v_1 & 0 \end{bmatrix} \tag{3-2}$$

where the $v_k$ is the component of the vector, $\vec{v}$.

The log operator of a 3-by-3 matrix from the previous study[65] is given by

$$z = \cos^{-1}\left(\frac{1}{2}\left(\mathrm{tr}\left(\mathbf{V}\right)-1\right)\right), \quad \log\left(\mathbf{V}\right) = \begin{cases} \mathbf{O}_{3\times 3} & (z=0) \\ \dfrac{z}{2\sin\left(z\right)\left(\mathbf{V}-\mathbf{V}^{\mathrm{T}}\right)} & (-\pi < z < \pi) \end{cases} \tag{3-3}$$

where $\mathbf{O}_{m\times n}$ denotes the m-by-n matrix with zero components and tr(**V**) indicates the trace of the matrix (**V**).

### 3.2.2. The co-rotational formulation of the two-node beam element

A three-dimensional two-node elastic beam element is considered (Figure 3-1). The nodal position and triads of the beam are pre-defined and each node has three degrees of freedom for translational and rotational motion, respectively. The initial and final nodal coordinates of a beam element are denoted as

$$ {}^{i}\vec{p}_N = \begin{bmatrix} {}^{i}x_N & {}^{i}y_N & {}^{i}z_N \end{bmatrix}^{\mathrm{T}}, \quad {}^{f}\vec{p}_N = \begin{bmatrix} {}^{f}x_N & {}^{f}y_N & {}^{f}z_N \end{bmatrix}^{\mathrm{T}} \tag{3-4} $$

where $i$ and $f$ represent the initial and final configuration and $N$ represents the node index of the beam element as $N = 1,2$. These initial and final configurations correspond to the configurations at the time step $t$ and $t + \Delta t$, respectively, in the nonlinear solution procedure.

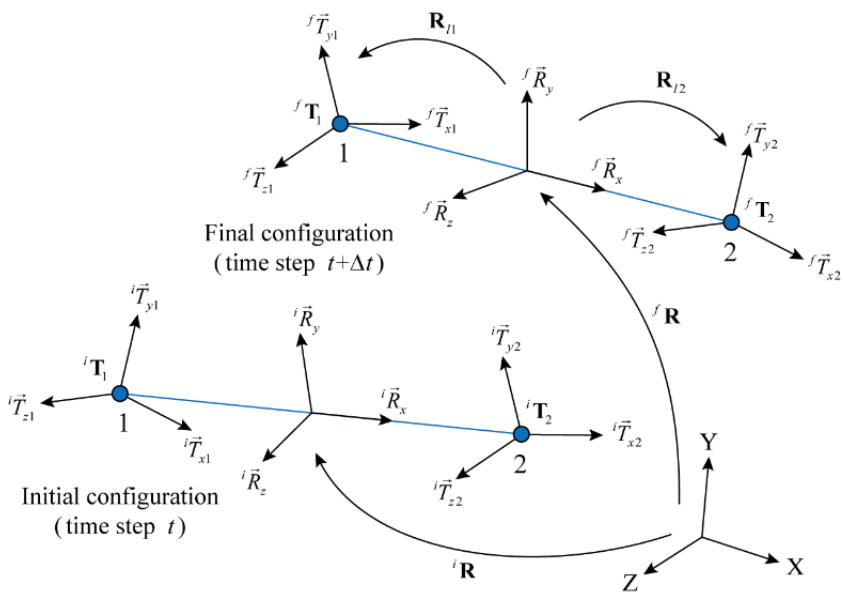


Figure 3-1. Initial and final configuration and the triads of a beam element.

The initial and final nodal triads of the beam can be expressed as

$$ {}^{i}\mathbf{T}_N = \begin{bmatrix} {}^{i}\vec{T}_{xN} & {}^{i}\vec{T}_{yN} & {}^{i}\vec{T}_{zN} \end{bmatrix}, \quad {}^{f}\mathbf{T}_N = \begin{bmatrix} {}^{f}\vec{T}_{xN} & {}^{f}\vec{T}_{yN} & {}^{f}\vec{T}_{zN} \end{bmatrix} \tag{3-5} $$

where $\vec{T}_{kN}$ represents the orthogonal axes of the nodal triads ($k = x, y, z$). Also, the

orientation of the beam, called the CR triad, is given in the initial configuration as

$$ {}^{i}\mathbf{R} = \left[ \, {}^{i}\vec{R}_x \quad {}^{i}\vec{R}_y \quad {}^{i}\vec{R}_z \, \right] \tag{3-6} $$

For the given initial and final configurations, the local deformation is derived. Using the initial and final nodal coordinates, the nodal displacement is calculated as

$$ \vec{u}_N = {}^{f}\vec{p}_N - {}^{i}\vec{p}_N \tag{3-7} $$

The initial and final length of the beam is obtained as

$$ L_i = \left\| {}^{i}\vec{p}_2 - {}^{i}\vec{p}_1 \right\|, \quad L_f = \left\| {}^{i}\vec{p}_2 + \vec{u}_2 - {}^{i}\vec{p}_1 - \vec{u}_1 \right\| \tag{3-8} $$

where $\|\vec{v}\|$ is the Euclidean norm or the magnitude of a vector, $\vec{v}$. The orthogonal matrices ($\mathbf{R}_{g1}$ and $\mathbf{R}_{g2}$) are determined to specify the orientation of the nodal triads in the final configuration from the initial CR triad as follows.

$$ \mathbf{R}_{gN} = {}^{f}\mathbf{T}_N \, {}^{i}\mathbf{R} \tag{3-9} $$

Auxiliary vectors ($\vec{q}_N$ and $\vec{q}$) are introduced to determine the orientation of the nodal triads as

$$ \vec{q}_N = \mathbf{R}_{gN} \, {}^{i}\mathbf{R} \begin{bmatrix} 0 & 1 & 0 \end{bmatrix}^T, \quad \vec{q} = \frac{1}{2}\left(\vec{q}_1 + \vec{q}_2\right) \tag{3-10} $$

Accordingly, the final orientation of CR triad is defined as

$$ {}^{f}\mathbf{R} = \left[ \, {}^{f}\vec{R}_x \quad {}^{f}\vec{R}_y \quad {}^{f}\vec{R}_z \, \right] \tag{3-11} $$

where the first axis (${}^{f}\vec{R}_x$) is defined by the line connecting two nodes and the other axis (${}^{f}\vec{R}_y$ and ${}^{f}\vec{R}_z$) are obtained from the auxiliary vector as

$$ {}^{f}\vec{r}_x = \frac{1}{L_f}\left( {}^{i}\vec{x}_2 + \vec{u}_2 - {}^{i}\vec{x}_1 - \vec{u}_1 \right), \quad {}^{f}\vec{r}_z = \frac{{}^{f}\vec{r}_x \times \vec{q}}{\left\| {}^{f}\vec{r}_x \times \vec{q} \right\|}, \quad {}^{f}\vec{r}_y = {}^{f}\vec{r}_z \times {}^{f}\vec{r}_x \tag{3-12} $$

The local rotation matrices ($\mathbf{R}_{lN}$) relative to the final CR triad is calculated by

$$\mathbf{R}_{lN} = {}^{f}\mathbf{R}\,\mathbf{R}_{gN}\,{}^{i}\mathbf{R} \tag{3-13}$$

Local translational and rotational deformation is now evaluated from the initial and current length of the beam and the local rotation matrices as

$$u_l = L_f - L_i, \qquad \vec{\phi}_N = \tilde{\mathbf{\Phi}}_N \tag{3-14}$$

where $u_l$ represents the translational deformation in the longitudinal direction of the beam along ${}^{f}\vec{r}_x$ and $\vec{\phi}_N$ is the nodal rotational deformation from initial to final configuration, which is derived by the upper tilde operator to the log matrix of the local rotation matrices given by

$$\mathbf{\Phi}_N = \log\left(\mathbf{R}_{lN}\right) \tag{3-15}$$

Finally, the local displacement vector is determined as

$$\vec{U}_l = \begin{bmatrix} u_l & \vec{\phi}_{l1}^{\mathrm{T}} & \vec{\phi}_{l2}^{\mathrm{T}} \end{bmatrix}^{\mathrm{T}} \tag{3-16}$$

### 3.2.3. Internal force vector in the global coordinate

The local internal force vector is calculated in the local CR triad using the local displacement vector as

$$\vec{F}_l = \mathbf{K}_l \vec{U}_n \tag{3-17}$$

where $\mathbf{K}_l$ is the 7-by-7 local stiffness matrix of the beam element, $\vec{F}_l$ is the local internal force vector, and $\vec{U}_n$ is the net displacement vector with respect to the relative geometry. This local stiffness matrix is derived for the beam element, which can consider the relative geometry and mechanical properties of between BPs. The construction of the local stiffness matrix and net displacement vector is described in the next section. On the other hands, the components of the internal force vector are expressed to be used in coordinate transformation as

$$\vec{F}_l = \begin{bmatrix} n_l & \vec{m}_{l1}^{\mathrm{T}} & \vec{m}_{l2}^{\mathrm{T}} \end{bmatrix}^{\mathrm{T}} \tag{3-18}$$

where $n_l$ and $\vec{m}_{lN}$ are the local axial force and moments at each node, respectively.

The internal force vector in the global coordinate is derived through coordinate transformations. The first transformation matrix is introduced as

$$\mathbf{B}_a = \begin{bmatrix} 1 & \mathbf{O}_{1\times3} & \mathbf{O}_{1\times3} \\ \mathbf{O}_{3\times1} & \mathbf{T}_s^{-1}\left(\vec{\phi}_{l1}\right) & \mathbf{O}_{3\times3} \\ \mathbf{O}_{3\times1} & \mathbf{O}_{3\times3} & \mathbf{T}_s^{-1}\left(\vec{\phi}_{l2}\right) \end{bmatrix} \tag{3-19}$$

where an inverse transformation function of a rotation vector ($\vec{\phi}$) is given by

$$\mathbf{T}_s^{-1}\left(\vec{\phi}\right) = \frac{\phi/2}{\tan\left(\phi/2\right)}\mathbf{I}_{3\times3} + \left(1 - \frac{\phi/2}{\tan\left(\phi/2\right)}\right)\hat{\phi}\hat{\phi}^{\mathrm{T}} - \frac{1}{2}\tilde{\vec{\phi}} \tag{3-20}$$

where $\phi$ is the magnitude of the rotation vector as $\phi = \left\|\vec{\phi}\right\|$, and $\hat{\phi}$ is the unit vector of the rotation vector as $\hat{\phi} = \vec{\phi}/\left\|\vec{\phi}\right\|$. For $\phi = 0$, the 3-by-3 identity matrix is obtained. Together, the first transformed internal force vector is computed from the transformation matrix $\mathbf{B}_a^{\mathrm{T}}$ as

$$\vec{F}_a = \mathbf{B}_a^{\mathrm{T}} \vec{F}_l = \begin{bmatrix} n_a & \vec{m}_{a1}^{\mathrm{T}} & \vec{m}_{a2}^{\mathrm{T}} \end{bmatrix}^{\mathrm{T}} \tag{3-21}$$

In the next step, the second transformation matrix is derived as follows.

$$\mathbf{B}_g = \begin{bmatrix} \vec{r}_g \\ \mathbf{P}\mathbf{E}^T \end{bmatrix} \tag{3-22}$$

where $\vec{r}_{\mathrm{g}}$ is the 1-by-12 row vector from local axial translation as

$$\vec{r}_g = \begin{bmatrix} -{}^f\vec{R}_x^{\mathrm{T}} & \mathbf{O}_{1\times 3} & {}^f\vec{R}_x^{\mathrm{T}} & \mathbf{O}_{1\times 3} \end{bmatrix} \tag{3-23}$$

Here, ${}^f\vec{R}_x$ was previously determined by the line connecting two nodes. And the matrix $\mathbf{E}$ is constructed using the local rotation matrix as

$$\mathbf{E} = \mathrm{diag}\left( {}^f\mathbf{R}, {}^f\mathbf{R}, {}^f\mathbf{R}, {}^f\mathbf{R} \right) \tag{3-24}$$

The 6-by-12 matrix $\mathbf{P}$ for the coordinate transformation is given by

$$\mathbf{P} = \begin{bmatrix} \mathbf{O}_{3\times 3} & \mathbf{I}_{3\times 3} & \mathbf{O}_{3\times 3} & \mathbf{O}_{3\times 3} \\ \mathbf{O}_{3\times 3} & \mathbf{O}_{3\times 3} & \mathbf{O}_{3\times 3} & \mathbf{I}_{3\times 3} \end{bmatrix} - \begin{bmatrix} \mathbf{G}^{\mathrm{T}} \\ \mathbf{G}^{\mathrm{T}} \end{bmatrix} \tag{3-25}$$

where the matrix $\mathbf{G}$ is given as

$$\mathbf{G} = \begin{bmatrix} 0 & 0 & \frac{\eta}{L_f} & \frac{\eta_{12}}{2} & -\frac{\eta_{11}}{2} & 0 & 0 & 0 & -\frac{\eta}{L_f} & \frac{\eta_{22}}{2} & -\frac{\eta_{21}}{2} & 0 \\ 0 & 0 & \frac{1}{L_f} & 0 & 0 & 0 & 0 & 0 & -\frac{1}{L_f} & 0 & 0 & 0 \\ 0 & -\frac{1}{L_f} & 0 & 0 & 0 & 0 & 0 & \frac{1}{L_f} & 0 & 0 & 0 & 0 \end{bmatrix}^{\mathrm{T}} \tag{3-26}$$

where the components are calculated as

$$\eta = \frac{s_1}{s_2}, \quad \eta_{11} = \frac{s_{11}}{s_2}, \quad \eta_{12} = \frac{s_{12}}{s_2}, \quad \eta_{21} = \frac{s_{21}}{s_2}, \quad \eta_{22} = \frac{s_{22}}{s_2} \tag{3-27}$$

Here, $s_j$ and $s_{ij}$ are the components of the vectors ${}^{f}\mathbf{R}^{\mathrm{T}}\vec{q}$ and ${}^{f}\mathbf{R}^{\mathrm{T}}\vec{q}_k$ as

$$\begin{aligned}\vec{s} &= {}^{f}\mathbf{R}^{\mathrm{T}}\vec{q} = \begin{bmatrix} s_1 & s_2 & 0 \end{bmatrix}^{\mathrm{T}} \\ \vec{s}_1 &= {}^{f}\mathbf{R}^{\mathrm{T}}\vec{q}_1 = \begin{bmatrix} s_{11} & s_{12} & s_{12} \end{bmatrix}^{\mathrm{T}} \\ \vec{s}_2 &= {}^{f}\mathbf{R}^{\mathrm{T}}\vec{q}_2 = \begin{bmatrix} s_{21} & s_{22} & s_{23} \end{bmatrix}^{\mathrm{T}}\end{aligned} \tag{3-28}$$

Consequently, the 12-by-1 internal force of the structural element in global coordinates ($\vec{F}_{\mathrm{G}}^{\mathrm{ST}}$) is obtained from the second transformation matrix $\mathbf{B}_{\mathrm{g}}^{\mathrm{T}}$ as

$$\vec{F}_{\mathrm{G}}^{\mathrm{ST}} = \mathbf{B}_{g}^{\mathrm{T}}\vec{F}_{a} \tag{3-29}$$

### 3.2.4. Stiffness matrix in the global coordinate

In the next step, to derive the stiffness matrix in the global coordinate, the local stiffness matrix is first transformed into

$$\mathbf{K}_a = \mathbf{B}_a^{\mathrm{T}} \mathbf{K}_l \mathbf{B}_a + \mathbf{K}_h \tag{3-30}$$

where the 7-by-7 matrix $\mathbf{K}_h$ is calculated as

$$\mathbf{K}_h = \begin{bmatrix} 0 & \mathbf{O}_{1\times 3} & \mathbf{O}_{1\times 3} \\ \mathbf{O}_{3\times 1} & \mathbf{J}\left(\vec{\phi}_{l1}, \vec{m}_{l1}\right)\mathbf{T}_s^{-1}\left(\vec{\phi}_{l1}\right) & \mathbf{O}_{3\times 3} \\ \mathbf{O}_{3\times 1} & \mathbf{O}_{3\times 3} & \mathbf{J}\left(\vec{\phi}_{l2}, \vec{m}_{l2}\right)\mathbf{T}_s^{-1}\left(\vec{\phi}_{l2}\right) \end{bmatrix} \tag{3-31}$$

The function $\mathbf{J}\left(\vec{\phi}, \vec{m}\right)$ is expressed as

$$\mathbf{J}\left(\vec{\phi}, \vec{m}\right) = \eta\left(\vec{\phi}\vec{m}^{\mathrm{T}} - 2\vec{m}\vec{\phi}^{\mathrm{T}} + \vec{\phi}^{\mathrm{T}}\vec{m}\mathbf{I}_{3\times 3}\right) + \mu\left(\vec{\phi}\right)^2\left(\vec{m}\vec{\phi}^{\mathrm{T}}\right) - \frac{1}{2}\tilde{\vec{m}} \tag{3-32}$$

where the variables are denoted as

$$\phi = \|\vec{\phi}\|, \quad \eta = \frac{2\sin\phi - \phi(1+\cos\phi)}{2\phi^2\sin\phi}, \quad \mu = \frac{\phi(\phi+\sin\phi) - 8\sin^2(\phi/2)}{4\phi^4\sin^2(\phi/2)} \tag{3-33}$$

Here, $\mathbf{J}\left(\vec{\phi}, \vec{m}\right) = -\tilde{\vec{m}}/2$ for $\phi = 0$.

For the second coordinate transformation, the 12-by-12 matrix $\mathbf{K}_m$ is computed from

$$\mathbf{K}_m = n_a\mathbf{D} - \mathbf{E}\mathbf{Q}\mathbf{G}^{\mathrm{T}}\mathbf{E}^{\mathrm{T}} + \mathbf{E}\mathbf{G}\,\vec{a}\,\vec{r} \tag{3-34}$$

where the matrix, D is given by

$$\mathbf{D} = \begin{bmatrix} \mathbf{D}_3 & \mathbf{O}_{3\times 3} & -\mathbf{D}_3 & \mathbf{O}_{3\times 3} \\ \mathbf{O}_{3\times 3} & \mathbf{O}_{3\times 3} & \mathbf{O}_{3\times 3} & \mathbf{O}_{3\times 3} \\ -\mathbf{D}_3 & \mathbf{O}_{3\times 3} & \mathbf{D}_3 & \mathbf{O}_{3\times 3} \\ \mathbf{O}_{3\times 3} & \mathbf{O}_{3\times 3} & \mathbf{O}_{3\times 3} & \mathbf{O}_{3\times 3} \end{bmatrix} \quad \mathbf{D}_3 = \frac{1}{L_f}\left(\mathbf{I}_{3\times 3} - {}^f\vec{R}_x\,{}^f\vec{R}_x^T\right) \tag{3-35}$$

Using the matrix **P** and the internal moments $\vec{m}_{lN}$, the 3-by-1 vectors $\vec{Q}_k$ are obtained as

$$\mathbf{P}^{\mathrm{T}}\vec{m} = \begin{bmatrix} \vec{Q}_1^{\mathrm{T}} & \vec{Q}_2^{\mathrm{T}} & \vec{Q}_3^{\mathrm{T}} & \vec{Q}_4^{\mathrm{T}} \end{bmatrix} \tag{3-36}$$

This provides the 12-by-3 matrix **Q** as

$$\mathbf{Q} = \begin{bmatrix} \vec{Q}_1^{\mathrm{T}} & \vec{Q}_2^{\mathrm{T}} & \vec{Q}_3^{\mathrm{T}} & \vec{Q}_4^{\mathrm{T}} \end{bmatrix}^{T} \tag{3-37}$$

where the under tilde operator generates a 3-by-3 skew-symmetric matrix of each component. And, using previous variables and the transformed internal force vector, the vector $\vec{a}$ is obtained by

$$\vec{a} = \begin{bmatrix} 0 & \dfrac{\eta}{L_f}\left(m_{a1x} + m_{a2x}\right) - \dfrac{1}{L_f}\left(m_{a1y} + m_{a2y}\right) & \dfrac{1}{L_f}\left(m_{a1z} + m_{a2z}\right) \end{bmatrix}^{\mathrm{T}} \tag{3-38}$$

where $m_{aNk}$ is the component of $\vec{m}_{aN}$. Together, the 12-by-12 stiffness matrix of the element as a structural motif in the global coordinate is derived as

$$\mathbf{K}_{\mathrm{G}}^{\mathrm{ST}} = \mathbf{B}_g^{\mathrm{T}}\mathbf{K}_a\mathbf{B}_g + \mathbf{K}_m \tag{3-39}$$

In summary, the global stiffness matrix ($\mathbf{K}_{\mathrm{G}}^{\mathrm{ST}}$) and the internal force vector ($\vec{F}^e$) of the element are derived from the local stiffness matrix ($\mathbf{K}_l$) and the internal force vector ($\vec{F}_l$) containing detailed information on relative geometry and mechanical properties. The following sections provide the details of the developed beam element to describe the relative geometry and mechanical properties of DNA at the BP level, and the characterization of intrinsic properties from molecular dynamics simulation.

## 3.3. Local stiffness matrix and internal force vector

On the elastic beam element, the local stiffness matrix ($\mathbf{K}_l$) and local internal force vector ($\vec{F}_l$) are derived by differentiating the total strain energy ($\Pi_{\mathrm{SE}}$) with respect to the net displacement vector ($\vec{U}_n$) as

$$\mathbf{K}_l = \frac{\partial^2 \Pi_{\mathrm{SE}}}{\partial \vec{U}_n \partial \vec{U}_n}, \quad \vec{F}_l = \frac{\partial \Pi_{\mathrm{SE}}}{\partial \vec{U}_n} \tag{3-40}$$

The total strain energy is, however, constructed in terms of the local strain field, which is formulated from the displacement field of the element, and the displacement field is interpolated by nodal net displacement. That is, the strain energy can be expressed in terms of nodal displacement.

### 3.3.1. Net displacement in the local coordinate

The local displacement vector was considered as

$$\vec{U}_l = \begin{bmatrix} u_l & \vec{\phi}_{l1}^{\mathrm{T}} & \vec{\phi}_{l2}^{\mathrm{T}} \end{bmatrix}^{\mathrm{T}} \tag{3-41}$$

where $u_l$ and $\vec{\phi}_{lN}$ represent the translational displacement and nodal rotation of the beam element, respectively. In the consideration of the relative geometry, which is described in two base-pairs, the net displacement vector for relative geometry is then expressed as

$$\begin{aligned} \vec{U}_n &= \begin{bmatrix} u_n & \vec{\phi}_{n1}^{\mathrm{T}} & \vec{\phi}_{n2}^{\mathrm{T}} \end{bmatrix}^{\mathrm{T}} \\ &= \begin{bmatrix} u_l - \left(L_g - L_i\right) & \vec{\phi}_{l1}^{\mathrm{T}} - \vec{\Theta}_{g1}^{\mathrm{T}} & \vec{\phi}_{l2}^{\mathrm{T}} - \vec{\Theta}_{g2}^{\mathrm{T}} \end{bmatrix}^{\mathrm{T}} \end{aligned} \tag{3-42}$$

where $u_n$ is the net axial displacement, $\vec{\phi}_{nN}$ is the net rotational displacement of each node, $L_i$ is the initial length, and $L_{\mathrm{g}}$ and $\vec{\Theta}_{\mathrm{g}N}$ represent the intrinsic length and rotation of the element, respectively.

The intrinsic length and rotation were estimated as

$$\begin{aligned} L_g &= \left[ \left(\Delta_{x2} - \Delta_{x1}\right)^2 + \left(\Delta_{y2} - \Delta_{y1}\right)^2 + \left(\Delta_{z2} - \Delta_{z1}\right)^2 \right]^{1/2} \\ \vec{\Theta}_{gN} &= \begin{bmatrix} \Theta_{xN} & \Theta_{yN} & \Theta_{zN} \end{bmatrix}^{\mathrm{T}} \end{aligned} \tag{3-43}$$

Here, $\Theta_{kN}$ and $\Delta_{kN}$ can be estimated from the molecular dynamics (MD) simulation.

### 3.3.2. Displacement field

The displacement field is derived from the net displacement. In order to describe the continuous displacement field, interpolation functions are defined as

$$N_1(x)=\frac{x}{L_g},\quad N_2(x)=x\left(1-\frac{x}{L_g}\right)^2,\quad N_3(x)=\frac{x}{L_g}\left(\frac{x}{L_g}-1\right) \tag{3-44}$$

where $x$ denotes an axial variable in the local coordinate of the beam. Then, using these interpolation functions, the translational deformation is given by

$$\Delta_x(x)=N_1u_n,\quad \Delta_y(x)=N_2\phi_{n1z}+N_3\phi_{n2z},\quad \Delta_z(x)=-N_2\phi_{n1y}-N_3\phi_{n2y} \tag{3-45}$$

where $\phi_{nNk}$ represent the rotational component of each node. And, its differentiation for $x$ is expressed as

$$\frac{\partial\Delta_x}{\partial x}=\frac{\partial N_1}{\partial x}u_n,\quad \frac{\partial\Delta_y}{\partial x}=\frac{\partial N_2}{\partial x}\phi_{n1z}+\frac{\partial N_3}{\partial x}\phi_{n2z},\quad \frac{\partial\Delta_z}{\partial x}=-\frac{\partial N_2}{\partial x}\phi_{n1y}-\frac{\partial N_3}{\partial x}\phi_{n2y} \tag{3-46}$$

with

$$\frac{\partial N_1}{\partial x}=\frac{1}{L_g},\quad \frac{\partial N_2}{\partial x}=\frac{1}{L_g^2}\left(3x-L_g\right)\left(x-L_g\right),\quad \frac{\partial N_3}{\partial x}=\frac{1}{L_g^2}x\left(3x-2L_g\right) \tag{3-47}$$

On the other hands, the rotational deformation is given as the averaged rotation by

$$\Theta_x=\frac{1}{2}\left(\phi_{n1x}+\phi_{n2x}\right),\quad \Theta_y=\frac{1}{2}\left(\phi_{n1y}+\phi_{n2y}\right),\quad \Theta_z=\frac{1}{2}\left(\phi_{n1z}+\phi_{n2z}\right) \tag{3-48}$$

The differentiation of rotation is also expressed in the sense of averaged difference of the rotation as

$$\frac{\partial\Theta_x}{\partial x}=\frac{1}{L_g}\left(\phi_{n2x}-\phi_{n1x}\right),\quad \frac{\partial\Theta_y}{\partial x}=\frac{1}{L_g}\left(\phi_{n2y}-\phi_{n1y}\right),\quad \frac{\partial\Theta_z}{\partial x}=\frac{1}{L_g}\left(\phi_{n2z}-\phi_{n1z}\right) \tag{3-49}$$

### 3.3.3. Strain field

The kinematics of the beam is described to express the local strain field from the displacement field (Figure 3-2). The kinematic model proposed by previous studies[20,66] was employed. The warping function was here neglected and the shear center was assumed to be located at the center of the beam.

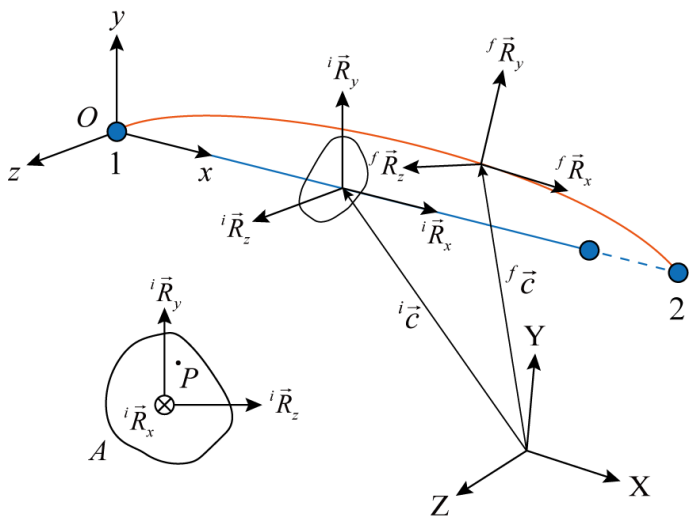


Figure 3-2. Local beam kinematics.

${}^{i}\vec{P}$ and ${}^{f}\vec{P}$ denoted the position vector of a point, $P$ on the cross-section in the only rotated initial and final configuration, respectively, given by

$$\begin{aligned} {}^{i}\vec{P}(x,y,z) &= {}^{i}\vec{c}(x) + y\,{}^{i}\vec{R}_y + z\,{}^{i}\vec{R}_z \\ {}^{f}\vec{P}(x,y,z) &= {}^{f}\vec{c}(x) + y\,{}^{f}\vec{R}_y(x) + z\,{}^{f}\vec{R}_z(x) \end{aligned} \tag{3-50}$$

where the beam position vectors are represented as

$${}^{i}\vec{c}(x) = \begin{bmatrix} {}^{i}c_x & {}^{i}c_y & {}^{i}c_z \end{bmatrix}^{\mathrm{T}}, \qquad {}^{f}\vec{c}(x) = \begin{bmatrix} {}^{f}c_x & {}^{f}c_y & {}^{f}c_z \end{bmatrix}^{\mathrm{T}} \tag{3-51}$$

and the final orientation of cross-section is specified from the initial orientation as

$$\begin{bmatrix} {}^{f}\vec{R}_x & {}^{f}\vec{R}_y & {}^{f}\vec{R}_z \end{bmatrix} = \mathbf{R}_l \begin{bmatrix} {}^{i}\vec{R}_x & {}^{i}\vec{R}_y & {}^{i}\vec{R}_z \end{bmatrix} \tag{3-52}$$

where the rotation matrix $\mathbf{R}_l$ is given in the second approximation as

$$\mathbf{R}_l = \mathbf{I}_{3\times 3} + \tilde{\vec{\Theta}} + \frac{1}{2}\tilde{\vec{\Theta}}^2 \tag{3-53}$$

with the local rotation vector as

$$\vec{\Theta}(x) = \begin{bmatrix} \Theta_x & \Theta_y & \Theta_z \end{bmatrix}^T \tag{3-54}$$

Then, the displacement vector of the point $P$ is evaluated as

$${}^P\vec{U}(x,y,z) = \begin{bmatrix} {}^PU_x & {}^PU_y & {}^PU_z \end{bmatrix}^T = \vec{P}_f - \vec{P}_i \tag{3-55}$$

The components of the displacement vector are exactly expressed as

$$\begin{aligned}
{}^PU_x(x,y,z) &= \Delta_x(x) + y\left(\frac{1}{2}\Theta_x\Theta_y - \Theta_z\right) + z\left(\frac{1}{2}\Theta_x\Theta_z + \Theta_y\right) \\
{}^PU_y(x,y,z) &= \Delta_y(x) - \frac{1}{2}y\left(\Theta_x^2 + \Theta_z^2\right) + z\left(\frac{1}{2}\Theta_y\Theta_z - \Theta_x\right) \\
{}^PU_z(x,y,z) &= \Delta_z(x) + y\left(\frac{1}{2}\Theta_y\Theta_z + \Theta_x\right) - \frac{1}{2}z\left(\Theta_x^2 + \Theta_y^2\right)
\end{aligned} \tag{3-56}$$

where the displacement components on the element are denoted as

$$\begin{aligned}
\Delta_x(x) &= {}^fc_x - {}^ic_x \\
\Delta_y(x) &= {}^fc_y - {}^ic_y \\
\Delta_z(x) &= {}^fc_z - {}^ic_z
\end{aligned} \tag{3-57}$$

Neglecting higher-order terms, the linear Green-Lagrange strain is derived as

$$\begin{aligned}
\varepsilon_{xx} &= \frac{\partial {}^PU_{x,x}}{\partial x} \simeq \varepsilon_c + yk_y + zk_z \\
2\varepsilon_{xy} &= \frac{\partial {}^PU_{x,y}}{\partial x} + \frac{\partial {}^PU_{y,x}}{\partial x} \simeq \gamma_{xy} - zk_x \\
2\varepsilon_{xz} &= \frac{\partial {}^PU_{x,z}}{\partial x} + \frac{\partial {}^PU_{z,x}}{\partial x} \simeq \gamma_{xz} + yk_x
\end{aligned} \tag{3-58}$$

with the components as

$$
\begin{aligned}
&k_x = \frac{\partial \Theta_x}{\partial x}, \qquad k_y = -\frac{\partial \Theta_z}{\partial x}, \qquad k_z = \frac{\partial \Theta_y}{\partial x} \\
&\varepsilon_c = \frac{\partial \Delta_x}{\partial x}, \qquad \gamma_{xy} = \frac{\partial \Delta_y}{\partial x} - \Theta_z, \qquad \gamma_{xz} = \frac{\partial \Delta_z}{\partial x} + \Theta_y
\end{aligned}
\tag{3-59}
$$

### 3.3.4. Strain energy

The strain field was expressed as a function of the displacement field. Accordingly, the total mechanical strain energy ($\Pi_{\mathrm{SE}}$) is constructed as the sum of energy from mechanical rigidity ($\Pi_{\mathrm{R}}$) and coupling ($\Pi_{\mathrm{C}}$) as

$$\Pi_{\mathrm{SE}} = \Pi_{\mathrm{R}} + \Pi_{\mathrm{C}} \tag{3-60}$$

The strain energy from mechanical rigidity is divided into axial ($\pi_{\mathrm{A}}$) and shear ($\pi_{\mathrm{S}}$) components expressed as

$$\Pi_{\mathrm{R}} = \int_{L_g} \left(\pi_{\mathrm{A}} + \pi_{\mathrm{S}}\right) dx \tag{3-61}$$

The first axial term is formulated in the elastic theory as

$$\pi_{\mathrm{A}} = \frac{1}{2}\int_A E\varepsilon_{xx}^2 dA = \frac{1}{2}EA\varepsilon_c^2 + \frac{1}{2}EI_y k_y^2 + \frac{1}{2}EI_z k_z^2 \tag{3-62}$$

with the stretching ($EA$) and bending rigidities ($EI_y$ and $EI_z$) as

$$EA = \int_A E dA, \quad EI_y = \int_A Ey^2 dA, \quad EI_z = \int_A Ez^2 dA \tag{3-63}$$

And, the second shear term is derived as

$$\pi_{\mathrm{S}} = \frac{1}{2}\int_A G\left[\left(2\varepsilon_{xy}\right)^2 + \left(2\varepsilon_{xz}\right)^2\right] dA = \frac{1}{2}GA_y + \frac{1}{2}GA_z + \frac{1}{2}GJ\,k_1^2 \tag{3-64}$$

where the torsional ($GJ$) and shear rigidities ($GA_y$ and $GA_z$) are expressed as

$$GJ = \int_A G\left(y^2 + z^2\right) dA, \quad GA_y = \int_A G\gamma_{xy}^2 dA, \quad GA_z = \int_A G\gamma_{xz}^2 dA \tag{3-65}$$

Likewise, the strain energy of mechanical coupling can be divided into the rotation-rotation ($\pi_{\mathrm{Rot-Rot}}$), translation-translation ($\pi_{\mathrm{Trans-Trans}}$), and rotation-translation terms ($\pi_{\mathrm{Rot-Trans}}$) expressed as

$$\Pi_{\mathrm{C}} = \int_{L_g} \left(\pi_{\text{Rot-Rot}} + \pi_{\text{Trans-Trans}} + \pi_{\text{Rot-Trans}}\right) dx \tag{3-66}$$

where each term is obtained as

$$\pi_{\text{Rot-Rot}} = \sum_{\substack{p,q=x,y \\ p\neq q}} \frac{1}{L_g} g\left(\Theta_p, \Theta_q\right) \int_{L_g} \frac{\partial \Theta_p}{\partial x} dx \int_{L_g} \frac{\partial \Theta_q}{\partial x} dx$$

$$\pi_{\text{Trans-Trans}} = \sum_{\substack{p,q=x,y \\ p\neq q}} \frac{1}{L_g} g\left(\Delta_p, \Delta_q\right) \int_{L_g} \frac{\Delta_p}{L_g} dx \int_{L_i} \frac{\Delta_q}{L_g} dx \tag{3-67}$$

$$\pi_{\text{Rot-Trans}} = \sum_{p,q=x,y} \frac{1}{L_g} g\left(\Theta_p, \Delta_q\right) \int_{L_g} \frac{\partial \Theta_p}{\partial x} dx \int_{L_g} \frac{\Delta_q}{L_g} dx$$

where the translation terms are integrated by the average value in order to prevent the zero value.

### 3.3.5. Stiffness matrix in the local coordinate

Together, the 7-by-7 local stiffness matrix ($\mathbf{K}_l$) is derived by the differentiation of the total mechanical strain energy with respect to the net displacement vector as

$$\mathbf{K}_l = \frac{\partial^2 \Pi_{\mathrm{SE}}}{\partial \vec{U}_n \partial \vec{U}_n} = \begin{bmatrix} \mathrm{K}_{11} & \mathbf{K}_{12} & \mathbf{K}_{13} \\ \mathbf{K}_{21} & \mathbf{K}_{22} & \mathbf{K}_{23} \\ \mathbf{K}_{31} & \mathbf{K}_{32} & \mathbf{K}_{33} \end{bmatrix} \tag{3-68}$$

with the components as

$$\mathrm{K}_{11} = \frac{EA}{L_i}$$

$$\mathbf{K}_{12} = \begin{bmatrix} -\frac{g(\Theta_x,\Delta_z)}{2L_i} & -\frac{g(\Delta_x,\Delta_z)}{24} & -\frac{g(\Theta_y,\Delta_z)}{2L_i} & \frac{g(\Delta_y,\Delta_z)}{24} & -\frac{g(\Theta_z,\Delta_z)}{2L_i} \end{bmatrix}_{3\times 1}$$

$$\mathbf{K}_{13} = \begin{bmatrix} \frac{g(\Theta_x,\Delta_z)}{2L_i} & \frac{g(\Delta_x,\Delta_z)}{24} & \frac{g(\Theta_y,\Delta_z)}{2L_i} & -\frac{g(\Delta_y,\Delta_z)}{24} & \frac{g(\Theta_z,\Delta_z)}{2L_i} \end{bmatrix}_{3\times 1}$$

$$\mathbf{K}_{21} = \mathbf{K}_{12}^{\mathrm{T}}$$

$$\mathbf{K}_{31} = \mathbf{K}_{13}^{\mathrm{T}}$$

$$\mathbf{K}_{22} = \begin{bmatrix} \frac{GJ}{L_i} & \frac{g(\Theta_x,\Delta_x)}{12} + \frac{g(\Theta_x,\Theta_y)}{L_i} & -\frac{g(\Theta_x,\Delta_y)}{12} + \frac{g(\Theta_x,\Theta_z)}{L_i} \\ & \frac{g(\Theta_y,\Delta_x)}{6} + \frac{23GA_zL_i}{60} + \frac{EI_{zz}}{L_i} & \frac{g(\Theta_z,\Delta_x)}{12} - \frac{g(\Theta_y,\Delta_y)}{12} \\ & & -\frac{g(\Delta_x,\Delta_y)L_i}{144} + \frac{g(\Theta_y,\Theta_z)}{L_i} \\ \text{sym.} & & -\frac{g(\Theta_z,\Delta_y)}{6} + \frac{23GA_yL_i}{60} + \frac{EI_{yy}}{L_i} \end{bmatrix}_{3\times 3} \tag{3-69}$$

$$\mathbf{K}_{23} = \begin{bmatrix} -\frac{GJ}{L_i} & -\frac{g(\Theta_x,\Delta_x)}{12} - \frac{g(\Theta_x,\Theta_y)}{L_i} & \frac{g(\Theta_x,\Delta_y)}{12} - \frac{g(\Theta_x,\Theta_z)}{L_i} \\ & -\frac{g(\Theta_y,\Delta_x)}{6} + \frac{13GA_zL_i}{60} - \frac{EI_{zz}}{L_i} & -\frac{g(\Theta_z,\Delta_x)}{12} + \frac{g(\Theta_y,\Delta_y)}{12} \\ & & +\frac{g(\Delta_x,\Delta_y)L_i}{144} - \frac{g(\Theta_y,\Theta_z)}{L_i} \\ \text{sym.} & & \frac{g(\Theta_z,\Delta_y)}{6} + \frac{13GA_yL_i}{60} - \frac{EI_{yy}}{L_i} \end{bmatrix}_{3\times 3}$$

$$\mathbf{K}_{32} = \mathbf{K}_{23}$$

$$\mathbf{K}_{33} = \mathbf{K}_{22}$$

### 3.3.6. Internal force vector in the local coordinate

The internal force vector ($\vec{F}_l$) is also obtained from the elastic strain energy as

$$\vec{F}_l = \frac{\partial \Pi_{\mathrm{SE}}}{\partial \vec{U}_n} = \mathbf{K}_l \vec{U}_n = \begin{bmatrix} n_l & \vec{m}_{l1}^{\mathrm{T}} & \vec{m}_{l2}^{\mathrm{T}} \end{bmatrix}^{\mathrm{T}} \tag{3-70}$$

with the components as

$$\begin{aligned} n_l &= \mathrm{K}_{11} u_n + \mathbf{K}_{12} \vec{\phi}_{n1} + \mathbf{K}_{13} \vec{\phi}_{n2} \\ \vec{m}_{l1} &= \mathbf{K}_{21} u_n + \mathbf{K}_{22} \vec{\phi}_{n1} + \mathbf{K}_{23} \vec{\phi}_{n2} \\ \vec{m}_{l2} &= \mathrm{K}_{31} u_n + \mathbf{K}_{32} \vec{\phi}_{n1} + \mathbf{K}_{33} \vec{\phi}_{n2} \end{aligned} \tag{3-71}$$

where $n_l$ and $\vec{m}_{lN}$ are the local axial force and the moment vectors at each node, respectively.

## 3.4. Intrinsic properties of the base-pair step

The intrinsic properties of a DNA base-pair (BP) step are estimated using the trajectories of molecular dynamics (MD) simulation following the approach of the previous study[18] for the regular, nicked, and CO-nick BP steps. This section introduces the characterizing procedure to estimate mechanical properties using relative geometric parameters.

### 3.4.1. Relative geometric parameters in the 3DNA definition

According to the definition of 3DNA[26], the relative geometric parameters of the BP step are represented by Tilt (Rx), Roll (Rx), Twist (Rz) for rotation, and Shift (Dx), Slide (Dy), and Rise (Dz) for translation, respectively (Figure 3-3). Tilt, Roll, and Twist have the original denotation of τ, ρ, and ω, but here they are denoted as Rx, Ry, and Rz to avoid confusion with other parameters.

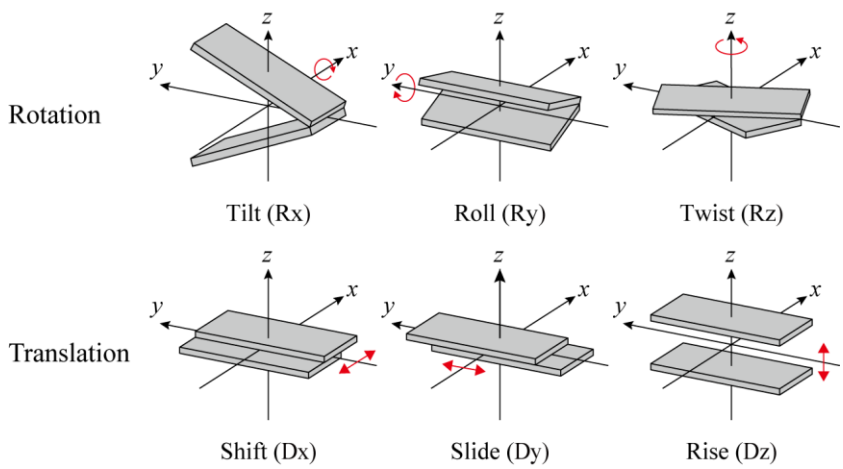


Figure 3-3. Relative geometric parameters of a BP step in 3DNA definition.

The following procedure describes how to calculate the relative geometry from the two BP triads following 3DNA definition[26] (Figure 3-4). The BP triads (${}^{\tau}\mathbf{B}_N$) and position (${}^{\tau}\vec{O}_N$) of successive two BPs were defined as

$$ {}^{\tau}\mathbf{B}_N = \left[ {}^{\tau}\vec{b}_{xN} \quad {}^{\tau}\vec{b}_{yN} \quad {}^{\tau}\vec{b}_{zN} \right], \quad {}^{\tau}\vec{O}_N = \left[ {}^{\tau}O_{xN} \quad {}^{\tau}O_{yN} \quad {}^{\tau}O_{zN} \right]^{\mathrm{T}} \tag{3-72} $$

with denoting two BPs as $N = 1,2$ at a simulation time ($\tau$) in the MD trajectory. Then, the hinge-axis (${}^{\tau}\vec{h}$) and the net bending angle (${}^{\tau}\Gamma$) are calculated as

$$ {}^{\tau}\vec{h} = \frac{{}^{\tau}\vec{b}_{z1} \times {}^{\tau}\vec{b}_{z2}}{\left\| {}^{\tau}\vec{b}_{z1} \times {}^{\tau}\vec{b}_{z2} \right\|}, \quad {}^{\tau}\Gamma = \cos^{-1}\left( {}^{\tau}\vec{b}_{z1} \cdot {}^{\tau}\vec{b}_{z2} \right) \tag{3-73} $$

Aligned BP triads (${}^{\tau}\mathbf{A}_N$) are obtained by rotating the half of the net bending angle around the hinge axis as

$$ \begin{aligned} {}^{\tau}\mathbf{A}_1 &= \left[ {}^{\tau}\vec{a}_{x1} \quad {}^{\tau}\vec{a}_{y1} \quad {}^{\tau}\vec{a}_{z1} \right] = \mathbf{R}\left( +\frac{{}^{\tau}\Gamma}{2} \right) {}^{\tau}\mathbf{B}_1 \\ {}^{\tau}\mathbf{A}_2 &= \left[ {}^{\tau}\vec{a}_{x2} \quad {}^{\tau}\vec{a}_{y2} \quad {}^{\tau}\vec{a}_{z2} \right] = \mathbf{R}\left( -\frac{{}^{\tau}\Gamma}{2} \right) {}^{\tau}\mathbf{B}_2 \end{aligned} \tag{3-74} $$

where a rotation matrix, about a vector $\vec{\theta}$ with the magnitude $\theta = \left\| \vec{\theta} \right\|$ and components $\theta_k$, is derived as

$$ \mathbf{R}(\vec{\theta}) = \begin{bmatrix} \cos\theta + (1-\cos\theta)\theta_x^2 & (1-\cos\theta)\theta_x\theta_y - \theta_z \sin\theta & (1-\cos\theta)\theta_x\theta_z + \theta_y \sin\theta \\ (1-\cos\theta)\theta_x\theta_y + \theta_z \sin\theta & \cos\theta + (1-\cos\theta)\theta_y^2 & (1-\cos\theta)\theta_y\theta_z - \theta_x \sin\theta \\ (1-\cos\theta)\theta_x\theta_z - \theta_y \sin\theta & (1-\cos\theta)\theta_y\theta_z + \theta_x \sin\theta & \cos\theta + (1-\cos\theta)\theta_z^2 \end{bmatrix} \tag{3-75} $$

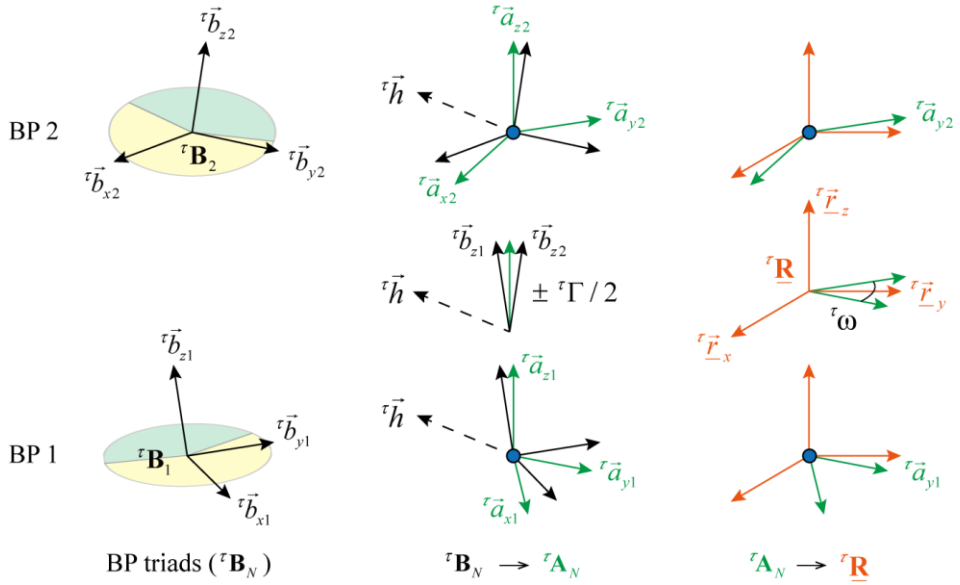


Figure 3-4. Generation of the middle triad from two BP triads.

Here, the z-axes of the two BPs are perfectly aligned after rotations ($^{\tau}\vec{a}_{z1} \parallel {}^{\tau}\vec{a}_{z2}$). The middle triad ($^{\tau}\underline{\mathbf{R}}$) is now determined by the average of aligned BP triads as

$$^{\tau}\underline{\mathbf{R}} = \left[ {}^{\tau}\underline{\vec{r}}_x \quad {}^{\tau}\underline{\vec{r}}_y \quad {}^{\tau}\underline{\vec{r}}_z \right]^{\mathrm{T}} = \frac{{}^{\tau}\mathbf{A}_1 + {}^{\tau}\mathbf{A}_2}{\left\| {}^{\tau}\mathbf{A}_1 + {}^{\tau}\mathbf{A}_2 \right\|} \tag{3-76}$$

where $^{\tau}\underline{\vec{r}}_k$ is a unit vector representing the axis of the middle triad. Noting that the stacked direction of the BP triads ($^{\tau}\underline{\vec{b}}_{zN}$) fluctuates around the direction connecting the origin of the BPs ($^{\tau}\vec{O}_2 - {}^{\tau}\vec{O}_1$), the middle triad can be considered as the local CR triad ($^{\tau}\mathbf{R}$), whose axial axis directs the line connecting the origins of two BPs as follows.

$$^{\tau}\mathbf{R} = \left[ {}^{\tau}\vec{R}_x \quad {}^{\tau}\vec{R}_y \quad {}^{\tau}\vec{R}_z \right]^{\mathrm{T}} = {}^{\tau}\underline{\mathbf{R}} \tag{3-77}$$

Using the local triads and BP coordinates, the translational relative geometry (Shift, Slide, and Rise) is calculated by projecting the vector linking BP origins on the axes of the middle triad as

$$\left[ {}^{\tau}\mathrm{Dx} \quad {}^{\tau}\mathrm{Dy} \quad {}^{\tau}\mathrm{Dz} \right] = \left( {}^{\tau}\vec{O}_2 - {}^{\tau}\vec{O}_1 \right)^{\mathrm{T}} {}^{\tau}\underline{\mathbf{R}} \tag{3-78}$$

The rotational relative geometry (Tilt, Roll, and Twist) is also computed as

$$\begin{aligned} {}^{\tau}\mathrm{Rx} &= {}^{\tau}\Gamma \sin\left( {}^{\tau}\varphi \right) \\ {}^{\tau}\mathrm{Ry} &= {}^{\tau}\Gamma \cos\left( {}^{\tau}\varphi \right) \\ {}^{\tau}\mathrm{Rz} &= \begin{cases} +\cos^{-1}\left( {}^{\tau}\vec{b}_{y1} \cdot {}^{\tau}\vec{b}_{y2} \right) & \text{if } \left( {}^{\tau}\vec{b}_{y1} \times {}^{\tau}\vec{b}_{y2} \right) \cdot {}^{\tau}\vec{r}_z \geq 0 \\ -\cos^{-1}\left( {}^{\tau}\vec{b}_{y1} \cdot {}^{\tau}\vec{b}_{y2} \right) & \text{if } \left( {}^{\tau}\vec{b}_{y1} \times {}^{\tau}\vec{b}_{y2} \right) \cdot {}^{\tau}\vec{r}_z < 0 \end{cases} \end{aligned} \tag{3-79}$$

where the phase angle ${}^{\tau}\varphi$, which is the angle from the hinge axis to the y-axis of the local triad, is given as

$${}^{\tau}\varphi = \begin{cases} -\left| \cos^{-1}\left( {}^{\tau}\vec{r}_y \cdot {}^{\tau}\vec{h} \right) \right| & \text{if } \left( {}^{\tau}\vec{r}_y \times {}^{\tau}\vec{h} \right) \cdot {}^{\tau}\vec{r}_z \geq 0 \\ +\left| \cos^{-1}\left( {}^{\tau}\vec{r}_y \cdot {}^{\tau}\vec{h} \right) \right| & \text{if } \left( {}^{\tau}\vec{r}_y \times {}^{\tau}\vec{h} \right) \cdot {}^{\tau}\vec{r}_z < 0 \end{cases} \tag{3-80}$$

In summary, for a specific BP step, the coordinate and triads are collected in the MD trajectory, providing the ensemble of the relative geometry.

### 3.4.2. Relative geometry and mechanical properties

The collected relative geometric parameters of the BP step were analyzed on the basis of quasi-harmonic strain energy, equivalent to linear elastic strain energy, which for the six deformable modes in the BP step was assumed to the following form.

$$\Pi(\vec{U}) = \frac{1}{2}\vec{U}^{T}\mathbf{k}\vec{U} = \frac{1}{2}\left(\vec{q} - \langle\vec{q}\rangle\right)^{T}\mathbf{k}\left(\vec{q} - \langle\vec{q}\rangle\right) \tag{3-81}$$

where $\vec{q}$ represents the relative geometric parameters of the BP step and $\langle\vec{q}\rangle$ is the ensemble average of collected parameters as

$$\begin{aligned}\vec{q} &= [\mathrm{Rx} \quad \mathrm{Ry} \quad \mathrm{Rz} \quad \mathrm{Dx} \quad \mathrm{Dy} \quad \mathrm{Dz}]^{T} \\ \langle\vec{q}\rangle &= \left[\langle\mathrm{Rx}\rangle \quad \langle\mathrm{Ry}\rangle \quad \langle\mathrm{Rz}\rangle \quad \langle\mathrm{Dx}\rangle \quad \langle\mathrm{Dy}\rangle \quad \langle\mathrm{Dz}\rangle\right]^{T}\end{aligned} \tag{3-82}$$

suggesting that difference between them ($\vec{q} - \langle\vec{q}\rangle$) indicates the displacement vector ($\vec{U}$), which represents the local deformation, and $\mathbf{k}$ is a local stiffness matrix for the relative geometric parameters, whose the six diagonal components indicate the mechanical stiffness for torsion, bending, stretching, and shearing, respectively, and remaining off-diagonal terms indicate mechanical coupling coefficients. This equation indicates the harmonic energy with respect to $\langle\vec{q}\rangle$, and each component represents the stiffness for one or two deformable directions.

The relation with the covariance matrix (**F**) of the relative geometric parameters was used to derive the local stiffness matrix of a BP step as follows.

$$\mathbf{k} = k_{\mathrm{B}}T\,\mathbf{F}^{-1} \tag{3-83}$$

where $k_{\mathrm{B}}$ is the Boltzmann constant, $T$ is the absolute temperature in MD simulation as 300 K, and the covariance matrix of a BP step from the collected BP step geometry is obtained as follows.

$$\mathrm{F}_{rs} = \left\langle \left({}^{\tau}q_r - \langle q_r\rangle\right)\left({}^{\tau}q_s - \langle q_s\rangle\right)\right\rangle \tag{3-84}$$

where ${}^{\tau}\vec{q}_r$ and ${}^{\tau}\vec{q}_s$ denote the relative geometric parameters in an MD time and $F_{rs}$ is the component of the covariance matrix. The mechanical rigidities of a BP step are then computed by multiplying the diagonal stiffness components to the axial length as the previous study[18].

$$\begin{aligned} B_{Rx} &= K_{RxRx}\langle Dz\rangle, \quad B_{Ry} = K_{RyRy}\langle Dz\rangle, \quad C_{Rz} = K_{RzRz}\langle Dz\rangle \\ Y_{Dx} &= K_{DxDx}\langle Dz\rangle, \quad Y_{Dy} = K_{DyDy}\langle Dz\rangle, \quad S_{Dz} = K_{DzDz}\langle Dz\rangle \end{aligned} \tag{3-85}$$

Here, $B_{Rx}$, $B_{Ry}$, $C_{Rz}$, $Y_{Dx}$, $Y_{Dy}$, and $S_{Dz}$ represent bending rigidities of tilt and roll, torsional rigidity, and shear rigidities of shift and slide for the BP step, respectively. Likewise, mechanical coupling coefficients of two different directions were calculated from off-diagonal stiffness components as

$$g(q_r, q_s) = K_{rs}\langle Dz\rangle \tag{3-86}$$

where $g(q_r, q_s)$ represent the mechanical coupling coefficient of two motion in the direction of $q_r$ and $q_s$. The symmetry of the stiffness matrix satisfies the below relation.

$$g(q_r, q_s) = g(q_s, q_r) \tag{3-87}$$

### 3.4.3. Modification of triad axes for beam element

Until now, the relative geometry, mechanical rigidities, and coupling coefficients are derived from the motion of BPs in the 3DNA definition. However, the defined BP triad in 3DNA has a different representation of axes from the nodal triad in the beam element. For example, the z-axis of a BP in the 3DNA indicates the direction linking BPs, whereas the x-axis of the beam element indicates the direction linking nodes. Thus, by modifying the axes of BPs as shown below, the calculated properties are converted into suitable values for the beam axes (Figure 3-5).

$$ {}^{\tau}\vec{T}_{xN} = {}^{\tau}\vec{b}_{zN}, \quad {}^{\tau}\vec{T}_{yN} = {}^{\tau}\vec{b}_{yN}, \quad {}^{\tau}\vec{T}_{zN} = -{}^{\tau}\vec{b}_{xN} \tag{3-88} $$

where ${}^{\tau}\vec{T}_{kN}$ represent the modified nodal triads in the beam coordinate as ${}^{\tau}\mathbf{T}_N = \left[{}^{\tau}\vec{T}_{xN} \quad {}^{\tau}\vec{T}_{yN} \quad {}^{\tau}\vec{T}_{zN}\right]$, ${}^{\tau}\vec{b}_{kN}$ is the BP triad in 3DNA definition, and $N$ indicates two BPs as $N = 1,2$.

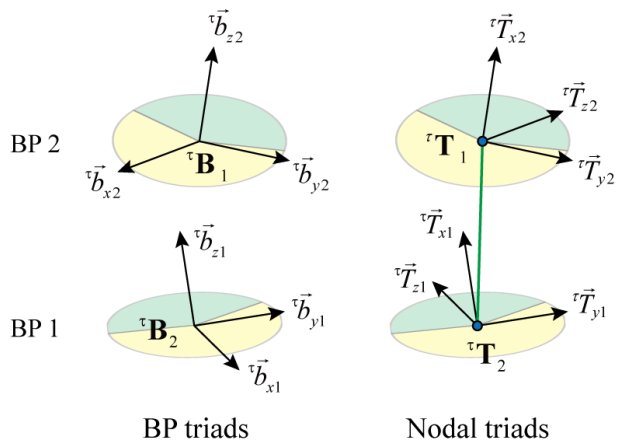


Figure 3-5. The modification of the BP triad in BP steps.

Notably, one of the primary axes in the base-pair plane was defined as the major groove direction (${}^{\tau}\vec{b}_{zN}$) in 3DNA definition, but in the beam, it is in the minor groove direction (${}^{\tau}\vec{T}_{xN}$).

### 3.4.4. Intrinsic properties of the BP step

Considering that only the direction and sign of triads were modified, the magnitude of the properties previously obtained remains the same, but their sign is changed. First, the relative geometry (Dx, Dy, Dz, Rx, Ry, Rz) in 3DNA definition are converted to those for the beam as

$$\left[\Delta_x \quad \Delta_y \quad \Delta_z \quad \Theta_x \quad \Theta_y \quad \Theta_z\right] = \left[\mathrm{Dz} \quad \mathrm{Dy} \quad -\mathrm{Dx} \quad \mathrm{Rz} \quad \mathrm{Ry} \quad -\mathrm{Rx}\right] \tag{3-89}$$

It was observed that the average direction of the fluctuating axis in the helical direction ($^{\tau}\vec{T}_{xN}$) nearly corresponds to the direction connecting two BP origins. This indicates that the middle triad of the BP step can be considered to the local CR triad. Also, the relative rotational or translational geometry between two BPs was defined as the difference between the two BPs with respect to the middle triad of two BP triads. Thus, the intrinsic nodal geometry corresponding to the first and second BPs are obtained from the half values of relative geometric parameters as below.

$$\Delta_{k1} = -\frac{1}{2}\langle\Delta_k\rangle, \quad \Delta_{k2} = +\frac{1}{2}\langle\Delta_k\rangle, \quad \Theta_{k1} = -\frac{1}{2}\langle\Theta_k\rangle, \quad \Theta_{k2} = +\frac{1}{2}\langle\Theta_k\rangle \tag{3-90}$$

where $k$ represents $x$, $y$, or $z$. Also, the intrinsic length of the BP step is calculated as

$$L_g = \left[\left(\Delta_{x2} - \Delta_{x1}\right)^2 + \left(\Delta_{y2} - \Delta_{y1}\right)^2 + \left(\Delta_{z2} - \Delta_{z1}\right)^2\right]^{1/2} \tag{3-91}$$

These relative geometry values were used to construct nodal displacement of beam elements previously described. Next, the mechanical rigidities are the same with calculated values, and the notation was only changed for the beam properties as

$$\left[EA \quad GA_y \quad GA_z \quad GJ \quad EI_y \quad EI_y\right] = \left[S_{\mathrm{Dz}} \quad Y_{\mathrm{Dy}} \quad Y_{\mathrm{Dx}} \quad C_{\mathrm{Rz}} \quad B_{\mathrm{Ry}} \quad B_{\mathrm{Rx}}\right] \tag{3-92}$$

Likewise, for the mechanical coupling coefficients, the sign of them is reversed when one relative geometric parameter belongs to Tilt (Rx) or Shift (Dx) and they are converted as follows.

$$
\begin{array}{lll}
g(\Theta_x,\Theta_y)=g(\mathrm{Rz},\mathrm{Ry}), & g(\Theta_y,\Theta_z)=-g(\mathrm{Ry},\mathrm{Rx}), & g(\Theta_x,\Theta_z)=-g(\mathrm{Rz},\mathrm{Rx}) \\
g(\Delta_x,\Delta_y)=g(\mathrm{Dz},\mathrm{Dy}), & g(\Delta_y,\Delta_z)=-g(\mathrm{Dy},\mathrm{Dx}), & g(\Delta_x,\Delta_z)=-g(\mathrm{Dz},\mathrm{Dx}) \\
g(\Theta_x,\Delta_x)=g(\mathrm{Rz},\mathrm{Dz}), & g(\Theta_x,\Delta_y)=g(\mathrm{Rz},\mathrm{Dy}), & g(\Theta_x,\Delta_z)=-g(\mathrm{Rz},\mathrm{Dx}) \\
g(\Theta_y,\Delta_x)=g(\mathrm{Ry},\mathrm{Dz}), & g(\Theta_y,\Delta_y)=g(\mathrm{Ry},\mathrm{Dy}), & g(\Theta_y,\Delta_z)=-g(\mathrm{Ry},\mathrm{Dx}) \\
g(\Theta_z,\Delta_x)=-g(\mathrm{Rx},\mathrm{Dz}), & g(\Theta_z,\Delta_y)=-g(\mathrm{Rx},\mathrm{Dy}), & g(\Theta_z,\Delta_z)=g(\mathrm{Rx},\mathrm{Dx})
\end{array}
\tag{3-93}
$$

In summary, for a specific BP step, the intrinsic properties such as relative geometry ($\vec{\mathrm{G}}$), mechanical rigidities ($\vec{\mathrm{R}}$), and coupling coefficients ($\vec{\mathrm{C}}$) are obtained from the MD simulation suitable to the beam element as follows (Figure 3-6).

$$
\begin{aligned}
\vec{\mathrm{G}} &= \left[\Delta_{xN} \quad \Delta_{yN} \quad \Delta_{zN} \quad \Theta_{xN} \quad \Theta_{yN} \quad \Theta_{zN}\right] \\
\vec{\mathrm{R}} &= \left[EA \quad GA_y \quad GA_z \quad GJ \quad EI_y \quad EI_y\right] \\
\vec{\mathrm{C}} &= \left[g(\Delta_r,\Delta_s) \quad g(\Theta_r,\Theta_s) \quad g(\Delta_r,\Theta_s)\right]
\end{aligned}
\tag{3-94}
$$

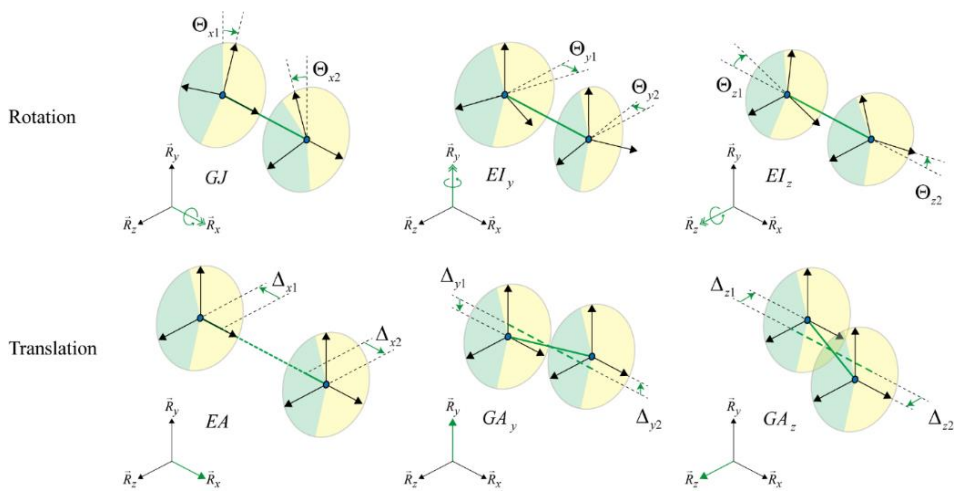


Figure 3-6. Relative geometry and mechanical properties of the BP step.

Following the procedures, the intrinsic properties obtained from the BP triad in 3DNA definitions can be converted to those for the beam triads. Alternatively, the properties of the beam can be directly estimated by introducing the beam triads (Table 3-1, Table 3-2, and Table 3-3).

Table 3-1. Intrinsic properties of regular BP steps.

| Properties | Unit | AA/TT | AG/CT | GA/TC | GG/CC | AC/GT |
|---|---|---|---|---|---|---|
| $\Delta_{x1}$ | nm | -0.1710 | -0.1697 | -0.1693 | -0.1786 | -0.1617 |
| $\Delta_{x2}$ | nm | 0.1710 | 0.1697 | 0.1693 | 0.1786 | 0.1617 |
| $\Delta_{y1}$ | nm | 0.0058 | 0.0131 | -0.0073 | 0.0256 | 0.0200 |
| $\Delta_{y2}$ | nm | -0.0058 | -0.0131 | 0.0073 | -0.0256 | -0.0200 |
| $\Delta_{z1}$ | nm | -0.0148 | -0.0147 | -0.0072 | -0.0061 | 0.0182 |
| $\Delta_{z2}$ | nm | 0.0148 | 0.0147 | 0.0072 | 0.0061 | -0.0182 |
| $\Theta_{x1}$ | deg | -18.200 | -16.138 | -19.509 | -17.131 | -16.052 |
| $\Theta_{x2}$ | deg | 18.200 | 16.138 | 19.509 | 17.131 | 16.052 |
| $\Theta_{y1}$ | deg | -3.0868 | -5.0915 | -1.8521 | -3.4265 | -2.5133 |
| $\Theta_{y2}$ | deg | 3.0868 | 5.0915 | 1.8521 | 3.4265 | 2.5133 |
| $\Theta_{z1}$ | deg | -1.8120 | -1.4955 | -0.5540 | 0.3858 | -0.2504 |
| $\Theta_{z2}$ | deg | 1.8120 | 1.4955 | 0.5540 | -0.3858 | 0.2504 |
| EA | pN | 1920.9 | 2087.3 | 2361.2 | 2145.3 | 1711.1 |
| $GA_y$ | pN | 872.97 | 789.85 | 835.18 | 560.77 | 753.74 |
| $GA_z$ | pN | 560.96 | 452.93 | 557.64 | 391.30 | 341.17 |
| GJ | $pNnm^2$ | 400.39 | 347.47 | 344.19 | 288.76 | 255.39 |
| $EI_y$ | $pNnm^2$ | 172.67 | 171.36 | 170.73 | 164.48 | 157.40 |
| $EI_z$ | $pNnm^2$ | 301.53 | 317.62 | 277.69 | 309.91 | 218.91 |
| $g(\Theta_x,\Theta_y)$ | $pNnm^2$ | 81.604 | 48.352 | 95.431 | 42.381 | 61.239 |
| $g(\Theta_x,\Theta_z)$ | $pNnm^2$ | -56.952 | -53.353 | 29.643 | -3.0857 | -30.881 |
| $g(\Theta_y,\Theta_z)$ | $pNnm^2$ | -34.640 | -49.66 | 5.9555 | -5.6173 | -20.259 |
| $g(\Delta_x,\Delta_y)$ | pN | 373.70 | 369.88 | 509.49 | 454.48 | 522.58 |
| $g(\Delta_x,\Delta_z)$ | pN | -209.90 | -190.45 | -102.12 | -46.047 | -45.336 |
| $g(\Delta_y,\Delta_z)$ | pN | -106.75 | 18.849 | -74.008 | 7.3865 | -16.899 |
| $g(\Delta_x,\Theta_x)$ | pNnm | -300.81 | -310.71 | -211.56 | -310.65 | -266.32 |
| $g(\Delta_x,\Theta_y)$ | pNnm | -90.127 | -102.98 | -61.430 | -10.539 | 73.026 |
| $g(\Delta_x,\Theta_z)$ | pNnm | 319.84 | 344.1 | 401.74 | 392.32 | -40.849 |
| $g(\Delta_y,\Theta_x)$ | pNnm | -206.97 | -114.53 | -167.93 | -227.37 | -127.09 |
| $g(\Delta_y,\Theta_y)$ | pNnm | -70.049 | 9.0814 | -45.222 | 14.627 | 36.298 |
| $g(\Delta_y,\Theta_z)$ | pNnm | 43.762 | 77.921 | -37.966 | 54.145 | 89.541 |
| $g(\Delta_z,\Theta_x)$ | pNnm | -37.990 | -108.65 | -13.205 | -78.298 | -26.975 |
| $g(\Delta_z,\Theta_y)$ | pNnm | 30.331 | -15.820 | 9.6913 | -26.714 | 1.4632 |
| $g(\Delta_z,\Theta_z)$ | pNnm | -30.908 | -83.178 | -84.867 | -135.35 | -34.434 |

Table 3-1 (Continued).

| Properties | Unit | AT/AT | GC/GC | TG/CA | TA/TA | CG/CG |
|---|---|---|---|---|---|---|
| $\Delta_{x1}$ | nm | -0.1662 | -0.1700 | -0.1760 | -0.1751 | -0.1763 |
| $\Delta_{x2}$ | nm | 0.1662 | 0.1700 | 0.1760 | 0.1751 | 0.1763 |
| $\Delta_{y1}$ | nm | 0.0240 | 0.0198 | 0.0076 | -0.0026 | -0.0090 |
| $\Delta_{y2}$ | nm | -0.0240 | -0.0198 | -0.0076 | 0.0026 | 0.0090 |
| $\Delta_{z1}$ | nm | 0.0096 | 0.0068 | -0.0007 | -0.0099 | -0.0157 |
| $\Delta_{z2}$ | nm | -0.0096 | -0.0068 | 0.0007 | 0.0099 | 0.0157 |
| $\Theta_{x1}$ | deg | -15.987 | -19.162 | -16.135 | -17.853 | -16.392 |
| $\Theta_{x2}$ | deg | 15.987 | 19.162 | 16.135 | 17.853 | 16.392 |
| $\Theta_{y1}$ | deg | -1.6639 | -1.0449 | -6.7855 | -4.4648 | -7.2335 |
| $\Theta_{y2}$ | deg | 1.6639 | 1.0449 | 6.7855 | 4.4648 | 7.2335 |
| $\Theta_{z1}$ | deg | -0.0642 | 0.0043 | 0.5195 | 0.9575 | -0.2401 |
| $\Theta_{z2}$ | deg | 0.0642 | -0.0043 | -0.5195 | -0.9575 | 0.2401 |
| EA | pN | 1475.6 | 2270.2 | 1396.0 | 1483.4 | 1401.2 |
| $GA_y$ | pN | 773.42 | 1340.78 | 478.38 | 380.62 | 595.34 |
| $GA_z$ | pN | 266.11 | 417.69 | 353.84 | 333.37 | 502.78 |
| GJ | $pNnm^2$ | 332.80 | 301.64 | 281.44 | 309.72 | 276.46 |
| $EI_y$ | $pNnm^2$ | 161.00 | 200.35 | 132.03 | 123.80 | 129.45 |
| $EI_z$ | $pNnm^2$ | 263.28 | 230.96 | 189.65 | 174.92 | 173.43 |
| $g(\Theta_x,\Theta_y)$ | $pNnm^2$ | 69.685 | 51.714 | 80.546 | 106.70 | 72.684 |
| $g(\Theta_x,\Theta_z)$ | $pNnm^2$ | -1.8624 | -2.5463 | 28.645 | 5.2257 | -0.51747 |
| $g(\Theta_y,\Theta_z)$ | $pNnm^2$ | -6.8634 | -1.6993 | 3.6606 | -5.5714 | -2.3106 |
| $g(\Delta_x,\Delta_y)$ | pN | 281.05 | 939.72 | 174.33 | 262.03 | 100.67 |
| $g(\Delta_x,\Delta_z)$ | pN | 15.493 | -20.407 | 48.676 | 5.5529 | -14.868 |
| $g(\Delta_y,\Delta_z)$ | pN | -4.8049 | -8.8281 | 46.566 | 0.78589 | 21.696 |
| $g(\Delta_x,\Theta_x)$ | pNnm | -164.19 | -363.29 | -274.23 | -237.07 | -335.03 |
| $g(\Delta_x,\Theta_y)$ | pNnm | 83.950 | 211.84 | -141.52 | -128.83 | -180.78 |
| $g(\Delta_x,\Theta_z)$ | pNnm | -4.5106 | 13.072 | 55.915 | 15.791 | 0.56556 |
| $g(\Delta_y,\Theta_x)$ | pNnm | -118.97 | -236.09 | -90.49 | -124.01 | -73.78 |
| $g(\Delta_y,\Theta_y)$ | pNnm | 26.747 | 91.816 | 23.679 | 13.858 | 71.972 |
| $g(\Delta_y,\Theta_z)$ | pNnm | -3.1108 | 16.626 | 20.369 | -7.5702 | -24.409 |
| $g(\Delta_z,\Theta_x)$ | pNnm | 6.5738 | -8.6395 | -36.086 | -8.6162 | -25.405 |
| $g(\Delta_z,\Theta_y)$ | pNnm | -11.116 | -1.3872 | 18.189 | -16.485 | -11.896 |
| $g(\Delta_z,\Theta_z)$ | pNnm | -10.368 | -123.64 | -41.356 | -21.113 | -138.13 |

Table 3-2. Intrinsic properties of nicked BP steps.

| Properties | Unit | AA/TnT | AnA/TT | AG/CnT | AnG/CT |
|---|---|---|---|---|---|
| $\Delta_{x1}$ | nm | -0.1687 | -0.1742 | -0.1663 | -0.1728 |
| $\Delta_{x2}$ | nm | 0.1687 | 0.1742 | 0.1663 | 0.1728 |
| $\Delta_{y1}$ | nm | 0.0029 | 0.0205 | -0.0022 | 0.0306 |
| $\Delta_{y2}$ | nm | -0.0029 | -0.0205 | 0.0022 | -0.0306 |
| $\Delta_{z1}$ | nm | -0.0162 | -0.0025 | -0.0097 | 0.0123 |
| $\Delta_{z2}$ | nm | 0.0162 | 0.0025 | 0.0097 | -0.0123 |
| $\Theta_{x1}$ | deg | -17.753 | -16.977 | -18.274 | -15.644 |
| $\Theta_{x2}$ | deg | 17.753 | 16.977 | 18.274 | 15.644 |
| $\Theta_{y1}$ | deg | -2.6582 | -2.5391 | -3.0229 | -3.3497 |
| $\Theta_{y2}$ | deg | 2.6582 | 2.5391 | 3.0229 | 3.3497 |
| $\Theta_{z1}$ | deg | -1.5030 | -1.8085 | -0.7840 | -1.4370 |
| $\Theta_{z2}$ | deg | 1.5030 | 1.8085 | 0.7840 | 1.4370 |
| EA | pN | 2090.2 | 1554.1 | 1869.1 | 1715.6 |
| $GA_y$ | pN | 675.11 | 375.11 | 707.18 | 604.48 |
| $GA_z$ | pN | 484.78 | 417.72 | 445.44 | 358.60 |
| GJ | $pNnm^2$ | 286.61 | 70.31 | 233.34 | 181.74 |
| $EI_y$ | $pNnm^2$ | 151.36 | 125.85 | 171.05 | 151.99 |
| $EI_z$ | $pNnm^2$ | 290.14 | 266.41 | 201.45 | 298.20 |
| $g(\Theta_x,\Theta_y)$ | $pNnm^2$ | 49.329 | 8.6665 | 80.219 | 42.157 |
| $g(\Theta_x,\Theta_z)$ | $pNnm^2$ | -67.62 | -13.953 | 11.181 | -32.729 |
| $g(\Theta_y,\Theta_z)$ | $pNnm^2$ | -31.258 | -22.053 | -6.6714 | -39.988 |
| $g(\Delta_x,\Delta_y)$ | pN | 341.34 | 130.68 | 350.56 | 226.87 |
| $g(\Delta_x,\Delta_z)$ | pN | -186.54 | -74.07 | -134.43 | -116.62 |
| $g(\Delta_y,\Delta_z)$ | pN | -66.564 | -113.27 | -94.541 | -81.753 |
| $g(\Delta_x,\Theta_x)$ | pNnm | -274.44 | -93.278 | -181.10 | -182.00 |
| $g(\Delta_x,\Theta_y)$ | pNnm | -59.668 | -43.745 | -107.53 | -125.54 |
| $g(\Delta_x,\Theta_z)$ | pNnm | 310.03 | 237.65 | 147.10 | 286.55 |
| $g(\Delta_y,\Theta_x)$ | pNnm | -143.15 | -51.191 | -147.34 | -126.19 |
| $g(\Delta_y,\Theta_y)$ | pNnm | -7.0325 | -0.75123 | -4.3438 | -5.5168 |
| $g(\Delta_y,\Theta_z)$ | pNnm | 66.301 | -38.304 | -23.518 | -12.906 |
| $g(\Delta_z,\Theta_x)$ | pNnm | 2.9982 | -80.932 | -3.5418 | -119.35 |
| $g(\Delta_z,\Theta_y)$ | pNnm | 32.847 | 33.307 | 21.854 | -1.332 |
| $g(\Delta_z,\Theta_z)$ | pNnm | -27.827 | -27.255 | -71.083 | -59.023 |

Table 3-2 (Continued).

| Properties | Unit | GA/TnC | GnA/TC | GG/CnC | GnG/CC |
|---|---|---|---|---|---|
| $\Delta_{x1}$ | nm | -0.1681 | -0.1774 | -0.1743 | -0.1806 |
| $\Delta_{x2}$ | nm | 0.1681 | 0.1774 | 0.1743 | 0.1806 |
| $\Delta_{y1}$ | nm | -0.0135 | -0.0025 | 0.0328 | 0.0585 |
| $\Delta_{y2}$ | nm | 0.0135 | 0.0025 | -0.0328 | -0.0585 |
| $\Delta_{z1}$ | nm | -0.0293 | -0.0089 | -0.0342 | 0.0270 |
| $\Delta_{z2}$ | nm | 0.0293 | 0.0089 | 0.0342 | -0.0270 |
| $\Theta_{x1}$ | deg | -18.864 | -21.025 | -15.344 | -15.593 |
| $\Theta_{x2}$ | deg | 18.864 | 21.025 | 15.344 | 15.593 |
| $\Theta_{y1}$ | deg | -0.6141 | -1.0901 | -2.8118 | -3.8210 |
| $\Theta_{y2}$ | deg | 0.6141 | 1.0901 | 2.8118 | 3.8210 |
| $\Theta_{z1}$ | deg | -0.0550 | -0.5030 | -0.3294 | 0.6405 |
| $\Theta_{z2}$ | deg | 0.0550 | 0.5030 | 0.3294 | -0.6405 |
| EA | pN | 2687.1 | 2019.5 | 2119.1 | 1779.8 |
| $GA_y$ | pN | 637.10 | 559.23 | 312.47 | 516.70 |
| $GA_z$ | pN | 447.93 | 387.43 | 298.30 | 383.00 |
| GJ | $pNnm^2$ | 181.00 | 155.48 | 93.54 | 159.88 |
| $EI_y$ | $pNnm^2$ | 179.17 | 152.94 | 177.56 | 152.00 |
| $EI_z$ | $pNnm^2$ | 325.46 | 264.98 | 305.26 | 274.88 |
| $g(\Theta_x,\Theta_y)$ | $pNnm^2$ | 46.989 | 37.697 | 20.345 | 24.920 |
| $g(\Theta_x,\Theta_z)$ | $pNnm^2$ | -22.901 | 13.492 | -30.511 | 42.536 |
| $g(\Theta_y,\Theta_z)$ | $pNnm^2$ | 27.461 | -0.7365 | 21.694 | -1.4057 |
| $g(\Delta_x,\Delta_y)$ | pN | 417.24 | 347.2 | 274.96 | 79.198 |
| $g(\Delta_x,\Delta_z)$ | pN | -204.61 | -95.376 | -6.6755 | -222.78 |
| $g(\Delta_y,\Delta_z)$ | pN | -54.012 | -55.182 | -40.452 | 103.97 |
| $g(\Delta_x,\Theta_x)$ | pNnm | -257.20 | -171.31 | -176.98 | -141.33 |
| $g(\Delta_x,\Theta_y)$ | pNnm | -5.8098 | -3.3071 | -59.601 | -41.632 |
| $g(\Delta_x,\Theta_z)$ | pNnm | 452.28 | 328.75 | 353.33 | 339.50 |
| $g(\Delta_y,\Theta_x)$ | pNnm | -124.4 | -139.39 | -84.933 | -142.39 |
| $g(\Delta_y,\Theta_y)$ | pNnm | 28.291 | 39.885 | 39.97 | 54.208 |
| $g(\Delta_y,\Theta_z)$ | pNnm | -12.567 | -79.288 | 97.199 | -93.379 |
| $g(\Delta_z,\Theta_x)$ | pNnm | 92.723 | -88.154 | 56.453 | -138.65 |
| $g(\Delta_z,\Theta_y)$ | pNnm | 7.4277 | -10.572 | -25.319 | 17.224 |
| $g(\Delta_z,\Theta_z)$ | pNnm | -120.75 | -89.548 | -122.11 | -147.25 |

Table 3-2 (Continued).

| Properties | Unit | AC/GnT | AnC/GT | AT/AnT | GC/GnC |
|---|---|---|---|---|---|
| $\Delta_{x1}$ | nm | -0.1685 | -0.1630 | -0.1664 | -0.1726 |
| $\Delta_{x2}$ | nm | 0.1685 | 0.1630 | 0.1664 | 0.1726 |
| $\Delta_{y1}$ | nm | 0.0185 | 0.0314 | 0.0265 | 0.0175 |
| $\Delta_{y2}$ | nm | -0.0185 | -0.0314 | -0.0265 | -0.0175 |
| $\Delta_{z1}$ | nm | 0.0124 | 0.0444 | -0.0154 | -0.0046 |
| $\Delta_{z2}$ | nm | -0.0124 | -0.0444 | 0.0154 | 0.0046 |
| $\Theta_{x1}$ | deg | -18.087 | -13.110 | -14.859 | -19.647 |
| $\Theta_{x2}$ | deg | 18.087 | 13.110 | 14.859 | 19.647 |
| $\Theta_{y1}$ | deg | -1.1073 | -2.0118 | -1.9482 | -0.0940 |
| $\Theta_{y2}$ | deg | 1.1073 | 2.0118 | 1.9482 | 0.0940 |
| $\Theta_{z1}$ | deg | -0.2590 | -0.5255 | 0.1217 | -0.1138 |
| $\Theta_{z2}$ | deg | 0.2590 | 0.5255 | -0.1217 | 0.1138 |
| EA | pN | 1604.9 | 1858.7 | 1204.6 | 2399.4 |
| $GA_y$ | pN | 386.34 | 525.50 | 275.60 | 1179.81 |
| $GA_z$ | pN | 245.79 | 278.56 | 226.68 | 338.34 |
| GJ | $pNnm^2$ | 109.01 | 107.29 | 113.60 | 181.73 |
| $EI_y$ | $pNnm^2$ | 155.95 | 152.75 | 133.80 | 225.72 |
| $EI_z$ | $pNnm^2$ | 218.39 | 244.64 | 238.99 | 236.59 |
| $g(\Theta_x,\Theta_y)$ | $pNnm^2$ | 24.749 | 40.286 | 43.675 | 6.804 |
| $g(\Theta_x,\Theta_z)$ | $pNnm^2$ | -23.987 | -4.8941 | 5.2401 | -11.823 |
| $g(\Theta_y,\Theta_z)$ | $pNnm^2$ | -9.0882 | -43.41 | 17.289 | 16.504 |
| $g(\Delta_x,\Delta_y)$ | pN | 353.19 | 444.22 | 21.039 | 816.8 |
| $g(\Delta_x,\Delta_z)$ | pN | -71.925 | -88.655 | 18.122 | 10.066 |
| $g(\Delta_y,\Delta_z)$ | pN | -3.9904 | -75.205 | 22.22 | -19.325 |
| $g(\Delta_x,\Theta_x)$ | pNnm | -155.16 | -170.8 | -70.625 | -291.72 |
| $g(\Delta_x,\Theta_y)$ | pNnm | 78.515 | 0.11174 | -26.422 | 214.44 |
| $g(\Delta_x,\Theta_z)$ | pNnm | -48.438 | -5.8161 | -70.881 | -41.639 |
| $g(\Delta_y,\Theta_x)$ | pNnm | -63.982 | -56.471 | -18.298 | -200.21 |
| $g(\Delta_y,\Theta_y)$ | pNnm | 82.572 | 28.136 | 8.3861 | 168.19 |
| $g(\Delta_y,\Theta_z)$ | pNnm | 73.252 | 6.7088 | -14.36 | 19.001 |
| $g(\Delta_z,\Theta_x)$ | pNnm | 53.179 | -74.829 | 65.708 | 82.349 |
| $g(\Delta_z,\Theta_y)$ | pNnm | 15.202 | 14.705 | -20.769 | 11.145 |
| $g(\Delta_z,\Theta_z)$ | pNnm | -60.261 | -31.397 | -18.474 | -138.14 |

Table 3-2 (Continued).

| Properties | Unit | TG/CnA | TnG/CA | TA/TnA | CG/CnG |
|---|---|---|---|---|---|
| $\Delta_{x1}$ | nm | -0.1796 | -0.1812 | -0.1719 | -0.1841 |
| $\Delta_{x2}$ | nm | 0.1796 | 0.1812 | 0.1719 | 0.1841 |
| $\Delta_{y1}$ | nm | 0.0030 | 0.0136 | 0.0146 | -0.0005 |
| $\Delta_{y2}$ | nm | -0.0030 | -0.0136 | -0.0146 | 0.0005 |
| $\Delta_{z1}$ | nm | 0.0022 | 0.0347 | -0.0174 | -0.0306 |
| $\Delta_{z2}$ | nm | -0.0022 | -0.0347 | 0.0174 | 0.0306 |
| $\Theta_{x1}$ | deg | -17.850 | -16.415 | -15.900 | -16.805 |
| $\Theta_{x2}$ | deg | 17.850 | 16.415 | 15.900 | 16.805 |
| $\Theta_{y1}$ | deg | -5.4520 | -5.8255 | -3.9780 | -6.3540 |
| $\Theta_{y2}$ | deg | 5.4520 | 5.8255 | 3.9780 | 6.3540 |
| $\Theta_{z1}$ | deg | 1.3415 | -0.7665 | 0.1578 | -0.2233 |
| $\Theta_{z2}$ | deg | -1.3415 | 0.7665 | -0.1578 | 0.2233 |
| EA | pN | 1520.0 | 1377.3 | 1093.2 | 1550.8 |
| $GA_y$ | pN | 465.77 | 443.81 | 245.38 | 513.39 |
| $GA_z$ | pN | 280.91 | 379.03 | 201.02 | 427.12 |
| GJ | $pNnm^2$ | 154.61 | 155.75 | 78.61 | 178.67 |
| $EI_y$ | $pNnm^2$ | 131.42 | 124.14 | 95.40 | 132.67 |
| $EI_z$ | $pNnm^2$ | 200.61 | 195.50 | 143.69 | 203.66 |
| $g(\Theta_x,\Theta_y)$ | $pNnm^2$ | 33.386 | 43.165 | 21.355 | 35.909 |
| $g(\Theta_x,\Theta_z)$ | $pNnm^2$ | 12.138 | 25.801 | -2.7793 | -26.968 |
| $g(\Theta_y,\Theta_z)$ | $pNnm^2$ | 16.621 | 6.4589 | 11.069 | 4.9053 |
| $g(\Delta_x,\Delta_y)$ | pN | 116.63 | 69.811 | 175.45 | 95.112 |
| $g(\Delta_x,\Delta_z)$ | pN | 35.51 | -80.498 | -61.409 | -8.662 |
| $g(\Delta_y,\Delta_z)$ | pN | 65.326 | 31.101 | -26.379 | 59.11 |
| $g(\Delta_x,\Theta_x)$ | pNnm | -178.02 | -165.23 | -112.3 | -224.17 |
| $g(\Delta_x,\Theta_y)$ | pNnm | -157.29 | -135.67 | -78.577 | -200.43 |
| $g(\Delta_x,\Theta_z)$ | pNnm | 11.776 | 105.7 | 78.892 | -93.836 |
| $g(\Delta_y,\Theta_x)$ | pNnm | -103.1 | -93.778 | -27.517 | -86.661 |
| $g(\Delta_y,\Theta_y)$ | pNnm | 51.819 | 36.076 | 22.013 | 66.902 |
| $g(\Delta_y,\Theta_z)$ | pNnm | 51.488 | 4.9759 | 48.421 | -9.406 |
| $g(\Delta_z,\Theta_x)$ | pNnm | 50.579 | -76.655 | 67.528 | 94.973 |
| $g(\Delta_z,\Theta_y)$ | pNnm | 27.779 | 16.727 | -4.2901 | 18.381 |
| $g(\Delta_z,\Theta_z)$ | pNnm | -68.885 | -98.712 | -16.639 | -175.43 |

Table 3-3. Intrinsic properties of CO-nick BP steps.

| Properties | Unit | AA-TnT | AnA-TT | AG-CnT | AnG-CT |
|---|---|---|---|---|---|
| $\Delta_{x1}$ | nm | -0.1635 | -0.1691 | -0.1701 | -0.1674 |
| $\Delta_{x2}$ | nm | 0.1635 | 0.1691 | 0.1701 | 0.1674 |
| $\Delta_{y1}$ | nm | 0.0333 | 0.0320 | 0.0442 | 0.0379 |
| $\Delta_{y2}$ | nm | -0.0333 | -0.0320 | -0.0442 | -0.0379 |
| $\Delta_{z1}$ | nm | 0.0325 | 0.0049 | 0.0448 | 0.0438 |
| $\Delta_{z2}$ | nm | -0.0325 | -0.0049 | -0.0448 | -0.0438 |
| $\Theta_{x1}$ | deg | -15.038 | -16.139 | -14.314 | -15.671 |
| $\Theta_{x2}$ | deg | 15.038 | 16.139 | 14.314 | 15.671 |
| $\Theta_{y1}$ | deg | -1.5789 | -2.7160 | -5.3140 | -4.8180 |
| $\Theta_{y2}$ | deg | 1.5789 | 2.7160 | 5.3140 | 4.8180 |
| $\Theta_{z1}$ | deg | 1.9080 | -1.1680 | -0.2626 | 0.3259 |
| $\Theta_{z2}$ | deg | -1.9080 | 1.1680 | 0.2626 | -0.3259 |
| EA | pN | 2019.6 | 2005.4 | 1410.0 | 2048.1 |
| $GA_y$ | pN | 738.36 | 783.33 | 865.01 | 838.95 |
| $GA_z$ | pN | 511.83 | 545.85 | 495.27 | 487.84 |
| GJ | $pNnm^2$ | 232.43 | 265.06 | 190.36 | 225.74 |
| $EI_y$ | $pNnm^2$ | 163.12 | 173.73 | 137.31 | 164.39 |
| $EI_z$ | $pNnm^2$ | 270.74 | 296.31 | 188.52 | 302.34 |
| $g(\Theta_x,\Theta_y)$ | $pNnm^2$ | 25.038 | 25.39 | 34.503 | 15.441 |
| $g(\Theta_x,\Theta_z)$ | $pNnm^2$ | 22.843 | -18.234 | 20.317 | 2.5212 |
| $g(\Theta_y,\Theta_z)$ | $pNnm^2$ | 13.533 | -29.953 | 0.62148 | -5.3474 |
| $g(\Delta_x,\Delta_y)$ | pN | 306.27 | 161.4 | 53.481 | 254.84 |
| $g(\Delta_x,\Delta_z)$ | pN | 97.947 | -145.56 | -112.1 | -34.74 |
| $g(\Delta_y,\Delta_z)$ | pN | 67.616 | -39.5 | 157.83 | 35.363 |
| $g(\Delta_x,\Theta_x)$ | pNnm | -186.07 | -152.11 | -153.63 | -173.1 |
| $g(\Delta_x,\Theta_y)$ | pNnm | -74.639 | -86.432 | -97.354 | -57.265 |
| $g(\Delta_x,\Theta_z)$ | pNnm | -117.46 | 314.11 | 111.23 | 209.76 |
| $g(\Delta_y,\Theta_x)$ | pNnm | -122.26 | -150.11 | -96.733 | -139.11 |
| $g(\Delta_y,\Theta_y)$ | pNnm | -4.6231 | 5.9892 | 8.6924 | 4.0103 |
| $g(\Delta_y,\Theta_z)$ | pNnm | -43.987 | -53.13 | -38.363 | -56.683 |
| $g(\Delta_z,\Theta_x)$ | pNnm | -62.866 | -97.014 | -83.746 | -123.26 |
| $g(\Delta_z,\Theta_y)$ | pNnm | -23.078 | 25.456 | 27.361 | -25.928 |
| $g(\Delta_z,\Theta_z)$ | pNnm | -50.268 | -69.483 | -75.714 | -73.567 |

Table 3-3 (Continued).

| Properties | Unit | GA-TnC | GnA-TC | GG-CnC | GnG-CC |
|---|---|---|---|---|---|
| $\Delta_{x1}$ | nm | -0.1577 | -0.1753 | -0.1689 | -0.1691 |
| $\Delta_{x2}$ | nm | 0.1577 | 0.1753 | 0.1689 | 0.1691 |
| $\Delta_{y1}$ | nm | -0.0187 | 0.0170 | 0.0660 | 0.0520 |
| $\Delta_{y2}$ | nm | 0.0187 | -0.0170 | -0.0660 | -0.0520 |
| $\Delta_{z1}$ | nm | 0.0358 | 0.0079 | 0.0350 | 0.0319 |
| $\Delta_{z2}$ | nm | -0.0358 | -0.0079 | -0.0350 | -0.0319 |
| $\Theta_{x1}$ | deg | -17.241 | -17.238 | -13.684 | -14.361 |
| $\Theta_{x2}$ | deg | 17.241 | 17.238 | 13.684 | 14.361 |
| $\Theta_{y1}$ | deg | -0.5125 | -1.4183 | -3.5647 | -3.4281 |
| $\Theta_{y2}$ | deg | 0.5125 | 1.4183 | 3.5647 | 3.4281 |
| $\Theta_{z1}$ | deg | 1.4000 | 0.6225 | 0.0065 | 0.9520 |
| $\Theta_{z2}$ | deg | -1.4000 | -0.6225 | -0.0065 | -0.9520 |
| EA | pN | 2047.0 | 2088.8 | 2163.2 | 1846.6 |
| $GA_y$ | pN | 599.83 | 730.49 | 979.15 | 735.94 |
| $GA_z$ | pN | 402.74 | 443.64 | 562.94 | 509.48 |
| GJ | $pNnm^2$ | 168.98 | 225.95 | 231.62 | 192.77 |
| $EI_y$ | $pNnm^2$ | 173.84 | 159.72 | 207.67 | 168.26 |
| $EI_z$ | $pNnm^2$ | 235.47 | 285.03 | 351.57 | 258.79 |
| $g(\Theta_x,\Theta_y)$ | $pNnm^2$ | 28.742 | 30.29 | 5.1797 | 21.05 |
| $g(\Theta_x,\Theta_z)$ | $pNnm^2$ | 13.727 | -1.85 | 13.239 | 47.297 |
| $g(\Theta_y,\Theta_z)$ | $pNnm^2$ | -17.229 | -3.0957 | -26.059 | 6.4228 |
| $g(\Delta_x,\Delta_y)$ | pN | 379.29 | 237.52 | 119.94 | 50.352 |
| $g(\Delta_x,\Delta_z)$ | pN | 32.464 | -125.68 | -64.871 | -61.295 |
| $g(\Delta_y,\Delta_z)$ | pN | -3.0285 | 11.757 | 58.348 | 131.32 |
| $g(\Delta_x,\Theta_x)$ | pNnm | -173.9 | -189.59 | -139.87 | -123.77 |
| $g(\Delta_x,\Theta_y)$ | pNnm | 10.14 | -24.624 | -105.55 | -69.331 |
| $g(\Delta_x,\Theta_z)$ | pNnm | -51.399 | 340.2 | 249.73 | 153.8 |
| $g(\Delta_y,\Theta_x)$ | pNnm | -91.493 | -163.19 | -146.63 | -126.07 |
| $g(\Delta_y,\Theta_y)$ | pNnm | -8.7543 | 43.442 | -4.4382 | 26.337 |
| $g(\Delta_y,\Theta_z)$ | pNnm | 4.0596 | -63.675 | -84.097 | -75.419 |
| $g(\Delta_z,\Theta_x)$ | pNnm | -55.159 | -89.108 | -187.34 | -121.44 |
| $g(\Delta_z,\Theta_y)$ | pNnm | -1.3847 | -33.946 | -5.5154 | -18.478 |
| $g(\Delta_z,\Theta_z)$ | pNnm | -89.123 | -105.52 | -88.343 | -97.079 |

Table 3-3 (Continued).

| Properties | Unit | AC-GnT | AnC-GT | AT-AnT | GC-GnC |
|---|---|---|---|---|---|
| $\Delta_{x1}$ | nm | -0.1671 | -0.1610 | -0.1557 | -0.1621 |
| $\Delta_{x2}$ | nm | 0.1671 | 0.1610 | 0.1557 | 0.1621 |
| $\Delta_{y1}$ | nm | 0.0298 | 0.0172 | 0.0329 | 0.0190 |
| $\Delta_{y2}$ | nm | -0.0298 | -0.0172 | -0.0329 | -0.0190 |
| $\Delta_{z1}$ | nm | 0.0209 | 0.0408 | 0.0425 | 0.0400 |
| $\Delta_{z2}$ | nm | -0.0209 | -0.0408 | -0.0425 | -0.0400 |
| $\Theta_{x1}$ | deg | -15.969 | -13.568 | -12.913 | -17.628 |
| $\Theta_{x2}$ | deg | 15.969 | 13.568 | 12.913 | 17.628 |
| $\Theta_{y1}$ | deg | -1.8935 | -3.9424 | -2.6004 | -1.1297 |
| $\Theta_{y2}$ | deg | 1.8935 | 3.9424 | 2.6004 | 1.1297 |
| $\Theta_{z1}$ | deg | 1.0985 | 0.7430 | 1.1510 | 1.7740 |
| $\Theta_{z2}$ | deg | -1.0985 | -0.7430 | -1.1510 | -1.7740 |
| EA | pN | 1954.6 | 1940.5 | 2122.0 | 2259.2 |
| $GA_y$ | pN | 673.64 | 694.21 | 777.99 | 1033.71 |
| $GA_z$ | pN | 336.32 | 399.66 | 479.00 | 457.91 |
| GJ | $pNnm^2$ | 169.38 | 167.76 | 235.04 | 160.49 |
| $EI_y$ | $pNnm^2$ | 155.98 | 145.48 | 174.17 | 203.09 |
| $EI_z$ | $pNnm^2$ | 228.74 | 234.20 | 282.68 | 189.46 |
| $g(\Theta_x,\Theta_y)$ | $pNnm^2$ | 26.005 | 30.064 | 31.571 | 11.234 |
| $g(\Theta_x,\Theta_z)$ | $pNnm^2$ | 26.38 | 10.705 | 16.253 | 37.718 |
| $g(\Theta_y,\Theta_z)$ | $pNnm^2$ | 7.5137 | 1.7037 | 3.1115 | -13.568 |
| $g(\Delta_x,\Delta_y)$ | pN | 290.64 | 368.1 | 378.85 | 737.92 |
| $g(\Delta_x,\Delta_z)$ | pN | 15.861 | 15.819 | 4.8369 | 104.89 |
| $g(\Delta_y,\Delta_z)$ | pN | 67.653 | 67.705 | 32.018 | 36.327 |
| $g(\Delta_x,\Theta_x)$ | pNnm | -162.16 | -170.12 | -163.23 | -241.14 |
| $g(\Delta_x,\Theta_y)$ | pNnm | 10.477 | -18.463 | -77.892 | 122.9 |
| $g(\Delta_x,\Theta_z)$ | pNnm | 93.152 | 1.8445 | 6.9411 | 7.432 |
| $g(\Delta_y,\Theta_x)$ | pNnm | -99.413 | -123.58 | -115.87 | -170.48 |
| $g(\Delta_y,\Theta_y)$ | pNnm | 37.445 | 10.051 | -38.097 | 72.877 |
| $g(\Delta_y,\Theta_z)$ | pNnm | -62.086 | -42.849 | -22.646 | 12.405 |
| $g(\Delta_z,\Theta_x)$ | pNnm | -95.424 | -43.478 | -62.32 | -79.421 |
| $g(\Delta_z,\Theta_y)$ | pNnm | -35.193 | -17.804 | 2.8568 | -31.847 |
| $g(\Delta_z,\Theta_z)$ | pNnm | -74.276 | -44.626 | -40.912 | -84.504 |

Table 3-3 (Continued).

| Properties | Unit | TG-CnA | TnG-CA | TA-TnA | CG-CnG |
|---|---|---|---|---|---|
| $\Delta_{x1}$ | nm | -0.1749 | -0.1666 | -0.1699 | -0.1768 |
| $\Delta_{x2}$ | nm | 0.1749 | 0.1666 | 0.1699 | 0.1768 |
| $\Delta_{y1}$ | nm | 0.0387 | 0.0316 | 0.0232 | 0.0235 |
| $\Delta_{y2}$ | nm | -0.0387 | -0.0316 | -0.0232 | -0.0235 |
| $\Delta_{z1}$ | nm | 0.0160 | 0.0426 | 0.0380 | 0.0505 |
| $\Delta_{z2}$ | nm | -0.0160 | -0.0426 | -0.0380 | -0.0505 |
| $\Theta_{x1}$ | deg | -16.055 | -13.320 | -14.561 | -12.004 |
| $\Theta_{x2}$ | deg | 16.055 | 13.320 | 14.561 | 12.004 |
| $\Theta_{y1}$ | deg | -6.3615 | -4.9373 | -5.3415 | -5.7920 |
| $\Theta_{y2}$ | deg | 6.3615 | 4.9373 | 5.3415 | 5.7920 |
| $\Theta_{z1}$ | deg | -0.1022 | 0.3224 | 0.3467 | 0.8630 |
| $\Theta_{z2}$ | deg | 0.1022 | -0.3224 | -0.3467 | -0.8630 |
| EA | pN | 1783.1 | 1551.0 | 1713.9 | 1971.7 |
| $GA_y$ | pN | 833.30 | 750.02 | 638.15 | 808.34 |
| $GA_z$ | pN | 428.22 | 475.63 | 470.63 | 425.01 |
| GJ | $pNnm^2$ | 252.62 | 187.58 | 210.41 | 183.73 |
| $EI_y$ | $pNnm^2$ | 175.48 | 142.62 | 135.87 | 171.25 |
| $EI_z$ | $pNnm^2$ | 243.47 | 202.89 | 218.23 | 241.32 |
| $g(\Theta_x,\Theta_y)$ | $pNnm^2$ | 31.345 | 32.979 | 29.162 | 17.677 |
| $g(\Theta_x,\Theta_z)$ | $pNnm^2$ | 8.0446 | 26.555 | 7.8035 | 21.211 |
| $g(\Theta_y,\Theta_z)$ | $pNnm^2$ | -2.8314 | -10.172 | -5.1662 | -6.0236 |
| $g(\Delta_x,\Delta_y)$ | pN | 104.57 | 80.927 | 192.58 | 395.56 |
| $g(\Delta_x,\Delta_z)$ | pN | -21.561 | -16.808 | -29.084 | 44.208 |
| $g(\Delta_y,\Delta_z)$ | pN | 28.515 | 125.17 | 71.294 | 71.624 |
| $g(\Delta_x,\Theta_x)$ | pNnm | -155.59 | -152.43 | -146.82 | -188.91 |
| $g(\Delta_x,\Theta_y)$ | pNnm | -79.409 | -75.593 | -77.162 | 23.141 |
| $g(\Delta_x,\Theta_z)$ | pNnm | 14.108 | 52.216 | 81.724 | 46.737 |
| $g(\Delta_y,\Theta_x)$ | pNnm | -157.04 | -87.152 | -89.611 | -131.63 |
| $g(\Delta_y,\Theta_y)$ | pNnm | 38.866 | 30.719 | 23.129 | 35.624 |
| $g(\Delta_y,\Theta_z)$ | pNnm | -2.9894 | -34.609 | -34.478 | -30.666 |
| $g(\Delta_z,\Theta_x)$ | pNnm | -3.9607 | -77.697 | -87.699 | -116.47 |
| $g(\Delta_z,\Theta_y)$ | pNnm | -13.648 | -10.775 | -19.385 | -44.227 |
| $g(\Delta_z,\Theta_z)$ | pNnm | -54.289 | -79.754 | -55.223 | -72.509 |

## 3.5. Intrinsic properties of the crossover step

The inter-helical base-pairs in crossover (CO step) was considered as a beam element between two BPs in the same way as the BP step. Like the characterization of the BP step, the relative geometry and mechanical properties are obtained using the motion of the BP triads of two successive BPs.

### 3.5.1. Modification of triad axes in the crossover step

In CO configuration, however, the direction linking two BPs toward the backbone is not aligned and perpendicular to the general axial direction of the BP step. Hence, BP triads in the CO site were modified so that the backbone axis ($^{\tau}\vec{b}_{zN}$) was in the axial direction of the beam (Figure 3-7).

$$^{\tau}\vec{T}_{yN} = -\,^{\tau}\vec{b}_{xN}, \quad ^{\tau}\vec{T}_{zN} = \pm\,^{\tau}\vec{b}_{zN}, \quad ^{\tau}\vec{T}_{xN} = {}^{\tau}\vec{T}_{yN} \times {}^{\tau}\vec{T}_{zN} \tag{3-95}$$

where $^{\tau}\vec{T}_{kN}$ represent the modified nodal triad of two BPs of the CO step ($N = 1,2$) at an MD time ($\tau$), $^{\tau}\vec{b}_{kN}$ is the BP triad in the 3DNA definition. The magnitude of $^{\tau}\vec{T}_{zN}$ is the same with $^{\tau}\vec{b}_{zN}$, but its direction was set to the helix direction.

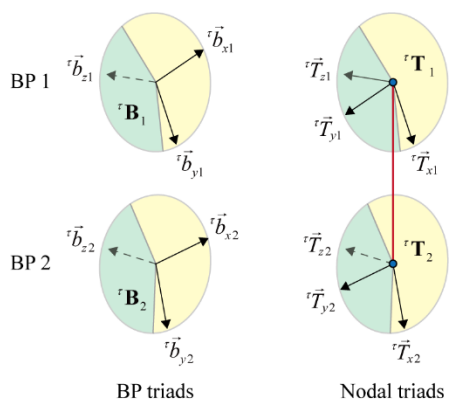


Figure 3-7. The modification of the BP triad in CO steps.

Using the modified triad of BPs, relative geometry and mechanical properties of CO steps about the middle triad ($^{\tau}\underline{\mathbf{R}}$) can be estimated as previously described.

### 3.5.2. Triad angle correction

It was observed that the average direction of the fluctuating axis in the backbone direction ($^{\tau}\vec{T}_{xN}$) deviates approximately 10° from the direction connecting two BP origins. That indicates that the nodal geometry from the middle triad of two BPs in the CO step could not be regarded as the half values of relative geometric parameters.

This can be corrected by introducing the angles between the middle and local CR triads (Figure 3-8). The local CR triad is first estimated by

$$^{\tau}\mathbf{R} = \left[ {}^{\tau}\vec{r}_x \quad {}^{\tau}\vec{r}_y \quad {}^{\tau}\vec{r}_z \right] \tag{3-96}$$

where the components are obtained for each time as

$$^{\tau}\vec{r}_x = \frac{^{\tau}\vec{O}_2 - {}^{\tau}\vec{O}_1}{\left\| {}^{\tau}\vec{O}_2 - {}^{\tau}\vec{O}_1 \right\|}, \quad {}^{\tau}\vec{r}_z = \frac{^{\tau}\vec{T}_{z1} + {}^{\tau}\vec{T}_{z2}}{\left\| {}^{\tau}\vec{T}_{z1} + {}^{\tau}\vec{T}_{z2} \right\|}, \quad {}^{\tau}\vec{r}_y = {}^{\tau}\vec{r}_z \times {}^{\tau}\vec{r}_x \tag{3-97}$$

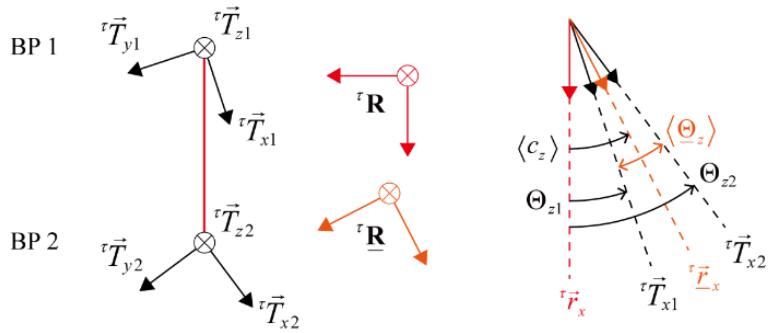


Figure 3-8. An example of triad angle correction.

The correction angles between the middle triad and the local CR triad are then determined as

$$\left[ {}^{\tau}c_x \quad {}^{\tau}c_y \quad {}^{\tau}c_z \right]^{\mathrm{T}} = {}^{\tau}\tilde{\mathbf{C}} \tag{3-98}$$

where $^{\tau}c_k$ represents the correction angle in each axis by tilde operation of the matrix $^{\tau}\tilde{\mathbf{C}}$ obtained as

$$^{\tau}\mathbf{C} = \log\left[\,^{\tau}\mathbf{R}^{\mathrm{T}}\,^{\tau}\underline{\mathbf{R}}\,\right] \tag{3-99}$$

where the middle triad ($^{\tau}\underline{\mathbf{R}}$) is obtained from the modified nodal axes ($^{\tau}\vec{T}_{yN}$) of the BPs following the previous procedure.

### 3.5.3. Intrinsic properties of the crossover step

The relative geometry of the CO step in the beam coordinate is then derived using the correction angle as

$$\begin{aligned}
&\Theta_{x1} = -\frac{1}{2}\left\langle \underline{\Theta}_x \right\rangle + \left\langle c_x \right\rangle \qquad \Theta_{y1} = -\frac{1}{2}\left\langle \underline{\Theta}_y \right\rangle + \left\langle c_y \right\rangle \qquad \Theta_{z1} = -\frac{1}{2}\left\langle \underline{\Theta}_z \right\rangle + \left\langle c_z \right\rangle \\
&\Theta_{x2} = +\frac{1}{2}\left\langle \underline{\Theta}_x \right\rangle + \left\langle c_x \right\rangle \qquad \Theta_{y2} = +\frac{1}{2}\left\langle \underline{\Theta}_y \right\rangle + \left\langle c_y \right\rangle \qquad \Theta_{z2} = +\frac{1}{2}\left\langle \underline{\Theta}_z \right\rangle + \left\langle c_z \right\rangle
\end{aligned} \tag{3-100}$$

where $\Theta_{kN}$ represents the intrinsic nodal geometry of the CO step in the beam coordinate.

The remaining properties of CO step are also characterized as previously described, providing the mechanical rigidities as $EA$, $GA_y$, $GA_z$, $GJ$, $EI_y$, and $EI_z$, and the coupling coefficients for the translation-translation as $\mathrm{g}(\Delta_r, \Delta_s)$, rotation-rotation as $\mathrm{g}(\Theta_r, \Theta_s)$, and rotation-translation as $\mathrm{g}(\Theta_r, \Delta_s)$, respectively (Figure 3-9).

Together, for the CO step, the intrinsic properties such as relative geometry ($\vec{\mathrm{G}}$), mechanical rigidities ($\vec{\mathrm{R}}$), and mechanical coupling coefficients ($\vec{\mathrm{C}}$) are finally obtained in the beam coordinate from the MD trajectory as follows (Table 3-4 and Table 3-5).

$$\begin{aligned}
\vec{\mathrm{G}} &= \left[\,\Delta_{xN} \quad \Delta_{yN} \quad \Delta_{zN} \quad \Theta_{xN} \quad \Theta_{yN} \quad \Theta_{zN}\,\right] \\
\vec{\mathrm{R}} &= \left[\,EA \quad GA_y \quad GA_z \quad GJ \quad EI_y \quad EI_y\,\right] \\
\vec{\mathrm{C}} &= \left[\,g\left(\Delta_r, \Delta_s\right) \quad g\left(\Theta_r, \Theta_s\right) \quad g\left(\Delta_r, \Theta_s\right)\,\right]
\end{aligned} \tag{3-101}$$

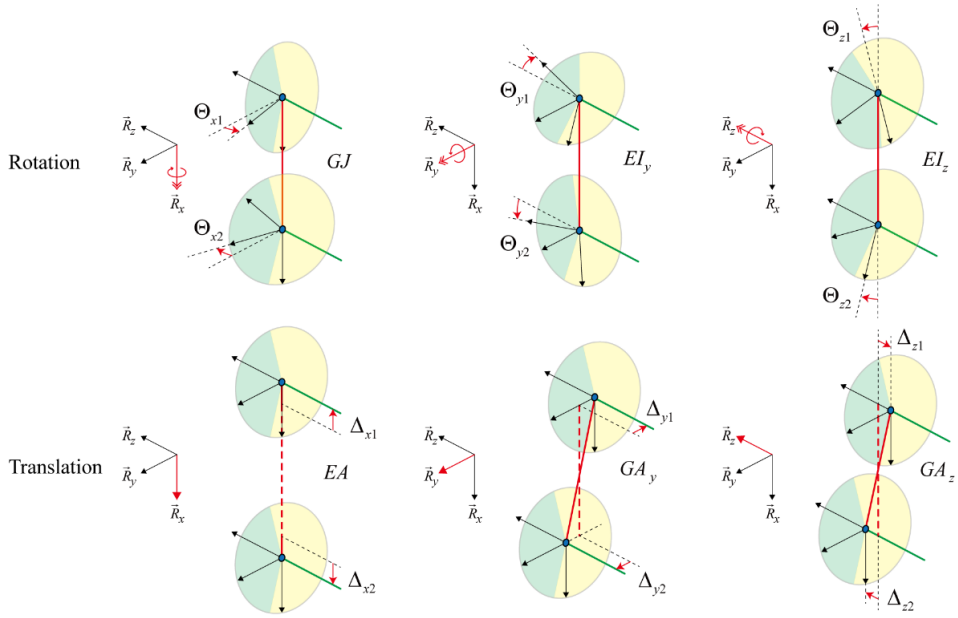


Figure 3-9. Relative geometry and mechanical properties of the CO step.

Table 3-4. Intrinsic properties of double CO steps.

| Properties | Unit | AA‖TT | TT‖AA | AG‖CT | CT‖AG |
|---|---|---|---|---|---|
| $\Delta_{x1}$ | nm | -0.9424 | -0.9555 | -0.9445 | -0.9414 |
| $\Delta_{x2}$ | nm | 0.9424 | 0.9555 | 0.9445 | 0.9414 |
| $\Delta_{y1}$ | nm | -0.1750 | -0.2415 | -0.1615 | -0.0770 |
| $\Delta_{y2}$ | nm | 0.1750 | 0.2415 | 0.1615 | 0.0770 |
| $\Delta_{z1}$ | nm | -0.0755 | -0.0454 | -0.0990 | -0.0650 |
| $\Delta_{z2}$ | nm | 0.0755 | 0.0454 | 0.0990 | 0.0650 |
| $\Theta_{x1}$ | deg | -2.2523 | -7.7279 | -0.5330 | 2.8158 |
| $\Theta_{x2}$ | deg | 1.0789 | 5.9061 | -1.9572 | -3.8129 |
| $\Theta_{y1}$ | deg | 4.9737 | 2.3670 | 9.9218 | 5.7582 |
| $\Theta_{y2}$ | deg | 4.2971 | 2.9595 | 2.0172 | 2.1102 |
| $\Theta_{z1}$ | deg | -30.523 | -36.711 | -32.148 | -14.940 |
| $\Theta_{z2}$ | deg | 8.8470 | 7.2790 | 11.902 | 6.0502 |
| EA | pN | 3605.5 | 4189.5 | 2324.1 | 4729.4 |
| $GA_y$ | pN | 1040.4 | 1210.6 | 699.85 | 1089.3 |
| $GA_z$ | pN | 564.97 | 639.00 | 489.84 | 696.81 |
| GJ | $pNnm^2$ | 318.62 | 314.28 | 293.69 | 325.46 |
| $EI_y$ | $pNnm^2$ | 416.21 | 413.22 | 359.51 | 482.83 |
| $EI_z$ | $pNnm^2$ | 325.13 | 313.45 | 264.76 | 479.84 |
| $g(\Theta_x,\Theta_y)$ | $pNnm^2$ | -6.0132 | -16.795 | 1.9683 | -26.227 |
| $g(\Theta_x,\Theta_z)$ | $pNnm^2$ | 12.504 | -5.0436 | -11.134 | 38.93 |
| $g(\Theta_y,\Theta_z)$ | $pNnm^2$ | 1.6077 | -7.9889 | 0.28967 | -21.005 |
| $g(\Delta_x,\Delta_y)$ | pN | 716.44 | 1304.76 | 437.74 | 452.54 |
| $g(\Delta_x,\Delta_z)$ | pN | 604.34 | 499.08 | 523.59 | 770.95 |
| $g(\Delta_y,\Delta_z)$ | pN | 191.08 | 267.88 | 146.51 | 141.52 |
| $g(\Delta_x,\Theta_x)$ | pNnm | 53.258 | 79.315 | 88.467 | 45.277 |
| $g(\Delta_x,\Theta_y)$ | pNnm | 12.196 | 65.300 | 58.164 | -148.37 |
| $g(\Delta_x,\Theta_z)$ | pNnm | -230.92 | -84.189 | -216.36 | -281.51 |
| $g(\Delta_y,\Theta_x)$ | pNnm | 55.862 | 75.912 | 46.734 | 31.177 |
| $g(\Delta_y,\Theta_y)$ | pNnm | -75.233 | -28.947 | -109.08 | -174.76 |
| $g(\Delta_y,\Theta_z)$ | pNnm | -17.765 | -2.9668 | 9.1735 | 105.77 |
| $g(\Delta_z,\Theta_x)$ | pNnm | 129.28 | 154.69 | 164.17 | 43.160 |
| $g(\Delta_z,\Theta_y)$ | pNnm | 3.7375 | 19.689 | 11.027 | -37.661 |
| $g(\Delta_z,\Theta_z)$ | pNnm | -67.042 | -37.158 | -83.956 | -31.782 |

Table 3-4 (Continued).

| Properties | Unit | GA‖TC | TC‖GA | GG‖CC | CC‖GG |
|---|---|---|---|---|---|
| $\Delta_{x1}$ | nm | -0.9230 | -0.9560 | -0.9518 | -0.9576 |
| $\Delta_{x2}$ | nm | 0.9230 | 0.9560 | 0.9518 | 0.9576 |
| $\Delta_{y1}$ | nm | -0.2635 | -0.1515 | -0.2390 | -0.2115 |
| $\Delta_{y2}$ | nm | 0.2635 | 0.1515 | 0.2390 | 0.2115 |
| $\Delta_{z1}$ | nm | -0.0705 | -0.0680 | -0.1065 | -0.0890 |
| $\Delta_{z2}$ | nm | 0.0705 | 0.0680 | 0.1065 | 0.0890 |
| $\Theta_{x1}$ | deg | -6.4552 | -7.5950 | -0.829 | -19.847 |
| $\Theta_{x2}$ | deg | 4.4998 | 6.4330 | -1.742 | 15.643 |
| $\Theta_{y1}$ | deg | 4.3086 | 3.3459 | 9.0020 | 5.9779 |
| $\Theta_{y2}$ | deg | 4.2612 | 4.7257 | 3.6723 | 4.6235 |
| $\Theta_{z1}$ | deg | -31.162 | -25.711 | -38.414 | -33.2110 |
| $\Theta_{z2}$ | deg | -2.0520 | 7.4695 | 9.0860 | 7.2790 |
| EA | pN | 3419.2 | 3511.4 | 2587.4 | 2020.8 |
| $GA_y$ | pN | 977.08 | 1227.7 | 908.68 | 609.18 |
| $GA_z$ | pN | 538.81 | 697.95 | 454.04 | 650.52 |
| GJ | $pNnm^2$ | 289.40 | 313.05 | 270.06 | 230.54 |
| $EI_y$ | $pNnm^2$ | 406.26 | 426.95 | 355.61 | 329.88 |
| $EI_z$ | $pNnm^2$ | 369.71 | 291.36 | 242.78 | 214.76 |
| $g(\Theta_x,\Theta_y)$ | $pNnm^2$ | 15.236 | 5.0508 | -8.4617 | -26.764 |
| $g(\Theta_x,\Theta_z)$ | $pNnm^2$ | 19.588 | -18.807 | 6.3731 | -22.431 |
| $g(\Theta_y,\Theta_z)$ | $pNnm^2$ | -0.96359 | 18.696 | -12.356 | -31.342 |
| $g(\Delta_x,\Delta_y)$ | pN | 979.48 | 1003.6 | 912.19 | 583.71 |
| $g(\Delta_x,\Delta_z)$ | pN | 548.57 | 567.32 | 427.32 | 680.38 |
| $g(\Delta_y,\Delta_z)$ | pN | 273.36 | 151.01 | 251.61 | 280.40 |
| $g(\Delta_x,\Theta_x)$ | pNnm | 29.617 | 134.22 | 32.120 | 217.77 |
| $g(\Delta_x,\Theta_y)$ | pNnm | 39.921 | 68.808 | 4.2158 | -15.264 |
| $g(\Delta_x,\Theta_z)$ | pNnm | -294.65 | -337.23 | -206.6 | -143.23 |
| $g(\Delta_y,\Theta_x)$ | pNnm | 74.667 | 93.983 | 65.881 | 122.26 |
| $g(\Delta_y,\Theta_y)$ | pNnm | -34.127 | -118.01 | -101.93 | -91.701 |
| $g(\Delta_y,\Theta_z)$ | pNnm | -122.18 | -59.656 | -61.210 | -89.760 |
| $g(\Delta_z,\Theta_x)$ | pNnm | 87.992 | 200.93 | 114.27 | 188.15 |
| $g(\Delta_z,\Theta_y)$ | pNnm | 63.509 | 73.045 | -17.183 | 27.734 |
| $g(\Delta_z,\Theta_z)$ | pNnm | -69.193 | -82.526 | -59.929 | -14.495 |

Table 3-4 (Continued).

| Properties | Unit | AC‖GT | GT‖AC | AT‖AT | GC‖GC |
|---|---|---|---|---|---|
| $\Delta_{x1}$ | nm | -0.9696 | -0.9513 | -0.9539 | -0.9649 |
| $\Delta_{x2}$ | nm | 0.9696 | 0.9513 | 0.9539 | 0.9649 |
| $\Delta_{y1}$ | nm | -0.1715 | -0.2365 | -0.2070 | -0.1725 |
| $\Delta_{y2}$ | nm | 0.1715 | 0.2365 | 0.2070 | 0.1725 |
| $\Delta_{z1}$ | nm | -0.0990 | -0.0780 | -0.0309 | -0.1500 |
| $\Delta_{z2}$ | nm | 0.0990 | 0.0780 | 0.0309 | 0.1500 |
| $\Theta_{x1}$ | deg | -6.1881 | 0.2107 | -5.6768 | 4.4260 |
| $\Theta_{x2}$ | deg | 3.0963 | -1.7657 | 4.3232 | -5.3116 |
| $\Theta_{y1}$ | deg | 9.7454 | 6.9380 | 3.1161 | 9.0444 |
| $\Theta_{y2}$ | deg | 1.8917 | 2.5079 | 0.5009 | 9.1812 |
| $\Theta_{z1}$ | deg | -34.37 | -30.240 | -33.039 | -33.340 |
| $\Theta_{z2}$ | deg | 13.361 | 1.3000 | 7.5710 | 12.210 |
| EA | pN | 3083.9 | 4274.5 | 4200.9 | 2519.8 |
| $GA_y$ | pN | 639.82 | 1023.5 | 1018.5 | 653.30 |
| $GA_z$ | pN | 723.58 | 543.68 | 572.57 | 649.85 |
| GJ | $pNnm^2$ | 348.99 | 341.76 | 314.54 | 264.34 |
| $EI_y$ | $pNnm^2$ | 443.67 | 484.42 | 415.14 | 453.87 |
| $EI_z$ | $pNnm^2$ | 300.49 | 352.44 | 340.87 | 315.43 |
| $g(\Theta_x,\Theta_y)$ | $pNnm^2$ | -16.321 | 24.656 | -12.811 | 31.266 |
| $g(\Theta_x,\Theta_z)$ | $pNnm^2$ | -40.595 | -24.706 | -1.3762 | 53.669 |
| $g(\Theta_y,\Theta_z)$ | $pNnm^2$ | -43.803 | -48.598 | -26.217 | -53.348 |
| $g(\Delta_x,\Delta_y)$ | pN | 668.41 | 941.96 | 781.00 | 551.14 |
| $g(\Delta_x,\Delta_z)$ | pN | 615.33 | 651.21 | 433.38 | 576.04 |
| $g(\Delta_y,\Delta_z)$ | pN | 294.25 | 265.74 | 172.30 | 173.97 |
| $g(\Delta_x,\Theta_x)$ | pNnm | 175.62 | 33.127 | 122.70 | 69.632 |
| $g(\Delta_x,\Theta_y)$ | pNnm | -109.54 | -38.103 | -43.782 | 48.189 |
| $g(\Delta_x,\Theta_z)$ | pNnm | -294.00 | -58.546 | -43.771 | -165.00 |
| $g(\Delta_y,\Theta_x)$ | pNnm | 107.54 | 80.676 | 84.710 | 14.556 |
| $g(\Delta_y,\Theta_y)$ | pNnm | -143.30 | 8.9491 | -70.125 | -111.79 |
| $g(\Delta_y,\Theta_z)$ | pNnm | -25.825 | -221.65 | -61.500 | 8.7235 |
| $g(\Delta_z,\Theta_x)$ | pNnm | 238.64 | 81.496 | 129.78 | 124.45 |
| $g(\Delta_z,\Theta_y)$ | pNnm | 39.003 | 104.40 | 33.025 | 73.286 |
| $g(\Delta_z,\Theta_z)$ | pNnm | -106.41 | -77.762 | -33.783 | -31.208 |

Table 3-4 (Continued).

| Properties | Unit | TG‖CA | CA‖TG | TA‖TA | CG‖CG |
|---|---|---|---|---|---|
| $\Delta_{x1}$ | nm | -0.9639 | -0.9539 | -0.9351 | -0.9503 |
| $\Delta_{x2}$ | nm | 0.9639 | 0.9539 | 0.9351 | 0.9503 |
| $\Delta_{y1}$ | nm | -0.2095 | -0.2060 | -0.1460 | -0.1835 |
| $\Delta_{y2}$ | nm | 0.2095 | 0.2060 | 0.1460 | 0.1835 |
| $\Delta_{z1}$ | nm | -0.0775 | -0.0975 | -0.0915 | -0.1200 |
| $\Delta_{z2}$ | nm | 0.0775 | 0.0975 | 0.0915 | 0.1200 |
| $\Theta_{x1}$ | deg | -3.6533 | -4.0184 | -3.8997 | -2.2954 |
| $\Theta_{x2}$ | deg | 1.4365 | 2.4816 | 2.5209 | 0.0058 |
| $\Theta_{y1}$ | deg | 5.9402 | 6.8225 | 6.2174 | 8.0909 |
| $\Theta_{y2}$ | deg | 3.2753 | 5.1123 | 5.0334 | 6.3740 |
| $\Theta_{z1}$ | deg | -37.739 | -29.698 | -28.079 | -33.110 |
| $\Theta_{z2}$ | deg | 11.891 | 4.3320 | 10.101 | 10.370 |
| EA | pN | 2796.6 | 3468.7 | 3217.7 | 3189.0 |
| $GA_y$ | pN | 1002.3 | 1212.0 | 957.42 | 1161.8 |
| $GA_z$ | pN | 512.09 | 878.58 | 657.24 | 736.63 |
| GJ | $pNnm^2$ | 305.15 | 432.63 | 332.88 | 304.61 |
| $EI_y$ | $pNnm^2$ | 371.32 | 600.03 | 437.10 | 436.16 |
| $EI_z$ | $pNnm^2$ | 274.16 | 355.00 | 382.94 | 301.09 |
| $g(\Theta_x,\Theta_y)$ | $pNnm^2$ | -53.49 | -9.0702 | 8.2535 | -15.996 |
| $g(\Theta_x,\Theta_z)$ | $pNnm^2$ | 1.2921 | -66.436 | -12.608 | 18.962 |
| $g(\Theta_y,\Theta_z)$ | $pNnm^2$ | -6.6605 | 21.134 | 8.4572 | -19.728 |
| $g(\Delta_x,\Delta_y)$ | pN | 939.55 | 1127.5 | 596.48 | 976.80 |
| $g(\Delta_x,\Delta_z)$ | pN | 510.01 | 829.07 | 574.02 | 700.62 |
| $g(\Delta_y,\Delta_z)$ | pN | 281.49 | 375.36 | 178.21 | 393.68 |
| $g(\Delta_x,\Theta_x)$ | pNnm | 51.807 | -50.731 | 72.230 | -22.882 |
| $g(\Delta_x,\Theta_y)$ | pNnm | 7.1253 | 32.187 | -38.344 | -21.484 |
| $g(\Delta_x,\Theta_z)$ | pNnm | -140.94 | -298.85 | -259.95 | -133.82 |
| $g(\Delta_y,\Theta_x)$ | pNnm | 49.151 | -38.662 | 75.922 | 45.893 |
| $g(\Delta_y,\Theta_y)$ | pNnm | -103.11 | -105.24 | -50.452 | -185.03 |
| $g(\Delta_y,\Theta_z)$ | pNnm | 40.186 | -49.714 | -9.3146 | -14.546 |
| $g(\Delta_z,\Theta_x)$ | pNnm | 169.97 | 160.18 | 158.45 | 147.97 |
| $g(\Delta_z,\Theta_y)$ | pNnm | -87.446 | -76.669 | -15.860 | -66.947 |
| $g(\Delta_z,\Theta_z)$ | pNnm | -18.766 | -4.6020 | -69.283 | -67.004 |

Table 3-5. Intrinsic properties of single CO steps.

| Properties | Unit | AA\|TT | TT\|AA | AG\|CT | CT\|AG |
|---|---|---|---|---|---|
| $\Delta_{x1}$ | nm | -0.9339 | -0.9323 | -0.9370 | -0.9719 |
| $\Delta_{x2}$ | nm | 0.9339 | 0.9323 | 0.9370 | 0.9719 |
| $\Delta_{y1}$ | nm | -0.0665 | -0.3635 | -0.1135 | -0.0325 |
| $\Delta_{y2}$ | nm | 0.0665 | 0.3635 | 0.1135 | 0.0325 |
| $\Delta_{z1}$ | nm | -0.0315 | 0.0590 | 0.1260 | 0.0695 |
| $\Delta_{z2}$ | nm | 0.0315 | -0.0590 | -0.1260 | -0.0695 |
| $\Theta_{x1}$ | deg | -5.3977 | -8.7594 | -15.603 | -14.779 |
| $\Theta_{x2}$ | deg | 3.7950 | 11.796 | 13.622 | 12.219 |
| $\Theta_{y1}$ | deg | 2.9780 | -5.6736 | 8.9421 | 1.6503 |
| $\Theta_{y2}$ | deg | 0.26005 | 0.47920 | -8.5399 | -9.8587 |
| $\Theta_{z1}$ | deg | -23.387 | -39.061 | -31.586 | -23.017 |
| $\Theta_{z2}$ | deg | 7.4327 | 8.7990 | 11.334 | 12.093 |
| EA | pN | 146.88 | 145.22 | 128.75 | 959.61 |
| $GA_y$ | pN | 229.52 | 401.07 | 181.29 | 283.53 |
| $GA_z$ | pN | 118.41 | 134.78 | 198.58 | 120.47 |
| GJ | $pNnm^2$ | 66.744 | 7.1619 | 140.31 | 133.20 |
| $EI_y$ | $pNnm^2$ | 114.96 | 61.202 | 264.77 | 147.79 |
| $EI_z$ | $pNnm^2$ | 109.86 | 74.088 | 133.97 | 186.02 |
| $g(\Theta_x,\Theta_y)$ | $pNnm^2$ | -4.6667 | -14.521 | -24.606 | 4.2933 |
| $g(\Theta_x,\Theta_z)$ | $pNnm^2$ | -8.9068 | 1.6744 | -64.867 | -7.0643 |
| $g(\Theta_y,\Theta_z)$ | $pNnm^2$ | 11.275 | 6.0194 | 43.469 | -12.396 |
| $g(\Delta_x,\Delta_y)$ | pN | 272.14 | 76.296 | 222.47 | -32.930 |
| $g(\Delta_x,\Delta_z)$ | pN | 118.79 | 50.398 | 19.632 | -21.793 |
| $g(\Delta_y,\Delta_z)$ | pN | 20.600 | 51.034 | -42.146 | -22.058 |
| $g(\Delta_x,\Theta_x)$ | pNnm | -6.1664 | -13.971 | 183.50 | -3.4410 |
| $g(\Delta_x,\Theta_y)$ | pNnm | -25.428 | 44.995 | -229.03 | 125.11 |
| $g(\Delta_x,\Theta_z)$ | pNnm | -17.736 | -58.913 | -34.755 | -33.898 |
| $g(\Delta_y,\Theta_x)$ | pNnm | 4.4645 | -1.0123 | -11.245 | -85.190 |
| $g(\Delta_y,\Theta_y)$ | pNnm | 1.6688 | 16.713 | -33.735 | 9.9344 |
| $g(\Delta_y,\Theta_z)$ | pNnm | -4.3443 | -80.254 | 73.769 | -11.387 |
| $g(\Delta_z,\Theta_x)$ | pNnm | 30.464 | 3.0271 | 63.612 | 55.290 |
| $g(\Delta_z,\Theta_y)$ | pNnm | -10.267 | 49.776 | -134.01 | 57.920 |
| $g(\Delta_z,\Theta_z)$ | pNnm | -3.1289 | 5.8120 | -92.943 | -55.974 |

Table 3-5 (Continued).

| Properties | Unit | GA\|TC | TC\|GA | GG\|CC | CC\|GG |
|---|---|---|---|---|---|
| $\Delta_{x1}$ | nm | -1.0271 | -0.9104 | -0.9693 | -0.8906 |
| $\Delta_{x2}$ | nm | 1.0271 | 0.9104 | 0.9693 | 0.8906 |
| $\Delta_{y1}$ | nm | 0.0865 | 0.1665 | 0.0229 | -0.0725 |
| $\Delta_{y2}$ | nm | -0.0865 | -0.1665 | -0.0229 | 0.0725 |
| $\Delta_{z1}$ | nm | 0.0395 | -0.1845 | 0.0188 | -0.0935 |
| $\Delta_{z2}$ | nm | -0.0395 | 0.1845 | -0.0188 | 0.0935 |
| $\Theta_{x1}$ | deg | 0.78570 | -5.1047 | -13.147 | -10.601 |
| $\Theta_{x2}$ | deg | -5.4883 | -2.2393 | 8.6328 | 10.002 |
| $\Theta_{y1}$ | deg | 8.7939 | 4.7405 | 9.6009 | -1.3412 |
| $\Theta_{y2}$ | deg | -13.061 | -9.3945 | -11.793 | 13.974 |
| $\Theta_{z1}$ | deg | -30.385 | -27.401 | -23.889 | -30.320 |
| $\Theta_{z2}$ | deg | 15.555 | 5.6888 | 14.631 | 5.5195 |
| EA | pN | 167.31 | 135.64 | 209.75 | 207.54 |
| $GA_y$ | pN | 520.16 | 725.94 | 578.27 | 1012.6 |
| $GA_z$ | pN | 309.44 | 689.49 | 261.19 | 395.59 |
| GJ | $pNnm^2$ | 265.94 | 157.49 | 198.96 | 230.36 |
| $EI_y$ | $pNnm^2$ | 187.77 | 268.18 | 201.07 | 321.07 |
| $EI_z$ | $pNnm^2$ | 96.329 | 254.79 | 327.50 | 209.22 |
| $g(\Theta_x,\Theta_y)$ | $pNnm^2$ | 49.863 | 42.074 | 2.9046 | -41.906 |
| $g(\Theta_x,\Theta_z)$ | $pNnm^2$ | -78.287 | 20.166 | 28.213 | -37.829 |
| $g(\Theta_y,\Theta_z)$ | $pNnm^2$ | 27.577 | 0.2669 | 85.611 | -31.002 |
| $g(\Delta_x,\Delta_y)$ | pN | -329.49 | -34.194 | 300.33 | 647.99 |
| $g(\Delta_x,\Delta_z)$ | pN | 1.3042 | 7.6287 | 104.86 | 530.50 |
| $g(\Delta_y,\Delta_z)$ | pN | -52.748 | 2.7672 | -58.555 | 68.202 |
| $g(\Delta_x,\Theta_x)$ | pNnm | -129.15 | -0.00354 | 94.740 | 171.43 |
| $g(\Delta_x,\Theta_y)$ | pNnm | 44.701 | 0.84116 | -212.35 | 179.44 |
| $g(\Delta_x,\Theta_z)$ | pNnm | 53.295 | -6.4471 | 11.905 | -356.00 |
| $g(\Delta_y,\Theta_x)$ | pNnm | -18.277 | -0.0937 | -122.10 | -107.59 |
| $g(\Delta_y,\Theta_y)$ | pNnm | -61.822 | -0.0478 | -47.011 | 80.949 |
| $g(\Delta_y,\Theta_z)$ | pNnm | 8.7260 | 3.8202 | 29.501 | -54.315 |
| $g(\Delta_z,\Theta_x)$ | pNnm | 158.17 | 0.88136 | 121.79 | 70.594 |
| $g(\Delta_z,\Theta_y)$ | pNnm | 50.998 | 23.647 | 10.916 | 55.794 |
| $g(\Delta_z,\Theta_z)$ | pNnm | -0.4385 | 1.1772 | 29.499 | -100.60 |

Table 3-5 (Continued).

| Properties | Unit | AC\|GT | GT\|AC | AT\|AT | GC\|GC |
|---|---|---|---|---|---|
| $\Delta_{x1}$ | nm | -0.8203 | -0.9823 | -0.9036 | -0.9479 |
| $\Delta_{x2}$ | nm | 0.8203 | 0.9823 | 0.9036 | 0.9479 |
| $\Delta_{y1}$ | nm | 0.1500 | 0.4465 | 0.2065 | 0.1050 |
| $\Delta_{y2}$ | nm | -0.1500 | -0.4465 | -0.2065 | -0.1050 |
| $\Delta_{z1}$ | nm | -0.3880 | 0.0600 | 0.0183 | -0.0520 |
| $\Delta_{z2}$ | nm | 0.3880 | -0.0600 | -0.0183 | 0.0520 |
| $\Theta_{x1}$ | deg | -8.6304 | -3.0756 | -2.5704 | -8.5292 |
| $\Theta_{x2}$ | deg | 2.7126 | -3.4328 | 1.6000 | 9.2759 |
| $\Theta_{y1}$ | deg | 5.1160 | 6.6081 | -3.3972 | -1.5615 |
| $\Theta_{y2}$ | deg | -5.0400 | -11.726 | 1.3180 | -7.7779 |
| $\Theta_{z1}$ | deg | -27.808 | -24.457 | -29.110 | -27.519 |
| $\Theta_{z2}$ | deg | 12.753 | 8.9570 | 7.6374 | 8.2190 |
| EA | pN | 562.07 | 102.36 | 211.44 | 329.69 |
| $GA_y$ | pN | 226.09 | 836.35 | 482.58 | 214.37 |
| $GA_z$ | pN | 269.59 | 334.48 | 179.06 | 116.12 |
| GJ | $pNnm^2$ | 36.100 | 282.06 | 143.11 | 142.26 |
| $EI_y$ | $pNnm^2$ | 201.46 | 164.19 | 135.05 | 243.08 |
| $EI_z$ | $pNnm^2$ | 205.98 | 193.67 | 128.94 | 120.68 |
| $g(\Theta_x,\Theta_y)$ | $pNnm^2$ | 38.149 | 66.599 | -3.4921 | 24.008 |
| $g(\Theta_x,\Theta_z)$ | $pNnm^2$ | 7.9831 | 52.423 | -20.516 | -10.003 |
| $g(\Theta_y,\Theta_z)$ | $pNnm^2$ | -11.893 | 52.604 | 26.973 | 0.019933 |
| $g(\Delta_x,\Delta_y)$ | pN | -97.530 | -490.17 | 636.50 | 126.93 |
| $g(\Delta_x,\Delta_z)$ | pN | 88.390 | -9.4864 | 149.80 | 154.75 |
| $g(\Delta_y,\Delta_z)$ | pN | 23.584 | -53.123 | 69.029 | 3.7880 |
| $g(\Delta_x,\Theta_x)$ | pNnm | -18.034 | 48.351 | -6.8440 | 0.53405 |
| $g(\Delta_x,\Theta_y)$ | pNnm | 54.283 | -124.97 | 28.430 | -67.079 |
| $g(\Delta_x,\Theta_z)$ | pNnm | 23.291 | -204.29 | 146.50 | 1.6111 |
| $g(\Delta_y,\Theta_x)$ | pNnm | 7.1730 | -192.18 | 43.781 | -50.446 |
| $g(\Delta_y,\Theta_y)$ | pNnm | -23.684 | -63.442 | 8.8922 | 0.040855 |
| $g(\Delta_y,\Theta_z)$ | pNnm | -147.95 | 36.161 | 18.575 | 0.72388 |
| $g(\Delta_z,\Theta_x)$ | pNnm | 47.417 | 246.19 | 47.430 | -1.3452 |
| $g(\Delta_z,\Theta_y)$ | pNnm | 203.87 | 71.648 | -3.6154 | 0.10553 |
| $g(\Delta_z,\Theta_z)$ | pNnm | 2.2321 | 73.233 | -11.000 | 0.29189 |

Table 3-5 (Continued).

| Properties | Unit | TG\|CA | CA\|TG | TA\|TA | CG\|CG |
|---|---|---|---|---|---|
| $\Delta_{x1}$ | nm | -1.1375 | -0.9271 | -0.8635 | -0.8875 |
| $\Delta_{x2}$ | nm | 1.1375 | 0.9271 | 0.8635 | 0.8875 |
| $\Delta_{y1}$ | nm | 0.3185 | -0.0245 | 0.4885 | -0.0441 |
| $\Delta_{y2}$ | nm | -0.3185 | 0.0245 | -0.4885 | 0.0441 |
| $\Delta_{z1}$ | nm | -0.0955 | 0.0127 | -0.1550 | 0.0915 |
| $\Delta_{z2}$ | nm | 0.0955 | -0.0127 | 0.1550 | -0.0915 |
| $\Theta_{x1}$ | deg | -3.6691 | -7.4163 | -5.8557 | -1.2125 |
| $\Theta_{x2}$ | deg | 4.7885 | 11.4837 | 4.8443 | 0.4091 |
| $\Theta_{y1}$ | deg | 3.6404 | 2.3213 | 13.813 | -4.2141 |
| $\Theta_{y2}$ | deg | 5.1469 | -4.9033 | 2.4309 | -7.3224 |
| $\Theta_{z1}$ | deg | -34.028 | -22.920 | -32.108 | -33.004 |
| $\Theta_{z2}$ | deg | 14.898 | 12.100 | 12.782 | 7.3859 |
| EA | pN | 143.92 | 554.87 | 82.104 | 197.15 |
| $GA_y$ | pN | 50.275 | 473.60 | 27.862 | 77.663 |
| $GA_z$ | pN | 75.002 | 200.91 | 34.630 | 94.433 |
| GJ | $pNnm^2$ | 42.409 | 141.40 | 21.209 | 25.520 |
| $EI_y$ | $pNnm^2$ | 119.84 | 268.04 | 48.269 | 82.438 |
| $EI_z$ | $pNnm^2$ | 73.292 | 136.91 | 38.856 | 56.958 |
| $g(\Theta_x,\Theta_y)$ | $pNnm^2$ | -12.103 | 14.259 | 18.250 | 2.0674 |
| $g(\Theta_x,\Theta_z)$ | $pNnm^2$ | -19.460 | -8.3286 | -11.497 | 4.7851 |
| $g(\Theta_y,\Theta_z)$ | $pNnm^2$ | 22.919 | -9.9858 | 1.8324 | 5.9619 |
| $g(\Delta_x,\Delta_y)$ | pN | -23.847 | 410.11 | -24.018 | -71.146 |
| $g(\Delta_x,\Delta_z)$ | pN | -29.002 | -12.035 | 7.1967 | 9.7432 |
| $g(\Delta_y,\Delta_z)$ | pN | -2.7363 | 1.5141 | -3.6710 | 23.944 |
| $g(\Delta_x,\Theta_x)$ | pNnm | 14.349 | 43.588 | -6.6265 | 6.7458 |
| $g(\Delta_x,\Theta_y)$ | pNnm | 36.434 | -85.773 | -19.378 | 5.8574 |
| $g(\Delta_x,\Theta_z)$ | pNnm | -16.086 | -2.4967 | -0.56284 | -28.534 |
| $g(\Delta_y,\Theta_x)$ | pNnm | -17.645 | 13.737 | 0.90783 | -3.2262 |
| $g(\Delta_y,\Theta_y)$ | pNnm | 10.926 | -33.184 | -1.9327 | -4.1972 |
| $g(\Delta_y,\Theta_z)$ | pNnm | 27.971 | 40.376 | -8.9827 | 27.789 |
| $g(\Delta_z,\Theta_x)$ | pNnm | -16.402 | 38.523 | -0.67308 | 25.772 |
| $g(\Delta_z,\Theta_y)$ | pNnm | -48.325 | 27.444 | 15.602 | -28.534 |
| $g(\Delta_z,\Theta_z)$ | pNnm | -7.4050 | -1.2581 | 8.9749 | 11.212 |

## 3.6. Characterization and modeling of single-stranded DNA

The single-stranded DNA (ssDNA) has the possibility of showing different mechanical properties depending on its end-to-end and contour length. The two-node of the ssDNA beam element represents the two-terminal BPs, indicating the end-to-end distance is regarded as the intrinsic length of the beam element.

### 3.6.1. Intrinsic end-to-end length

For long ssDNA, the ssDNA model is established such as the worm-like-chain or freely-jointed-chain models, predicting mechanical behavior consistent with the single-molecule experiments. And, its equilibrated end-to-end length can be neglected since the end-to-end length is much smaller compared to the contour length. However, short ssDNA such as gap[67] could show finite end-to-end length and considerable mechanical stiffness in equilibrium. This suggests that the end-to-end length cannot be ignored (Figure 3-10).

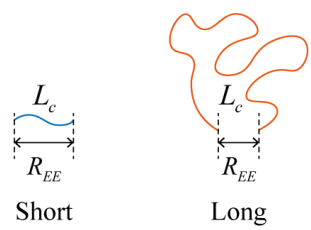


Figure 3-10. The end-to-end length and contour length of short and long ssDNA.

Here, to express the end-to-end length with respect to the contour length, the normalized length was introduced as $r = R_{EE}/L_c$, where $R_{EE}$ and $L_c$ represent the equilibrated end-to-end and contour length of ssDNA, respectively. Then, the probability density function of equilibrated end-to-end distance, $P(r)$ is expressed in terms of the normalized length in the previous studies[68] (Figure 3-11) as

$$P(r) = 4\pi C \frac{r^2}{(1-r^2)^{9/2}} \exp\left(-\frac{3t}{4}\frac{1}{(1-r^2)}\right) \tag{3-102}$$

where $t$ is defined as $t = L_c/L_B$, $C$ is the normalization constant was given by

$$C = \left[\pi^{3/2} e^{-\alpha} \alpha^{-3/2} \left(1 + 3\alpha^{-1} + 15\alpha^{-2}/4\right)\right]^{-1}, \qquad \alpha = 3t/4 \qquad (3\text{-}103)$$

and $L_B$ is the bending persistence length of ssDNA as 0.74 nm measured in 20 mM $MgCl_2$ conditions[21].

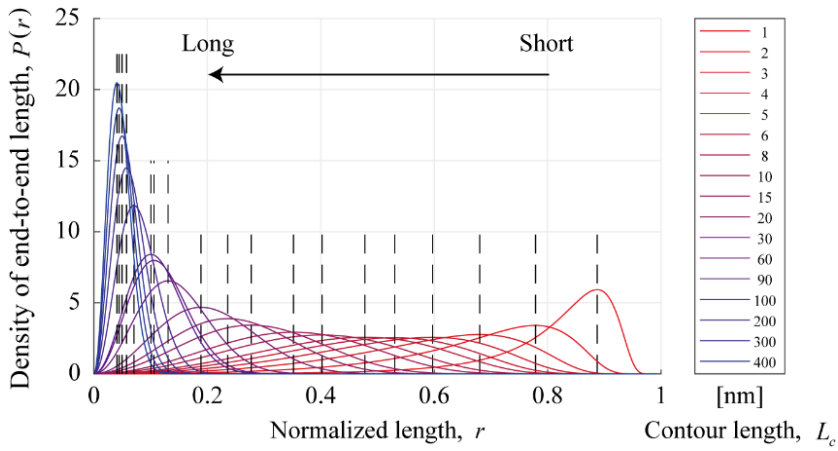


Figure 3-11. The probability density function of the equilibrated end-to-end length for contour length.

The peak point of the probability density function provides the most probable equilibrated end-to-end distance ($\bar{r}$) for the contour length as

$$\left.\frac{dP(r)}{dr}\right|_{r=\bar{r}} = 0, \quad \rightarrow \quad \bar{r} = \sqrt{\frac{\eta + \sqrt{\eta^2 + 14}}{7}}, \qquad \eta = \frac{5}{2} - \frac{3L_c}{4L_B} \qquad (3\text{-}104)$$

Finally, the end-to-end distance is explicitly expressed in terms of contour length as

$$\begin{aligned} R_{EE} &= \gamma_{ss} L_c \bar{r} = \gamma_{ss} L_c \sqrt{\frac{\eta + \sqrt{\eta^2 + 14}}{7}} \\ &= \gamma_{ss} L_c \sqrt{\frac{5}{14} - \frac{3L_c}{28L_B} + \frac{1}{7}\sqrt{\left(\frac{5}{2} - \frac{3L_c}{4L_B}\right)^2 + 14}} \end{aligned} \qquad (3\text{-}105)$$

where $\gamma_{ss}$ was employed as a correction factor, of which value is 1 for the independent ssDNA. Here, in the case of ssDNA in the DNA assemblies, the ratio of the end-to-end length to the contour length may be larger than theoretically expected, due to the interference in the structure. This implies the correction factor greater than 1. We found that the tested structures showed reasonable prediction for $\gamma_{ss} = 2$, in which the end-to-end length was specified to contour length if $\gamma_{ss}\bar{r} > 1$, and this relation also showed good agreement with the previous result[69] (Figure 3-12).

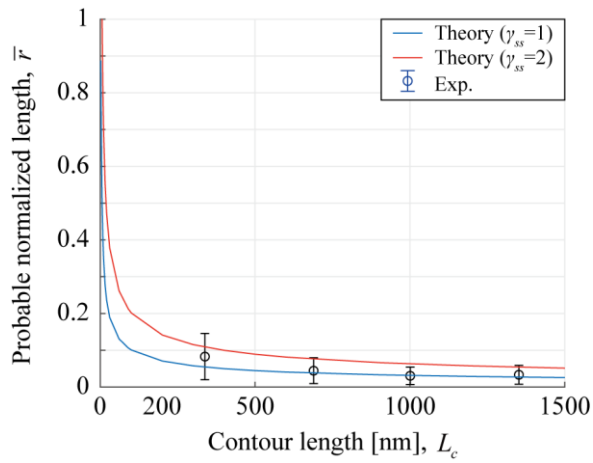


Figure 3-12. The most probable normalized end-to-end length with respect to the contour length.

### 3.6.2. Single-stranded DNA properties

ssDNA is highly flexible in the direction perpendicular to the axial direction, but because it is covalently linked, the stretching rigidity varies with normalized length as the end-to-end length divided by the contour length. The force-displacement curve for ssDNA was well-established such as the extensible freely-jointed-chain model, predicting mechanical behavior consistent with the single-molecule experiments, given by

$$\frac{x_{EE}}{L_c} = \left( \coth\left( \frac{FL_K}{k_B T} \right) - \frac{k_B T}{f_{ss} L_K} \right)\left( 1 + \frac{F}{S} \right) \tag{3-106}$$

where $x_{EE}$, $L_c$, $L_K$, $S$, $F$ denote the current end-to-end length, contour length, Kuhn length, stretching modulus, and stretching force of ssDNA, respectively. The Kuhn length was set to $1.48\ \mathrm{nm}$ from the relation with the bending persistence length as $L_K = 2L_B$.

The stretching stiffness ($k_{Stretch}$) is then obtained by differentiating stretching force with respect to the displacement as

$$k_{Stretch} = \frac{EA}{L_c} = \frac{\partial F}{\partial x_{EE}} \tag{3-107}$$

The stretching rigidity ($EA$) is thus derived for the stretching force as

$$\begin{aligned} EA &= \frac{\partial F}{\partial (x_{EE} / L_c)} \\ &= \left[ \begin{array}{l} \dfrac{1}{S}\left( \coth\left( \dfrac{FL_k}{k_B T} \right) - \dfrac{k_B T}{FL_k} \right) \\ + \left( \dfrac{k_B T}{F^2 L_k} - \dfrac{L_k}{k_B T}\left[ \coth^2\left( \dfrac{FL_k}{k_B T} \right) - 1 \right] \right)\left( 1 + \dfrac{F}{S} \right) \end{array} \right]^{-1} \end{aligned} \tag{3-108}$$

As discussed, when the current end-to-end length is smaller than the contour length in relaxed conformation, the stretching rigidity is small enough not to exert a tensional or compressive force (low-force region). On the other hand, the stretching

rigidity value approaches the given stretch modulus when ssDNA is stretched (high-force region).

However, the stretching rigidity is expressed in terms of not the current end-to-end length, but an implicit form of force, which is not suitable for the present finite element formulation. Hence, we alternatively modeled the stretching rigidity as a continuous function in terms of the normalized length (Figure 3-13) as

$$EA = \begin{cases} EA^H & \left(\frac{x_{EE}}{L_c} \geq 1.2\right) \\ \frac{EA^H - EA^L}{0.4}\left(\frac{x_{EE}}{L_c} - 1\right) + \frac{EA^H + EA^L}{2} & \left(0.8 \leq \frac{x_{EE}}{L_c} < 1.2\right) \\ EA^L & \left(\frac{x_{EE}}{L_c} < 0.8\right) \end{cases} \quad \text{(3-109)}$$

where $EA^L$ and $EA^H$ represent the stretching rigidities at the low and high force region, respectively, as $EA^L = 5\ pN$ and $EA^H = 710\ pN$ as previously reported[21].

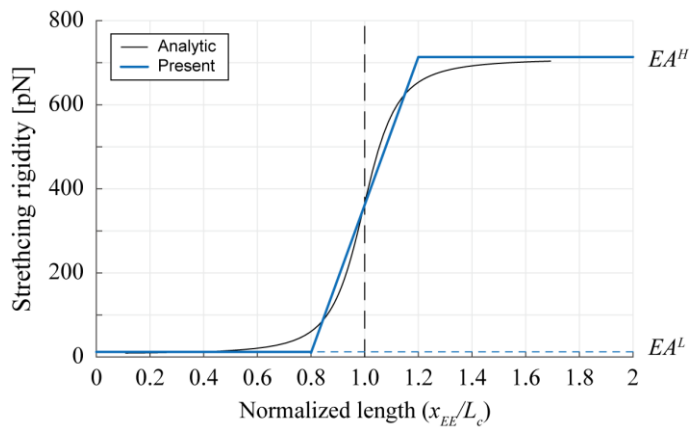


Figure 3-13. Stretching rigidity modeling of ssDNA.

Taken together, nodal geometric values ($\vec{G}$) were determined using the element configuration at the former time step since the relative geometry of ssDNA cannot be determined. Except for stretching rigidity, the other rigidities ($\vec{R}$) were determined to negligible values of 10, and all coupling coefficients ($\vec{C}$) were set to zero.

## 3.7. Finite element framework for electrostatic interaction

Through the multiscale modeling, the structural elements with intrinsic properties are inter-connected and assembled to form DNA nanostructures. However, the resulting structures exist without any interaction between the helix. Therefore, as an upscaling effect, the inter-helical interaction, especially the electrostatic force due to high charged DNA, was considered to accurately predict the DNA constructs[14,70,71].

### 3.7.1. Electrostatic interaction model

The electrostatic repulsive forces between base-pairs are expected to be exerted in the general DNA nanostructure conditions of the $MgCl_2$ 20 mM. To reproduce this electrostatic force, we employed the Debye-Hückel potential as the explicit electrostatic theory following the previous studies[13,14,70,71].

Considering that two BPs in difference helix interact with each other with a distance ($r$), the electrostatic energy ($\Pi_{ES}$) is given by

$$\Pi_{ES}(r) = \frac{q^2}{4\pi\varepsilon_0\varepsilon r}\exp\left(-\frac{r}{\lambda_D}\right) \tag{3-110}$$

where $q$ is the effective charge with the unit of the elementary charge ($e$), $\varepsilon_0$ is the vacuum permittivity, $\varepsilon$ is the relative permittivity of water, and $\lambda_D$ is the Debye screening length as a function of absolute temperature ($T$) and ionic strength ($I$) as

$$\lambda_D = \sqrt{\frac{\varepsilon_0\varepsilon_r k_B T}{2N_A e^2 I}} \tag{3-111}$$

where $k_B$ is the Boltzmann constant, and $N_A$ is the Avogadro's number. The ionic strength is

$$I = \frac{1}{2}\sum_i c_i z_i^2 \tag{3-112}$$

with the molar concentration of ions ($c_i$) and the charge number of ions ($z_i$).

### 3.7.2. Finite element model of electrostatic interaction

When the parameters such as ionic strength ($I$) and temperature ($T$) were determined, the electrostatic potential energy is a function of the distance ($r$) between BP nodes as $\Pi_{ES} = \Pi_{ES}(r)$, without the requirement of the rotational degree of freedom. This indicates that the electrostatic interaction can be modeled as an equivalent truss element with material nonlinearity. Here, we employed the nonlinear truss element based on the Total-Lagrange (TL) formulation[72].

The stiffness matrix and the internal force vector were derived in the truss element. The electrostatic force is dependent on the distance between two nodes, which is given as the length of the truss. In addition, all the other deformation except for an axial deformation was neglected.

The axial extension of a truss was considered for the prismatic and homogeneous truss of the initial length ($r_i$) at the time step $t$, and the truss is stretched to the final length ($r_f$) at the time step $t + \Delta t$ as follows (Figure 3-14).

$$r_i = \left\| {}^{i}\vec{p}_2 - {}^{i}\vec{p}_1 \right\|, \quad r_f = \left\| {}^{f}\vec{p}_2 - {}^{f}\vec{p}_1 \right\| \tag{3-113}$$

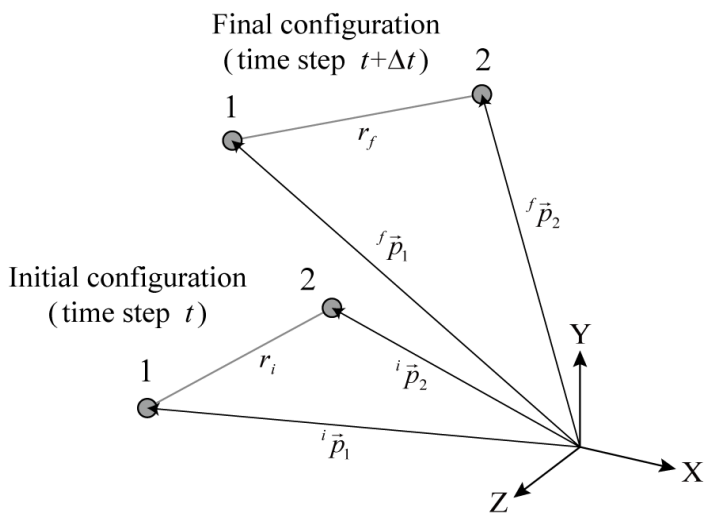


Figure 3-14. Extension of the truss element.

where the initial and final nodal coordinates of the truss element are given as

$$ {}^{i}\vec{p}_N = \begin{bmatrix} {}^{i}x_N & {}^{i}y_N & {}^{i}z_N \end{bmatrix}^{\mathrm{T}}, \quad {}^{f}\vec{p}_N = \begin{bmatrix} {}^{f}x_N & {}^{f}y_N & {}^{f}z_N \end{bmatrix}^{\mathrm{T}} \tag{3-114} $$

To estimate the Green-Lagrange (GL) strain, the deformation gradient tensor (${}^{f}_{i}\mathbf{X}$) from the initial to the final configuration is defined as

$$ {}^{f}_{i}\mathbf{X} = \frac{\partial^{f}(x,y,z)}{\partial^{i}(x,y,z)} = \begin{bmatrix} \frac{\partial^{f}x}{\partial^{i}x} & \frac{\partial^{f}x}{\partial^{i}y} & \frac{\partial^{f}x}{\partial^{i}z} \\ \frac{\partial^{f}y}{\partial^{i}x} & \frac{\partial^{f}y}{\partial^{i}y} & \frac{\partial^{f}y}{\partial^{i}z} \\ \frac{\partial^{f}z}{\partial^{i}x} & \frac{\partial^{f}z}{\partial^{i}y} & \frac{\partial^{f}z}{\partial^{i}z} \end{bmatrix} = \begin{bmatrix} r_f / r_i & 0 & 0 \\ 0 & 1 & 0 \\ 0 & 0 & 1 \end{bmatrix} \tag{3-115} $$

The right Cauchy-Green deformation tensor (${}^{f}_{i}\mathbf{C}$) is then obtained as follows.

$$ {}^{f}_{i}\mathbf{C} = {}^{f}_{i}\mathbf{X}^{\mathrm{T}}\,{}^{f}_{i}\mathbf{X} = \begin{bmatrix} \left(r_f / r_i\right)^2 & 0 & 0 \\ 0 & 1 & 0 \\ 0 & 0 & 1 \end{bmatrix} \tag{3-116} $$

The GL strain tensor (${}^{f}_{i}\mathbf{e}$) is expressed in terms of the right Cauchy-Green deformation tensor as

$$ {}^{f}_{i}\mathbf{e} = \frac{1}{2}\left({}^{f}_{i}\mathbf{C} - \mathbf{I}_{3\times 3}\right) = \frac{1}{2}\begin{bmatrix} \left(r_f / r_i\right)^2 - 1 & 0 & 0 \\ 0 & 0 & 0 \\ 0 & 0 & 0 \end{bmatrix} \tag{3-117} $$

Accordingly, as the first axial component in the GL strain tensor, the GL strain of the truss element ($e$) is expressed as

$$ e = {}^{f}_{i}e_{xx} = \frac{r_f^2 - r_i^2}{2r_i^2} \tag{3-118} $$

The second Piola-Kirchhoff (PK2) stress is derived as the standard stress measure of the GL strain in the TL formulation.

This PK2 stress tensor ($_i^f\mathbf{S}$) is expressed as

$$
\begin{aligned}
{}_i^f\mathbf{S} &= \det\left({}_i^f\mathbf{X}\right) {}_f^i\mathbf{X}\, {}^f\boldsymbol{\tau}\, {}_f^i\mathbf{X}^{\mathrm{T}} \\
&= \frac{r_f}{r_i}\begin{bmatrix} r_i/r_f & 0 & 0 \\ 0 & 1 & 0 \\ 0 & 0 & 1 \end{bmatrix}\begin{bmatrix} \tau_{\mathrm{ES}} & 0 & 0 \\ 0 & 0 & 0 \\ 0 & 0 & 0 \end{bmatrix}\begin{bmatrix} r_i/r_f & 0 & 0 \\ 0 & 1 & 0 \\ 0 & 0 & 1 \end{bmatrix}^{\mathrm{T}} \\
&= \tau_{\mathrm{ES}}\begin{bmatrix} r_i/r_f & 0 & 0 \\ 0 & 0 & 0 \\ 0 & 0 & 0 \end{bmatrix}
\end{aligned}
\tag{3-119}
$$

where ${}^f\boldsymbol{\tau}$ is the Cauchy stress tensor with the only axial component as $\tau_{xx} = \tau_{\mathrm{ES}}$ by the electrostatic force, and the deformation gradient tensor has the nature of ${}_i^f\mathbf{X} = {}_f^i\mathbf{X}^{-1}$. Accordingly, the PK2 stress ($S$) of the truss element is expressed as the first diagonal component in PK2 stress tensor in terms of the electrostatic energy as

$$
S = {}_i^f S_{xx} = \frac{r_i}{r_f}\tau_{\mathrm{ES}} = \frac{r_i}{r_f}\frac{F_{\mathrm{ES}}}{A_{\mathrm{ES}}} = \frac{r_i}{r_f}\frac{1}{A_{\mathrm{ES}}}\frac{\partial \Pi_{\mathrm{ES}}\left(r_f\right)}{\partial r_f} \tag{3-120}
$$

where $A_{\mathrm{ES}}$ represents a virtual constant area of the electrostatic element and $F_{\mathrm{ES}}$ denotes the electrostatic force derived by the differentiation of Debye-Hückel electrostatic energy as

$$
\frac{\partial \Pi_{\mathrm{ES}}\left(r_f\right)}{\partial r_f} = -\frac{q^2}{4\pi\varepsilon_0\varepsilon r_f}\left(\frac{1}{r_f^2} + \frac{1}{\lambda_D r_f}\right)\exp\left(-\frac{r_f}{\lambda_D}\right) \tag{3-121}
$$

The tangent elastic modulus ($E$) is defined as the gradient of the PK2 stress ($S$) with respect to the GL strain ($e$) given by

$$
E = \frac{\partial S}{\partial e} = \frac{\partial S}{\partial r_f}\frac{\partial r_f}{\partial e} = \frac{q^2 r_i^3\left(3\lambda_D^2 + 3\lambda_D r_f + r_f^2\right)}{4\pi\varepsilon_0\varepsilon A_{\mathrm{ES}}\lambda_D^2 r_f^5}\exp\left(-\frac{r_f}{\lambda_D}\right) \tag{3-122}
$$

Together, in the global coordinate, the 12-by-12 stiffness matrix of the element ($\mathbf{K}_{\mathrm{G}}^{\mathrm{ES}}$) for the electrostatic interaction is computed by the sum of material and geometric terms as follows. Noting that the truss element does not contain rotational degrees of freedom when assembling the global stiffness matrix, rotational

components are zero values.

$$\mathbf{K}_{\mathrm{G}}^{\mathrm{ES}} = K\mathbf{P}_M + \frac{F}{r_f}\mathbf{P}_G \tag{3-123}$$

where the matrices are given by

$$\mathbf{P}_M = \begin{bmatrix} \mathbf{p} & \mathbf{O}_{3\times3} & -\mathbf{p} & \mathbf{O}_{3\times3} \\ \mathbf{O}_{3\times3} & \mathbf{O}_{3\times3} & \mathbf{O}_{3\times3} & \mathbf{O}_{3\times3} \\ -\mathbf{p} & \mathbf{O}_{3\times3} & \mathbf{p} & \mathbf{O}_{3\times3} \\ \mathbf{O}_{3\times3} & \mathbf{O}_{3\times3} & \mathbf{O}_{3\times3} & \mathbf{O}_{3\times3} \end{bmatrix} \quad \mathbf{P}_{\mathrm{G}} = \begin{bmatrix} \mathbf{I}_{3\times3} & \mathbf{O}_{3\times3} & -\mathbf{I}_{3\times3} & \mathbf{O}_{3\times3} \\ \mathbf{O}_{3\times3} & \mathbf{O}_{3\times3} & \mathbf{O}_{3\times3} & \mathbf{O}_{3\times3} \\ -\mathbf{I}_{3\times3} & \mathbf{O}_{3\times3} & \mathbf{I}_{3\times3} & \mathbf{O}_{3\times3} \\ \mathbf{O}_{3\times3} & \mathbf{O}_{3\times3} & \mathbf{O}_{3\times3} & \mathbf{O}_{3\times3} \end{bmatrix} \tag{3-124}$$

with the component matrix as

$$\mathbf{p} = \begin{bmatrix} c_x^2 & c_x c_y & c_x c_z \\ c_x c_y & c_y^2 & c_y c_z \\ c_x c_z & c_y c_z & c_z^2 \end{bmatrix} \tag{3-125}$$

introducing the direction cosines as

$$c_x = \frac{x_2 - x_1}{r_f}, \quad c_y = \frac{y_2 - y_1}{r_f}, \quad c_z = \frac{z_2 - z_1}{r_f} \tag{3-126}$$

and the stiffness ($K$) and the force terms ($F$) are calculated as

$$\begin{aligned} K &= \frac{r_f^2}{r_i^3} EA_{\mathrm{ES}} = \frac{q^2}{4\pi\varepsilon_0\varepsilon\lambda_D^2 r_f^3}\left(3\lambda_D^2 + 3\lambda_D r_f + r_f^2\right)\exp\left(-\frac{r_f}{\lambda_D}\right) \\ F &= \frac{r_f}{r_i} SA_{\mathrm{ES}} = -\frac{q^2\left(\lambda_D + r_f\right)}{4\pi\varepsilon_0\varepsilon\lambda_D r_f^2}\exp\left(-\frac{r_f}{\lambda_D}\right) \end{aligned} \tag{3-127}$$

The 12-by-1 internal force vector is also obtained as below.

$$\vec{F}_{\mathrm{G}}^{\mathrm{ES}} = F\begin{bmatrix} -c_x & -c_y & -c_z & c_x & c_y & c_z \end{bmatrix}^{\mathrm{T}} \tag{3-128}$$

## 3.8. Estimation of characteristic values on the electrostatic interaction

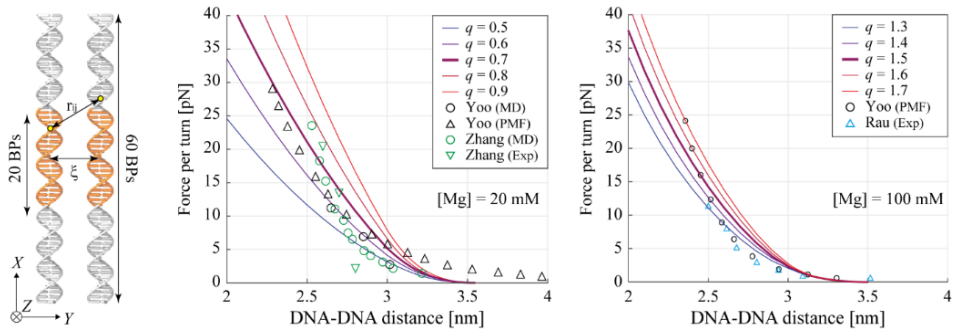


Figure 3-15. The estimation of effective charge in the Mg condition.

The effective charge ($q$) was then determined for the $MgCl_2$ buffer condition through the pairwise inter-DNA system[22,23,73] (Figure 3-15). Referring to the previous literature[22], to measure the inter-DNA force between a pair of 20-BP-long DNA helices of two-turn, we constructed the finite element system of the helices, which has the intrinsic properties of BP steps. The electrostatic force per helical turn was obtained for different effective charge values using the electrostatic truss elements. Here, to simulate the effects of two 20-BP-long DNAs bound infinitely by periodic boundary conditions, the 60-BP-long DNAs were generated and the force between the central 20-BP was estimated. The length of the 60-BP-long DNA molecules exceeds the effective electrostatic distance of the central 20-BP-long segments, thus providing a sufficient electrostatic effect. The effective electrostatic force acting on the central helices was calculated as the summation on the $\xi$-directional contribution of electrostatic force using the distance ($r_{ij}$) between nodes $i$ and $j$ following the previous study[22]. From the previous results[22,23,73], the effective charge was determined as $q = 0.7$ for 20 mM of [Mg] and $q = 1.5$ for 100 mM of [Mg], respectively, showing the agreement with the previous models[13,70]. The effective charge of the electrostatic element was represented in terms of the Mg concentration ($C_{\mathrm{Mg}}$) by simple linear interpolation as $q = 0.01C_{\mathrm{Mg}} + 0.5$. However, we expect that further research on the electrostatic interaction of DNA nanostructures could

suggest the refined relation of effective charge and Mg concentration.

A cutoff distance ($r_{\mathrm{cut}}$) was introduced for the computational efficiency by suppressing numerous negligible electrostatic interactions. The cutoff distance was used as a criterion whether electrostatic elements are generated or not by measuring the distance between nodes in a nonlinear solution procedure. By testing the various structures, the cutoff distance was determined to 2.5 nm, which is approximately twice of Debye length in the Mg 20 mM.

## 3.9. Construction of initial configuration

Previously, we provided the multiscale framework, from the intrinsic properties and connection of component elements, that the structural and electrostatic elements establish a global stiffness matrix. From the global stiffness matrix, we could find the final configuration of the stable position and triads of structured BPs, which satisfies their intrinsic properties. However, to rapidly obtain the physically correct solution, it is essential to properly construct the initial configuration of elements from the original design. The initial configuration was, therefore, generated by defining the raw coordinates and triad of all BPs of a structure, and then, modifying the BP triads in the consideration of the orientation of CO steps of inter-connecting helices.

### 3.9.1. General description

The raw information of a DNA structure was loaded from the connectivity design of the caDNAno[74] file using an open script[17,33]. The initial length of the BP step was set to 0.34 nm. By fixing the coordinate of a BP, the position of the remaining BPs in one helix was specified. In the initial configuration, every helix was assumed to be all straight lines. Using the initial CO distance as 2.25 nm and lattice-type of structures (honeycomb or square lattice), the position of all BPs in the remaining helix was determined around one helix created. Assigning the initial twist angle, $\omega_i$ of a BP step produced all BP triads for all the BPs in the helix to rotate gradually. The initial twist angle was set to $\omega_i = 720°/21 \sim 34.29°$ and $\omega_i = 1080°/32 = 33.75°$ following the rule of the honeycomb (two-turn per 21 BPs) and square (three-turn per 32 BPs) lattice structures, respectively. The major groove angle, which indicates the included angle between two complementary bases, was set to $150°$. BP triads of the CO steps were established to satisfy the physical orientation of strands connecting helices, and all BP triads were constructed. The BP triads were then used to generate nodal triads of structural elements, in which the relative geometry, mechanical rigidities, and coupling coefficients were assigned.

### 3.9.2. Initial BP triads for the 2-helix-bundle structure

For the detailed description of the generation of the initial configuration, we introduce an ideal 21-BP-long 2-helix-bundle (2HB) structure of the honeycomb lattice without nicks, BP insertion, and BP deletion (Figure 3-16). The component BP or CO steps are constructed using the idealized values, which indicates the absence of mechanical stress in structural elements. In the 2HB structure, we denoted helices and BPs as $h$ and $n$, respectively.

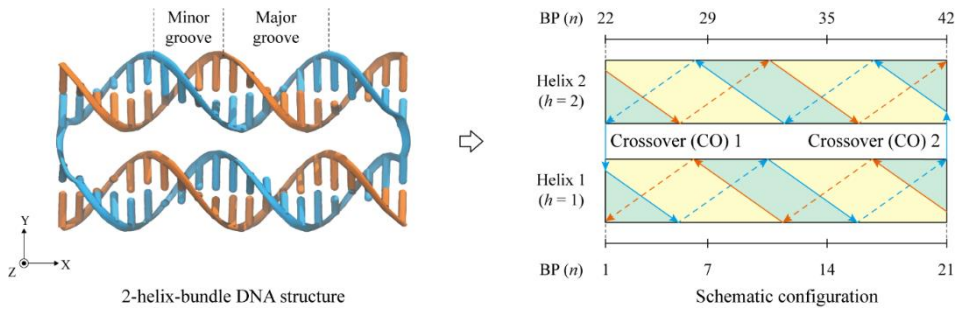


Figure 3-16. Schematic configuration of a 2-helix-bundle structure.

In each helix, relative rotation between successive BPs is $\omega_i$ of $34.29°$. The positions of BPs in two helices (Helix 1 and 2) were aligned to the X-axis, and the two helices were located in the Y-axis direction. The blue and orange strands of each helix rotate and blue strand intersects between the two helices forming two COs (CO 1 and 2) at the end BPs (Plane 1 and 2). The direction of the strands of the two helices is exactly symmetric about the Z-axis, indicating that the strand direction of two COs in planes 1 and 2 should be symmetric. Noting that each helix rotates two turns when proceeding by 21 BPs in the X-direction ($21\omega_i = 720°$), the difference in the rotation of end triads, at Y-Z plane 1 and 2 about the X-axis, comes to be $\omega_i$. This indicates that the rotational difference between two BP triads at plane 1 and plane 2 in a helix is $\omega_i$. In addition, considering that the plane 1 and 2 are symmetric about Z-axis, the strands connecting the CO (blue strand) should be connected while rotated by $\omega_i$ about X-axis. Then, BP triads of planes 1 and 2 at CO sites can be defined.

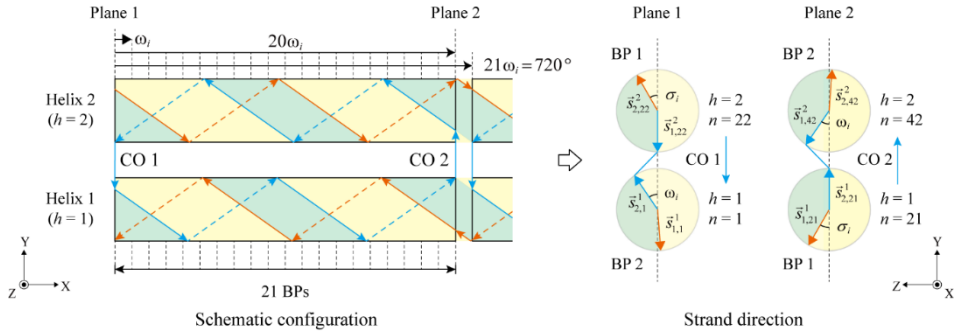


Figure 3-17. Strand direction at the crossovers in 2-helix-bundle structure.

For example, the strand connection and BP triads are considered for the CO step in plane 1 (Figure 3-17). We denoted $\vec{s}_{r,n}^{\,h}$ as a strand vector of a helix projected onto the Y-Z plane, where $h$, $r$, and $n$ indicate the helix, strand, and BP indication, respectively. The magnitude of strand vectors is one. When the blue strand vector ($\vec{s}_{1,22}^{\,2}$), which directs out of the first BP (BP 1), was set parallel to a vector connecting the positions of two BPs (-Y direction), the direction of the blue strand vector ($\vec{s}_{2,1}^{\,1}$) of the second BP (BP 2) was determined with the rotation by $\omega_i$ satisfying the relation as

$$\cos^{-1}\left[\vec{s}_{2,22}^{\,2}\cdot\left(-\vec{s}_{2,1}^{\,1}\right)\right] = \omega_i \tag{3-129}$$

The direction of remaining orange strand vectors is then estimated by introducing an opening angle ($\sigma_i = 30°$), which is defined from the angle between blue and orange strand vectors, satisfying $\sigma_i = \cos^{-1}\left[\vec{s}_{1,n}^{\,h}\cdot\left(-\vec{s}_{2,n}^{\,h}\right)\right]$. The tilted strand vectors divide the BP plane into the major and minor groove and provide the z-axis of the BP triad ($^{i}\vec{t}_{zn}$ for $n = 1, 22$) toward the minor groove direction as

$$^{i}\vec{t}_{zn} = \frac{\vec{s}_{1,n}^{\,h} + \vec{s}_{2,n}^{\,h}}{\left\|\vec{s}_{1,n}^{\,h} + \vec{s}_{2,n}^{\,h}\right\|} \tag{3-130}$$

For convenience, the x-axes of the BP triads were set to a global X-axis direction in helix 1 ($^{i}\vec{t}_{xn} = [1 \quad 0 \quad 0]^{\mathrm{T}}$ for $n = 1, 21$), and the x-axes of BP triads in the other helix were specified in the opposite X-axis direction ($^{i}\vec{t}_{xn} = [-1 \quad 0 \quad 0]^{\mathrm{T}}$ for $n =$

22, 42). Then, the y-axes were naturally determined as ${}^{i}\vec{t}_{yn} = {}^{i}\vec{t}_{zn} \times {}^{i}\vec{t}_{xn}$ in both plane 1 or 2. Here, the angle difference between each y-axis of BP triads and the orange strand vector is the half of the opening angle ($\sigma_i/2 = 15°$). Together, the BP triads at CO sites were determined, and then, all remaining triads of BPs were obtained by rotating BP triads at the CO sites by initial twist angle ($\omega_i$) about X-axis. We denoted the BP triads as

$$ {}^{i}\mathbf{t}_n = \left[ {}^{i}\vec{t}_{xn} \quad {}^{i}\vec{t}_{yn} \quad {}^{i}\vec{t}_{zn} \right] \tag{3-131} $$

In brief, by introducing the initial twist angle and length of BP and CO step and the strand-connection of CO, the position and triads of BPs were determined in each helix.

### 3.9.3. Initial configuration of structural elements for base-pair steps

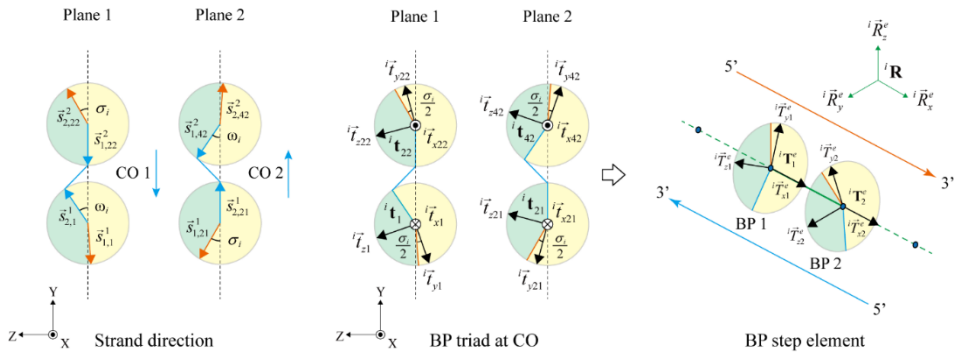


Figure 3-18. Generation of structural elements for BP steps.

Until here, the initial structural elements were constructed in the consideration of the connectivity of structural motifs using the BP triads. We first considered structural elements for BP steps (Figure 3-18), which contain the initial position, nodal triads, and local CR triad as

$$
\begin{aligned}
{}^{i}\vec{p}_N^{\,e} &= \begin{bmatrix} {}^{i}x_N^e & {}^{i}y_N^e & {}^{i}z_N^e \end{bmatrix}^{\mathrm{T}} \\
{}^{i}\mathbf{T}_N^{e} &= \begin{bmatrix} {}^{i}\vec{T}_{xN}^{\,e} & {}^{i}\vec{T}_{yN}^{\,e} & {}^{i}\vec{T}_{zN}^{\,e} \end{bmatrix} \\
{}^{i}\mathbf{R}^{e} &= \begin{bmatrix} {}^{i}\vec{R}_x^e & {}^{i}\vec{R}_y^e & {}^{i}\vec{R}_z^e \end{bmatrix}
\end{aligned}
\tag{3-132}
$$

where ${}^{i}\vec{p}_N^{\,e}$ is the nodal position of a structural element, ${}^{i}\mathbf{T}_N^{e}$ and ${}^{i}\mathbf{R}^{e}$ represents the nodal triads and local CR triad of the element, respectively, $N$ denotes the node number of the element ($N = 1,2$), and $e$ indicates each element. By the connection in BP steps, two of BP triads ( ${}^{i}\mathbf{t}_n$ ) were used as the nodal triads of elements ( ${}^{i}\mathbf{T}_N^{e}$ ). The local CR triad ( ${}^{i}\mathbf{R}^{e}$ ) was determined by the average of two nodal triads[75] as

$$
{}^{i}\mathbf{R}^{e} = {}^{i}\mathbf{T}_1^{e}\left[\left({}^{i}\mathbf{T}_1^{e}\right)^{\mathrm{T}}\,{}^{i}\mathbf{T}_2^{e}\right]^{1/2} = {}^{i}\mathbf{T}_2^{e}\left[\left({}^{i}\mathbf{T}_2^{e}\right)^{\mathrm{T}}\,{}^{i}\mathbf{T}_1^{e}\right]^{1/2}
\tag{3-133}
$$

Next, structural elements for CO steps were also constructed. Initial nodal position ( ${}^{i}\vec{p}_N^{\,e}$ ) was determined using the location of BPs, but the modification was necessary to obtain nodal ( ${}^{i}\mathbf{T}_N^{e}$ ) and CR triads ( ${}^{i}\mathbf{R}^{e}$ ) from two of BP triads ( ${}^{i}\mathbf{t}_n$ ) comprising CO steps. Here, $e$ indicates each element. To determine nodal triads,

the y-axis in the nodal triad of the element was determined using the z-axis of BP triads in the CO sites as

$$ {}^{i}\vec{T}^{e}_{yN} = {}^{i}\vec{t}_{zn} \tag{3-134} $$

The z-axis ( ${}^{i}\vec{T}^{e}_{zN}$ ) of the nodal triad was then set to the outward direction in each CO. For example, the z-axes of nodal triads were set to -X direction in plane 1 and set to +X direction in plane 2, respectively. The x-axis was subsequently computed as ${}^{i}\vec{T}^{e}_{xN} = {}^{i}\vec{T}^{e}_{yN} \times {}^{i}\vec{T}^{e}_{zN}$ . These nodal triads were consistent with the triads used in the previous description for the characterization of the intrinsic properties of CO steps.

### 3.9.4. Initial configuration of structural elements for crossover steps

Meanwhile, the CR triad in the CO step ( ${}^{i}\mathbf{R}^{e}$ ) could not be aligned to the CO direction. Hence, to construct an aligned CR triad in CO steps (Figure 3-19), the x-axis ( ${}^{i}\vec{R}_{x}^{e}$ ) was determined as the unit vector connecting the two BPs positions ( ${}^{i}\vec{p}_{N}^{e}$ ) as

$$ {}^{i}\vec{R}_{x}^{e} = \frac{{}^{i}\vec{p}_{2}^{e} - {}^{i}\vec{p}_{1}^{e}}{\left\| {}^{i}\vec{p}_{2}^{e} - {}^{i}\vec{p}_{1}^{e} \right\|} \tag{3-135} $$

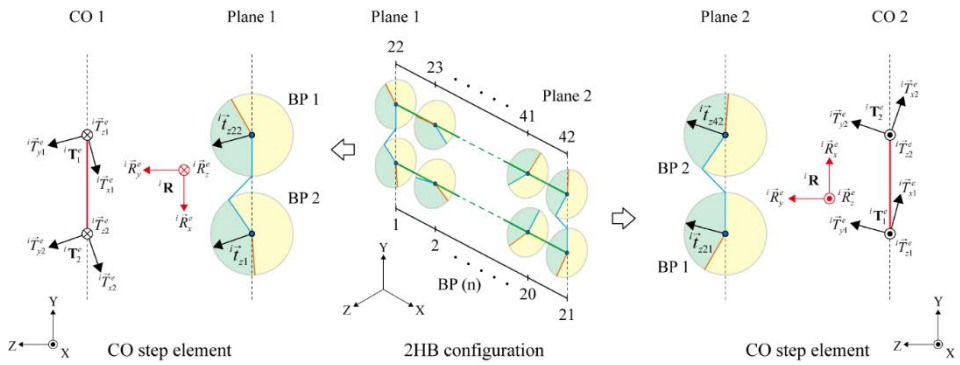


Figure 3-19. Generation of structural elements for CO steps.

The z-axis ( ${}^{i}\vec{R}_{z}^{e}$ ) was computed as the averaged vector of two z-axes in BP triads as

$$ {}^{i}\vec{R}_{z}^{e} = \frac{{}^{i}\vec{T}_{z1}^{e} + {}^{i}\vec{T}_{z2}^{e}}{\left\| {}^{i}\vec{T}_{z1}^{e} + {}^{i}\vec{T}_{z2}^{e} \right\|} \tag{3-136} $$

The y-axis ( ${}^{i}\vec{R}_{y}^{e}$ ) was finally obtained as ${}^{i}\vec{R}_{y}^{e} = {}^{i}\vec{R}_{z}^{e} \times {}^{i}\vec{R}_{x}^{e}$.

In summary, as like BP steps, the initial position ( ${}^{i}\vec{p}_{N}^{e}$ ), nodal triads ( ${}^{i}\mathbf{T}_{N}^{e}$ ), and CR triad ( ${}^{i}\mathbf{R}^{e}$ ) of CO steps were established as

$$ \begin{aligned} {}^{i}\vec{p}_{N}^{e} &= \begin{bmatrix} {}^{i}x_{N}^{e} & {}^{i}y_{N}^{e} & {}^{i}z_{N}^{e} \end{bmatrix}^{\mathrm{T}} \\ {}^{i}\mathbf{T}_{N}^{e} &= \begin{bmatrix} {}^{i}\vec{T}_{xN}^{e} & {}^{i}\vec{T}_{yN}^{e} & {}^{i}\vec{T}_{zN}^{e} \end{bmatrix} \\ {}^{i}\mathbf{R}^{e} &= \begin{bmatrix} {}^{i}\vec{R}_{x}^{e} & {}^{i}\vec{R}_{y}^{e} & {}^{i}\vec{R}_{z}^{e} \end{bmatrix} \end{aligned} \tag{3-137} $$

### 3.9.5. Generation of electrostatic elements

Electrostatic truss elements were constructed at each time step. The element was generated with the two nodal positions within the cutoff distance ($r_{\text{cut}}$) as

$$ {}^{i}\vec{p}_N^{\,e} = \begin{bmatrix} {}^{i}x_N^e & {}^{i}y_N^e & {}^{i}z_N^e \end{bmatrix}^{\mathrm{T}} \tag{3-138} $$

satisfying

$$ \left| {}^{i}\vec{p}_1^{\,e} - {}^{i}\vec{p}_2^{\,e} \right| \le r_{\text{cut}} \tag{3-139} $$

## 3.10. Nonlinear solution procedure

The initial system for a DNA nanostructure was constructed as an ideal configuration. Here, each element contains the unique structural or electrostatic properties. Thus, as a next step, the final stable configuration is obtained from the initial configuration. However, due to the material and geometric nonlinearity of the system, it is difficult to derive the final configuration immediately when assigning intrinsic properties to each structural element and generating electrostatic elements between neighboring nodes. We derived, thus, the final configuration via a static nonlinear solution procedure, with incrementally changing the element properties.

### 3.10.1. Overview of the solution procedure

The time step, in the solution process, corresponding to initial and final configuration was introduced as $t_i$ and $t_f$, respectively. In most cases, the steps were initially set to $t_i = 1$ and $t_f = 30$ with $\Delta t = 1$, indicating that the properties were divided by 30 steps.

The converged solution at each time step ($t = t_i, t_i + \Delta t, t_i + 2\Delta t, \cdots, t_f$) represents an intermediate configuration with gradually changing properties. The updated configuration at $t + \Delta t$ from $t$ was obtained by an iterative solution method. However, with a fixed time interval, $\Delta t = 1$, the solution at $t + \Delta t$ may diverge. Thus, $\Delta t$ was automatically divided in the range of $0 < \Delta t \leq 1$ until reaching the updated configuration of $t + \Delta t$ until $\Delta t = 1$. This procedure is summarized in the flow chart below (Figure 3-20).

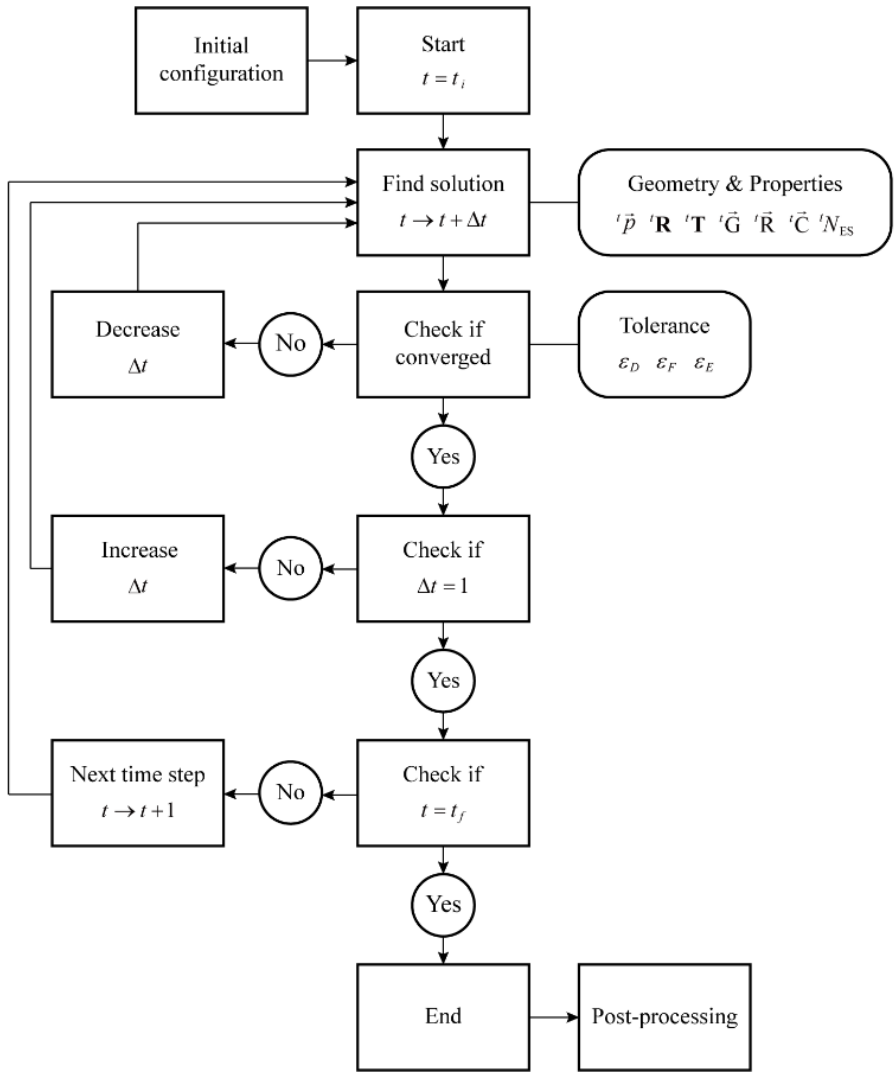


Figure 3-20. Flow chart of the overall nonlinear solution procedure.

### 3.10.2. Element properties in the initial and final configuration

In the final configuration, structural elements have their relative geometry and mechanical rigidity and coupling coefficients, determined from MD simulation as below.

$$
\begin{aligned}
{}^{f}\mathbf{G} &= \left[ {}^{f}\vec{\mathrm{G}}^{1},\ {}^{f}\vec{\mathrm{G}}^{2},\cdots,\ {}^{f}\vec{\mathrm{G}}^{N_{\mathrm{ST}}} \right] \\
{}^{f}\mathbf{R} &= \left[ {}^{f}\vec{\mathrm{R}}^{1},\ {}^{f}\vec{\mathrm{R}}^{2},\cdots,\ {}^{f}\vec{\mathrm{R}}^{N_{\mathrm{ST}}} \right] \\
{}^{f}\mathbf{C} &= \left[ {}^{f}\vec{\mathrm{C}}^{1},\ {}^{f}\vec{\mathrm{C}}^{2},\cdots,\ {}^{f}\vec{\mathrm{C}}^{N_{\mathrm{ST}}} \right] \\
{}^{f}\vec{\mathrm{G}}^{e} &= \left[ {}^{f}\Delta^{e}_{xN} \quad {}^{f}\Delta^{e}_{yN} \quad {}^{f}\Delta^{e}_{zN} \quad {}^{f}\Theta^{e}_{xN} \quad {}^{f}\Theta^{e}_{yN} \quad {}^{f}\Theta^{e}_{zN} \right] \\
{}^{f}\vec{\mathrm{R}}^{e} &= \left[ {}^{f}EA^{e} \quad {}^{f}GA^{e}_{y} \quad {}^{f}GA^{e}_{z} \quad {}^{f}GJ^{e} \quad {}^{f}EI^{e}_{y} \quad {}^{f}EI^{e}_{z} \right] \\
{}^{f}\vec{\mathrm{C}}^{e} &= \left[ {}^{f}g^{e}\left(\Delta_r,\Delta_s\right) \quad {}^{f}g^{e}\left(\Theta_r,\Theta_s\right) \quad {}^{f}g^{e}\left(\Theta_r,\Delta_s\right) \right]
\end{aligned}
\tag{3-140}
$$

where ${}^{f}\vec{G}^{e}$ includes the final translational ( ${}^{f}\Delta^{e}_{kN}$ ) and rotational ( ${}^{f}\Theta^{e}_{kN}$ ) geometry for the nodes ($N = 1,2$), ${}^{f}\vec{\mathrm{R}}^{e}$ and ${}^{f}\vec{\mathrm{C}}^{e}$ contain the set of all mechanical rigidities and coupling coefficients of the element, respectively, $r$ and $s$ represent one of axis directions ($x$, $y$, and $z$), $e$ is the element index ($e = 1,2,\cdots,N_{\mathrm{ST}}$), and $N_{\mathrm{ST}}$ is the number of structural elements. The property values of all elements were then collected to form sets as ${}^{f}\mathbf{G}$, ${}^{f}\mathbf{R}$, and ${}^{f}\mathbf{C}$.

Likewise, for the initial configuration, the values can be similarly expressed as follows.

$$
\begin{aligned}
{}^{i}\mathbf{G} &= \left[ {}^{i}\vec{\mathrm{G}}^{1},\ {}^{i}\vec{\mathrm{G}}^{2},\cdots,\ {}^{i}\vec{\mathrm{G}}^{N_{\mathrm{ST}}} \right] \\
{}^{i}\mathbf{R} &= \left[ {}^{i}\vec{\mathrm{R}}^{1},\ {}^{i}\vec{\mathrm{R}}^{2},\cdots,\ {}^{i}\vec{\mathrm{R}}^{N_{\mathrm{ST}}} \right] \\
{}^{i}\mathbf{C} &= \left[ {}^{i}\vec{\mathrm{C}}^{1},\ {}^{i}\vec{\mathrm{C}}^{2},\cdots,\ {}^{i}\vec{\mathrm{C}}^{N_{\mathrm{ST}}} \right] \\
{}^{i}\vec{\mathrm{G}}^{e} &= \left[ {}^{i}\Delta^{e}_{xN} \quad {}^{i}\Delta^{e}_{yN} \quad {}^{i}\Delta^{e}_{zN} \quad {}^{i}\Theta^{e}_{xN} \quad {}^{i}\Theta^{e}_{yN} \quad {}^{i}\Theta^{e}_{zN} \right] \\
{}^{i}\vec{\mathrm{R}}^{e} &= \left[ {}^{i}EA^{e} \quad {}^{i}GA^{e}_{y} \quad {}^{i}GA^{e}_{z} \quad {}^{i}GJ^{e} \quad {}^{i}EI^{e}_{y} \quad {}^{i}EI^{e}_{z} \right] \\
{}^{i}\vec{\mathrm{C}}^{e} &= \left[ {}^{i}g^{e}\left(\Delta_r,\Delta_s\right) \quad {}^{i}g^{e}\left(\Theta_r,\Theta_s\right) \quad {}^{i}g^{e}\left(\Theta_r,\Delta_s\right) \right]
\end{aligned}
\tag{3-141}
$$

where the translational geometry values were calculated as

$$
{}^{i}\Delta^{e}_{x} = \left\| {}^{i}\vec{p}^{e}_{2} - {}^{i}\vec{p}^{e}_{1} \right\|, \qquad {}^{i}\Delta^{e}_{y} = {}^{i}\Delta^{e}_{z} = 0 \tag{3-142}
$$

and the initial rotation of an element was computed from its initial triads as

$$ {}^{i}\Theta_{kN}^{e} = \underset{\sim}{\mathbf{V}}^{e}, \quad \mathbf{V}^{e} = \log\left[ \left( {}^{i}\mathbf{R}^{e} \right)^{\mathrm{T}} {}^{i}\mathbf{T}_{N}^{e} \right] \tag{3-143} $$

The mechanical rigidities were properly assigned from final values for the rapid convergence as

$$ \begin{aligned} {}^{i}GJ^{e} &= \frac{1}{2}\,{}^{f}GJ^{e}, \quad {}^{i}EI_{y}^{e} = {}^{f}EI_{y}^{e}, \quad {}^{i}EI_{z}^{e} = {}^{f}EI_{z}^{e} \\ {}^{i}EA^{e} &= \frac{1}{5}\,{}^{f}EA^{e}, \quad {}^{i}GA_{y}^{e} = {}^{f}GJ^{e}, \quad {}^{i}GA_{z}^{e} = {}^{f}GA_{z}^{e} \end{aligned} \tag{3-144} $$

Finally, every coupling coefficient was set to zero.

### 3.10.3. Boundary condition

All degrees of freedom (three translations and three rotations), for one node in a central element of BP steps, was fixed, and the other nodes have the free condition.

### 3.10.4. Control of properties in structural elements

To control the property values in structural elements in the time step, we introduced a coefficient function (Figure 3-21), ${}^{t}\alpha_{\mathrm{ST}}^{k}$ in terms of the time step $(t)$ as

$$ {}^{t}\alpha_{\mathrm{ST}}^{1} = 1 - \frac{(t - t_f)}{(t_i - t_f)}, \quad {}^{t}\alpha_{\mathrm{ST}}^{2} = 1 - \frac{(t - t_f)^2}{(t_i - t_f)^2}, \quad \cdots \tag{3-145} $$

satisfying the initial and final conditions as

$$ {}^{t}\alpha_{\mathrm{ST}}^{k} = \begin{cases} 0 & (t = t_{\mathrm{i}}) \\ 1 & (t = t_{\mathrm{f}}) \end{cases} \tag{3-146} $$

where $k$ is the power of the polynomial term to control the degree of change in the property value, and the initial time step is one ($t_i = 1$). The condition of $k = 1$ was universal due to the linear variation of properties. The condition of $k = 2$ was sometimes appropriate to find a global solution by assigning final mechanical properties rapidly when electrostatic interactions are regarded.

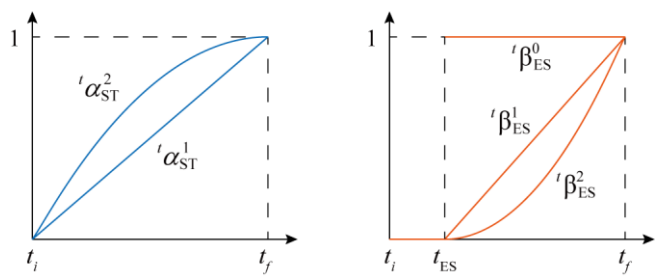


Figure 3-21. Coefficients functions.

Using this coefficient function, the property values were changed in time steps by the linear interpolation as

$$ \begin{aligned} {}^{t}\mathbf{G} &= {}^{i}\mathbf{G} + {}^{t}\alpha_{\mathrm{ST}}\left({}^{f}\mathbf{G} - {}^{i}\mathbf{G}\right) \\ {}^{t}\mathbf{R} &= {}^{i}\mathbf{R} + {}^{t}\alpha_{\mathrm{ST}}\left({}^{f}\mathbf{R} - {}^{i}\mathbf{R}\right) \\ {}^{t}\mathbf{C} &= {}^{i}\mathbf{C} + {}^{t}\alpha_{\mathrm{ST}}\left({}^{f}\mathbf{C} - {}^{i}\mathbf{C}\right) \end{aligned} \tag{3-147} $$

### 3.10.5. Control of the number of electrostatic elements

To create an electrostatic element applying repulsion force between inter-helical BPs, the distances between all nodes were measured every time step. The electrostatic elements were then generated for nodes between distances less than the cutoff distance ($r_{\text{cut}}$). However, generating all the possible electrostatic elements in every time step significantly increases the computational time, which makes the procedure inefficient. Hence, as the solution reaches mechanical equilibrium in advancing the time step, further consideration of the electrostatic interaction can be effective in finding the correct configuration while reducing the iteration time.

For this effective generation of electrostatic elements, $t_{\text{ES}}$ was introduced as the initiating time step of the electrostatic effect, which was excluded when the time step was smaller than $t_{\text{ES}}$ ($t_i \leq t_{\text{ES}} < t_f$).

Next, similar to the coefficient function for structural properties, another coefficient function, ${}^t\beta_{\text{ES}}^k$ for controlling the number of electrostatic elements was introduced (Figure 3-21) as follows.

$$ {}^t\beta_{\text{ES}}^0 = 1, \quad {}^t\beta_{\text{ES}}^1 = \frac{t - t_{\text{ES}}}{t_f - t_{\text{ES}}}, \quad {}^t\beta_{\text{ES}}^2 = \left( \frac{t - t_{\text{ES}}}{t_f - t_{\text{ES}}} \right)^2, \quad \cdots \tag{3-148} $$

$$ {}^t\beta_{\text{ES}}^k = \begin{cases} 0 & (t \leq t_{\text{ES}}) \\ 1 & (t = t_{\text{f}}) \end{cases} \tag{3-149} $$

where $k$ is the degree of the polynomial term and $k$ was generally set to two. A large $k$ decreases the number of electrostatic elements considered in the intermediate time step.

This coefficient function then provides the number of electrostatic elements to be generated at a time step as

$$ {}^tN_{\text{ES}} = {}^t\beta_{\text{ES}}^k \, {}^t\tilde{N}_{\text{ES}} \tag{3-150} $$

where ${}^tN_{\text{ES}}$ electrostatic elements were generated out of all possible ${}^t\tilde{N}_{\text{ES}}$ elements connecting two nodes within a cutoff radius at a specific time step ($t$).

### 3.10.6. Iterative solution methods

At a time step ($t$), the stiffness matrix ( ${}^{t}\mathbf{K}_{\mathrm{G}}$ ) and the internal force vector ( ${}^{t}\vec{F}_{\mathrm{G}}$ ) in the global coordinate were computed by assembling the structural ( ${}^{t}\mathbf{K}_{\mathrm{G}}^{\mathrm{ST}}$ , ${}^{t}\vec{F}_{\mathrm{G}}^{\mathrm{ST}}$ ) and electrostatic ( ${}^{t}\mathbf{K}_{\mathrm{G}}^{\mathrm{ES}}$ , ${}^{t}\vec{F}_{\mathrm{G}}^{\mathrm{ES}}$ ) elements ($e$).

$$\begin{aligned} {}^{t}\mathbf{K}_{\mathrm{G}} &= {}^{t}\mathbf{K}_{\mathrm{G}}\left({}^{t}\mathbf{K}_{\mathrm{G}}^{\mathrm{ST},e}, {}^{t}\mathbf{K}_{\mathrm{G}}^{\mathrm{ES},e}\right) \\ {}^{t}\vec{F}_{\mathrm{G}} &= {}^{t}\vec{F}_{\mathrm{G}}\left({}^{t}\vec{F}_{\mathrm{G}}^{\mathrm{ST},e}, {}^{t}\vec{F}_{\mathrm{G}}^{\mathrm{ES},e}\right) \end{aligned} \tag{3-151}$$

where each component was previously derived from the position, triads, and properties as follows.

$$\begin{aligned} {}^{t}\mathbf{K}_{\mathrm{G}}^{\mathrm{ST},e} &= {}^{t}\mathbf{K}_{\mathrm{G}}^{\mathrm{ST},e}\left({}^{t}\vec{p}_{N}^{\,e}, {}^{t}\mathbf{R}^{e}, {}^{t}\mathbf{T}_{N}^{e}, {}^{t}\vec{\mathrm{G}}^{e}, {}^{t}\vec{\mathrm{R}}^{e}, {}^{t}\vec{\mathrm{C}}^{e}\right) \\ {}^{t}\vec{F}_{\mathrm{G}}^{\mathrm{ST},e} &= {}^{t}\vec{F}_{\mathrm{G}}^{\mathrm{ST},e}\left({}^{t}\vec{p}_{N}^{\,e}, {}^{t}\mathbf{R}^{e}, {}^{t}\mathbf{T}_{N}^{e}, {}^{t}\vec{\mathrm{G}}^{e}, {}^{t}\vec{\mathrm{R}}^{e}, {}^{t}\vec{\mathrm{C}}^{e}\right) \\ {}^{t}\mathbf{K}_{\mathrm{G}}^{\mathrm{ES},e} &= {}^{t}\mathbf{K}_{\mathrm{G}}^{\mathrm{ES},e}\left({}^{t}\vec{p}_{N}^{\,e}, q, \lambda_{D}\right) \\ {}^{t}\vec{F}_{\mathrm{G}}^{\mathrm{ES},e} &= {}^{t}\vec{F}_{\mathrm{G}}^{\mathrm{ES},e}\left({}^{t}\vec{p}_{N}^{\,e}, q, \lambda_{D}\right) \end{aligned} \tag{3-152}$$

The solution process was performed to find a configuration that satisfies the updated properties from a time step ($t$) to the next step ($t+\Delta t$). The force equilibrium below was satisfied at the next time step ($t+\Delta t$).

$${}^{t+\Delta t}\vec{F}_{\mathrm{G}} = {}^{t+\Delta t}\vec{R} \tag{3-153}$$

which indicates that the internal force vector ( ${}^{t+\Delta t}\vec{F}$ ) by the strain energy is equal to the external force vector ( ${}^{t+\Delta t}\vec{R}$ ). The external force vector was introduced as a zero vector.

Due to the general difficulty determining the configuration analytically at the time step ($t+\Delta t$), we employed the iterative algorithm[72] of the Newton-Raphson method ($t \rightarrow t+\Delta t$). The Newton-Raphson procedure is summarized as below.

$$
\begin{aligned}
{}^{t+\Delta t}\mathbf{K}_{\mathrm{G}}^{(i-1)}\Delta\vec{U}^{(i)} &= {}^{t+\Delta t}\vec{R} - {}^{t+\Delta t}\vec{F}_{\mathrm{G}}^{(i-1)} \\
{}^{t+\Delta t}\vec{U}^{(i)} &= {}^{t+\Delta t}\vec{U}^{(i-1)} + \Delta\vec{U}^{(i)} \\
{}^{t+\Delta t}\vec{p}^{(i)} &= {}^{t}\vec{p} + {}^{t+\Delta t}\vec{U}^{(i)} \\
{}^{t+\Delta t}\mathbf{T}^{(i)} &= {}^{t+\Delta t}\mathbf{T}^{(i)}\left(\Delta\vec{U}^{(i)}, {}^{t+\Delta t}\mathbf{T}^{(i-1)}\right) \\
{}^{t+\Delta t}\mathbf{R}^{(i)} &= {}^{t+\Delta t}\mathbf{R}^{(i)}\left({}^{t+\Delta t}\vec{p}^{(i-1)}, {}^{t+\Delta t}\vec{p}^{(i)}, {}^{t+\Delta t}\mathbf{T}^{(i)}, {}^{t+\Delta t}\mathbf{R}^{(i-1)}\right) \\
{}^{t+\Delta t}\mathbf{K}_{\mathrm{G}}^{(i)} &= {}^{t+\Delta t}\mathbf{K}_{\mathrm{G}}^{(i)}\left({}^{t+\Delta t}\vec{p}^{(i)}, {}^{t+\Delta t}\mathbf{T}^{(i)}, {}^{t+\Delta t}\mathbf{R}^{(i)}\right) \\
{}^{t+\Delta t}\vec{F}_{\mathrm{G}}^{(i)} &= {}^{t+\Delta t}\vec{F}_{\mathrm{G}}^{(i)}\left({}^{t+\Delta t}\vec{p}^{(i)}, {}^{t+\Delta t}\mathbf{T}^{(i)}, {}^{t+\Delta t}\mathbf{R}^{(i)}\right)
\end{aligned}
\tag{3-154}
$$

with the initial conditions as

$$
{}^{t+\Delta t}\mathbf{K}_{\mathrm{G}}^{(0)} = {}^{t}\mathbf{K}_{\mathrm{G}}, \quad {}^{t+\Delta t}\vec{F}_{\mathrm{G}}^{(0)} = {}^{t}\vec{F}_{\mathrm{G}}, \quad {}^{t+\Delta t}\vec{U}^{(0)} = {}^{t}\vec{U} \tag{3-155}
$$

Here, ${}^{t+\Delta t}\mathbf{K}_{\mathrm{G}}^{(i)}$ and ${}^{t+\Delta t}\vec{F}_{\mathrm{G}}^{(i)}$ are updated from the results of the previous iteration as previously described. This iterative procedure ($i = 0,1,\cdots$) was performed until satisfying the convergence criteria[72] of finite element system given by

$$
\begin{aligned}
\frac{\left\|\Delta\vec{U}^{(i)}\right\|}{\left\|{}^{t+\Delta t}\vec{U}^{(i)}\right\|} &\le \varepsilon_D \\
\frac{\left\|{}^{t+\Delta t}\vec{R} - {}^{t+\Delta t}\vec{F}_{\mathrm{G}}^{(i)}\right\|}{\left\|{}^{t+\Delta t}\vec{R} - {}^{t}\vec{F}_{\mathrm{G}}\right\|} &\le \varepsilon_F \\
\frac{\Delta\vec{U}^{(i)}\cdot\left({}^{t+\Delta t}\vec{R} - {}^{t+\Delta t}\vec{F}_{\mathrm{G}}^{(i-1)}\right)}{\Delta\vec{U}^{(1)}\cdot\left({}^{t+\Delta t}\vec{R} - {}^{t}\vec{F}_{\mathrm{G}}\right)} &\le \varepsilon_E
\end{aligned}
\tag{3-156}
$$

where $\varepsilon_D$, $\varepsilon_F$, and $\varepsilon_E$ represent the tolerance values for displacement, force, and energy, respectively. we specified $1$, $10^{-3}$, and $10^{-6}$ for $\varepsilon_D$, $\varepsilon_F$, and $\varepsilon_E$, respectively, in that it was efficient to set two of three tolerance values.

### 3.10.7. Subdivision of time interval

In a fixed time interval ($\Delta t = 1$), the system at a time step ($t$) is updated to the next configuration ($t + \Delta t$). However, the previous iterative process ($t \rightarrow t + \Delta t$) could not find a converged solution at once, but find an updated configuration for a smaller time interval ($\Delta t < 1$). This indicates a need that the degree of change in properties should be controlled depending on the time step. It could be a simple way to set the larger total time steps and reduce the time interval. But this may require unnecessary iteration to find a trivial solution in the next time step.

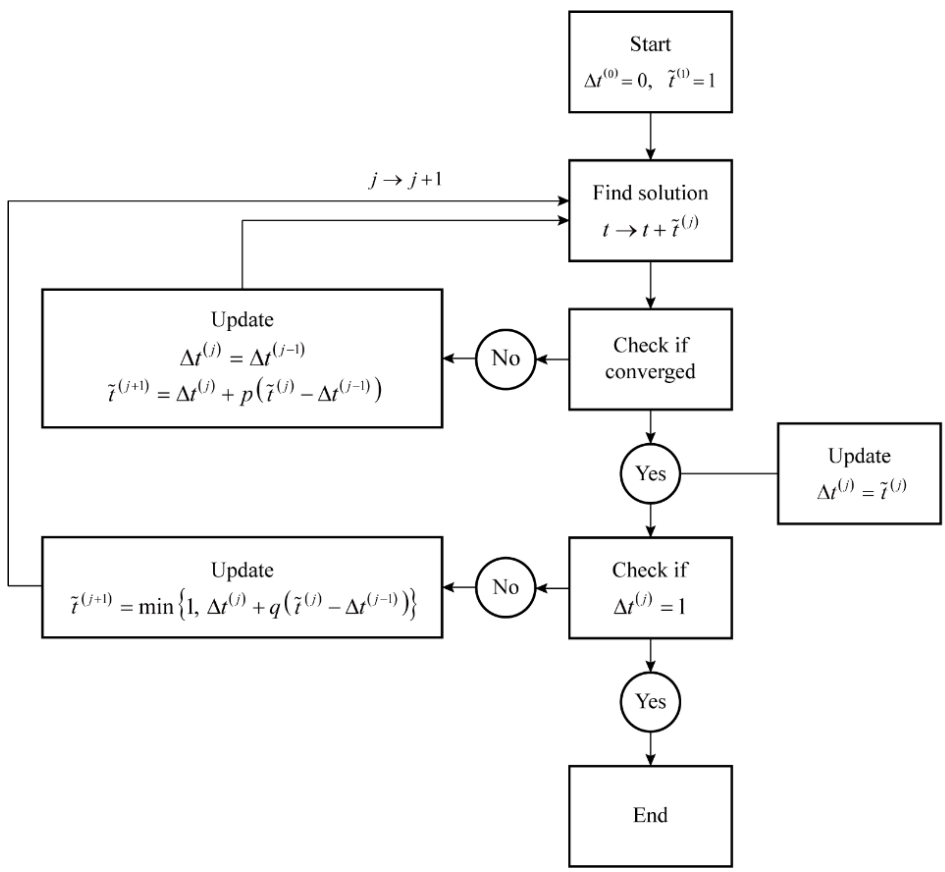


Figure 3-22. Flow chart of the control of the time interval in a time step.

Alternatively, in this work, the time interval was automatically subdivided in the range of $0 < \Delta t \leq 1$ (Figure 3-22). To subdivide the time interval, another iteration ($j$) was introduced, and the trial time interval was denoted as $\tilde{t}^{(j)}$ with a range of $0 < \tilde{t}^{(j)} \leq 1$, providing the converged time interval as $\Delta t^{(j)}$. This iteration was conducted until reaching the next configuration ($\Delta t^{(j)} = 1$) as following the flow chart. $p$ and $q$ indicate the decreasing and increasing factors of the time interval, and the values were used as $p = 0.75$ and $q = 1.25$.

### 3.10.8. Condition number of stiffness matrix

In order to investigate whether the stiffness matrix is ill-conditioned by the computation errors and how accurate the solution is, the condition number of the stiffness matrix is calculated[72] by

$$\mathrm{cond}(\mathbf{K}_{\mathrm{G}}) = \frac{\lambda_{\max}}{\lambda_{\min}} \tag{3-157}$$

where the $\lambda_{\max}$ and $\lambda_{\min}$ represent the largest and smallest eigenvalues, respectively, obtained by normal mode analysis. A large condition number indicates that the solution could be inaccurate by the truncation and round-off errors. In the predicted DNA nanostructures, the condition number of the stiffness matrices was approximately $10^9$.

Using the condition number, the precision digit in the solution ($s_p$) can be estimated[72] as

$$s_p \geq t_p - \log_{10}\left[\mathrm{cond}(\mathbf{K}_{\mathrm{G}})\right] \tag{3-158}$$

where $t_p$ represents the precision digit in computation as $t_p = 16$ in double-precision computer. This indicates that the precision in the solution is at least 7 digits.

## 3.11. Molecular dynamics simulation of DNA nanostructures

We first considered the combination of sequences in the structural motifs. One of the BP and CO steps were sequence-dependently represented by M, N, P, and Q, which denote one of the elementary sequences as adenine (A), guanine (G), thymine (T), and cytosine (C), respectively. The regular BP steps were expressed as MN/PQ, where the MN represents the successive bases from 5 ' to 3' direction, and PQ indicates the remaining complementary bases in the 5 ' to 3' direction. That is, the pairs of M:Q and N:P are complementary bases. In detail, there exist ten kinds of unique regular BP steps: AA/TT, AG/CT, GA/TC, GG/CC, AC/GT, AT/AT, GC/GC, TG/CA, TA/TA, and CG/CG steps. Next, the nicked BP steps were represented as MN/PnQ or MnN/PQ, where a nick existing between bases was indicated by ‘n’, and there exist sixteen nicked BP steps: AA/TnT, AG/CnT, GA/TnC, GG/CnC, AnA/TT, AnG/CT, GnA/TC, GnG/CC, AC/GnT, AnC/GT, AT/AnT, GC/GnC, TG/CnA, TnG/CA, TA/TnA, and CG/CnG. The representation of sixteen CO-nick BP steps was denoted as MN-PnQ or MnN-PQ, similar to the nicked BP steps: AA-TnT, AG-CnT, GA-TnC, GG-CnC, AnA-TT, AnG-CT, GnA-TC, GnG-CC, AC-GnT, AnC-GT, AT-AnT, GC-GnC, TG-CnA, TnG-CA, TA-TnA, and CG-CnG. Here, 'n' indicates the disconnection of MN or PQ bases by strands leaving out to connect the helix in the CO site. Likewise, the double CO steps were denoted as MN||PQ (16 kinds): AA||TnT, AG||CT, GA||TC, GG||CC, AA||TT, AG||CT, GA||TC, GG||CC, AC||GT, AC||GT, AT||AT, GC||GC, TG||CA, TG||CA, TA||TA, and CG||CG. The single CO steps were similarly represented as MN|PQ (16 kinds): AA|TnT, AG|CT, GA|TC, GG|CC, AA|TT, AG|CT, GA|TC, GG|CC, AC|GT, AC|GT, AT|AT, GC|GC, TG|CA, TG|CA, TA|TA, and CG|CG. In CO steps, the backbone was connected from M to N between helices.

Secondly, to characterize the intrinsic properties of the structural motifs, we performed MD simulation of DNA nanostructures containing all the structural motifs considering the sequence combinations. For the regular and nicked BP steps, we employed the previously reported results of intrinsic properties[18] measured in the

3DNA definitions and converted them to values suitable to the beam coordinates (Table 3-1 and Table 3-2). To quantify the properties of the remaining structural motifs related to CO (CO-nick BP step, double CO step, and single CO step), the MD trajectories of the previous[67,76] and additional structures were used. The caDNAno[74] designs of the simulated structures were provided in Figure 3-23. We carefully selected the types and numbers of structural motifs in each simulated structure, listed in Table 3-6. The MD trajectories of the structural motifs were analyzed every 100 ns in equilibrium to obtain their intrinsic properties. At this time, there may be a CO step, in which the base-pairing is broken and it could be difficult to apply the quasi-harmonic assumption. Therefore, in collecting properties, an CO step, of which axial translation is less than 1.7 nm or greater than 2.1 nm, was excluded in consideration of its mean length (approximate 1.9 nm).

Following general protocol, MD simulation for each structure was performed using the NAMD[29] with the CHARMM36 force-field for nucleic acids[30], the TIP3P[35] model of water, ion concentration of 20 mM $MgCl_2$ in the cubic cell of a periodic boundary with a padding distance of more than 15 Å. The simulations employed the time step of 2 fs and short-range electrostatic potentials with 12 Å cut-off. The long-range electrostatic interactions were computed using the Particle-Mesh-Ewald method[36] with a grid spacing of 1 Å. The potential energy was minimized more than 10000 steps. After thermalization of more than 10 ns, the production run was performed under the isobaric-isothermal (NPT) ensemble, where the pressure and temperature were maintained at 1 bar and 300 K using the Nosé-Hoover Langevin piston scheme[37] and Langevin thermostat[29]. The trajectories were collected for at least 100 ns in final equilibrium states of structures. The information and RMSD trajectory of simulated structures were provided in Figure 3-24 and Table 3-7.


Figure 3-23. MD-simulated designs. The connectivity and sequences were carefully selected in the caDNAno designs.

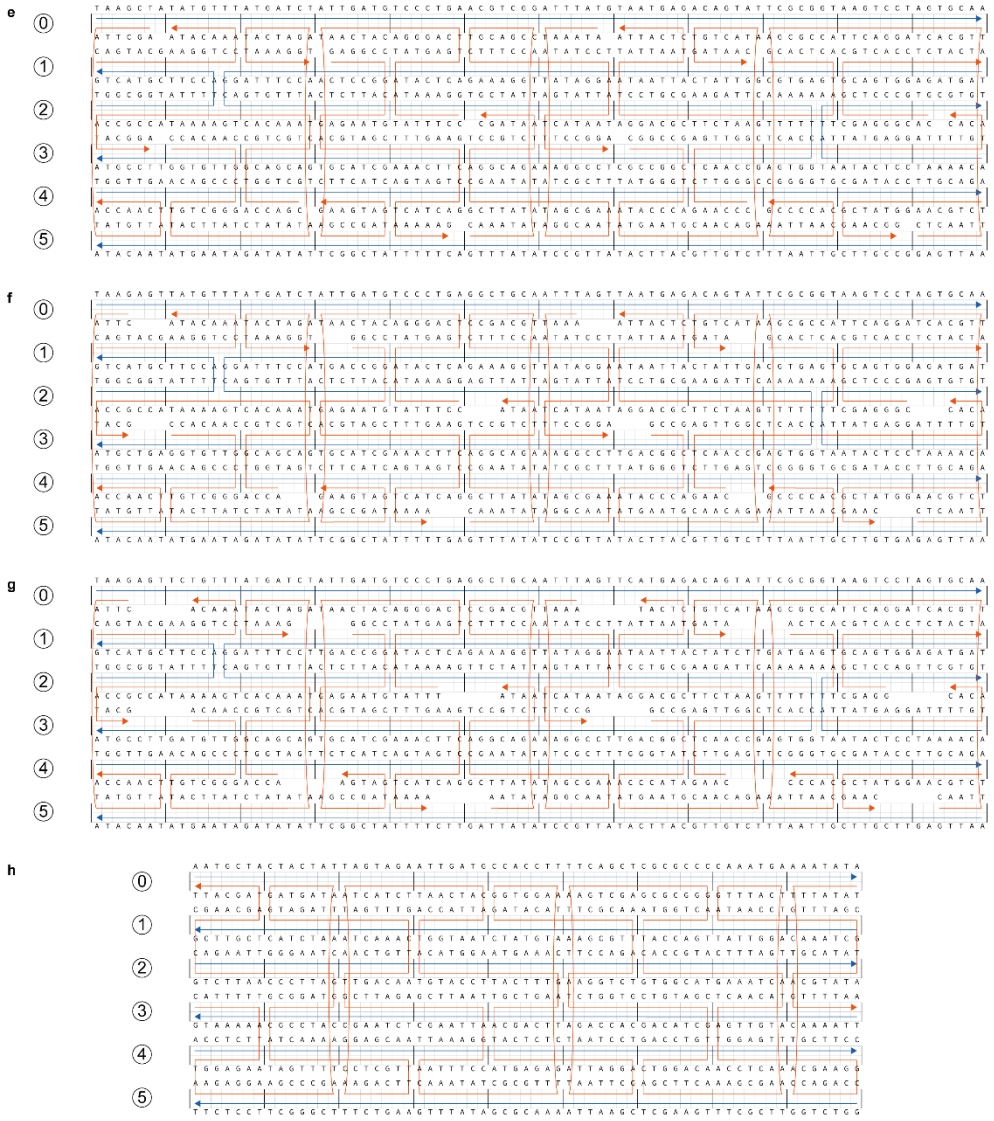

Figure 3-23 (Continued).


Figure 3-23 (Continued).

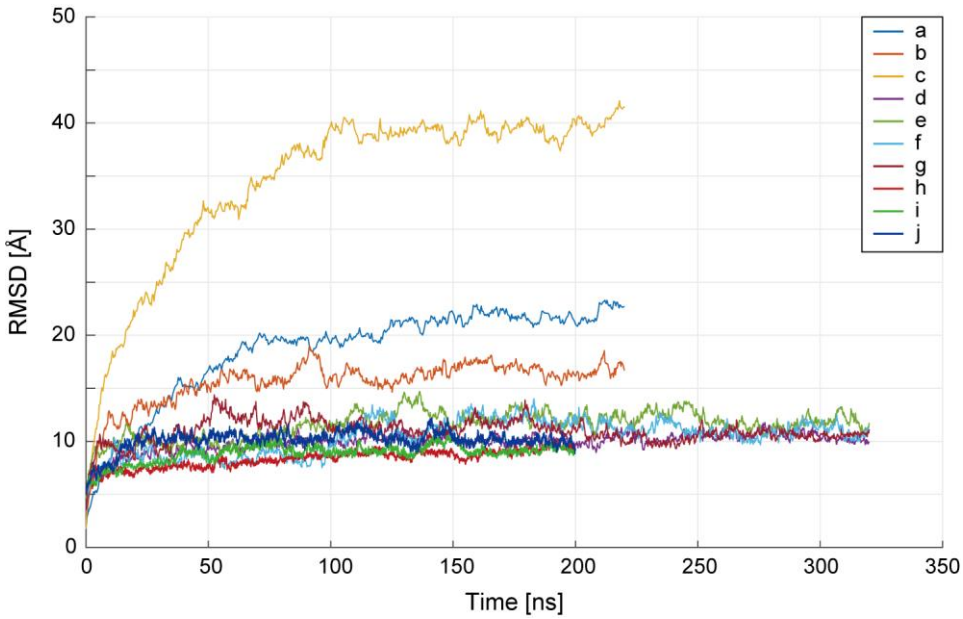


Figure 3-24. Root-mean-square-deviation (RMSD) of MD-simulated structures. RMSD values of a structure were calculated from its minimized structure. Each design (**a-j**) corresponds to the simulated structures (Figure 3-23).

Table 3-6. The number of structural motifs in the MD-simulated structures. Each design (**a-j**) corresponds to the simulated structures (Figure 3-23).

| CO-nick steps | **a** | **b** | **c** | **d** | **e** | **f** | **g** | **h** | **i** | **j** |
|---|---|---|---|---|---|---|---|---|---|---|
| **AA/TnT** | 0 | 0 | 0 | 5 | 4 | 4 | 5 | 3 | 5 | 5 |
| **AnA/TT** | 6 | 8 | 0 | 5 | 5 | 5 | 5 | 7 | 3 | 3 |
| **AG/CnT** | 3 | 3 | 17 | 4 | 3 | 4 | 4 | 1 | 1 | 0 |
| **AnG/CT** | 5 | 4 | 17 | 2 | 1 | 1 | 1 | 3 | 5 | 5 |
| **GA/TnC** | 0 | 1 | 0 | 3 | 4 | 3 | 3 | 1 | 0 | 1 |
| **GnA/TC** | 1 | 6 | 0 | 1 | 3 | 3 | 3 | 2 | 2 | 3 |
| **GG/CnC** | 1 | 0 | 0 | 1 | 1 | 1 | 1 | 0 | 1 | 1 |
| **GnG/CC** | 3 | 3 | 0 | 1 | 1 | 1 | 1 | 2 | 3 | 2 |
| **AC/GnT** | 2 | 4 | 0 | 2 | 2 | 2 | 2 | 2 | 1 | 3 |
| **AnC/GT** | 1 | 1 | 0 | 1 | 1 | 1 | 1 | 2 | 0 | 2 |
| **AT/AnT** | 1 | 1 | 0 | 2 | 2 | 2 | 2 | 2 | 1 | 1 |
| **GC/GnC** | 3 | 1 | 0 | 1 | 1 | 1 | 1 | 1 | 0 | 0 |
| **TG/CnA** | 2 | 0 | 0 | 1 | 1 | 1 | 1 | 1 | 0 | 2 |
| **TnG/CA** | 1 | 0 | 0 | 4 | 4 | 4 | 4 | 3 | 2 | 0 |
| **TA/TnA** | 1 | 0 | 0 | 6 | 6 | 6 | 6 | 2 | 4 | 3 |
| **CG/CnG** | 0 | 0 | 0 | 1 | 1 | 1 | 1 | 0 | 4 | 1 |

Table 3-6 (Continued).

| Double CO steps | **a** | **b** | **c** | **d** | **e** | **f** | **g** | **h** | **i** | **j** |
|---|---|---|---|---|---|---|---|---|---|---|
| **AA\|\|TT** | 0 | 0 | 0 | 4 | 4 | 4 | 4 | 2 | 4 | 5 |
| **TT\|\|AA** | 0 | 0 | 0 | 8 | 6 | 7 | 7 | 1 | 2 | 3 |
| **AG\|\|CT** | 0 | 0 | 0 | 1 | 1 | 1 | 1 | 3 | 2 | 2 |
| **CT\|\|AG** | 0 | 0 | 0 | 1 | 2 | 1 | 1 | 1 | 2 | 0 |
| **GA\|\|TC** | 0 | 4 | 0 | 3 | 3 | 3 | 3 | 4 | 1 | 3 |
| **TC\|\|GA** | 0 | 0 | 0 | 2 | 2 | 1 | 1 | 2 | 0 | 0 |
| **GG\|\|CC** | 0 | 0 | 0 | 2 | 2 | 2 | 2 | 3 | 3 | 1 |
| **CC\|\|GG** | 0 | 0 | 0 | 3 | 2 | 3 | 3 | 0 | 0 | 0 |
| **AC\|\|GT** | 0 | 0 | 0 | 1 | 1 | 1 | 1 | 2 | 0 | 1 |
| **GT\|\|AC** | 0 | 4 | 0 | 1 | 1 | 1 | 1 | 0 | 1 | 2 |
| **AT\|\|AT** | 0 | 0 | 0 | 3 | 3 | 3 | 3 | 7 | 2 | 3 |
| **GC\|\|GC** | 0 | 0 | 0 | 0 | 1 | 1 | 1 | 0 | 1 | 2 |
| **TG\|\|CA** | 0 | 0 | 0 | 2 | 2 | 2 | 2 | 2 | 6 | 3 |
| **CA\|\|TG** | 0 | 0 | 0 | 1 | 1 | 1 | 1 | 1 | 1 | 1 |
| **TA\|\|TA** | 0 | 0 | 0 | 6 | 7 | 7 | 7 | 4 | 4 | 3 |
| **CG\|\|CG** | 0 | 0 | 0 | 2 | 2 | 2 | 2 | 0 | 3 | 3 |

Table 3-6 (Continued).

| Single CO steps | **a** | **b** | **c** | **d** | **e** | **f** | **g** | **h** | **i** | **j** |
|---|---|---|---|---|---|---|---|---|---|---|
| **AA\|TT** | 1 | 1 | 0 | 0 | 0 | 0 | 0 | 0 | 1 | 1 |
| **TT\|AA** | 1 | 0 | 0 | 1 | 1 | 1 | 1 | 0 | 0 | 0 |
| **AG\|CT** | 2 | 5 | 0 | 0 | 0 | 0 | 0 | 0 | 0 | 0 |
| **CT\|AG** | 1 | 1 | 0 | 0 | 0 | 0 | 0 | 0 | 0 | 0 |
| **GA\|TC** | 1 | 2 | 0 | 0 | 0 | 0 | 0 | 0 | 0 | 0 |
| **TC\|GA** | 1 | 0 | 0 | 0 | 0 | 0 | 0 | 0 | 0 | 0 |
| **GG\|CC** | 2 | 1 | 0 | 0 | 0 | 0 | 0 | 0 | 0 | 0 |
| **CC\|GG** | 2 | 0 | 0 | 0 | 0 | 0 | 0 | 0 | 0 | 0 |
| **AC\|GT** | 1 | 1 | 20 | 0 | 0 | 0 | 0 | 0 | 0 | 0 |
| **GT\|AC** | 1 | 0 | 0 | 0 | 0 | 0 | 0 | 0 | 0 | 0 |
| **AT\|AT** | 1 | 3 | 0 | 2 | 2 | 2 | 2 | 0 | 1 | 0 |
| **GC\|GC** | 1 | 1 | 0 | 0 | 0 | 0 | 0 | 1 | 0 | 0 |
| **TG\|CA** | 1 | 0 | 0 | 0 | 0 | 0 | 0 | 0 | 1 | 1 |
| **CA\|TG** | 0 | 1 | 0 | 0 | 0 | 0 | 0 | 1 | 1 | 1 |
| **TA\|TA** | 0 | 0 | 0 | 1 | 1 | 1 | 1 | 1 | 0 | 1 |
| **CG\|CG** | 1 | 0 | 0 | 0 | 0 | 0 | 0 | 1 | 0 | 0 |

Table 3-7. Information of the MD-simulated structures. Each design (a-j) corresponds to the simulated structures (Figure 3-23).

| Design | Total time [ns] | Sampled time [ns] | Frame | Box size [Å$^3$] | Atom number |
|---|---|---|---|---|---|
| **a** | 120 | 100 | 50000 | 235.0×118.2×137.7 | 379958 |
| **b** | 120 | 100 | 50000 | 240.5×111.4×97.1 | 258613 |
| **c** | 220 | 200 | 100000 | 311.3×80.2×163.0 | 403476 |
| **d** | 320 | 200 | 100000 | 304.8×92.8×87.1 | 247330 |
| **e** | 320 | 200 | 100000 | 305.0×93.0×87.3 | 247248 |
| **f** | 320 | 200 | 100000 | 305.4×93.1×87.3 | 247557 |
| **g** | 320 | 200 | 100000 | 305.4×93.1×87.4 | 247889 |
| **h** | 200 | 100 | 50000 | 238.0×106.1×114.6 | 266283 |
| **i** | 200 | 100 | 50000 | 244.8×111.2×111.6 | 279715 |
| **j** | 200 | 100 | 50000 | 246.9×108.5×117.3 | 289858 |

# 4. Structural analysis of DNA nanostructures

## 4.1. Abstract

We presented and discussed the results of the structural analysis using the proposed multiscale approach. The structural features of the comprehensive DNA nanostructures were predicted through the proposed model. First, we investigated the electrostatic effects on the lattice-based structures and the structural flexibility controlled by the crossover spacing. Secondly, the single-stranded DNA model was verified using the polymorphic structures. Also, we investigated that the mean helicity of DNA affects the structural shape. In addition, the DNA nanostructures through the design principle of base-pair insertion or deletion, of base-pairs were predicted. Furthermore, the controlled designs through the insertion and removal of the base-pairs in the structure were predicted. Finally, structural details such as translational or rotational parameters between base-pairs inside the structure were captured as well. It was confirmed that the results of all tested designs showed a quantitative agreement with the ones through experiments and atomic simulations.

## 4.2. Shape prediction of monomeric structures

### 4.2.1. Electrostatic effects on the structural shape

To verify the proposed multiscale model, we analyzed a comprehensive set of DNA origami nanostructures in the literature from straight to highly curved or twisted structures designed on a honeycomb or square lattice. First of all, the effect of electrostatic repulsion on the shape could be captured effectively with our model based on the Debye-Hückel theory. Results for 32-helix-bundle (32HB) structures[17] where the CO spacing was systematically increased from 21 to 42, 63, and 84 BPs along the helical axis confirmed the loss of structural integrity with the reduction of CO density (Figure 4-1 and Figure 4-2). Since the helices between COs became more flexible as the CO spacing got increased, they were less aligned in the honeycomb lattice and the cross-section got wider and taller. Analysis of a 64HB structure designed on a square lattice[77] showed a similar result in that more noticeable undulation of helices could be observed on the lattice plane where some COs were intentionally omitted in the design (Figure 4-3).

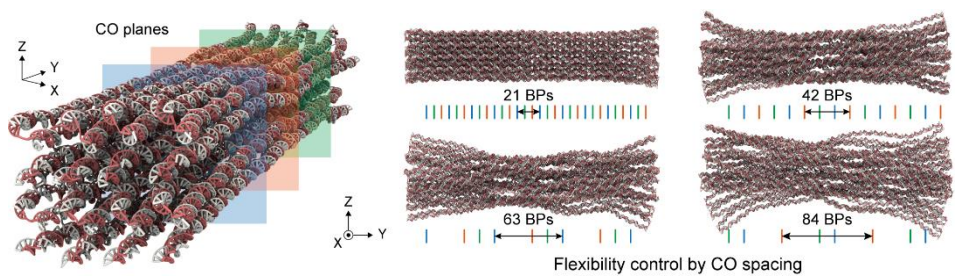


Figure 4-1. Flexibility control by CO spacing. The structural flexibility was controlled for the 32HB structures, where the CO spacing was systematically regulated from 21 to 42, 63, and 84 BPs along the helical axis. Since the helices between COs became more flexible as the CO spacing got increased, they were less aligned in the honeycomb lattice and the cross-section got wider and taller.

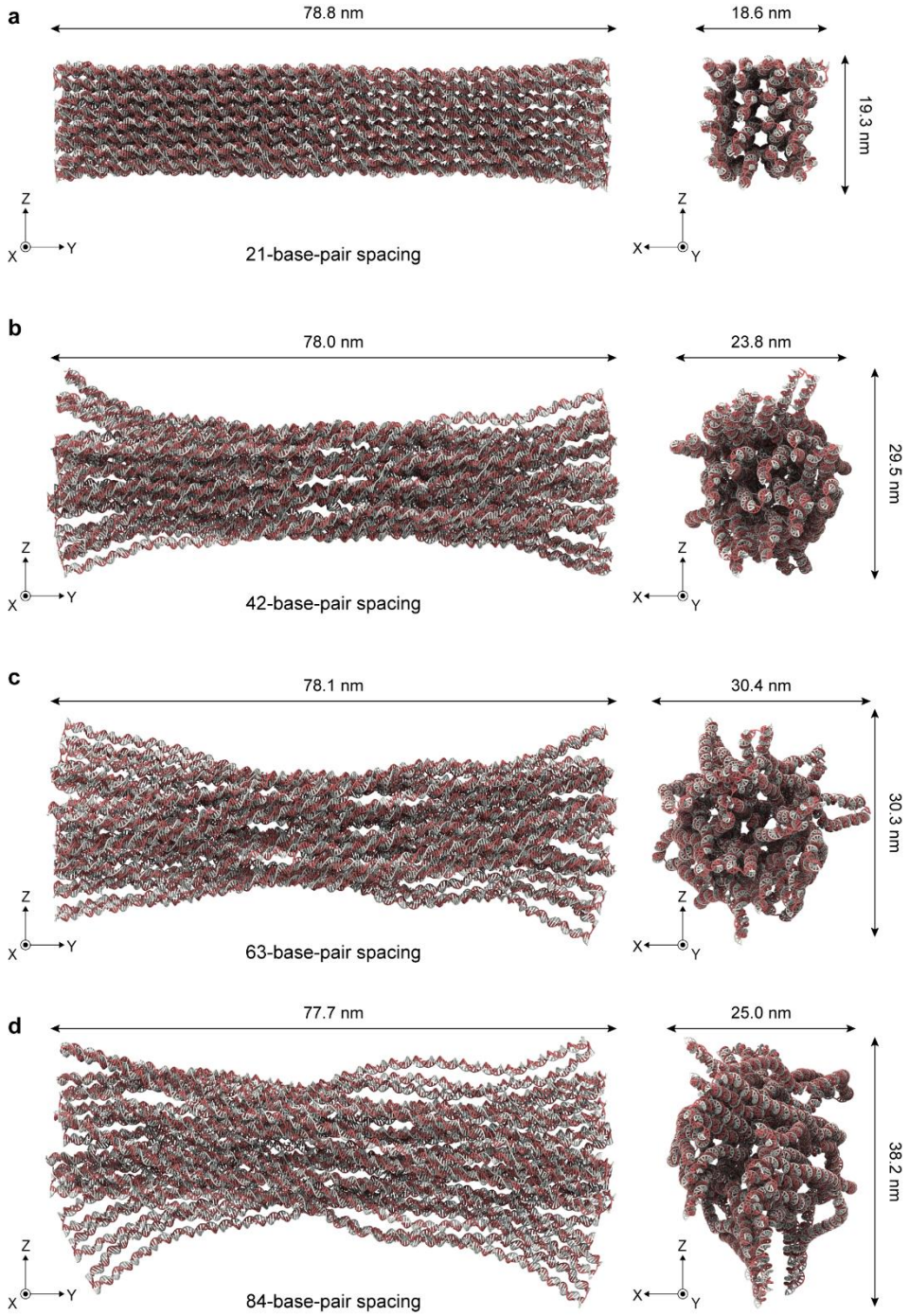


Figure 4-2. 32-helix-bundle (32HB) structures on the honeycomb lattice (HC). The CO plane was located in the interval of 21 (**a**), 42 (**b**), 63 (**c**), and 84 BPs (**d**) as previously reported.

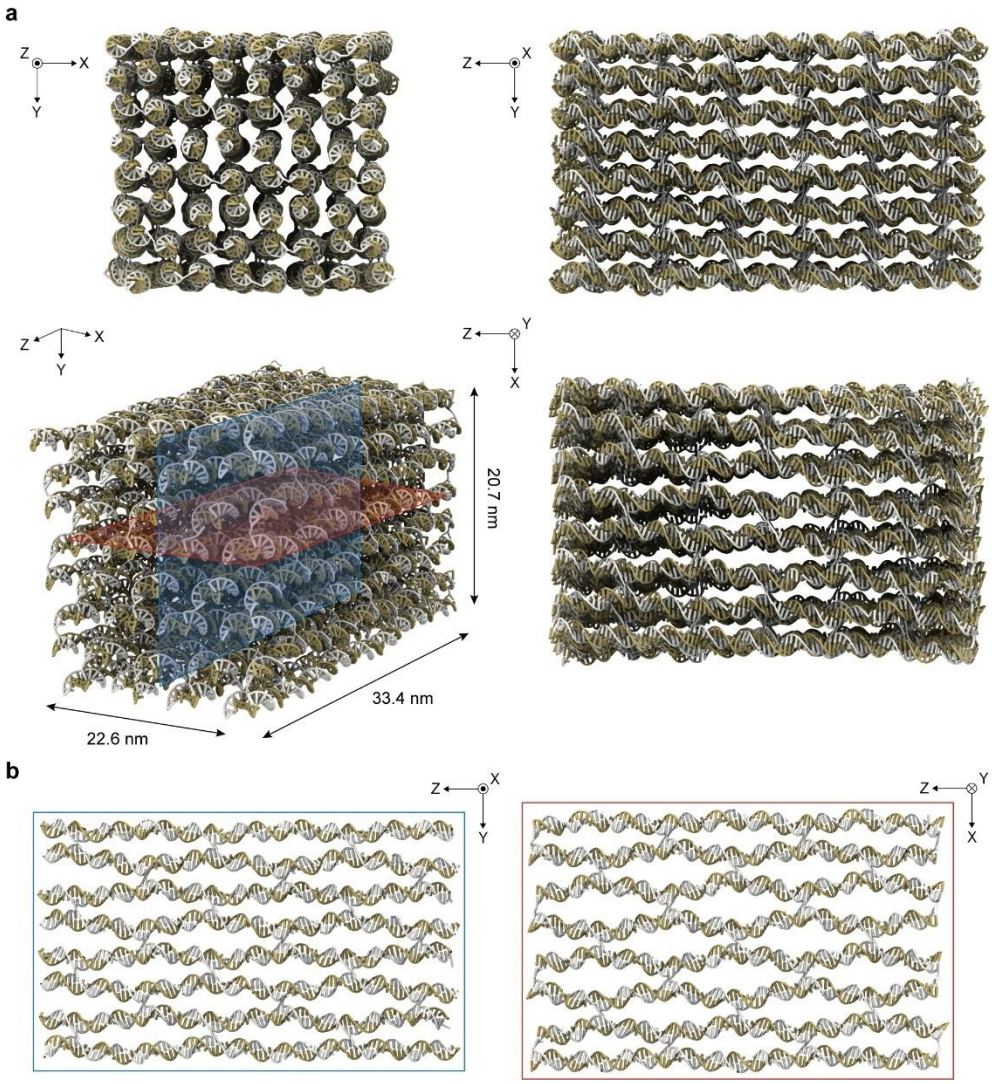


Figure 4-3. 64-helix-bundle (64HB) structure on the square lattice (SQ). **(a)** The configuration of the predicted structure in different orientations in the previous design. (**b**) Investigation on two orthogonal lattice planes. The crossovers, parallel to the y-z plane (blue), were constructed, whereas orthogonal ones (red) were intentionally omitted. Different planar shapes were observed by inter-helical repulsion, suggesting that the inter-helical distance in structure could be adjusted by controlling the arrangement of crossovers.

### 4.2.2. Control of included angle in hinge structures

The modified model for ssDNA was tested by analyzing the polymorphic 12HB structures[10] whose included angle was controlled by the stiffness of the hinge module at the center and the variable-length adjuster module at the terminals (Figure 4-4). The hinge module consists of both single and double strands and hence its stiffness is governed by the bending stiffness of the duplex and the entropic tensional force of ssDNA. The predicted included angles agreed well with the experimentally measured ones ranging from 15° to 150° at the interval of 15° (Figure 4-5). Note that the included angles larger than 120° could not be predicted accurately using either the wormlike-chain model or the modified freely-jointed-chain model in our previous work[10]. The structural polymorphism by varying the location and number of hinges and the length of the adjuster were reproduced as well[10] (Figure 4-6).

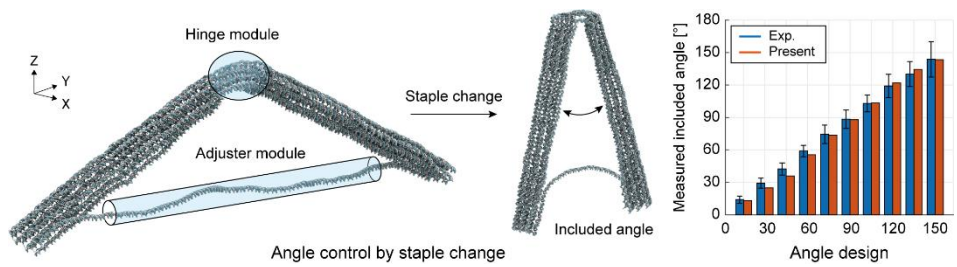


Figure 4-4. Angle control by staple change. For the 12HB structures, included angles were controlled by the hinge and adjuster via staple change.

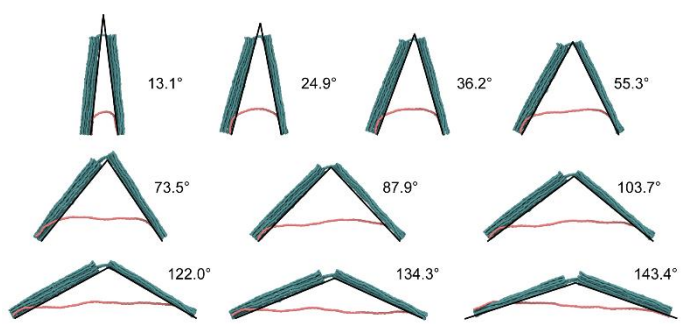


Figure 4-5. Angle estimation of the polymorphic design. Green frame and red helix represent the structural frame and the adjusting helix, respectively.

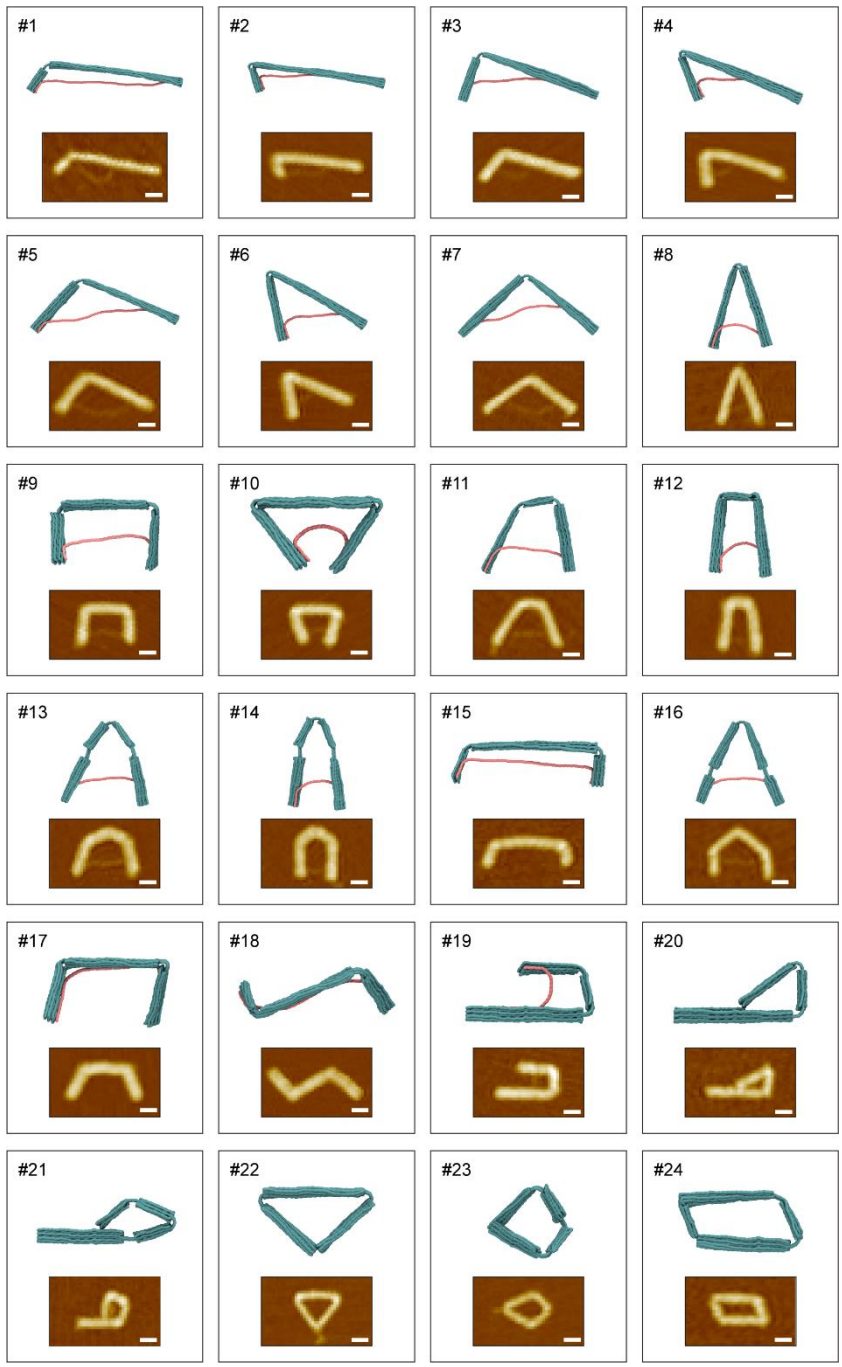


Figure 4-6. Polymorphic shape prediction through multiple-hinge designs. Green and red parts represent the structural frame and adjuster, respectively. AFM images were reproduced from the previous study. Scale bars: 30 nm.

### 4.2.3. Structural distortion by the mean helicity

Typically, DNA origami nanostructures were designed assuming that the mean helicity of B-form DNA was 10.5 BP per turn. However, it has become more and more evident from recent studies[11,78] that the helicity is rather closer to 10.44 BP per turn, which is also supported by our MD simulation results revealing the twist angle of regular BP steps is 10.43 BP per turn on average. To investigate, we analyzed the multilayer structures designed on a honeycomb lattice expected to be folded into straight blocks (Figure 4-7). Results showed that the thinnest 2-layer block might not be straight in solution as it's too flexible to withstand the internal stresses due to the discrepancy of the assumed helicity (10.5 BP per turn) in the design from the one (10.43 BP per turn) used in our analysis. Nevertheless, this non-straight, twisted configuration became almost unnoticeable in thicker blocks due to their higher torsional stiffness (Figure 4-7 and Figure 4-8), which was why it was often not problematic to design a structure assuming the helicity of 10.5 BP per turn. Similar deformations could be captured for the multilayer blocks designed on a square lattice as well (Figure 4-9).

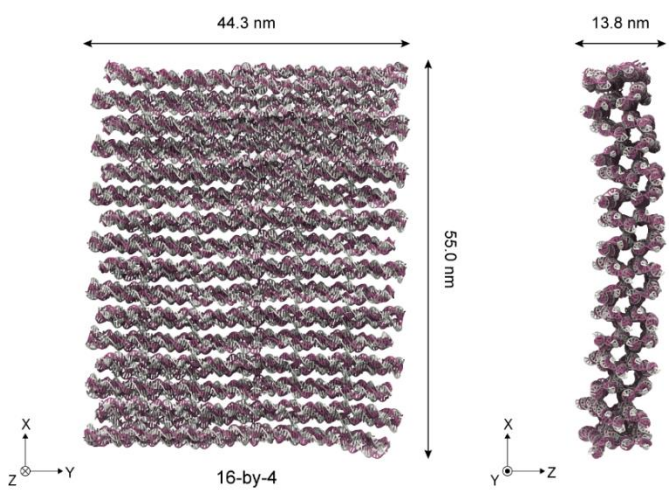


Figure 4-7. DNA origami blocks on the honeycomb lattice. The structures of the various cross-sections were predicted using the honeycomb latticed designs.

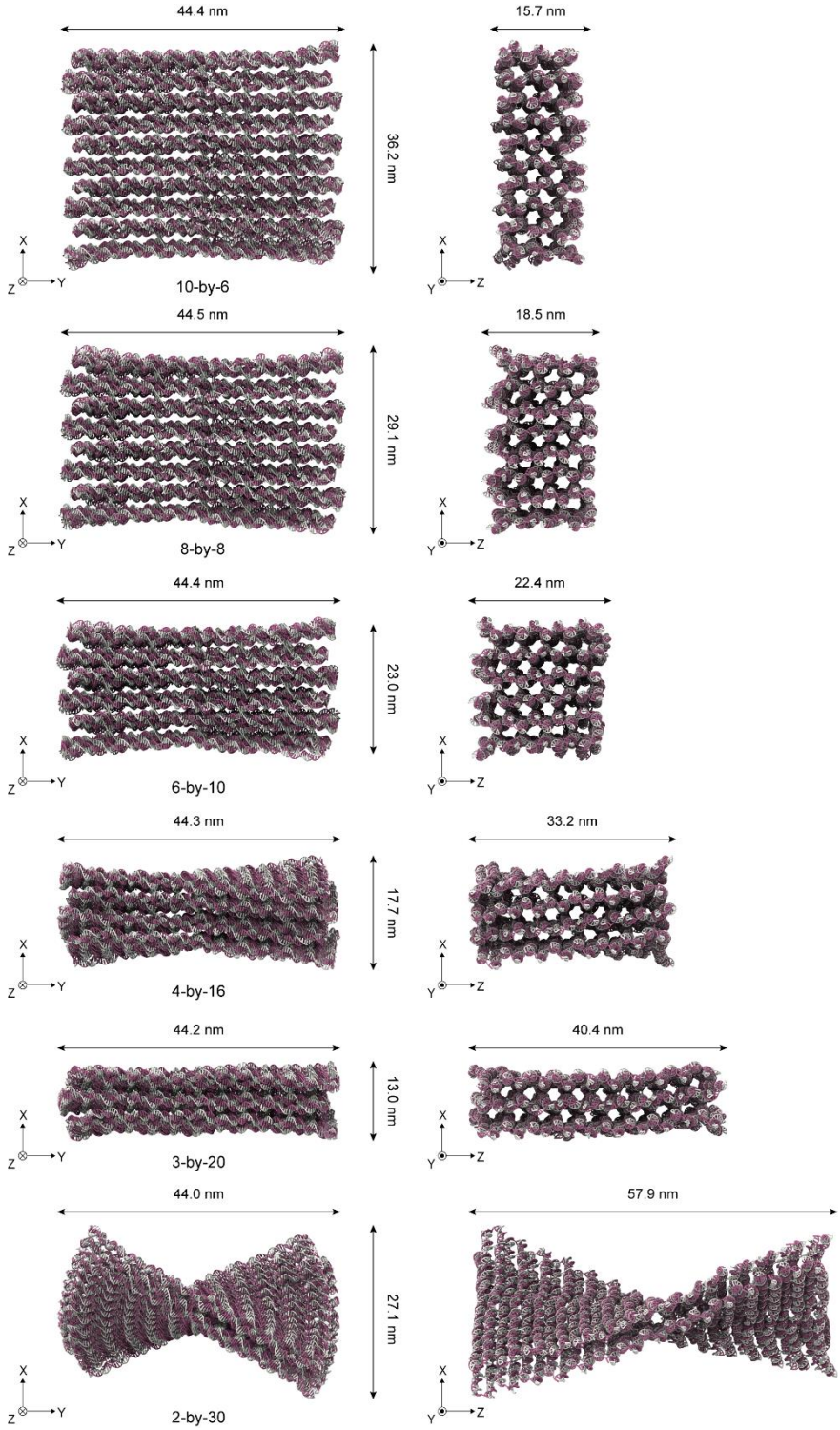


Figure 4-7 (Continued).

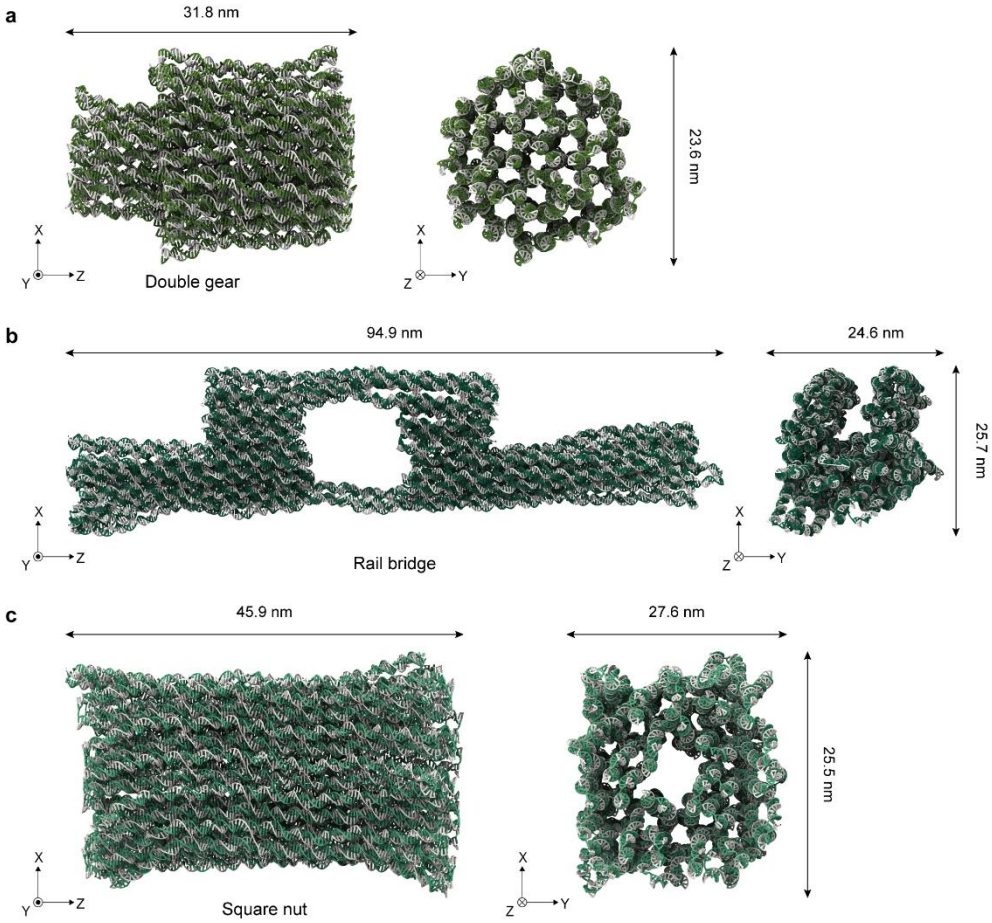


Figure 4-8. Three-dimensional DNA origami structures. As in the previous results, three-dimensional shapes were predicted for (**a**) the double gear, (**b**) rail bridge, and (**c**) square nut structures.

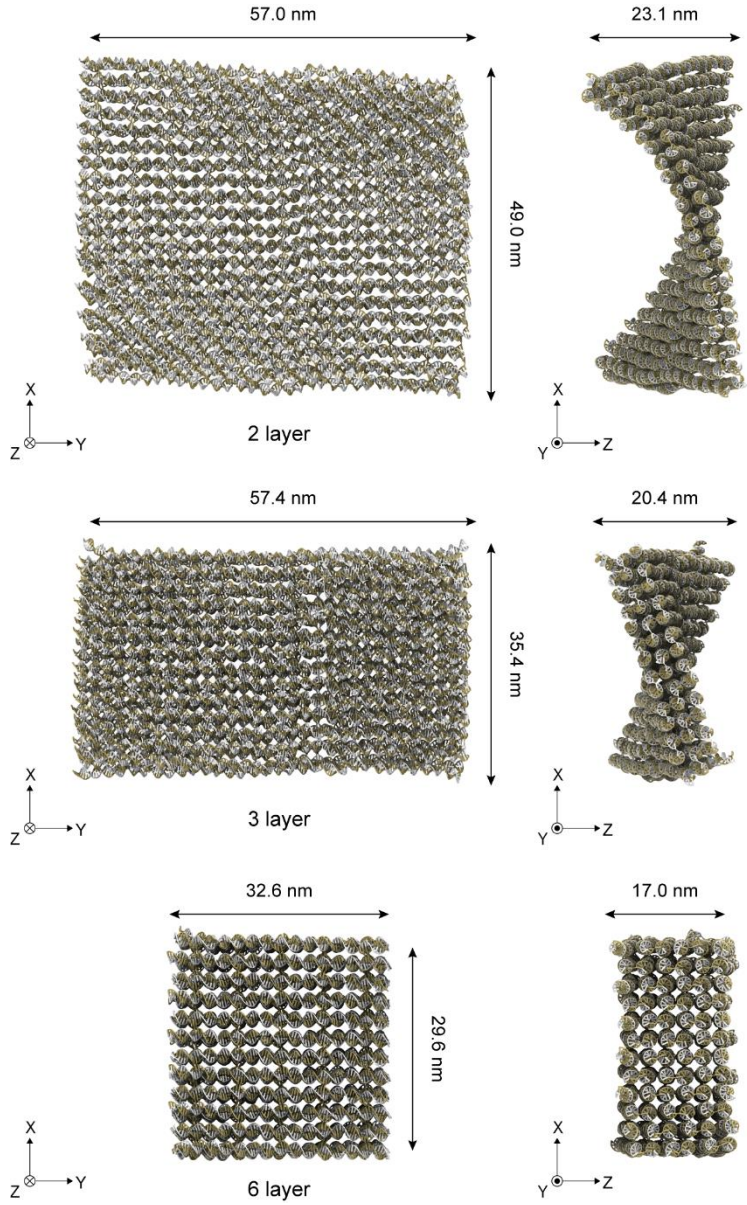


Figure 4-9. DNA origami blocks on the square lattice. Structures with 2, 3, and 6 layers on the square lattice were predicted as previously reported. The structure with eight layers was provided in Figure 4-3.

### 4.2.4. Bending and twist control by inserting or deleting base-pairs

Various curved or twisted structures designed with BP insertions and/or deletions[7] were then examined. For example, the radius of curvature, the twist angle, and the helical pitch were quantified for the quarter and half circles[79] (Figure 4-10 and Figure 4-11), twisted monolith blocks (Figure 4-12 and Figure 4-13), and spring-like structures (Figure 4-14), respectively, which were consistent with the experimental measurement within the standard deviation. Bent shapes of other designs including the protractor, gear, spiral, and S structures were successfully predicted as well (Figure 4-15, Figure 4-16, and Figure 4-17). Unintended out-of-plane bending was captured with the current model in S design as predicted also by other models[14,17] and in spiral design inferred from diverse non-spiral configurations in the micrographs.

The proposed multiscale model was also able to capture the effect of nicked BP steps on the shape effectively. A sharp corner at the vertex of A-like structure was seen in the predicted shape (Figure 4-18) as reported previously[17]. Note that the bending stiffness of a nicked BP step at the vertex was arbitrarily reduced in the previous model to obtain the sharp corner.

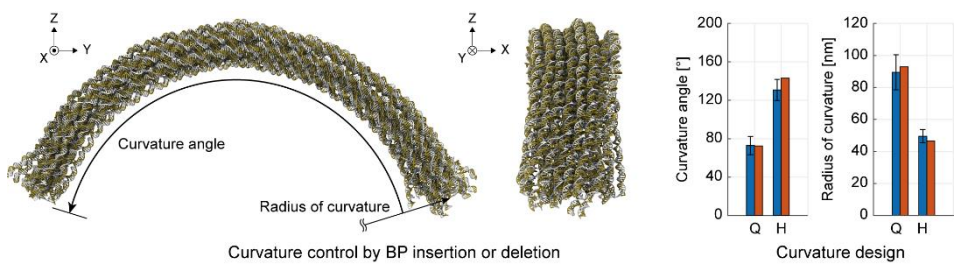


Figure 4-10. Curvature control by BP insertion or deletion. The radius of curvature and the curvature angle were quantified for the quarter (Q) and half (H) circle designs by BP insertion or deletion.

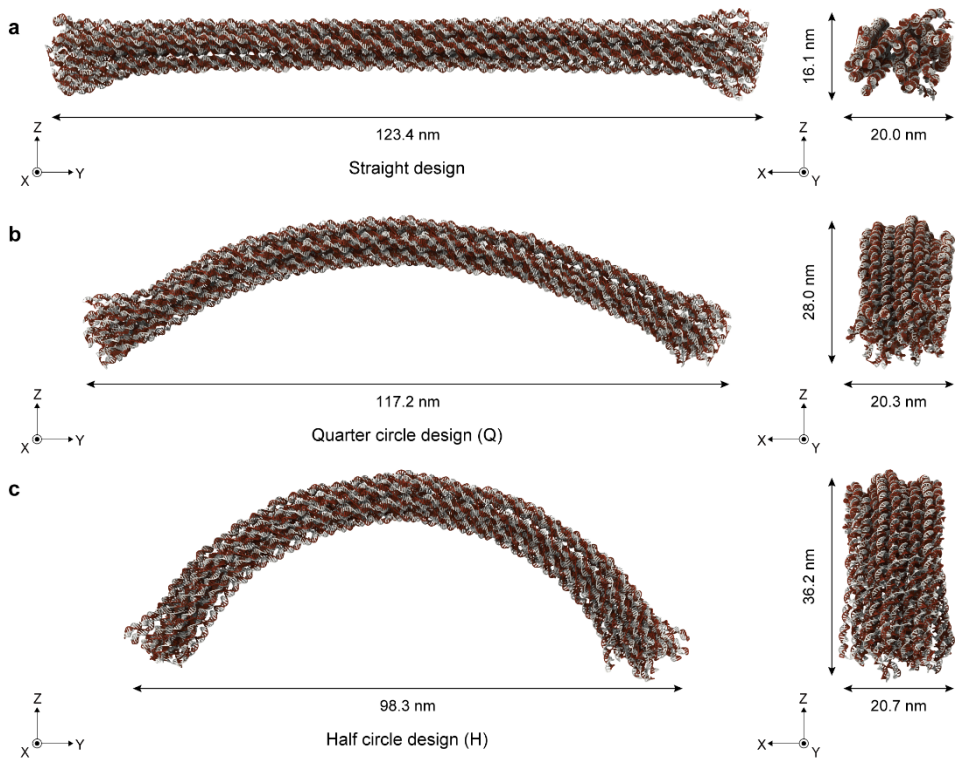


Figure 4-11. Curved DNA origami structures. By controlling the BP insertion or deletion inside the structures, the degree of curvature and dimensions was regulated to provide straight (**a**), a quarter (**b**), and a half (**c**) circular shapes as previously reported images.

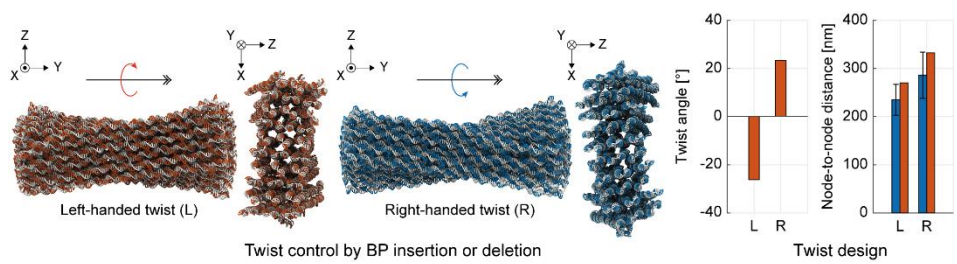


Figure 4-12. Twist control by BP insertion or deletion. For the left-handed (L) and right-handed (R) twist structures, their twist angles were predicted in opposite directions. The node-to-node-distance as torsional wave length was estimated from the twist angle and axial length.

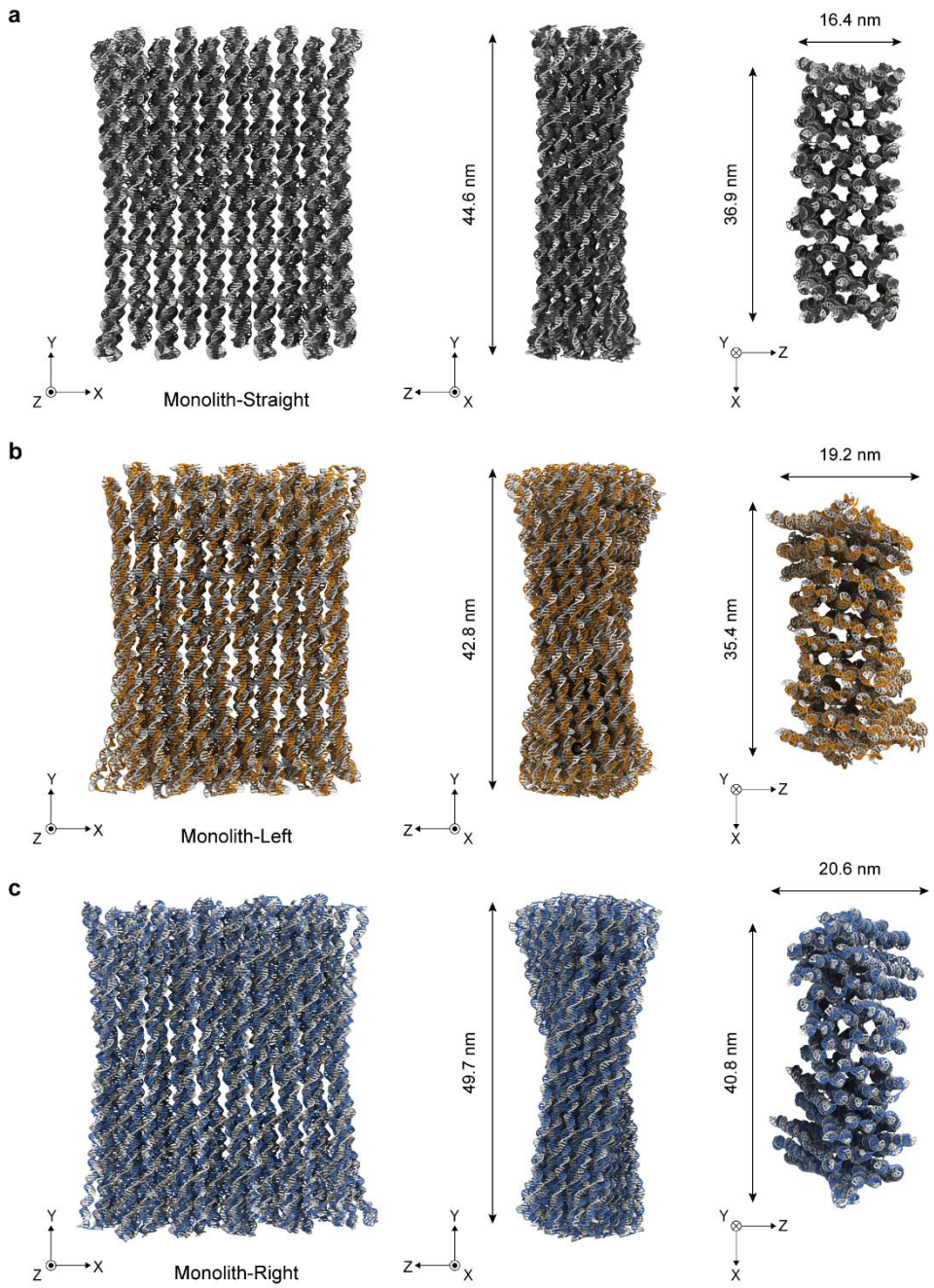


Figure 4-13. Straight and twisted monolith structures. Straight (**a**), left-handed (**b**), and right-handed (**c**) structures were predicted as previous studies.

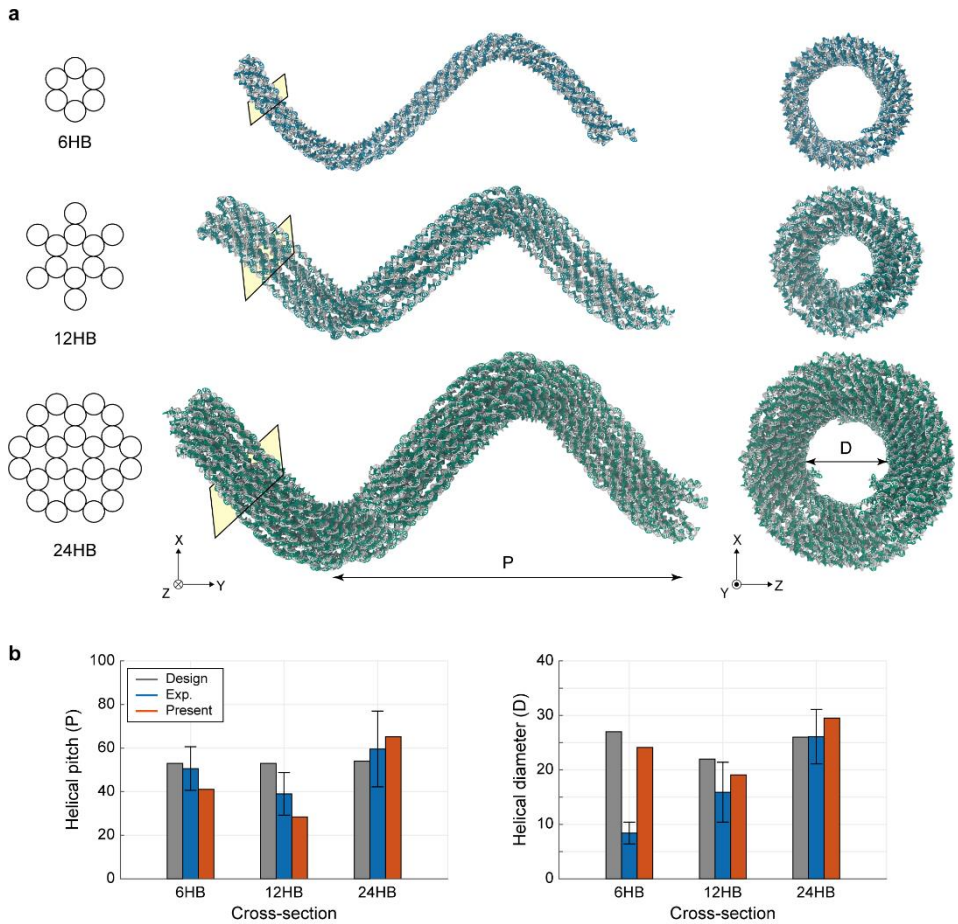


Figure 4-14. Spring-like DNA nanostructures by both controlling bending and torsion. (**a**) 6HB, 12HB, and 24HB structures were designed to have a unique pitch (P) and diameter (D) in a previous study. (**b**) Comparison of the measured pitch and inner diameter of helices. The helical pitch and diameter were calculated by the least-squares method from the helix fitting program, HELFIT. The radius of the 6HB structure was measured as designed but may differ from the experimental results due to its structural vulnerability by thin and distorted configuration.

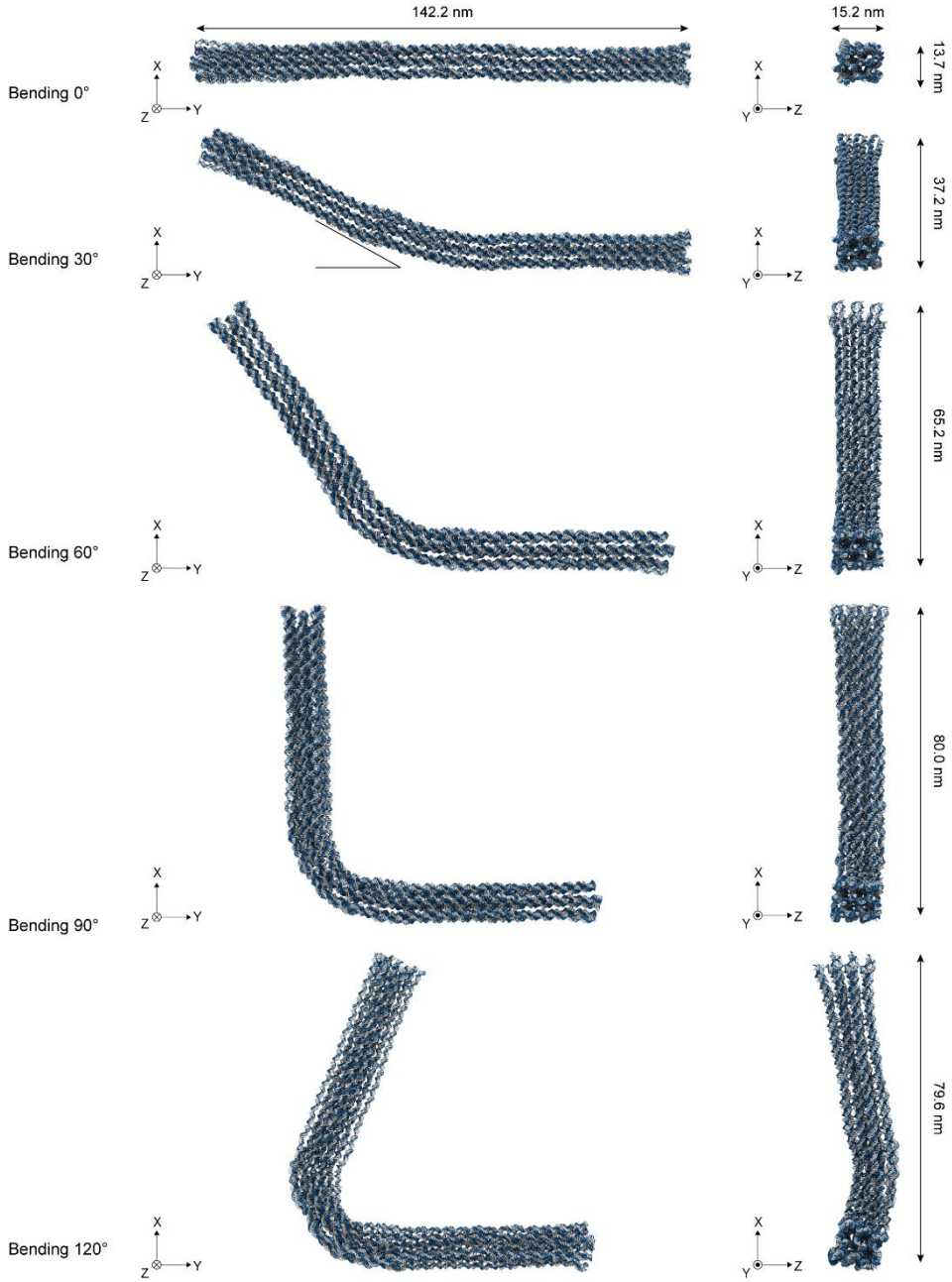


Figure 4-15. Globally bent structures by the insertion and deletion of BPs. The bending angles were measured as 0°, 29°, 58°, 90°, and 118°, in line with the previous study. The bent structures of 150° and 180° were more distorted than expected in the central curved section, of which the base-pairs could be broken to release stress concentration.

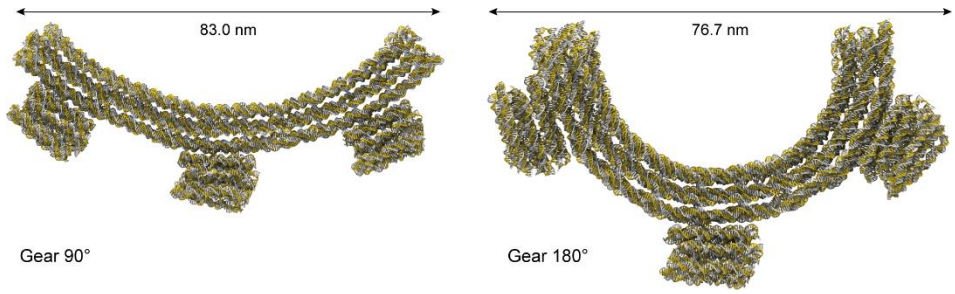


Figure 4-16. Gear structures by BP insertion or deletion. The gear structures were predicted and showed good agreement as reported.

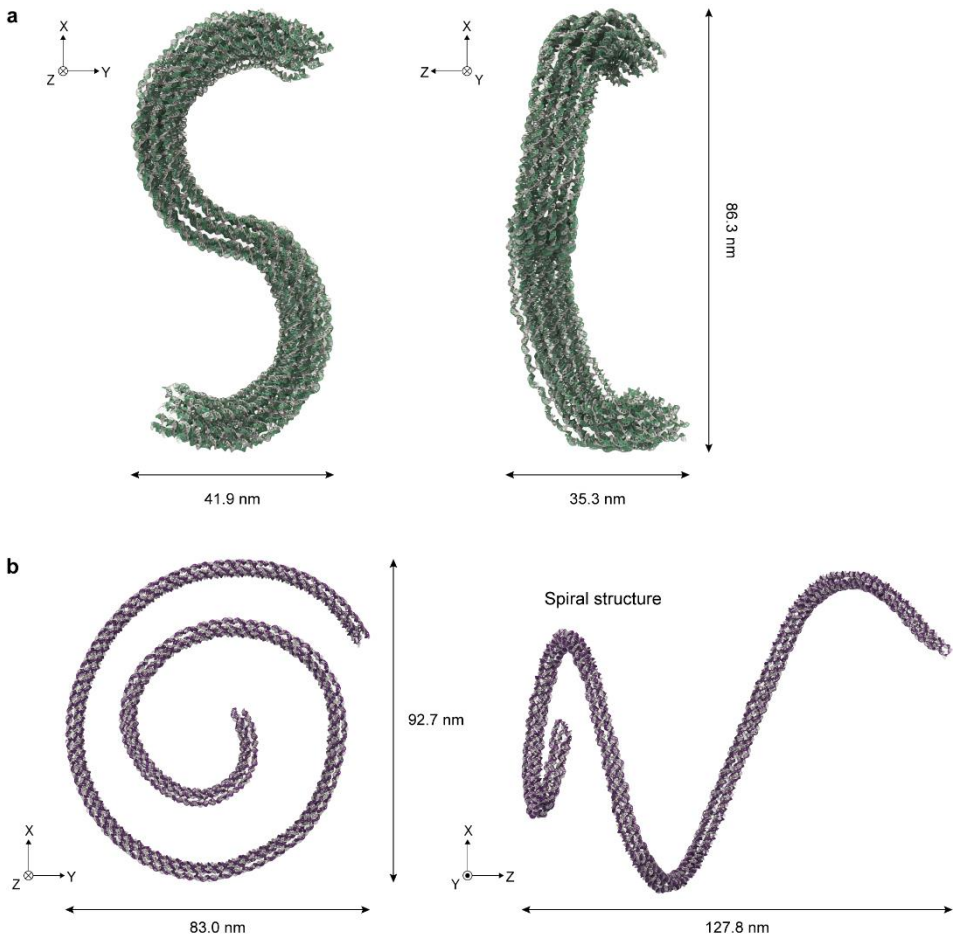


Figure 4-17. S-shaped DNA origami structure. The S-shaped (**a**) and spiral (**b**) structure were predicted as reported previously. In the spiral structure, due to the out-of-plane bending, non-uniform conformation could be observed.

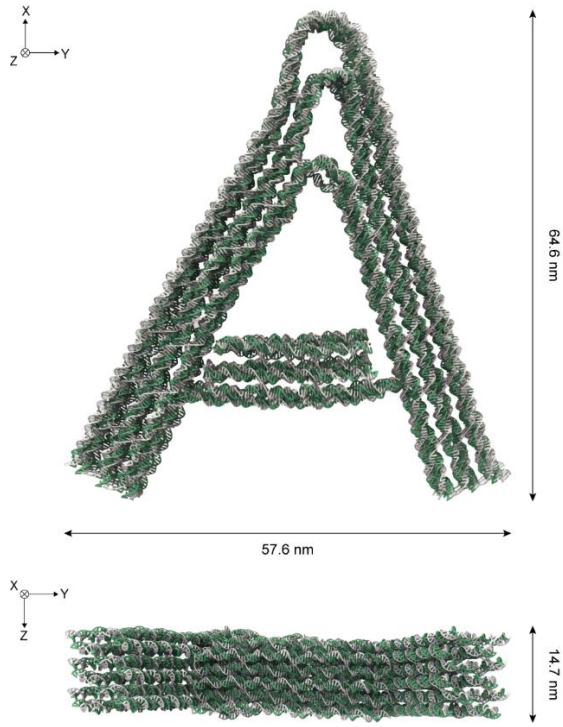


Figure 4-18. A-shaped DNA origami structure. The A-shape structure was predicted as previously reported.

## 4.3. Shape prediction of hierarchical assemblies

### 4.3.1. Control of opening angle in geometrically-constrained V brick

The efficiency of the proposed method enabled us to analyze much larger structures consisting of tens to hundreds of DNA origami monomers. To demonstrate, hierarchical assemblies of DNA blocks were examined for a quantitative comparison with experimental results. As a representative example[11], a V brick comprising two asymmetric sub-structures with spacer helices was first analyzed thoroughly. Its central opening angle was controlled by the number of BPs in short (N1) and long (N2) spacer helices connecting two sub-structures. Predicted angles for eleven sets of N1/N2 values were all well matched with the experimentally characterized ones (Figure 4-19a, Figure 4-20, Figure 4-21, and Figure 4-22). Among them, the V brick with 22/55 spacer helices was characterized to hold the opening angle of approximately 30° and shown to be assembled side-by-side into a planar self-limiting ring structure with eleven bricks in most cases. Our model predicts the opening angle of 31.2° for it leading to the eleven-brick ring structure with a diameter of 195 nm and a height of 34 nm (Figure 4-19b).

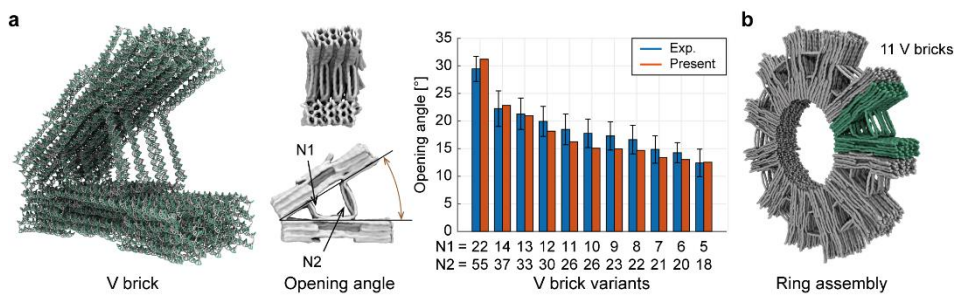


Figure 4-19. Prediction of V brick structure. (**a**) The V brick comprises two asymmetric sub-structures with spacer helices. The opening angle was controlled by the number of BPs in short (N1) and long (N2) spacer helices connecting two sub-structures. (**b**) Prediction of a ring assembly. The self-limiting flat ring assembly was constructed using the eleven V bricks (22/55).

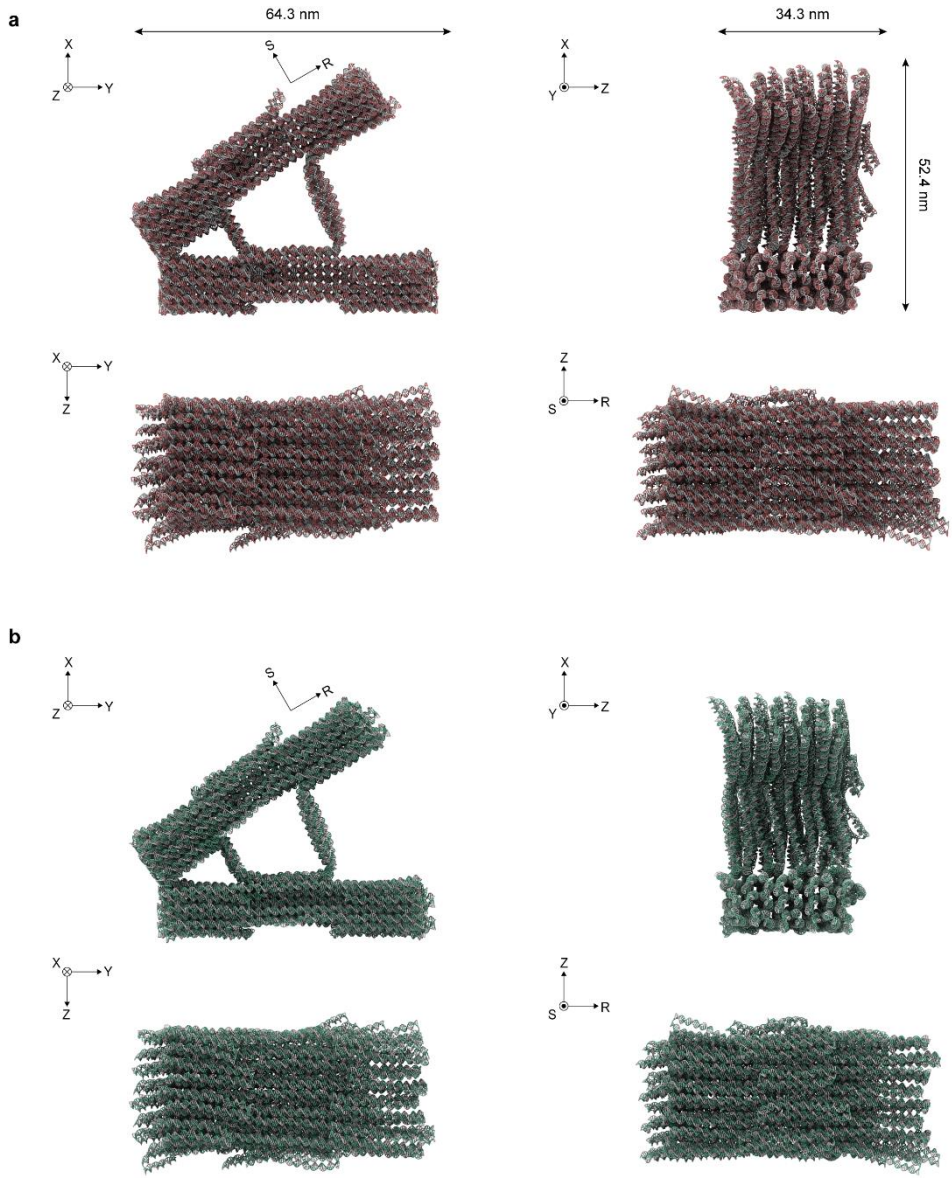


Figure 4-20. V brick prediction. We predicted the V-brick structure. The structure composed of two asymmetric monomers and double-helical spacers. The set of double-helical spacers defines the opening angle. Initial and twist-corrected structures were represented as red (**a**), and green (**b**) color.

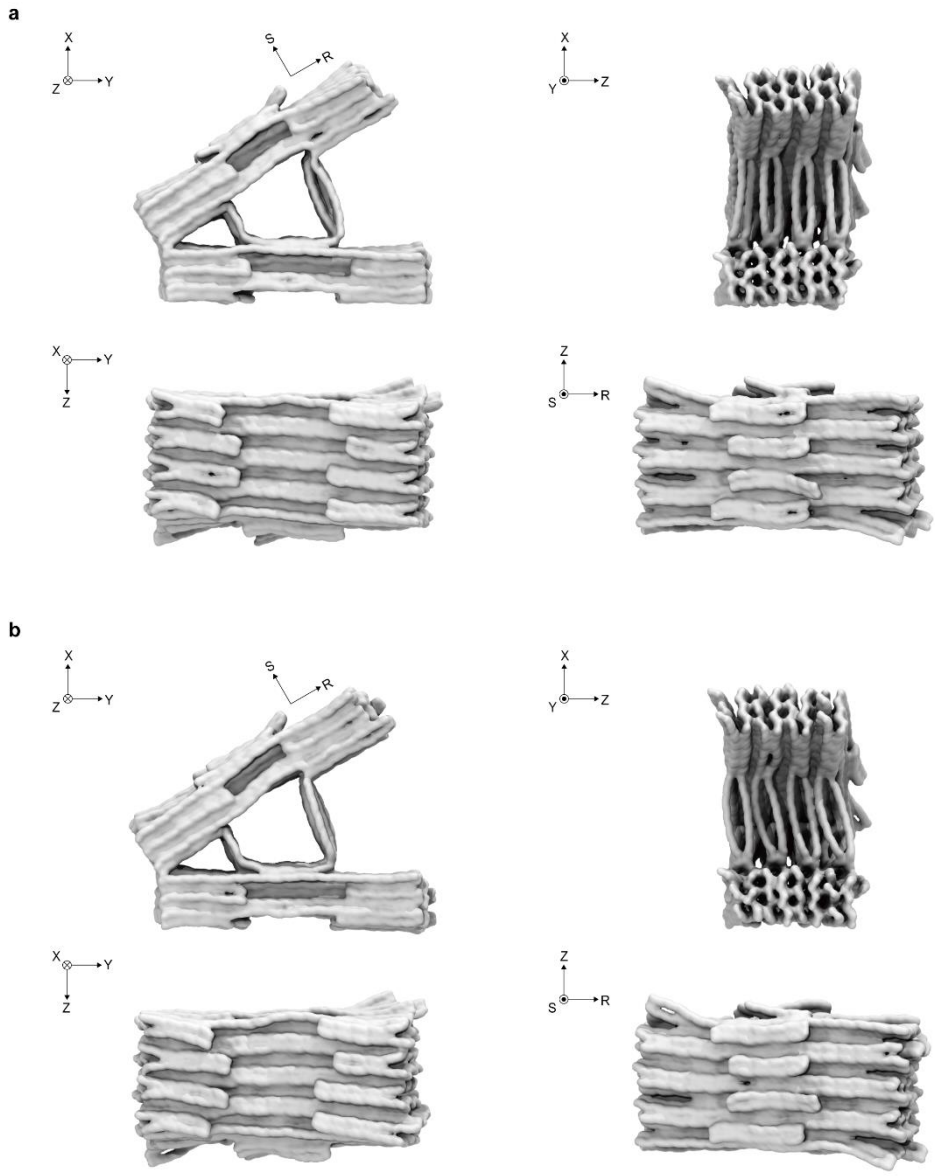


Figure 4-21. Density map of V brick. For the initial (**a**) and twist-corrected V bricks (**b**), the density map was generated using the plugin, volmap in VMD with a resolution of 4 Å.

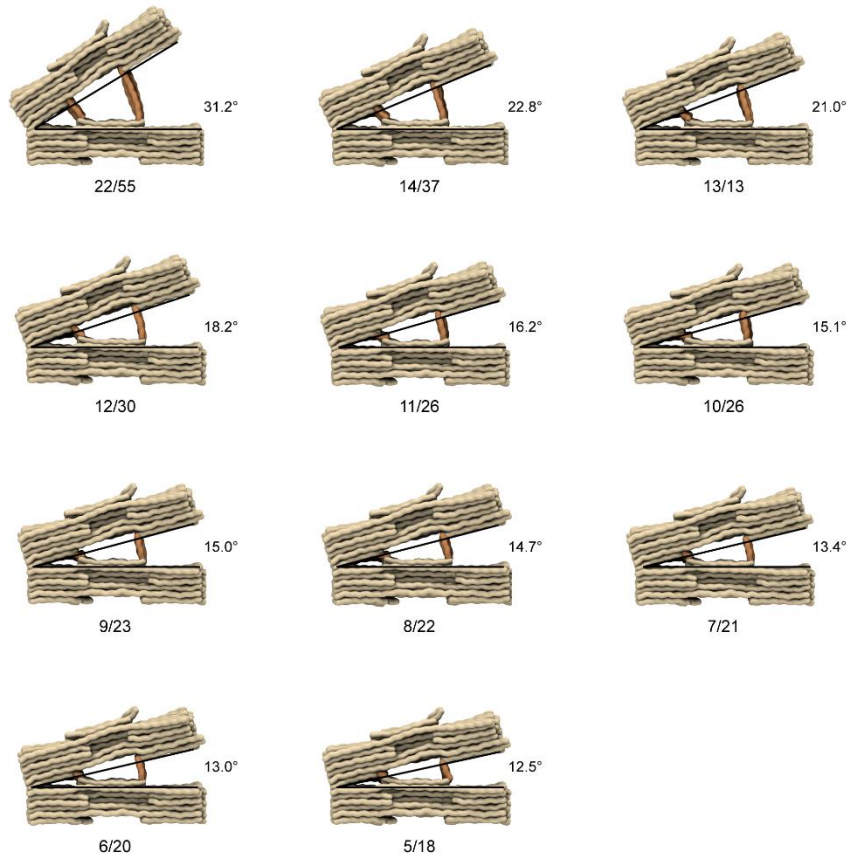


Figure 4-22. Opening angle estimation of the V-bricks. The central opening angle of the V-brick was controlled by the number of BPs in two short (N1) and long (N2) helices to connect the centers, and the prediction of variants (expressed as N1/N2) confirmed the previous study[11].

### 4.3.2. Assessment of the twist-correction effect in the tube structure

Higher-level assemblies could be constructed by stacking flat ring structures via the shape-complementary interlocking between the front and back faces (Figure 4-23). We built two tubular assemblies using the initial (red) and twist-corrected (green) V bricks. The predicted tube shapes confirmed the existence of the global distortion with initial V bricks while the straight tube was obtained with twist-corrected V bricks as experiments[11]. The twisted tube showed the apparent shear angle of around 5° that was induced by the amplification of the twist per ring of about 2° (Figure 4-24). This was because the initial V brick was designed on the honeycomb lattice assuming the helicity of 10.5 BP per turn (or 34.29° rotation per BP). The discrepancy between this assumed helicity and the measured one from MD results (10.43 BP per turn or 34.51° rotation per BP, Table 3-1) induced the torsional deformation of the tube. In the modified design, one BP was deliberately deleted every 170 BPs along the helix to correct this unwanted twist. Our analysis results suggest a similar level of twist correction on average corresponding to the deletion of one BP per 156 BPs (=34.29°/(34.51°-34.29°)). It would be crucial to consider this fact particularly in the design of hierarchical supramolecular structures where a small mismatch in design could be amplified significantly in reality.

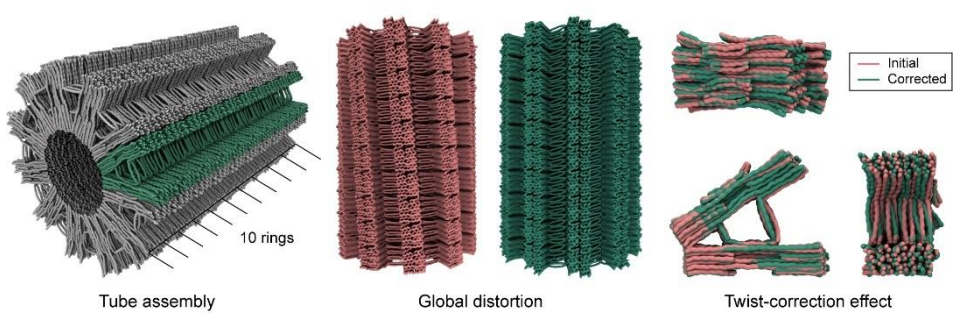


Figure 4-23. Prediction of a tube assembly and twist-correction effect. A small torsional deformation was observed in the V brick. This produced a global distortion, which predicted about 2° per ring in the tube (red). The twist-corrected tube reduced the distortion through deliberately deleting BPs (green).

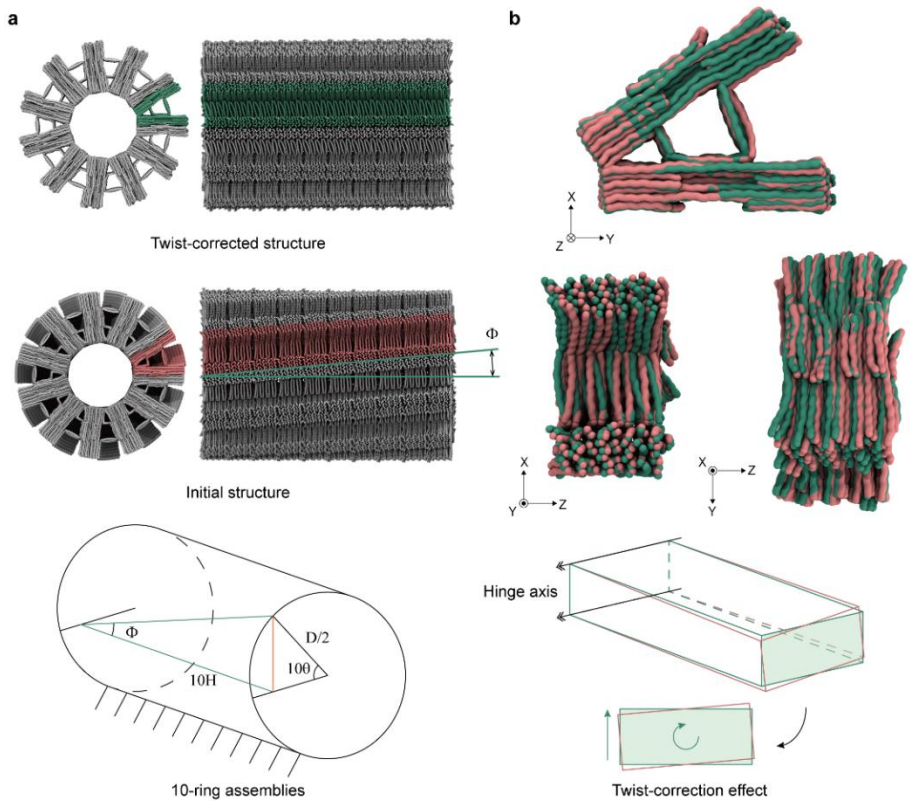


Figure 4-24. The twist-correction effect in tube assembly. The tube structures stacking ten twist-corrected and initial rings were represented as green and pink color (**a**). For the initial structure, the apparent angle ($\phi$) and the twist angle per ring ($\theta$) have the relation as $Dsin(10\theta)/2 = 10H\tan(\phi)$, where $D$ and $H$ are the diameter and height of each ring structure. From the measured apparent angle (5.5°), diameter (195 nm), and height (34 nm), the twist per angle was calculated as around 2.0° in line with the previous result. Twist-correction effects were observed for the V bricks by introducing counter-twist through the BP deletion (**b**). The cross-section of the initial V brick (red) shows small right-handed twist deformation for the hinge axis, whereas the twist of the in twist-corrected V brick (green) showed straight cross-section.

### 4.3.3. Prediction of hierarchically assembled polyhedral structures

We also investigated the three-dimensional polyhedral cage structures (Figure 4-25). Three twist-corrected building blocks (embossed V brick and recessed triangular and connector bricks)[11] were analyzed first (Figure 4-25a, Figure 4-26, Figure 4-27, and Figure 4-28). They were integrated into three-fold assemblies by using three variants of embossed V bricks whose opening angles were predicted as 55.1°, 34.7°, and 22.3° similar to experimentally characterized angles of 54.2 ± 6.3°, 35.2 ± 3.8°, and 22.3 ± 2.6 °, respectively[11] (Figure 4-25a and Figure 4-29). These three-fold structures were further hierarchically assembled into the three-dimensional self-limiting tetrahedrons, hexahedrons, and dodecahedrons. Their radii were estimated as 120 nm, 140 nm, and 200 nm comparable to 125 ± 28.4 nm, 150 ± 28.2 nm, and 210 ± 24.9 nm in experiments, respectively (Figure 4-25b, Figure 4-29, and Figure 4-30).

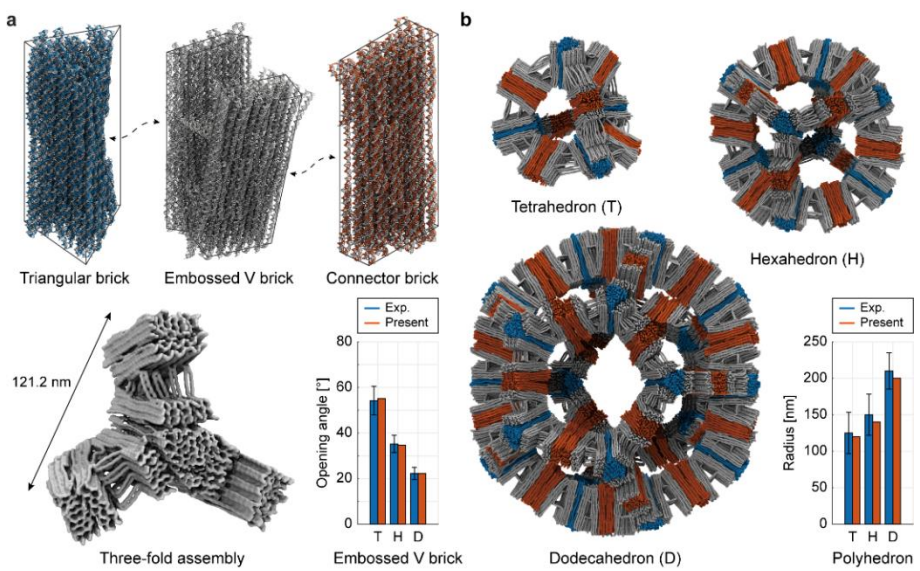


Figure 4-25. Prediction of hierarchical DNA nanostructures. (**a**) Prediction of a three-fold assembly. Twist-corrected triangle brick, embossed V brick, and connector brick were assembled to the three-fold assembly. (**b**) Prediction of the polyhedrons. The three-dimensional self-limiting tetrahedrons (T), hexahedrons (H), and dodecahedrons (D).

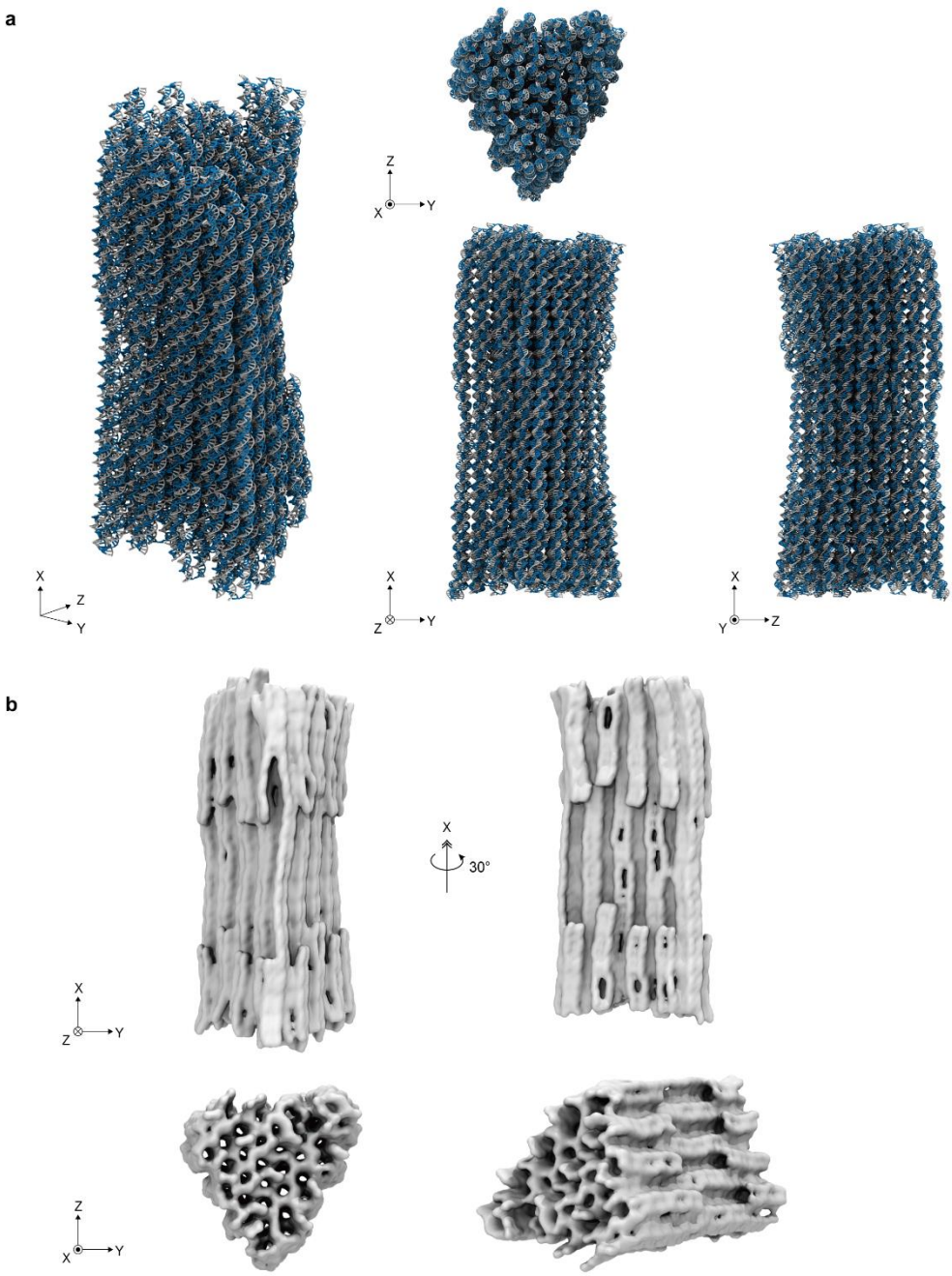


Figure 4-26. Triangular brick prediction. Atomic representation (**a**) and density map (**b**) were constructed. The density map was generated using the plugin, volmap in VMD with a resolution of 4 Å.

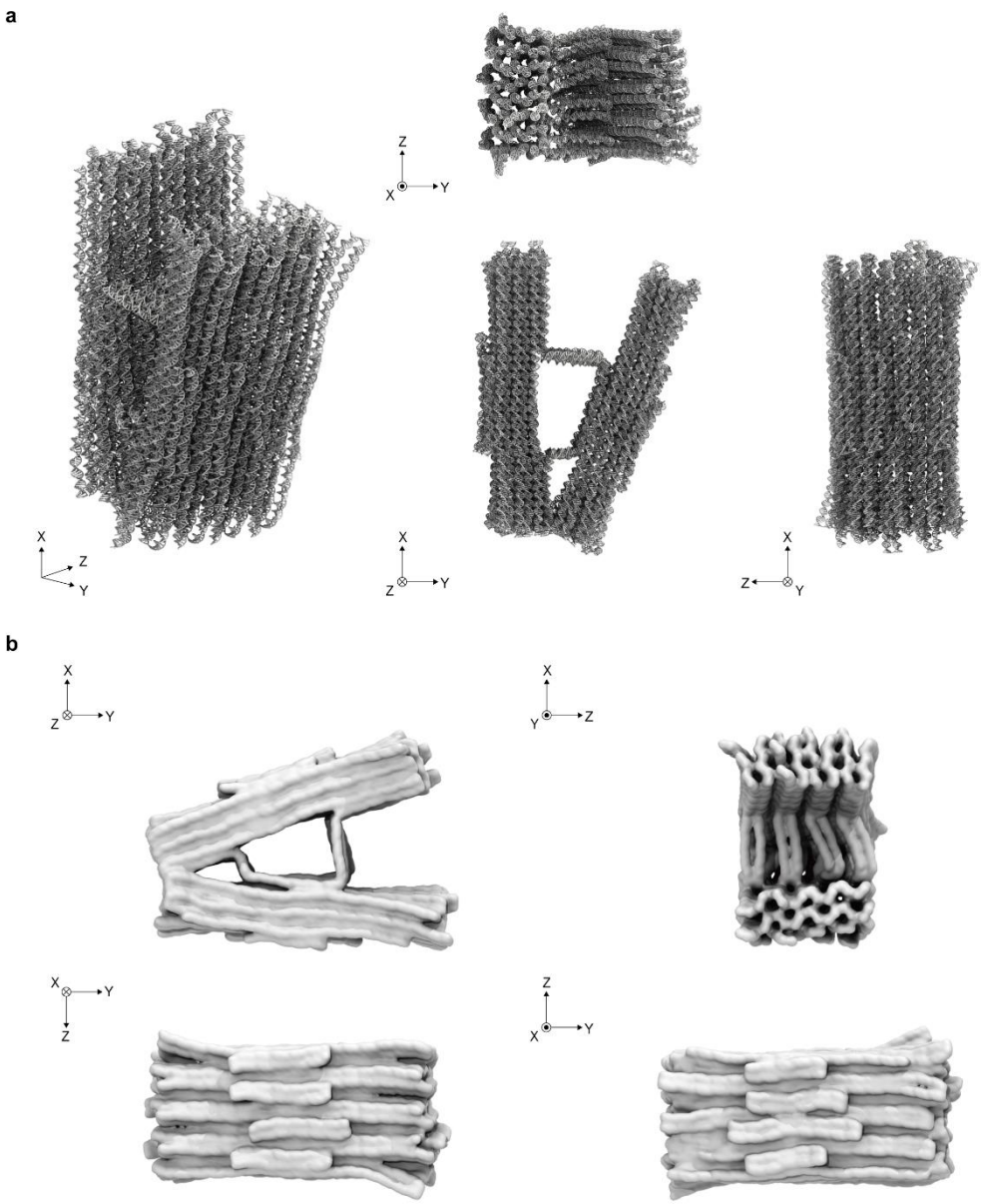


Figure 4-27. Embossed V brick prediction. Atomic representation (**a**) and density map (**b**) were constructed. The density map was generated using the plugin, volmap in VMD with a resolution of 4 Å.

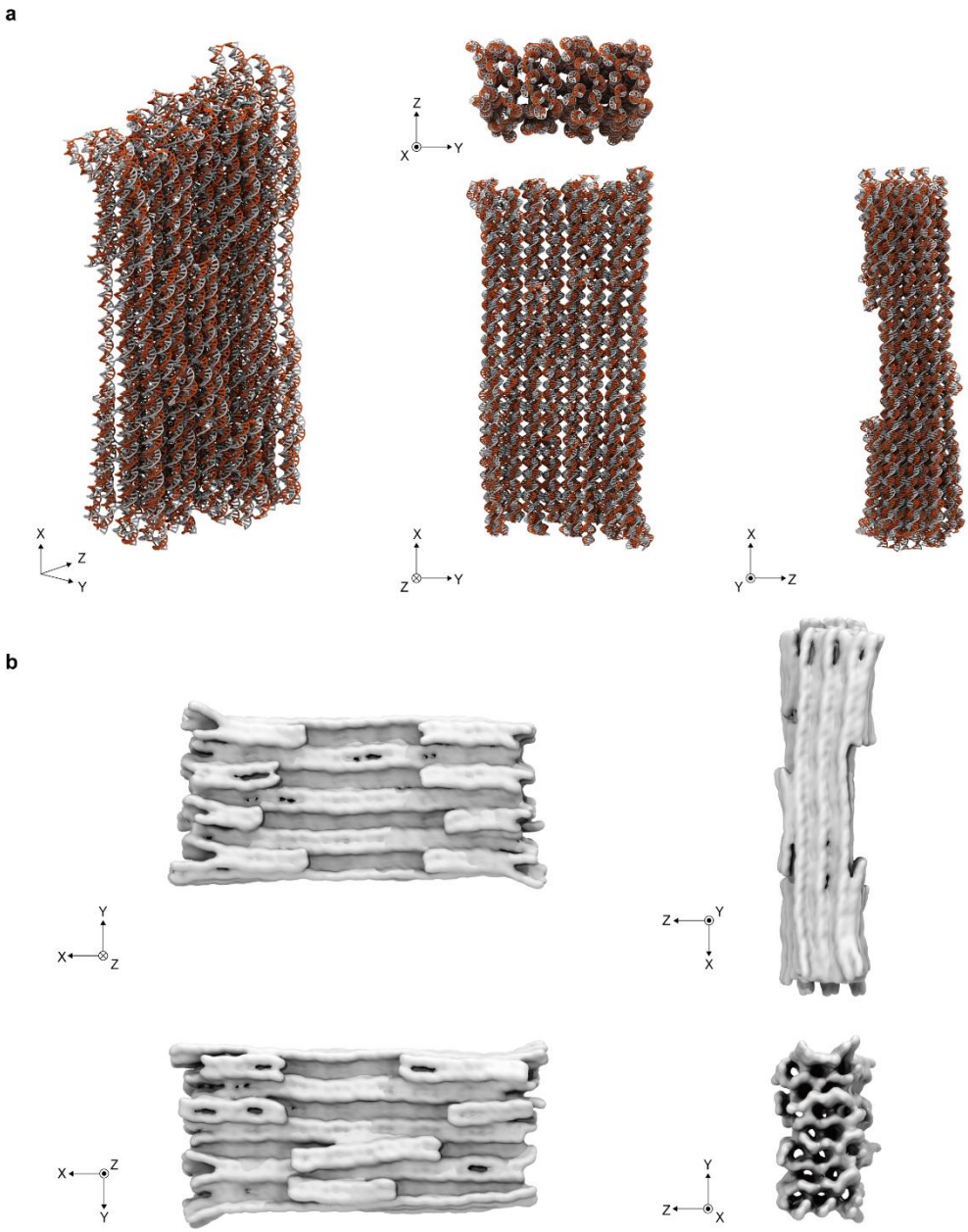


Figure 4-28. Connector brick prediction. Atomic representation (**a**) and density map (**b**) were constructed. The density map was generated using the plugin, volmap in VMD with a resolution of 4 Å.

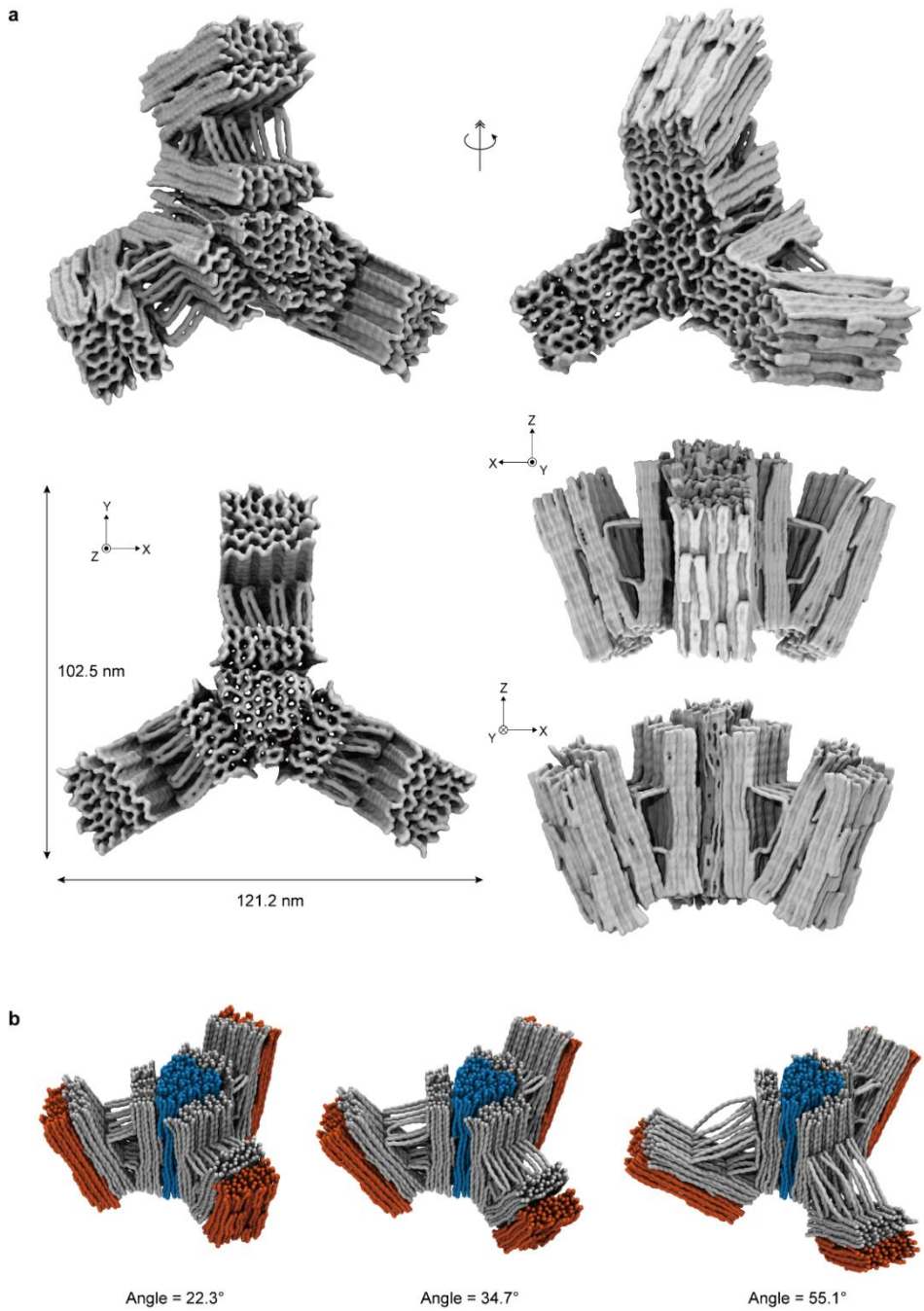


Figure 4-29. Three-fold structure prediction. (**a**) The density map was generated using the plugin, volmap in VMD with a resolution of 4 Å. (**b**) The three-fold structures were assembled using V bricks of different opening angles.

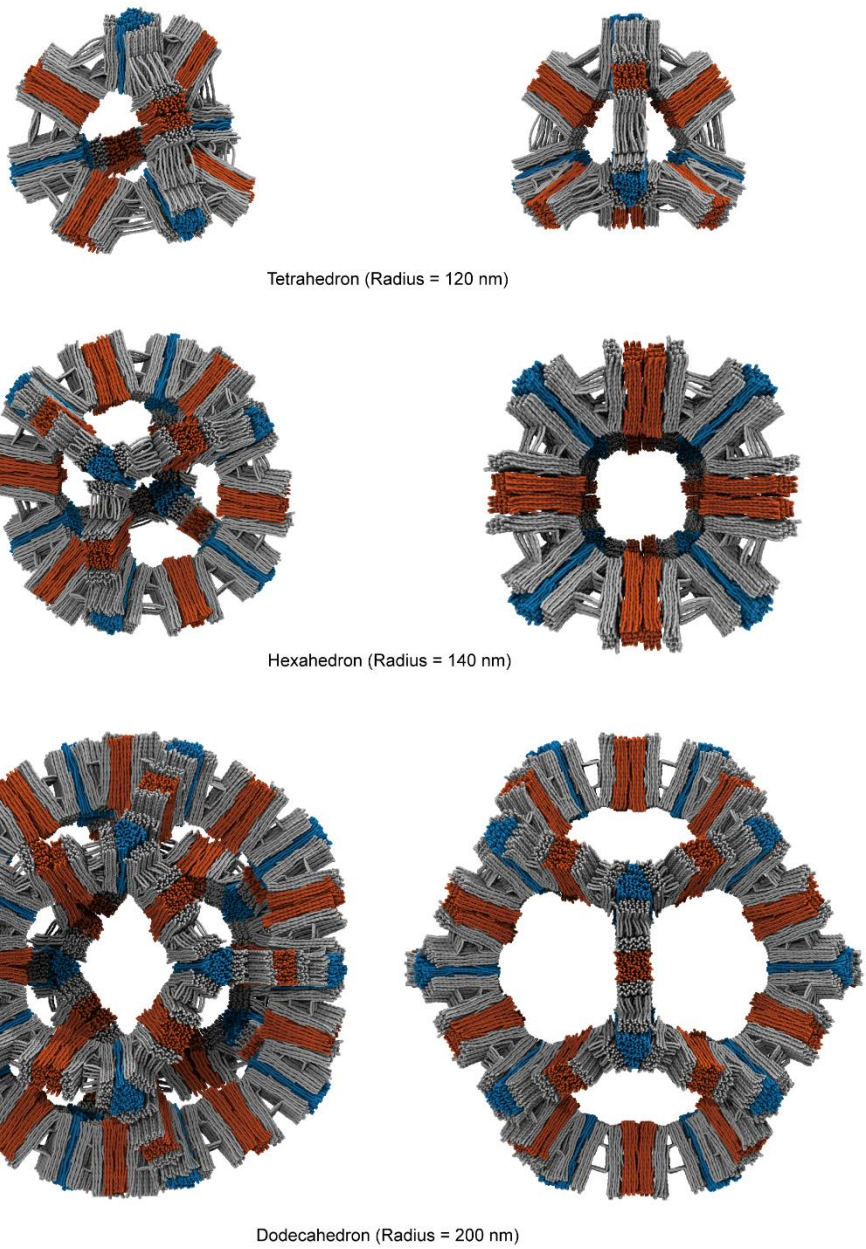


Figure 4-30. Prediction of polyhedral assemblies. Three-fold assemblies by V brick variants produce different polyhedral cages in the self-limiting fashion as reported. The radius of the assembled tetrahedron, hexahedron, and dodecahedron was estimated to 120 nm, 140 nm, and 200 nm, respectively.

## 4.4. Structural details at the base-pair level

### 4.4.1. The dimension of the pointer structure

To evaluate the proposed model more quantitatively in structural details, we analyzed the pointer design (Figure 4-31) whose high-resolution structure was determined by cryo-electron microscopy (cryo-EM)[80] and examined computationally through all-atom MD[32] and coarse-grained oxDNA[15] simulations. A right-handed global twist about the helical axis was observed as it was designed on the square lattice with the helicity of 10.67 BP per turn (Figure 4-32 and Figure 4-33). The overall dimension of the structure was slightly underestimated in two transverse directions compared to the experimental structure, which was also observed in the MD simulation results[32]. In general, the model accuracy for the inter-helical distance due to the electrostatic repulsion and the out-of-plane distortion was high inside the structure, but relatively low in outer helices (Figure 4-34). It might be partly because the current model does not include the effect of the solvent surrounding the structure explicitly. The root-mean-square-deviation (RMSD) to the cryo-EM structure was estimated as 1.5 nm for our model, which was slightly larger than 0.84 nm for oxDNA[15] and 0.92 nm for MD[32] but still sufficiently accurate considering the experimental resolution of 0.97 nm at the core and 1.4 nm at the periphery[80] as well as the simplicity and efficiency of the model.

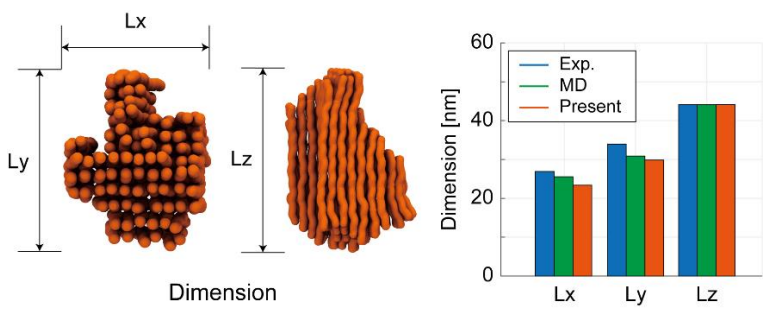


Figure 4-31. Comparison of structural dimension. Helical dimension (Lz) was comparable and the other dimensions in two transverse directions (Lx and Ly) were slightly underestimated compared to the experimental structure.

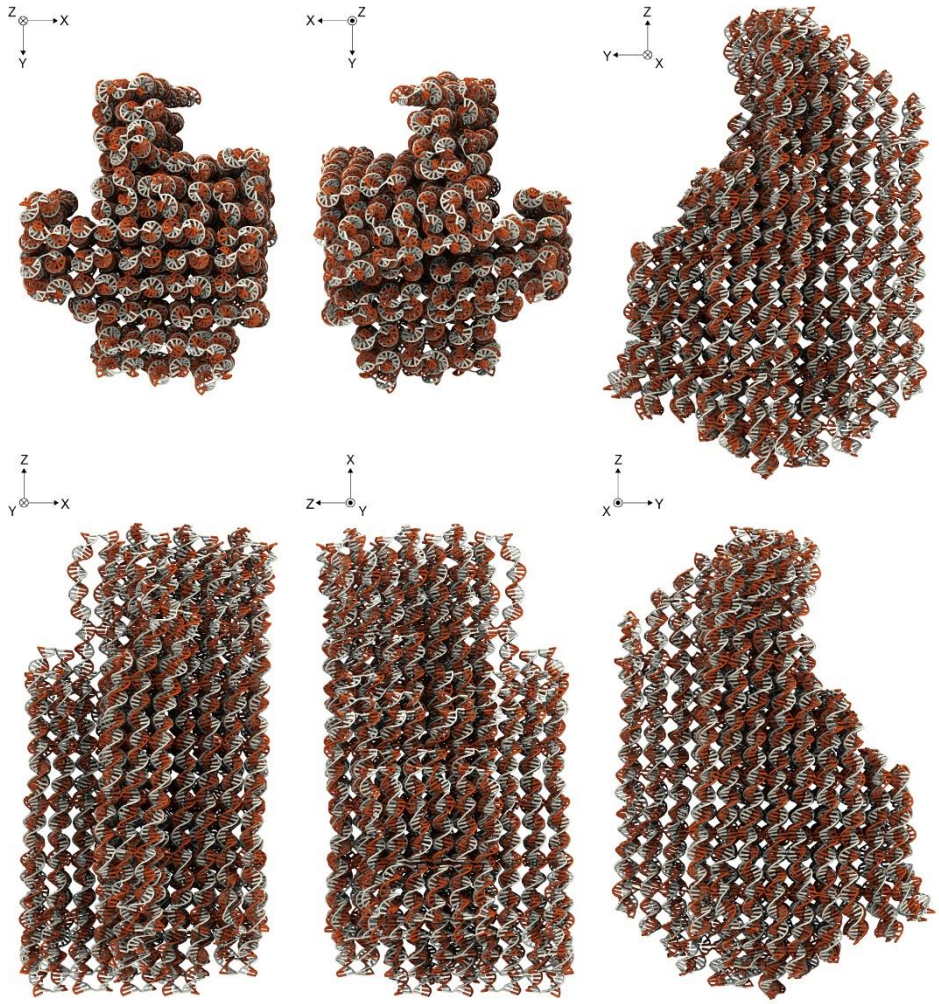


Figure 4-32. Prediction of the pointer structure. The pointer structure was represented in orthogonal orientations and showed a global twist by the square lattice design. Root-mean-square-deviation (RMSD) value compared to the cryo-EM structure was 1.5 nm. The density map was generated from the atomic coordinates with a resolution of 4 Å.

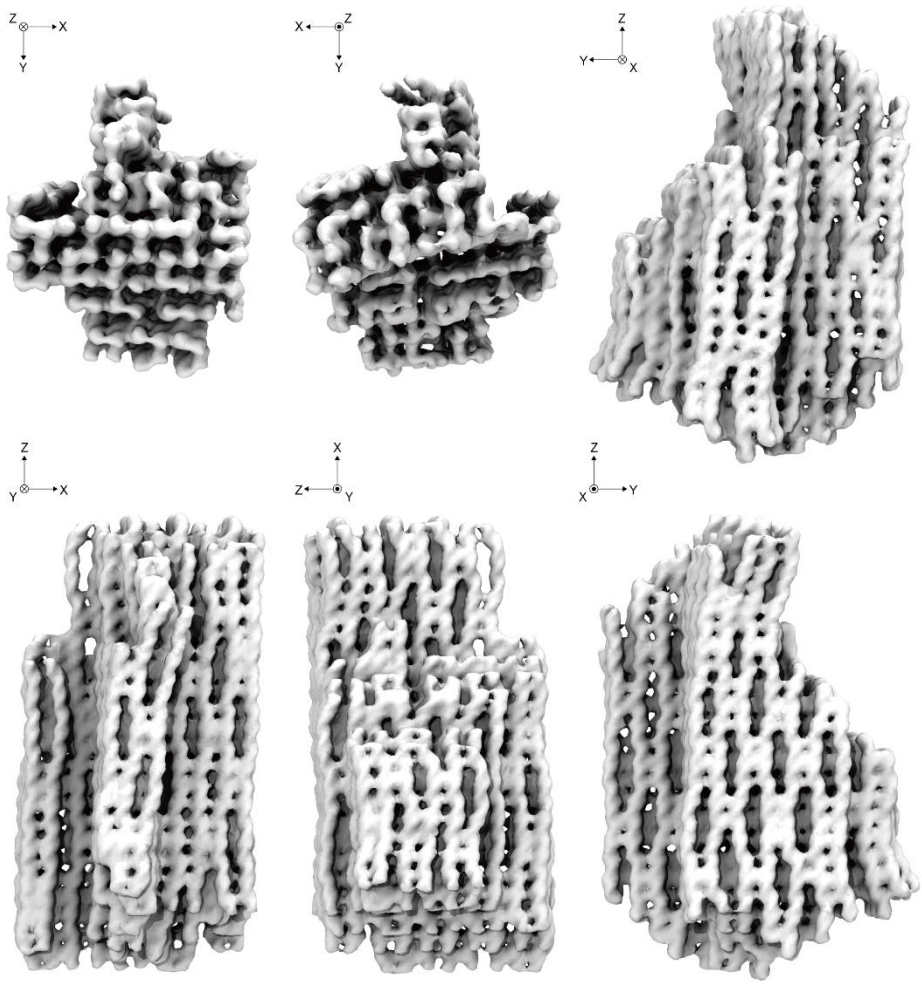

Figure 4-33. Density map of pointer structure. The density map was generated using the plugin, volmap in VMD with a resolution of 4 Å.

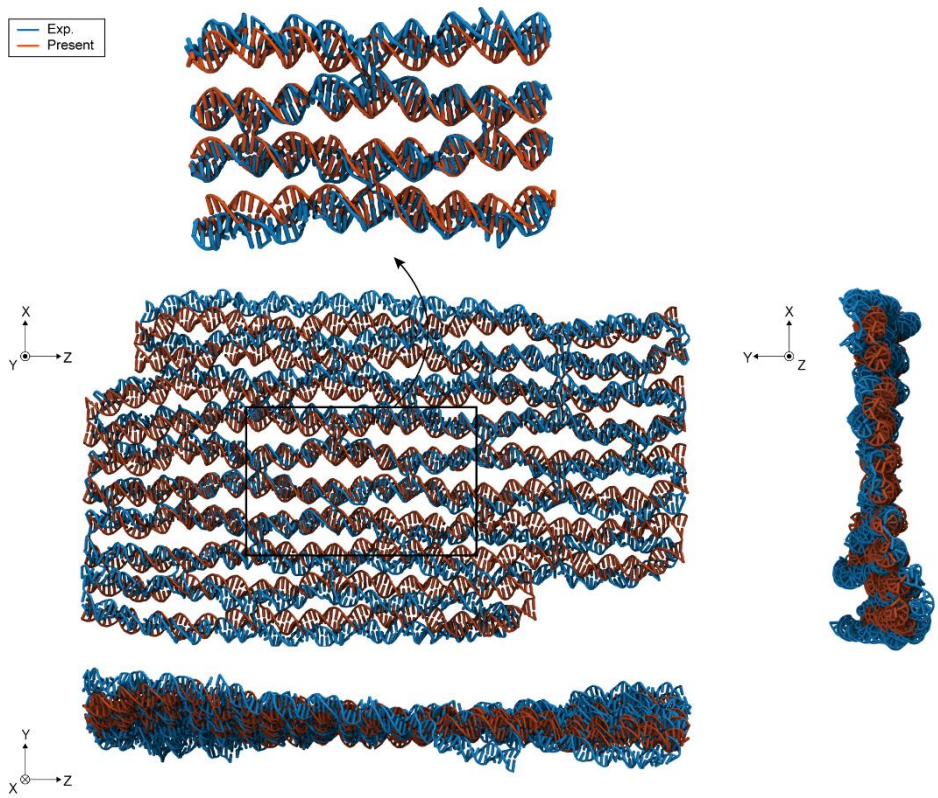


Figure 4-34. Central plane in the pointer structure. The central plane for the cryo-EM structure was compared to the previous study. This comparison shows the general agreement at the core, such as the inter-helical distance due to the electrostatic repulsion, but indicates the mismatch in the outer helices.

### 4.4.2. Prediction of the base-pair and crossover configuration

More specifically, we investigated the characteristic conformational parameters of CO and BP steps. First, three representative CO angles were calculated following the previous definition[80] (Figure 4-35). Results demonstrated that the CO angles predicted by the proposed model were consistent with the experimental values and those by MD simulations. They were, in fact, closer to MD simulation results[32] probably because the intrinsic properties of our model were directly estimated by MD simulations. Good agreement between our model and MD results was also observed when analyzing CO conformations of an 18HB structure designed on the honeycomb lattice[31] (Figure 4-36).

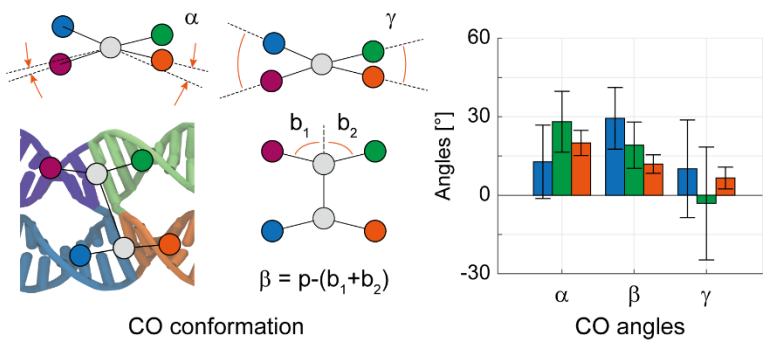


Figure 4-35. Comparison of the CO angles. Three representative CO angles were calculated following the previous definition using the vectors connecting the six points, which were determined as two mean coordinates of two CO-nick BP steps and four coordinates of the two BPs away from the CO in each lag. The mean and standard deviation were calculated using the measured values for all CO steps.

Also, six BP step parameters (shift, slide, rise, tilt, roll, and twist)[26] of the structure obtained by our model agreed well with those characterized for the cryo-EM structure (Figure 4-37). These results clearly illustrate the model's capability in capturing the key structural features at the base-pair level quickly through the multiscale modeling approach.

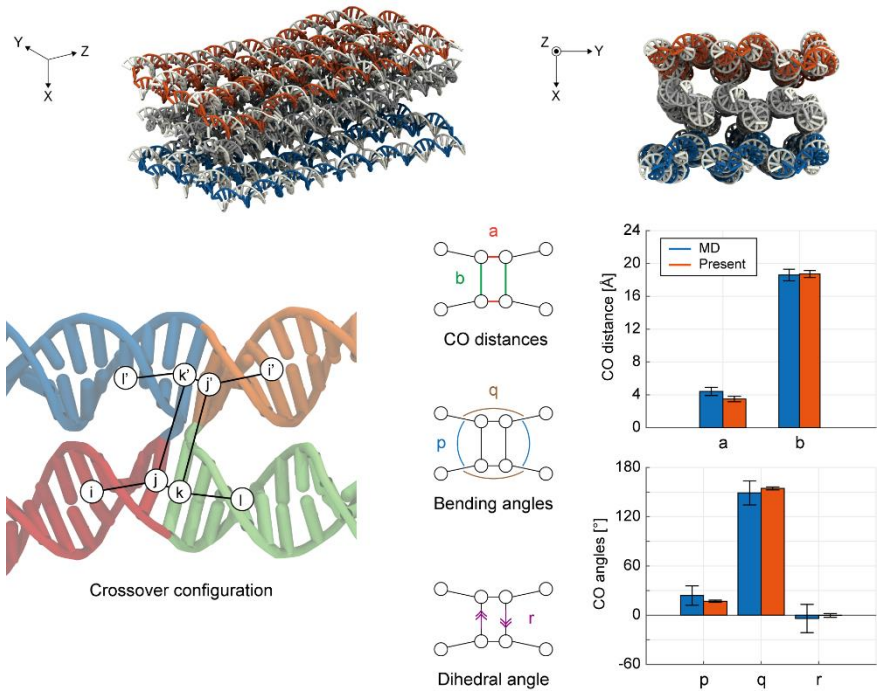


Figure 4-36. DNA origami structures of honeycomb. In the structure, the distance and angles at crossover sites were measured and compared with the MD results. Three representative CO angles were determined from the vectors connecting the eight points, which were determined as coordinates of four BPs at the crossover sites and four coordinates of the three BPs away from the crossover in each lag.

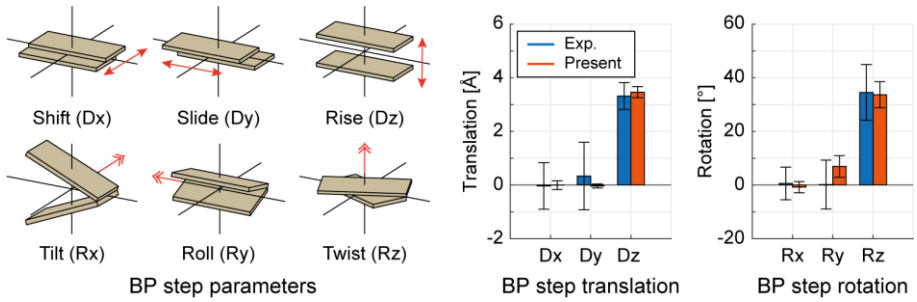


Figure 4-37. Comparison of BP step parameters. The translational and rotational parameters of all BP steps in the structure were consistent with the previous results. The mean and standard deviation were calculated using the measured values for all BP steps.

# 5. Twist control of DNA nanostructures through sequence design

## 5.1. Abstract

To control the twist of the DNA nanostructures sequence design principle was proposed, and it was verified through experiments and the proposed multiscale approach. The identified sequence-dependent mechanical properties were used to control the global twisted shape through only the design of the base sequence. In particular, focusing on the reduction of the torsional rigidity at the nick sites, the details of designing nick sequences in the DNA nanostructures to regulate its twist angle was described. We demonstrated that the global twist angle of the bundle structures can be modulated by designing the sequence at the nick sites therein from atomic force microscopy analysis. This design principle and results were further verified through the proposed multiscale method. Since it is easy to program the sequences at nick sites in the design of self-assembling DNA nanostructures, we expect that our mechanical data and sequence-design approach for precise control would be useful in the field of structural DNA nanotechnology.

## 5.2. Methods

### 5.2.1. Mechanical analysis of DNA structures with base-pair insertion

We theoretically investigated mechanical parameters related to the twist angle of a DNA bundle structure with BP-insertion. A two-helix-bundles (2HB) structure was introduced as the smallest twisting structure by BP-insertion (A), where terminal ends were constraint by Holliday-junctions. It was assumed that two identical and straight helices (H1 and H2) have the radius of r, bending rigidity of B, and torsional rigidity of C. Also, there was nothing to induce strain energy since the end of two helices cross exactly at both ends.

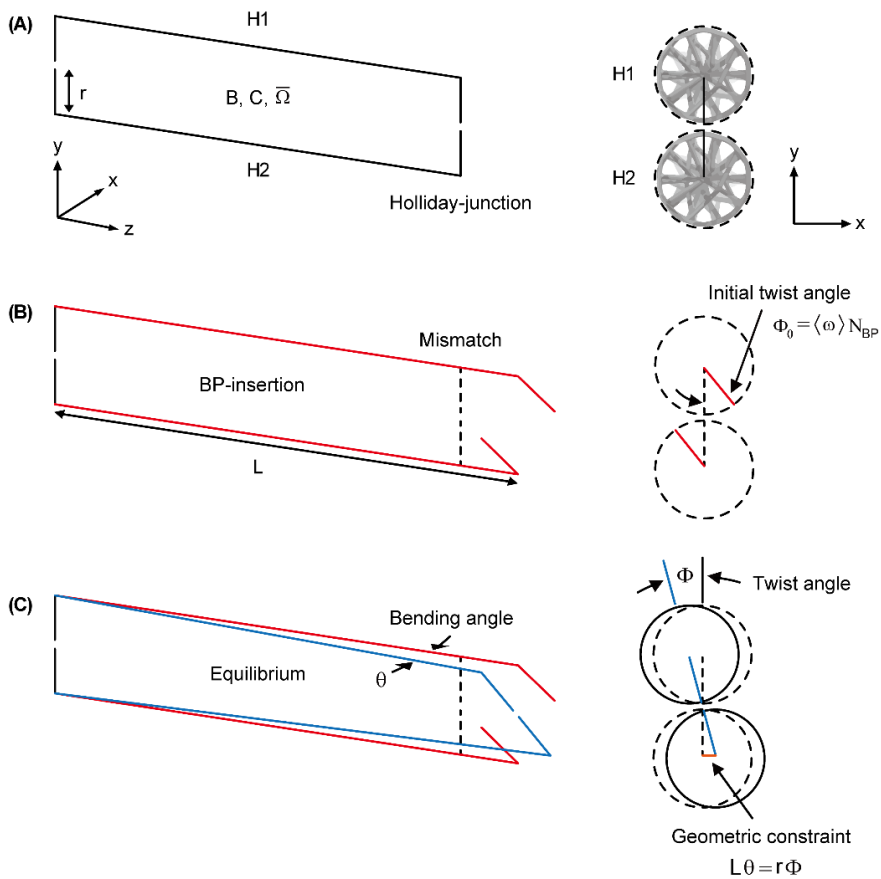


Figure 5-1. Mechanical analysis of DNA bundle structures.

When BPs are inserted but one of the Holliday-junctions is not constrained (**B**), the initial twist angle due to the helicity of DNA can be regarded as

$$\Phi_0 = \langle\omega\rangle N_{BP} \tag{5-1}$$

where $\langle\omega\rangle$ is the mean twist angle of each helix and the number of inserted BPs was denoted as $N_{BP}$. Also, each helix is elongated to a longitudinal length of L.

In equilibrium with the constraints at both ends of the helices (**C**), bending and torsional strain energy is induced at each helix to align the mismatch of connectivity and the center of twist. Besides, bending and torsional angle should satisfy a geometric constraint equation $(g)$ as

$$g = L\theta - r\Phi = 0 \tag{5-2}$$

where $\theta$ and $\Phi$ represent the equilibrium bending and twist angle of a helix. Then, the induced strain energy in the helix can be described using the method of Lagrange multipliers as

$$\pi = \int_0^L \frac{1}{2}\frac{M_b^2}{B}dx + \int_0^L \frac{1}{2}\frac{M_z^2}{C}dx + \lambda g \tag{5-3}$$

where the bending ($M_b$) and torsional moment ($M_z$) were derived as

$$M_b = B\frac{\Delta\theta}{L} \tag{5-4}$$

$$M_z = C\frac{\Delta\Phi}{L} \tag{5-5}$$

where the zero initial bending and initial twist angle by BP-insertion yield the angle deformation as

$$\Delta\theta = \theta \tag{5-6}$$

$$\Delta\Phi = \Phi - \Phi_0 = \Phi - \langle\omega\rangle N_{BP} \tag{5-7}$$

Then, the strain energy is derived using the above equations as

$$\pi(\theta, \Phi, \lambda) = \frac{1}{2L} B\theta^2 + \frac{1}{2L} C(\Phi - \langle\omega\rangle N_{BP})^2 + \lambda(L\theta - r\Phi) \quad (5\text{-}8)$$

The equilibrium configuration minimizes this strain energy, suggesting that the gradient of the strain energy is zero vector. We, therefore, obtain the system of equations as

$$\frac{\partial \pi}{\partial \theta} = \frac{1}{L} B\theta + \lambda L = 0 \quad (5\text{-}9)$$

$$\frac{\partial \pi}{\partial \Phi} = \frac{1}{L} C(\Phi - \langle\omega\rangle N_{BP}) - \lambda r = 0 \quad (5\text{-}10)$$

$$\frac{\partial \pi}{\partial \lambda} = L\theta - r\Phi = 0 \quad (5\text{-}11)$$

From the equations (5-9) and (5-11), the Lagrange multiplier, indicating the constraint force, was derived as

$$\lambda = -\frac{1}{L^2} B\theta = \frac{1}{rL} C(\Phi - \langle\omega\rangle N_{BP}) \quad (5\text{-}12)$$

Here, the bending angle ($\theta$) can be substituted to twist angle ($\Phi$) with the constraint equation (5-11), providing a relation of twist angle with rigidities of each helix and the number of inserted BPs as

$$\Phi = \langle\omega\rangle N_{BP} \left(1 + \frac{r^2/L^2}{C/B}\right)^{-1} \quad (5\text{-}13)$$

This relation suggests that DNA bundle structures could be more twisted when BPs are more inserted or $C/B$ is increased in helices. We found that nicks have significant effects on the reduction of torsional rigidity ($C$) rather than the reduction of bending rigidity ($B$). It is, therefore, speculated that the twist angle of bundle structures could be controlled by adjusting the location of nicks to control $C/B$ value. Here, we defined that $C/B$ ratio of nicked BP steps normalized by

corresponding regular BP steps as $(C/B)^{nicked}/(C/B)^{regular}$ to quantify the effects of nicks from an ideal structure consisting of all regular BP steps. Utilizing the $C/B$ ratio data from MD simulation, the twist angle of the structures with high $C/B$ ratio could be deliberately designed greater than that with low $C/B$ ratio, suggesting that the torsional energy stored by BP-insertion could be controlled by adjusting nicked BP steps. Future studies based on nonlinear analysis are promising to produce a more realistic theoretical prediction on the DNA structures since our approach is limited to only provide the insight of finding parameters to affect bundle structure due to the simple and linear assumption.

### 5.2.2. Design and simulation of twisted DNA origami structures

To identify and apply the mechanical properties of BP steps to DNA nanostructure, we designed six-helix-bundle (6HB) DNA origami structures with BP-insertion. Our theoretical analysis suggested that the ratio of torsional rigidity (C) to bending rigidity (B) of DNA helix dominates the twist angle of bundle structure for the given number of inserted BPs. The single equivalent bending rigidity (B) was determined by the harmonic mean of anisotropic tilt and roll bending rigidities ($B_\tau$ and $B_\rho$). Here, we defined $C/B$ ratio of nicked BP steps normalized by corresponding regular BP steps as $C/B\ \text{ratio} = (C/B)^{\text{nicked}}/(C/B)^{\text{regular}}$. The standard deviations of $(C/B)^{\text{regular}}$, $(C/B)^{\text{nicked}}$, and $C/B$ ratios were calculated as $\sigma_{\alpha/\beta} = \alpha/\beta\left(\sigma_\alpha^2/\alpha^2 + \sigma_\beta^2/\beta^2\right)^{1/2}$, where $\alpha$ and $\beta$ represent the mean values of two different properties, and $\sigma_\alpha$ and $\sigma_\beta$ indicate the standard deviations (Table 5-1). This sequence-dependent $C/B$ ratio quantified the potential effect of a nick on the twist angle with respect to an ideal 6HB structure consisting of regular BP steps only.

Based on $C/B$ ratio data from MD simulation, we controlled the global twist angle of 6HB structures by deliberately locating the sequence of nicked BP steps where staple strands met (Table 5-2). To approximately predict the twist angle of the 6HB structures, the elastic network-guided MD simulation[32] was performed on the segments of the 6HB structures (Figure 5-2 and Figure 5-3). We also conducted the CanDo simulation[17,34] of entire 6HB structures.

Table 5-1. Rigidity ratio of nicked BP steps compared to regular BP steps. Equivalent isotropic bending rigidity was used to calculate rigidity ratio values. The standard derivation (Std) of rigidity ratios in nicked BP steps compared to regular BP steps ($\sigma_{N/R}$) was approximated based on statistical theory as $\sigma_{\alpha/\beta} = \alpha/\beta\left(\sigma_\alpha^2/\alpha^2 + \sigma_\beta^2/\beta^2\right)^{1/2}$ where $\alpha$ and $\beta$ represent the mean values of two independent properties, and $\sigma_\alpha$ and $\sigma_\beta$ indicate their standard deviations, respectively.

| Rigidity ratio (nicked/ regular) | C/B ratio | | | C ratio | | | B ratio | | |
|---|---|---|---|---|---|---|---|---|---|
| | Mean | Std | Rank | Mean | Std | Rank | Mean | Std | Rank |
| AA/TnT | 0.79 | 0.15 | 2 | 0.72 | 0.09 | 1 | 0.91 | 0.12 | 11 |
| AnA/TT | 0.23 | 0.04 | 16 | 0.18 | 0.02 | 16 | 0.78 | 0.11 | 16 |
| AG/CnT | 0.81 | 0.15 | 1 | 0.67 | 0.09 | 2 | 0.83 | 0.11 | 14 |
| AnG/CT | 0.58 | 0.11 | 5 | 0.52 | 0.07 | 9 | 0.90 | 0.12 | 12 |
| GA/TnC | 0.48 | 0.09 | 10 | 0.53 | 0.07 | 8 | 1.09 | 0.14 | 1 |
| GnA/TC | 0.49 | 0.10 | 9 | 0.45 | 0.06 | 10 | 0.92 | 0.13 | 9 |
| GG/CnC | 0.31 | 0.06 | 15 | 0.32 | 0.04 | 14 | 1.04 | 0.14 | 4 |
| GnG/CC | 0.61 | 0.13 | 3 | 0.55 | 0.08 | 5 | 0.91 | 0.13 | 10 |
| AC/GnT | 0.43 | 0.09 | 11 | 0.43 | 0.06 | 11 | 0.99 | 0.15 | 7 |
| AnC/GT | 0.41 | 0.09 | 12 | 0.42 | 0.06 | 12 | 1.03 | 0.15 | 5 |
| AT/AnT | 0.40 | 0.08 | 13 | 0.34 | 0.05 | 13 | 0.86 | 0.12 | 13 |
| GC/GnC | 0.56 | 0.10 | 7 | 0.60 | 0.08 | 4 | 1.08 | 0.14 | 3 |
| TG/CnA | 0.54 | 0.11 | 8 | 0.55 | 0.08 | 7 | 1.02 | 0.15 | 6 |
| TnG/CA | 0.57 | 0.12 | 6 | 0.55 | 0.08 | 6 | 0.98 | 0.15 | 8 |
| TA/TnA | 0.32 | 0.07 | 14 | 0.25 | 0.04 | 15 | 0.79 | 0.13 | 15 |
| CG/CnG | 0.60 | 0.13 | 4 | 0.65 | 0.10 | 3 | 1.08 | 0.17 | 2 |

Table 5-2. The number of nicked BP steps used in the experimental design and mean rigidity ratio. The mean rigidity ratio was used as a reference value to design DNA origami structures. The mean rigidity ratio of each structure was calculated by dividing the summation of multiplying each rigidity ratio and the corresponding number of nicked BP steps by sixty as the total number of nicked BP steps. A figure below the table shows the mean rigidity ratio values for each structure.

| The number of nicked BP steps | 1-BP-insertion | | 2-BP-insertion | | | | | |
|---|---|---|---|---|---|---|---|---|
| | Stiff | Flex. | Stiff 1 | Stiff 2 | Mod. 1 | Mod. 2 | Flex. | Flex. 2 |
| AA/TnT | 24 | 0 | 21 | 17 | 0 | 3 | 0 | 0 |
| AnA/TT | 0 | 26 | 0 | 0 | 0 | 5 | 23 | 23 |
| AG/CnT | 12 | 0 | 6 | 10 | 0 | 0 | 0 | 0 |
| AnG/CT | 1 | 0 | 4 | 5 | 12 | 5 | 0 | 0 |
| GA/TnC | 0 | 0 | 0 | 0 | 16 | 4 | 2 | 1 |
| GnA/TC | 0 | 3 | 0 | 0 | 5 | 5 | 2 | 2 |
| GG/CnC | 0 | 13 | 0 | 0 | 1 | 6 | 11 | 15 |
| GnG/CC | 2 | 0 | 2 | 3 | 0 | 4 | 0 | 0 |
| AC/GnT | 0 | 1 | 0 | 0 | 11 | 1 | 1 | 2 |
| AnC/GT | 0 | 0 | 0 | 0 | 4 | 3 | 4 | 5 |
| AT/AnT | 1 | 5 | 1 | 1 | 2 | 2 | 4 | 1 |
| GC/GnC | 4 | 0 | 4 | 3 | 1 | 3 | 0 | 0 |
| TG/CnA | 4 | 0 | 7 | 6 | 6 | 9 | 0 | 0 |
| TnG/CA | 1 | 0 | 2 | 2 | 2 | 3 | 0 | 0 |
| TA/TnA | 0 | 11 | 0 | 0 | 0 | 4 | 13 | 11 |
| CG/CnG | 11 | 1 | 13 | 13 | 0 | 3 | 0 | 0 |
| Sum | 60 | 60 | 60 | 60 | 60 | 60 | 60 | 60 |

| Mean rigidity ratio | 1-BP-insertion | | 2-BP-insertion | | | | | |
|---|---|---|---|---|---|---|---|---|
| | Stiff | Flex. | Stiff 1 | Stiff 2 | Mod. 1 | Mod. 2 | Flex. 1 | Flex. 2 |
| C/B ratio | 0.7062 | 0.2986 | 0.6737 | 0.6710 | 0.4915 | 0.4803 | 0.3062 | 0.3023 |
| C ratio | 0.6580 | 0.2617 | 0.6352 | 0.6394 | 0.4889 | 0.4649 | 0.2722 | 0.2736 |
| B ratio | 0.9431 | 0.8607 | 0.9536 | 0.9633 | 0.9979 | 0.9591 | 0.8706 | 0.8864 |

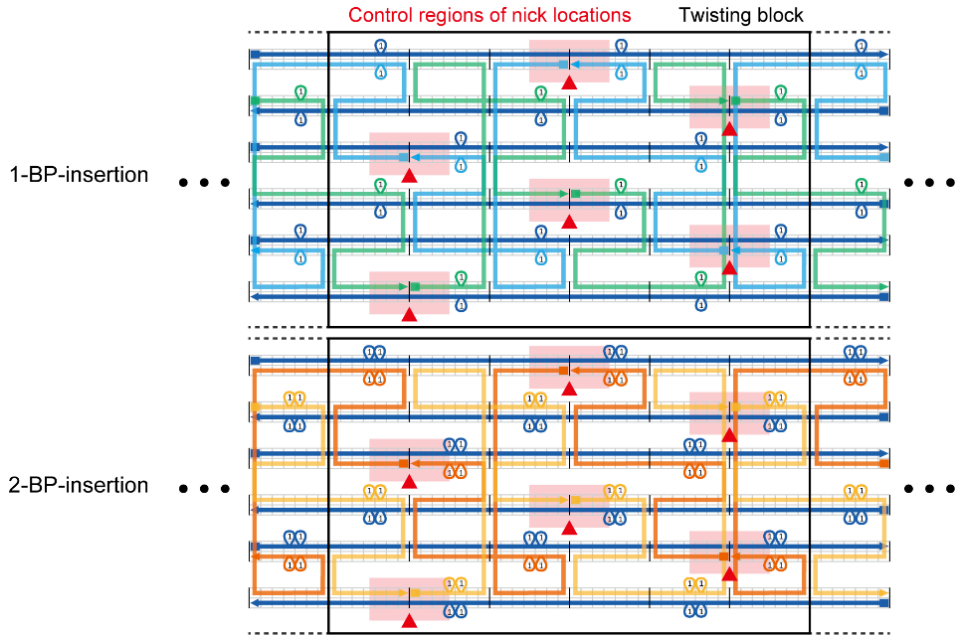


Figure 5-2. The caDNAno designs of twisting blocks with one or two BP-insertion.

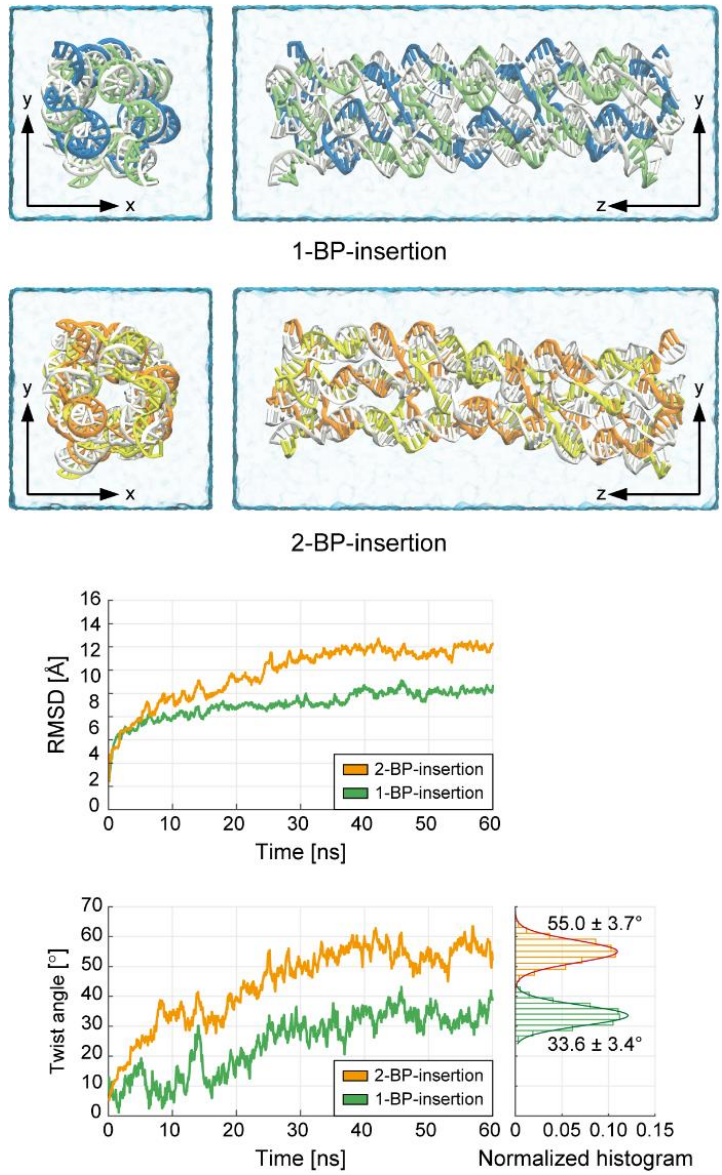


Figure 5-3. Final configurations of twisting blocks in equilibrium by MD simulation and the RMSD and twist angle trajectories of twisting blocks. RMSD trajectory was calculated for the minimized structure. Gaussian distribution of twist angles was obtained using the final 20-ns-long trajectory with mean and standard deviation as 33.6 ± 3.4° and 55.0 ± 3.7° for one and two BPs inserted blocks, respectively. The twist angles of 6HB structures with ten twisting blocks were then estimated as 336 ± 11° and 550 ± 12° for 1 and 2-BP-insertion.

### 5.2.3. Molecular dynamics simulation of 6-helix-bundle blocks

We performed MD simulations of 6HB DNA origami structures with BP-insertion (Figure 5-2 and Figure 5-3). At each end of the simulated structure, 7-BP-long strands were added to eliminate the boundary effect. Since it was difficult to observe the effects of sequence control of nicked BP steps due to the limited system size, the MD result of an arbitrary sequence was used to predict an approximately twist angle of 6HB structures. For the fast convergence of equilibrium states, the initial all-atom structures were developed after 100-ps-long the elastic network-guided simulation[32]. All-atom explicit solvent simulations were then performed after energy minimization as previously described for DNA oligomers. To smoothly convert the induced strain energy by BP-insertion into global torsion of structures, we applied weak harmonic constraints to Watson–Crick base-pairing from 0.5 kcal $mol^{-1}$ $Å^{-2}$ to zero during the 60-ns-long simulation as previous MD studies on DNA origami structures[31,32]. Final 20-ns-long equilibrated trajectories were sampled to calculate twist angle.

### 5.2.4. Measurement of the twist angle of 6-helix-bundle structures

The twist angle of a 6HB structure was calculated by the summation of local twist angles of twisting blocks between sequential hexagonal cross-sections locating at Holliday-junctions. To obtain the local twist angle between hexagonal cross-sections, we defined six vertexes locating at helices of the 6HB structure as the averaged point of local origins in four neighboring BPs next to the hexagonal cross-section (Figure 5-4).

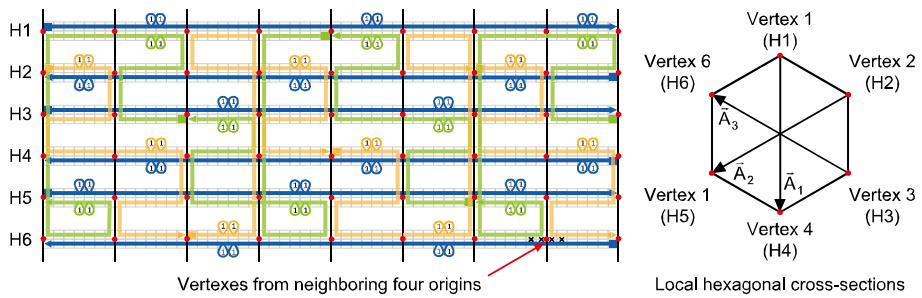


Figure 5-4. Vertex and vector definition of 6HB structure.

A hexagonal cross-section was determined to satisfy the smallest sum of the distance between each vertex and an arbitrary plane. Auxiliary vectors ($\vec{A}_1, \vec{A}_2, \vec{A}_3$) were defined in hexagonal cross-sections: $\vec{A}_1$, $\vec{A}_2$, and $\vec{A}_3$ were defined as the vectors from vertex 1 to 4, 2 to 5, and 3 to 6, respectively. Subsequently, the triads in hexagonal cross-sections were determined: x-vector ($\vec{x}$) representing normalized axial direction was defined as a normal vector of each cross-section, y-vector ($\vec{y}$) in the hexagonal cross-sections was described as a normalized vector with the projection of an averaged vector of auxiliary vectors on the cross-section, and the z-vector ($\vec{z}$) was calculated using the cross product of x- and y-vector. A rotation matrix (**R**) between sequential triads was then obtained using the triads as

$$[\vec{x}_{i+1} \quad \vec{y}_{i+1} \quad \vec{z}_{i+1}] = \mathbf{R}\,[\vec{x}_i \quad \vec{y}_i \quad \vec{z}_i] \tag{5-14}$$

where $i$ and $i+1$ represent successive hexagonal cross-sections. The rotation vector ($\vec{\omega}$) equivalent to the rotation matrix was obtained as

$$\vec{\omega} = [-W_{23} \quad W_{13} \quad -W_{12}]^T \tag{5-15}$$

where $W_{ij}$ is a component of the skew-symmetric matrix ($\mathbf{W}$) defined as

$$\mathbf{W} = \frac{1}{2}(\mathbf{R} - \mathbf{R}^T). \tag{5-16}$$

The local twist angle between sequential hexagonal cross-sections ($\Omega$) was finally calculated as

$$\Omega = \sin^{-1}(\vec{\omega} \cdot \vec{x}_i) \tag{5-17}$$

We obtained the Gaussian mean and standard deviation of the twist angle in the unit twisting block from MD simulation (Figure 5-2 and Figure 5-3). If the twist angle of the unit twisting block ($\Phi_u$) follows Gaussian distribution ($N_u$) as

$$N_u = N_u(\Phi, \Phi_{u0}, \sigma_u) = \frac{1}{\sigma_u\sqrt{2\pi}} \exp\left(-\frac{(\Phi - \Phi_{u0})^2}{2\sigma_u^2}\right) \tag{5-18}$$

where $\Phi_{u0}$ and $\sigma_u$ are the Gaussian mean and standard deviation of the twist angle of the twisting block, we could calculate the twist angle ($\Phi$) of a DNA structure, in which same twisting blocks are connected in sequence and the number of twisting blocks is $m$, as the sum of the independent Gaussian distributions of the twisting blocks based on the probability theory as

$$N = N(\Phi, \Phi_0, \sigma) = mN_u = N(\Phi, m\Phi_{u0}, \sqrt{m}\sigma_u) \tag{5-19}$$

Since ten twisting blocks were employed in the entire structure, the approximate range of twist angle of the structure was estimated as the mean of $10\Phi_{u0}$ and the standard deviation of $\sqrt{10}\sigma_u$ using those of unit twisting blocks ($\Phi_{u0}$ and $\sigma_u$) by MD simulation.

### 5.2.5. CanDo simulation based on finite element method

We performed CanDo simulation[17,33,34] for DNA origami structures used in experiments with the default setting (Figure 5-5), where a double-stranded DNA was assumed as generic B-form DNA: geometry of diameter of 2.25 nm, an axial rise of 0.34 nm per BP step, the helicity of 10.5 BPs per turn, stretch rigidity (S) of 1100 pN, bending rigidity (B) of 230 pN $nm^2$, and torsional rigidity (C) of 460 pN $nm^2$. BP steps were modeled as two-node linear elastic beam elements, and Holliday-junctions were modeled as rigid beam elements. To observe the effects of nicks on deformed shapes of DNA origami structures, we modeled nicks as the same two-node beam elements, but bending and torsional rigidities of nicked elements were modified by multiplying the mean B and C ratios of from experimental design as scale factors (Table 5-2).

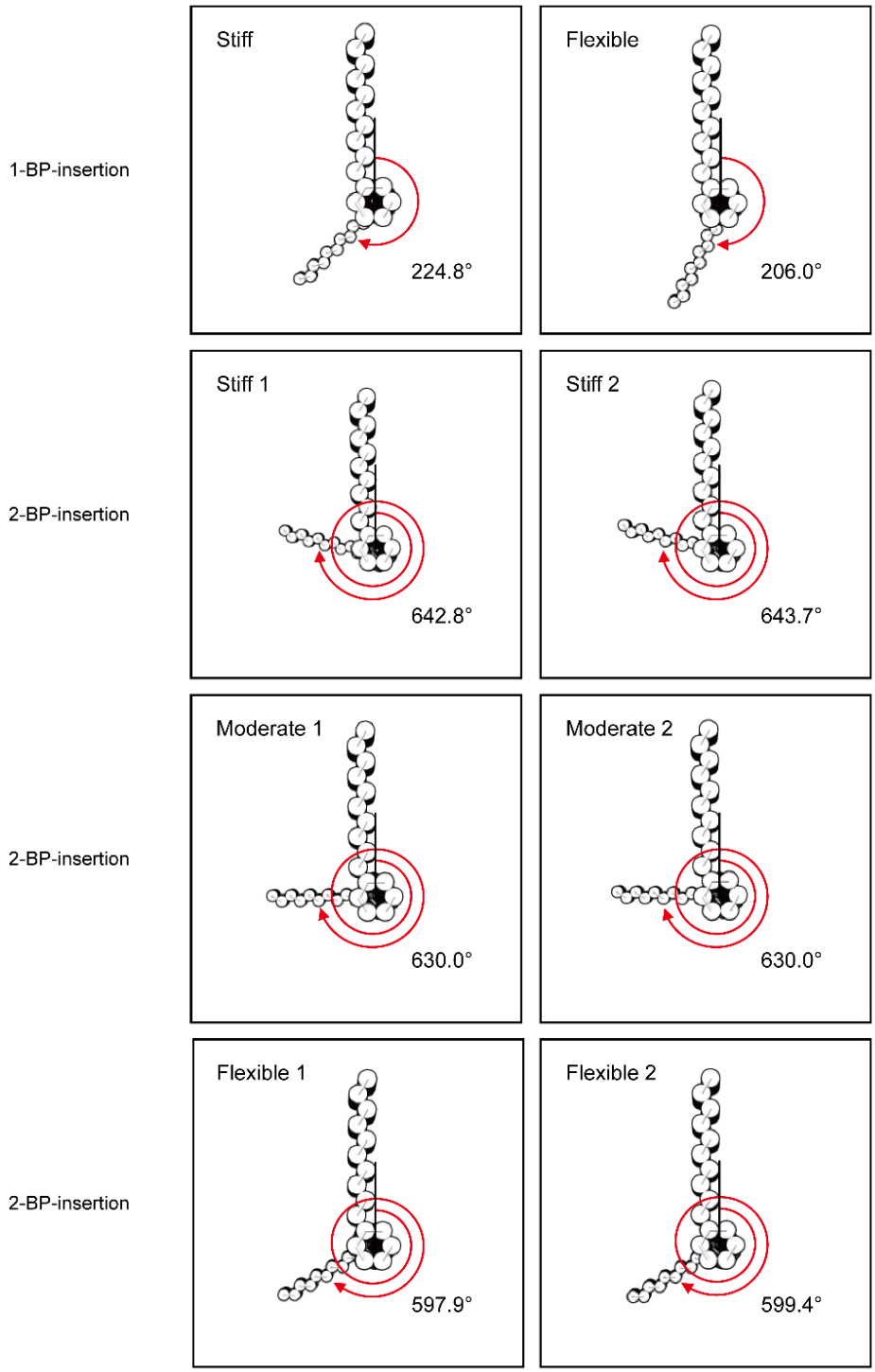


Figure 5-5. CanDo results of 6HB DNA origami structures with different helicities and nick rigidities.

### 5.2.6. Relation of the trans ratio with the global twist angle

We followed the details of derivation in the previous study[81]. Assuming that 6HB origami structures fluctuate in a harmonic potential, the Gaussian distribution of twist angle can be derived from the Boltzmann distribution as

$$N(\Phi, \Phi_0, \sigma) = N_0 \exp\left(-\frac{E}{k_B T}\right) = \frac{1}{\sigma\sqrt{2\pi}} \exp\left(-\frac{(\Phi - \Phi_0)^2}{2\sigma^2}\right) \quad (5\text{-}20)$$

where $N_0$ is the normalization coefficient as $1/(\sigma\sqrt{2\pi})$, $E$ is torsional harmonic energy as $E = k_t(\Phi - \Phi_0)^2/2$, $\Phi$ is the twist angle of 6HB structure, $\Phi_0$ is the equilibrium twist angle, $\sigma$ is the standard deviation of twist angle as $k_t/(k_B T)$, and $k_B T$ is the product of the Boltzmann constant, $k_B$, and the absolute temperature, $T$. Here, the torsional stiffness of 6HB structure ($k_t$) has a relation with torsional persistence length ($L_P$) and the length of 6HB structure (L) as

$$k_t = \frac{C_{6HB}}{L} = \frac{L_P k_B T}{L} \quad (5\text{-}21)$$

with

$$L_P = \frac{C_{6HB}}{k_B T} \quad (5\text{-}22)$$

where the torsional persistence length of 6HB DNA structures ($L_P$) was reported as 530 nm in a previous study[82], and the length of our structure is approximately 300 nm in AFM images (Figure 5-8). Using the equations above, the torsional harmonic energy yields the standard deviation of twist angle as

$$\sigma = \sqrt{\frac{k_B T}{k_t}} = \sqrt{\frac{L}{L_P}} = \sqrt{\frac{300}{530}} \simeq 0.7524 \text{ [rad]} \quad (5\text{-}23)$$

with

$$\frac{1}{2} k_t \sigma^2 = \frac{1}{2} k_B T \quad (5\text{-}24)$$

The probability to deposit into trans monomer of the 6HB structures is obtained as

$$f(\Phi) = \frac{|\Phi - 2k\pi|}{\pi} \text{ at } (2k-1)\pi \le \Phi \le (2k+1)\pi \tag{5-25}$$

where $k$ is an integer as a parametric variable $(\cdots, -2, -1, 0, 1, 2, \cdots)$. This probability to deposit into trans monomer is a kind of triangular function (Figure 5-6)

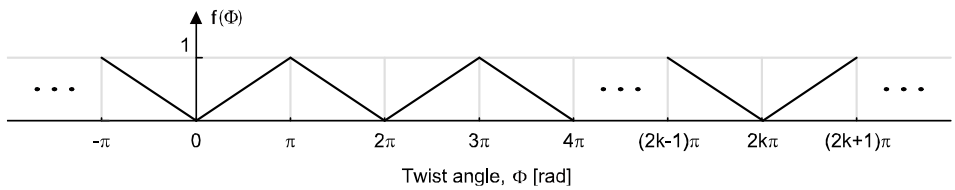


Figure 5-6. The probability to deposit into trans monomer.

The trans ratio, $TR(\Phi_0)$ in equilibrium is derived by the average probability of twist angle weighted in $\Phi_0$ for all $\Phi$ domain as

$$TR(\Phi_0) = \int_{-\infty}^{\infty} f(\Phi) N(\Phi, \Phi_0, \sigma) d\Phi$$

$$= \sum_k \int_{(2k-1)\pi}^{(2k+1)\pi} \frac{|\Phi - 2k\pi|}{\pi} \frac{1}{\sigma\sqrt{2\pi}} \exp\left(-\frac{(\Phi - \Phi_0)^2}{2\sigma^2}\right) d\Phi$$

$$= \frac{1}{\sigma\pi\sqrt{2\pi}} \sum_k \left\{ \begin{array}{l} \int_{2k\pi}^{(2k+1)\pi} \Phi \exp\left(-\frac{(\Phi - \Phi_0)^2}{2\sigma^2}\right) d\Phi \\ -\int_{(2k-1)\pi}^{2k\pi} \Phi \exp\left(-\frac{(\Phi - \Phi_0)^2}{2\sigma^2}\right) d\Phi \\ -2k\pi \int_{2k\pi}^{(2k+1)\pi} \exp\left(-\frac{(\Phi - \Phi_0)^2}{2\sigma^2}\right) d\Phi \\ +2k\pi \int_{(2k-1)\pi}^{2k\pi} \exp\left(-\frac{(\Phi - \Phi_0)^2}{2\sigma^2}\right) d\Phi \end{array} \right\} \tag{5-26}$$

Using the Gaussian integrals,

$$\int \Phi\psi(A + B\Phi) d\Phi = -\frac{1}{b^2}\left(\psi(a + b\Phi) + a\Psi(a + b\Phi)\right) + \text{Const.} \tag{5-27}$$

$$\int \psi(A + B\Phi)d\Phi = \frac{1}{b}\Psi(a + b\Phi) + \text{Const.} \tag{5-28}$$

where

$$\psi(a + b\Phi) = \frac{1}{\sqrt{2\pi}}\exp\left(-\frac{1}{2}(a + b\Phi)^2\right) \tag{5-29}$$

$$\Psi(a + b\Phi) = \int_{-\infty}^{\Phi}\psi(t)dt = \frac{1}{2}\left(1 + \text{erf}(\frac{\Phi}{\sqrt{2}})\right) \tag{5-30}$$

$$\text{erf}(\Phi) = \frac{1}{\sqrt{\pi}}\int_{-\Phi}^{\Phi}\exp(-t^2)dt \tag{5-31}$$

$$a + b\Phi = \frac{\Phi - \Phi_0}{\sigma} \tag{5-32}$$

$$a = -\frac{\Phi_0}{\sigma} \tag{5-33}$$

$$b = \frac{1}{\sigma} \tag{5-34}$$

We then obtained the four integral terms in the equation (5-26) as

$$\begin{aligned}\int_{2k\pi}^{(2k+1)\pi}\Phi\exp\left(-\frac{(\Phi - \Phi_0)^2}{2\sigma^2}\right)d\Phi \\ = -\sigma^2\left[\exp\left(-\frac{(2k\pi + \pi - \Phi_0)^2}{2\sigma^2}\right)\right. \\ \left. - \exp\left(-\frac{(2k\pi - \Phi_0)^2}{2\sigma^2}\right)\right] \\ + \frac{\sigma\Phi_0\sqrt{\pi}}{\sqrt{2}}\left[\text{erf}\left(\frac{2k\pi + \pi - \Phi_0}{\sigma\sqrt{2}}\right) - \text{erf}\left(\frac{2k\pi - \Phi_0}{\sigma\sqrt{2}}\right)\right]\end{aligned} \tag{5-35}$$

$$\int_{(2k-1)\pi}^{2k\pi} \Phi \exp\left(-\frac{(\Phi-\Phi_0)^2}{2\sigma^2}\right) d\Phi = -\sigma^2\left[\exp\left(-\frac{(2k\pi-\Phi_0)^2}{2\sigma^2}\right) - \exp\left(-\frac{(2k\pi-\pi-\Phi_0)^2}{2\sigma^2}\right)\right] + \frac{\sigma\Phi_0\sqrt{\pi}}{\sqrt{2}}\left[\mathrm{erf}\left(\frac{2k\pi-\Phi_0}{\sigma\sqrt{2}}\right) - \mathrm{erf}\left(\frac{2k\pi-\pi-\Phi_0}{\sigma\sqrt{2}}\right)\right] \quad (5\text{-}36)$$

$$\int_{2k\pi}^{(2k+1)\pi} \exp\left(-\frac{(\Phi-\Phi_0)^2}{2\sigma^2}\right) d\Phi = k\sigma\pi\sqrt{2\pi}\left[\mathrm{erf}\left(\frac{2k\pi+\pi-\Phi_0}{\sigma\sqrt{2}}\right) - \mathrm{erf}\left(\frac{2k\pi-\Phi_0}{\sigma\sqrt{2}}\right)\right] \quad (5\text{-}37)$$

$$\int_{(2k-1)\pi}^{2k\pi} \exp\left(-\frac{(\Phi-\Phi_0)^2}{2\sigma^2}\right) d\Phi = k\sigma\pi\sqrt{2\pi}\left[\mathrm{erf}\left(\frac{2k\pi-\Phi_0}{\sigma\sqrt{2}}\right) - \mathrm{erf}\left(\frac{2k\pi-\pi-\Phi_0}{\sigma\sqrt{2}}\right)\right] \quad (5\text{-}38)$$

Hence, by substituting the equations (5-35), (5-36), (5-37), and (5-38) into the equation (5-26), the relation of trans ratio with twist angle is derived as

$$\mathrm{TR}(\Phi_0) = \sum_k \left\{ -\frac{\sigma}{\pi\sqrt{2\pi}}\begin{bmatrix} \exp\left(-\frac{(2k\pi+\pi-\Phi_0)^2}{2\sigma^2}\right) \\ -2\exp\left(-\frac{(2k\pi-\Phi_0)^2}{2\sigma^2}\right) \\ +\exp\left(-\frac{(2k\pi-\pi-\Phi_0)^2}{2\sigma^2}\right) \end{bmatrix} + \left(\frac{\Phi_0}{2\pi}-k\right)\begin{bmatrix} \mathrm{erf}\left(\frac{2k\pi+\pi-\Phi_0}{\sigma\sqrt{2}}\right) \\ -2\mathrm{erf}\left(\frac{2k\pi-\Phi_0}{\sigma\sqrt{2}}\right) \\ +\mathrm{erf}\left(\frac{2k\pi-\pi-\Phi_0}{\sigma\sqrt{2}}\right) \end{bmatrix} \right\} \quad (5\text{-}39)$$

Here, the arguments in the k-summation rapidly approach to zero when $\Phi_0$ is out of the range of $[(2k-1)\pi, (2k+1)\pi]$. This relation is illustrated in the range of $0 \leq \Phi \leq 4\pi$ (Figure 5-7).

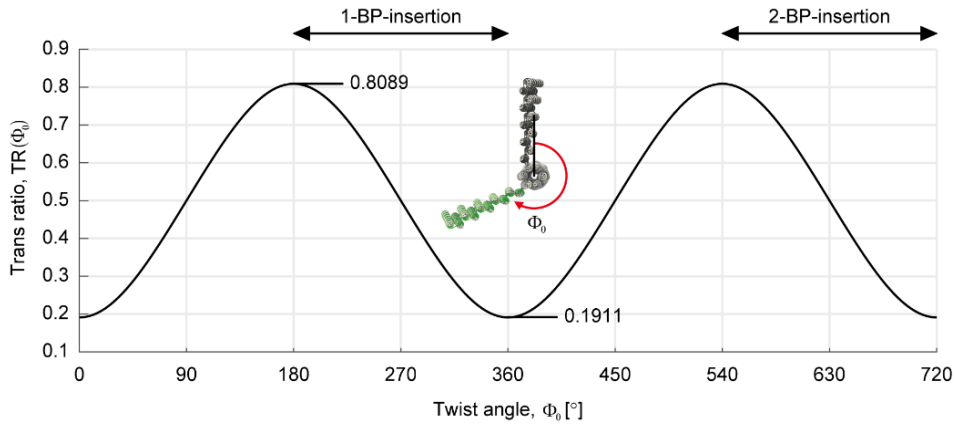


Figure 5-7. The relation of trans ratio versus twist angle.

Here, since multiple solutions of twist angle existed for a specific trans ratio, we obtained the approximate domain of twist angle from MD results of twisting blocks ($336 \pm 11°$ for 1-BP-insertion and $550 \pm 12°$ for 2-BP-insertion in Figure 5-3) and CanDo results of entire 6HB structures (206-225° for 1-BP-insertion and 598-644° for 2-BP-insertion in Figure 5-5). This suggests the twist angle of structures would be in the range of 180-360° for 1-BP-insertion and 540-720° for 2-BP-insertion, respectively, as expressed above. We then present the numerical solution of the twist angle for a representative trans ratio using the equation (5-39) as below (Table 5-3).

Table 5-3. Numerical solution of trans ratio for different structures.

| Numerical solution | | Trans ratio | | | | | | |
|---|---|---|---|---|---|---|---|---|
| | | 0.2 | 0.3 | 0.4 | 0.5 | 0.6 | 0.7 | 0.8 |
| Twist angle [°] | 1-BP-ins. | 346.8 | 311.6 | 289.7 | 270.0 | 250.3 | 228.4 | 193.2 |
| | 2-BP-ins. | 706.8 | 671.6 | 649.7 | 630.0 | 610.3 | 588.4 | 553.2 |

### 5.2.7. Preparation of DNA origami structures

Sequence and connectivity information in 6HB DNA origami structures were designed using caDNAno software[74], and the sequences of all constituting staples were selected[18]. We purchased the M13mp18 single-stranded DNA of 7249 nucleotides for scaffold strands from New England Biolabs (N4040s), staple strands less than 50 nucleotides from Bioneer Corporation, and reagents from Sigma-Aldrich. All oligonucleotides were purified by the reverse-phase cartridge (Bio-RP) method provided by Bioneer Corporation. We also used the staples purified with the polyacrylamide gel electrophoresis (PAGE) method to examine any potential effect of purification method, but no clear dependence of the results on the purification method was observed (See next section). For the assembly of DNA structures, the folding mixture containing 10 nM of scaffold DNA, 100 nM of each staple strand, 20 mM of $MgCl_2$, and 1 × TAE buffer (40 mM Tris-acetate and 1 mM EDTA) was annealed using a thermocycler (T100, Bio-Rad) with a temperature gradient from 80 to 65 °C by −0.25 °C per minute and 65 to 25 °C by −1 °C per hour.

### 5.2.8. Image analysis using atomic force microscopy

To observe the shape of the assembled 6HB DNA origami structures, we diluted the samples to approximately 0.5 nM with a folding buffer of 1 × TAE and 20 mM $MgCl_2$, and the samples were deposited on a freshly cleaved mica substrate (highest grade V1 Mica, Ted-Pella Corporation). After incubation for 5 minutes, the substrate was washed with DI water and gently dried by $N_2$ gun (< 0.1 kgf $cm^{-2}$). AFM images were taken by NX10 (Park Systems) using non-contact mode in SmartScan software. A PPP-NCHR probe with a spring constant of 42 N $m^{-1}$ was used in the measurements (Nanosensors). Measured images were flattened with linear and quadratic orders using XEI 4.1.0 program (Park Systems). For all experimental cases, at least eleven positions on the mica substrate were scanned and more than a thousand monomer structures were collected (Figure 5-8, Table 5-4, and Table 5-5). Here, the twist angle of structures was indirectly measured from two-dimensional AFM images. Each monomer structure took either the cis state (flags on the same side) or the trans state (flags in the opposite sides) in the AFM image. The number of monomeric structures in each state was then counted to calculate the trans ratio as the number of monomeric structures in the trans state divided by the total number of monomers. The trans ratio (TR) was finally converted to the twist angle from the theoretical function[81] as $TR = f(\Phi_0, \sigma, k)$, where $\Phi_0$ is the equilibrium twist angle of structures, $\sigma$ is the standard deviation of the twist angle by thermal fluctuation estimated as 0.7524 rad for the torsional persistence length of 530 nm proposed in the previous studies[81,82] and the axial length of 300 nm in our 6HB structures, and $k$ is a parametric integer indicating the range of twist angle of 6HB structures. We calculated the trans ratios for each AFM image of a structure from which their mean and standard deviation were calculated.

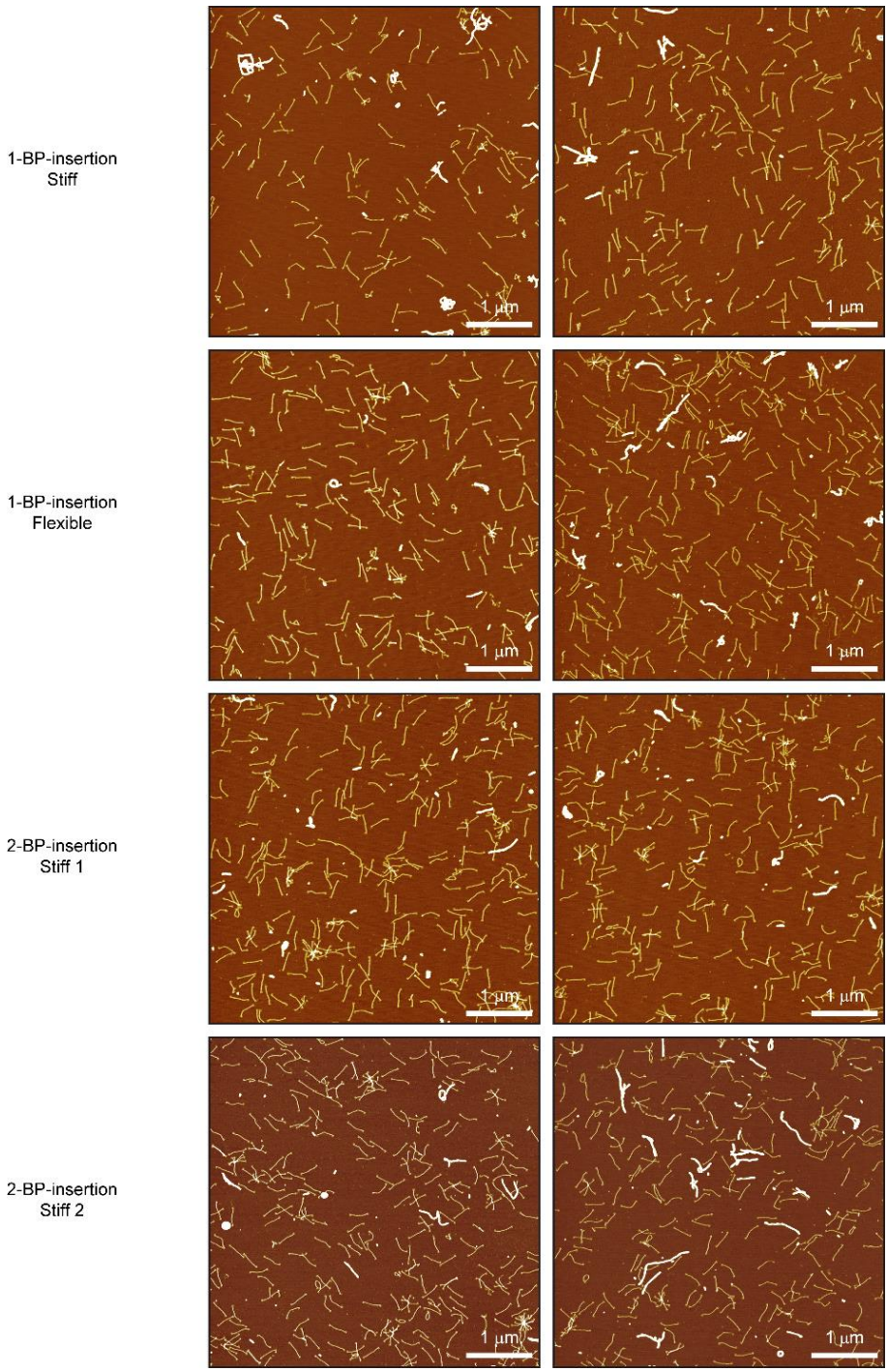


Figure 5-8. Atomic force microscope (AFM) images of twisted 6HB DNA origami structures. All scale bars represent 1 µm.

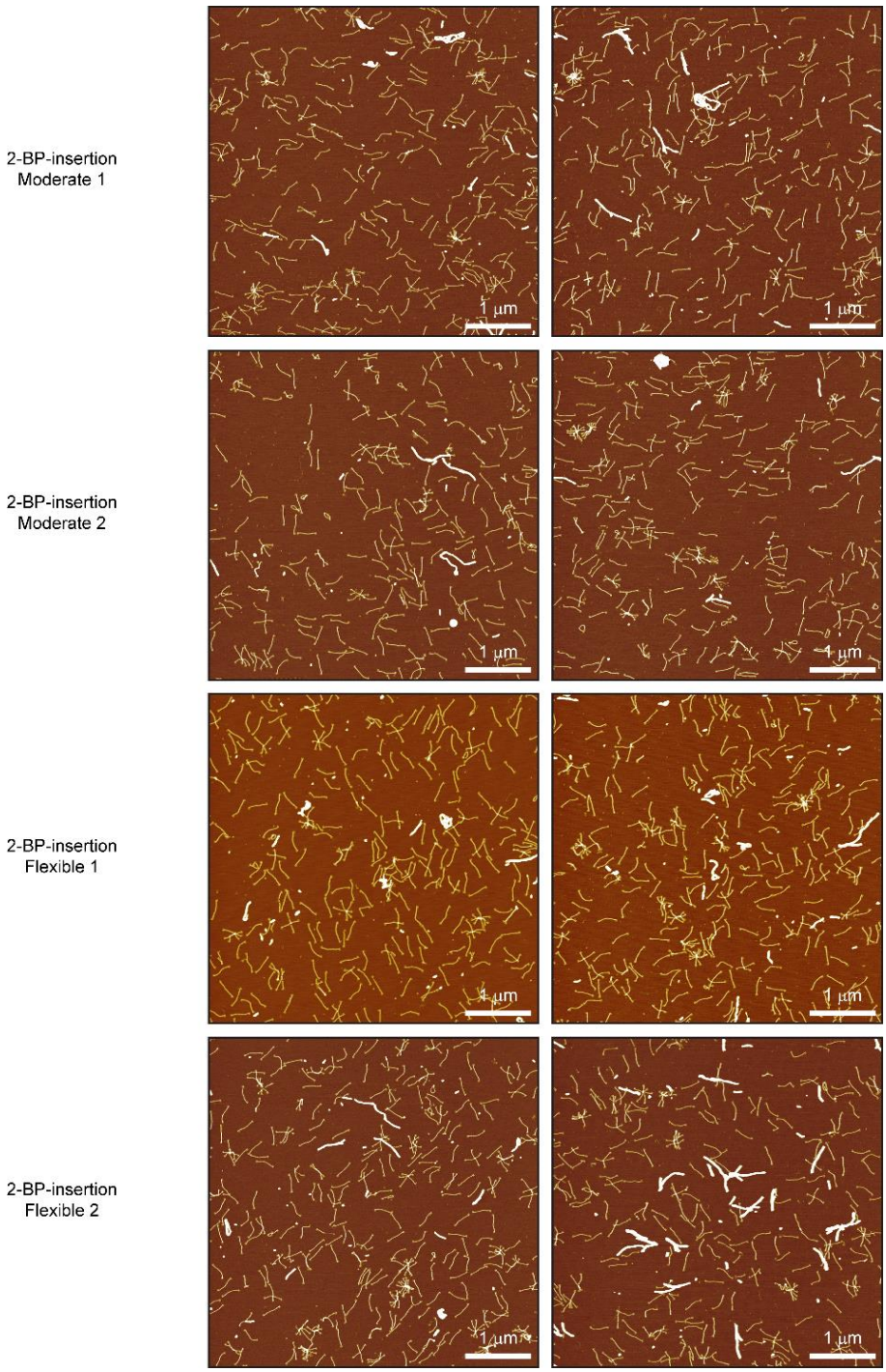


Figure 5-8 (Continued).

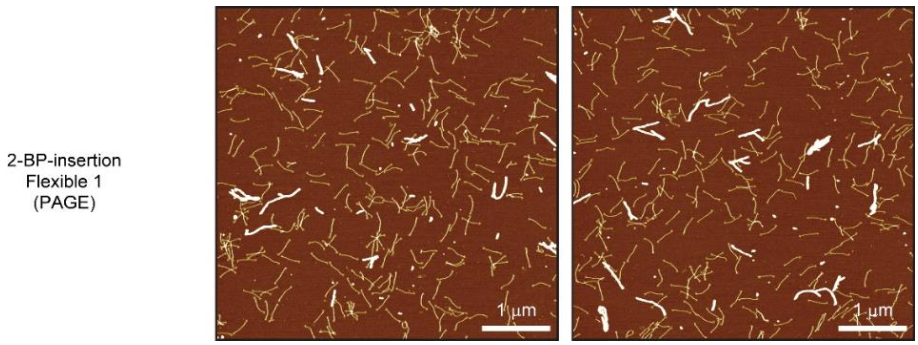


Figure 5-8 (Continued).

Table 5-4. Summary of AFM analysis. The trans ratio of DNA origami structures was calculated as the ratio of trans monomers for the total number of monomers. Trans ratio values of AFM images were used to calculate the standard deviation in brackets.

| The number of monomers | 1-BP-insertion | | 2-BP-insertion | | | | | | |
|---|---|---|---|---|---|---|---|---|---|
| | Stiff | Flex. | Stiff 1 | Stiff 2 | Mod. 1 | Mod. 2 | Flex. 1 | Flex. 2 | Flex. 1 (PAGE) |
| Trans | 760 | 860 | 722 | 681 | 714 | 895 | 818 | 788 | 523 |
| Cis | 1223 | 1308 | 631 | 490 | 489 | 498 | 311 | 317 | 203 |
| Trans + Cis | 1983 | 2168 | 1353 | 1171 | 1203 | 1393 | 1129 | 1105 | 887 |

| Results | 1-BP-insertion | | 2-BP-insertion | | | | | | |
|---|---|---|---|---|---|---|---|---|---|
| | Stiff | Flex. | Stiff 1 | Stiff 2 | Mod. 1 | Mod. 2 | Flex. 1 | Flex. 2 | Flex. 1 (PAGE) |
| Trans ratio (Std) | 0.38 (0.08) | 0.40 (0.07) | 0.534 (0.052) | 0.582 (0.057) | 0.594 (0.024) | 0.642 (0.044) | 0.725 (0.061) | 0.7131 (0.030) | 0.720 (0.027) |
| Twist angle [°] (Std) | 293.3 (16.0) | 290.5 (13.8) | 624.0 (8.5) | 613.8 (11.4) | 611.6 (4.8) | 601.5 (9.6) | 582.1 (17.6) | 585.0 (9.5) | 582.2 (7.2) |

Table 5-5. The number of monomers and trans-cis ratio from AFM images.

| 1-BP-insertion designs | | | | | | | |
|---|---|---|---|---|---|---|---|
| Structure design | AFM image | The number of monomers | | | | Trans ratio | Cis ratio |
| | | Trans | Cis | Cis + Trans | | | |
| Stiff | 1 | 22 | 32 | 54 | | 0.4074 | 0.5926 |
| | 2 | 37 | 50 | 87 | | 0.4253 | 0.5747 |
| | 3 | 52 | 59 | 111 | | 0.4685 | 0.5315 |
| | 4 | 45 | 60 | 105 | | 0.4286 | 0.5714 |
| | 5 | 33 | 50 | 83 | | 0.3976 | 0.6024 |
| | 6 | 23 | 68 | 91 | | 0.2527 | 0.7473 |
| | 7 | 20 | 53 | 73 | | 0.2740 | 0.7260 |
| | 8 | 22 | 59 | 81 | | 0.2716 | 0.7284 |
| | 9 | 25 | 60 | 85 | | 0.2941 | 0.7059 |
| | 10 | 21 | 59 | 80 | | 0.2625 | 0.7375 |
| | 11 | 26 | 58 | 84 | | 0.3095 | 0.6905 |
| | 12 | 35 | 74 | 109 | | 0.3211 | 0.6789 |
| | 13 | 48 | 65 | 113 | | 0.4248 | 0.5752 |
| | 14 | 45 | 77 | 122 | | 0.3689 | 0.6311 |
| | 15 | 52 | 55 | 107 | | 0.4860 | 0.5140 |
| | 16 | 60 | 70 | 130 | | 0.4615 | 0.5385 |
| | 17 | 35 | 66 | 101 | | 0.3465 | 0.6535 |
| | 18 | 37 | 49 | 86 | | 0.4302 | 0.5698 |
| | 19 | 34 | 47 | 81 | | 0.4198 | 0.5802 |
| | 20 | 47 | 51 | 98 | | 0.4796 | 0.5204 |
| | 21 | 41 | 61 | 102 | | 0.4020 | 0.5980 |
| | Sum | 760 | 1223 | 1983 | Mean | 0.3833 | 0.6167 |
| | | | | | Std | 0.0767 | 0.0767 |
| Flexible | 1 | 54 | 61 | 115 | | 0.4696 | 0.5304 |
| | 2 | 47 | 64 | 111 | | 0.4234 | 0.5766 |
| | 3 | 49 | 55 | 104 | | 0.4712 | 0.5288 |
| | 4 | 42 | 51 | 93 | | 0.4516 | 0.5484 |
| | 5 | 49 | 54 | 103 | | 0.4757 | 0.5243 |
| | 6 | 56 | 53 | 109 | | 0.5138 | 0.4862 |
| | 7 | 26 | 64 | 90 | | 0.2889 | 0.7111 |
| | 8 | 29 | 66 | 95 | | 0.3053 | 0.6947 |
| | 9 | 20 | 58 | 78 | | 0.2564 | 0.7436 |
| | 10 | 36 | 67 | 103 | | 0.3495 | 0.6505 |
| | 11 | 35 | 55 | 90 | | 0.3889 | 0.6111 |
| | 12 | 45 | 80 | 125 | | 0.3600 | 0.6400 |
| | 13 | 51 | 65 | 116 | | 0.4397 | 0.5603 |
| | 14 | 36 | 68 | 104 | | 0.3462 | 0.6538 |
| | 15 | 41 | 60 | 101 | | 0.4059 | 0.5941 |
| | 16 | 44 | 60 | 104 | | 0.4231 | 0.5769 |
| | 17 | 43 | 60 | 103 | | 0.4175 | 0.5825 |
| | 18 | 33 | 74 | 107 | | 0.3084 | 0.6916 |
| | 19 | 44 | 76 | 120 | | 0.3667 | 0.6333 |
| | 20 | 38 | 57 | 95 | | 0.4000 | 0.6000 |
| | 21 | 42 | 60 | 102 | | 0.4118 | 0.5882 |
| | Sum | 860 | 1308 | 2168 | Mean | 0.3967 | 0.6033 |
| | | | | | Std | 0.0679 | 0.0679 |

Table 5-5 (Continued).

| 2-BP-insertion designs | | | | | | | |
|---|---|---|---|---|---|---|---|
| Structure designs | AFM image | The number of monomers | | | | Trans ratio | Cis ratio |
| | | Trans | Cis | Cis + Trans | | | |
| Stiff 1 | 1 | 48 | 54 | 102 | | 0.4706 | 0.5294 |
| | 2 | 67 | 49 | 116 | | 0.5776 | 0.4224 |
| | 3 | 64 | 57 | 121 | | 0.5289 | 0.4711 |
| | 4 | 61 | 47 | 108 | | 0.5648 | 0.4352 |
| | 5 | 63 | 65 | 128 | | 0.4922 | 0.5078 |
| | 6 | 58 | 62 | 120 | | 0.4833 | 0.5167 |
| | 7 | 62 | 34 | 96 | | 0.6458 | 0.3542 |
| | 8 | 51 | 52 | 103 | | 0.4951 | 0.5049 |
| | 9 | 59 | 56 | 115 | | 0.5130 | 0.4870 |
| | 10 | 57 | 50 | 107 | | 0.5327 | 0.4673 |
| | 11 | 76 | 52 | 128 | | 0.5938 | 0.4063 |
| | 12 | 56 | 53 | 109 | | 0.5138 | 0.4862 |
| | Sum | 722 | 631 | 1353 | Mean | 0.5336 | 0.4664 |
| | | | | | Std | 0.0519 | 0.0519 |
| Stiff 2 | 1 | 62 | 55 | 117 | | 0.5299 | 0.4701 |
| | 2 | 66 | 57 | 123 | | 0.5366 | 0.4634 |
| | 3 | 56 | 47 | 103 | | 0.5437 | 0.4563 |
| | 4 | 60 | 45 | 105 | | 0.5714 | 0.4286 |
| | 5 | 76 | 32 | 108 | | 0.7037 | 0.2963 |
| | 6 | 58 | 43 | 101 | | 0.5743 | 0.4257 |
| | 7 | 70 | 42 | 112 | | 0.6250 | 0.3750 |
| | 8 | 70 | 37 | 107 | | 0.6542 | 0.3458 |
| | 9 | 56 | 41 | 97 | | 0.5773 | 0.4227 |
| | 10 | 57 | 45 | 102 | | 0.5588 | 0.4412 |
| | 11 | 50 | 46 | 96 | | 0.5208 | 0.4792 |
| | Sum | 681 | 490 | 1171 | Mean | 0.5816 | 0.4184 |
| | | | | | Std | 0.0571 | 0.0571 |

Table 5-5 (Continued).

| 2-BP-insertion designs | | | | | | | |
|---|---|---|---|---|---|---|---|
| Structure designs | AFM image | The number of monomers | | | | Trans ratio | Cis ratio |
| | | Trans | Cis | Cis + Trans | | | |
| Mod. 1 | 1 | 73 | 54 | 127 | | 0.5748 | 0.4252 |
| | 2 | 63 | 37 | 100 | | 0.6300 | 0.3700 |
| | 3 | 53 | 34 | 87 | | 0.6092 | 0.3908 |
| | 4 | 52 | 41 | 93 | | 0.5591 | 0.4409 |
| | 5 | 53 | 41 | 94 | | 0.5638 | 0.4362 |
| | 6 | 70 | 46 | 116 | | 0.6034 | 0.3966 |
| | 7 | 58 | 42 | 100 | | 0.5800 | 0.4200 |
| | 8 | 61 | 42 | 103 | | 0.5922 | 0.4078 |
| | 9 | 65 | 42 | 107 | | 0.6075 | 0.3925 |
| | 10 | 59 | 34 | 93 | | 0.6344 | 0.3656 |
| | 11 | 58 | 41 | 99 | | 0.5859 | 0.4141 |
| | 12 | 49 | 35 | 84 | | 0.5833 | 0.4167 |
| | Sum | 714 | 489 | 1203 | Mean | 0.5935 | 0.4065 |
| | | | | | Std | 0.0239 | 0.0239 |
| Mod. 2 | 1 | 102 | 45 | 147 | | 0.6939 | 0.3061 |
| | 2 | 85 | 41 | 126 | | 0.6746 | 0.3254 |
| | 3 | 67 | 38 | 105 | | 0.6381 | 0.3619 |
| | 4 | 67 | 51 | 118 | | 0.5678 | 0.4322 |
| | 5 | 69 | 39 | 108 | | 0.6389 | 0.3611 |
| | 6 | 65 | 47 | 112 | | 0.5804 | 0.4196 |
| | 7 | 74 | 43 | 117 | | 0.6325 | 0.3675 |
| | 8 | 72 | 31 | 103 | | 0.6990 | 0.3010 |
| | 9 | 71 | 34 | 105 | | 0.6762 | 0.3238 |
| | 10 | 78 | 53 | 131 | | 0.5954 | 0.4046 |
| | 11 | 79 | 37 | 116 | | 0.6810 | 0.3190 |
| | 12 | 66 | 39 | 105 | | 0.6286 | 0.3714 |
| | Sum | 895 | 498 | 1393 | Mean | 0.6425 | 0.3575 |
| | | | | | Std | 0.0442 | 0.0442 |

Table 5-5 (Continued).

| 2-BP-insertion designs | | | | | | | |
|---|---|---|---|---|---|---|---|
| Structure designs | AFM image | The number of monomers | | | | Trans ratio | Cis ratio |
| | | Trans | Cis | Trans + Cis | | | |
| Flex. 1 | 1 | 104 | 27 | 131 | | 0.7939 | 0.2061 |
| | 2 | 68 | 37 | 105 | | 0.6476 | 0.3524 |
| | 3 | 76 | 31 | 107 | | 0.7103 | 0.2897 |
| | 4 | 64 | 23 | 87 | | 0.7356 | 0.2644 |
| | 5 | 75 | 31 | 106 | | 0.7075 | 0.2925 |
| | 6 | 87 | 36 | 123 | | 0.7073 | 0.2927 |
| | 7 | 81 | 26 | 107 | | 0.7570 | 0.2430 |
| | 8 | 72 | 25 | 97 | | 0.7423 | 0.2577 |
| | 9 | 75 | 26 | 101 | | 0.7426 | 0.2574 |
| | 10 | 77 | 21 | 98 | | 0.7857 | 0.2143 |
| | 11 | 39 | 28 | 67 | | 0.5821 | 0.4179 |
| | Sum | 818 | 311 | 1129 | Mean | 0.7245 | 0.2755 |
| | | | | | Std | 0.0609 | 0.0609 |
| Flex. 2 | 1 | 61 | 26 | 87 | | 0.7011 | 0.2989 |
| | 2 | 54 | 29 | 83 | | 0.6506 | 0.3494 |
| | 3 | 67 | 26 | 93 | | 0.7204 | 0.2796 |
| | 4 | 67 | 21 | 88 | | 0.7614 | 0.2386 |
| | 5 | 79 | 30 | 109 | | 0.7248 | 0.2752 |
| | 6 | 59 | 27 | 86 | | 0.6860 | 0.3140 |
| | 7 | 62 | 28 | 90 | | 0.6889 | 0.3111 |
| | 8 | 76 | 31 | 107 | | 0.7103 | 0.2897 |
| | 9 | 65 | 24 | 89 | | 0.7303 | 0.2697 |
| | 10 | 78 | 27 | 105 | | 0.7429 | 0.2571 |
| | 11 | 62 | 27 | 89 | | 0.6966 | 0.3034 |
| | 12 | 58 | 21 | 79 | | 0.7342 | 0.2658 |
| | Sum | 788 | 317 | 1105 | Mean | 0.7131 | 0.2869 |
| | | | | | Std | 0.0298 | 0.0298 |
| Flex. 1 (PAGE) | 1 | 70 | 26 | 96 | | 0.7292 | 0.2708 |
| | 2 | 74 | 32 | 106 | | 0.6981 | 0.3019 |
| | 3 | 77 | 24 | 101 | | 0.7624 | 0.2376 |
| | 4 | 69 | 26 | 95 | | 0.7263 | 0.2737 |
| | 5 | 71 | 33 | 104 | | 0.6827 | 0.3173 |
| | 6 | 83 | 29 | 112 | | 0.7411 | 0.2589 |
| | 7 | 79 | 33 | 112 | | 0.7054 | 0.2946 |
| | Sum | 523 | 203 | 726 | Mean | 0.7204 | 0.2796 |
| | | | | | Std | 0.0272 | 0.0272 |

### 5.2.9. Agarose gel electrophoresis

Assembled 6HB DNA origami structures were electrophoresed using 1.5% agarose gels containing 0.5 × TBE (45 mM Tris-borate and 1 mM EDTA), 12 mM of $MgCl_2$, and 0.5 μg $ml^{-1}$ of ethidium bromide (EtBr, Noble Bioscience Corporation). The 6HB structures were then electrophoresed for 1.5 hours at 75 V bias voltage (~3.7 V $cm^{-1}$) in an ice-water cooling chamber (i-Myrun, Cosmo Bio Corporation). Gel imaging was performed using a GelDoc XR+ device and Image Lab v5.1 program of Bio-Rad (Figure 5-9).

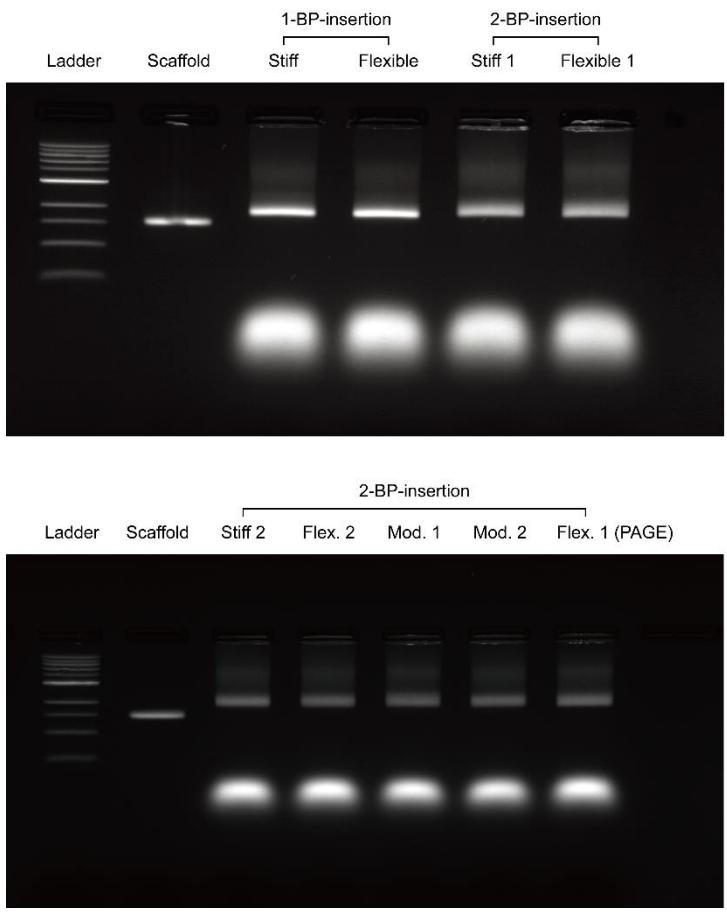


Figure 5-9. Agarose gel electrophoresis result of twisted 6HB DNA origami structures. Ladder: 1kb DNA ladder (New England Biolabs N3232S). Scaffold: M13mp18 single-stranded scaffold DNA.

### 5.2.10. Comparison of Bio-RP and PAGE in the purification of staples

We investigated whether the purification method used in the synthesis of oligonucleotides affects the trans ratio of assembled DNA origami structures. Here, 60 staples comprising ten twisting blocks of the flexible 1 design with 2-BP-insertion were purified using the polyacrylamide gel electrophoresis (PAGE) method, in which the manufacturer guarantees a higher purity of more than 95%. We obtained the matrix-assisted laser desorption/ionization time-of-flight mass spectrometry (MALDI-TOF) data for representative ten staples (one staple per each twisting block) purified by both methods (Table 5-6). According to the result of MALDI-TOF, purified staples using reverse-phase cartridge (Bio-RP) and PAGE showed an almost identical mass spectrum with a single and clear peak, indicating only oligonucleotides with the desired length existed in the stock solution (Figure 5-10). Noting that the maximum error of the MALDI-TOF spectrum is typically around 0.24%, we could confirm that both Bio-RP and PAGE methods were reliable to obtain the full-length and same sequence of staples. Also, we constructed two versions of the flexible 1 design using the staples purified with Bio-RP and PAGE methods (Figure 5-8). No distinguishable difference in the trans ratio was observed between these two versions of structures (Table 5-4). The mean and standard deviation of the trans ratio by two methods were 0.7245 and 0.0609 for Bio-RP, and 0.7204 and 0.0272 for PAGE, respectively. Accordingly, we concluded that the trans ratio was hardly affected by the purification method for staples because both methods yield sufficiently high purity.

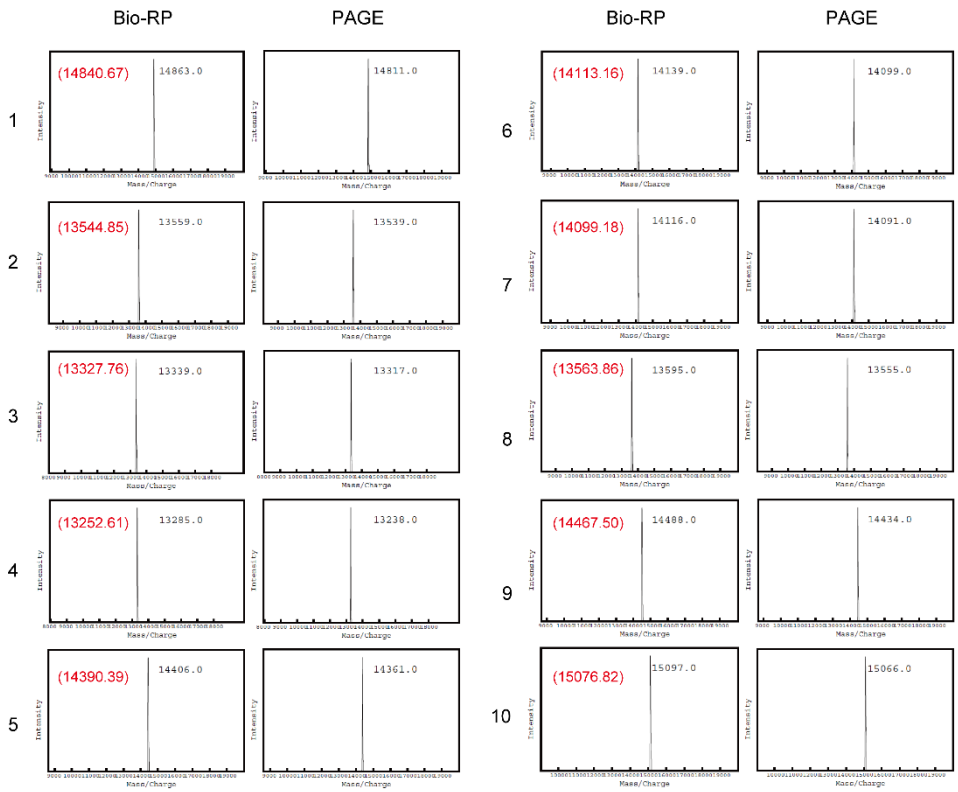


Figure 5-10. The results of MALDI-TOF using Bio-RP and PAGE methods. We obtained the MALDI-TOF results for representative ten staples (one staple per each twisting block). Red numbers in brackets indicate the ideal molecular weight of the staple sequence (Table 5-6).

Table 5-6. MALDI-TOF results by Bio-RP and PAGE methods. For the comparison of Bio-RP and PAGE methods in oligonucleotides purification, representative ten staples were used to MALDI-TOF (Figure 5-10). The error is the difference in molecular weight divided by the reference value.

| Index | Staple sequence | Molecular weight [Da] (Reference) |
|---|---|---|
| 1 | TCGTCTTTGCACTAACGAGGCATAGTAAGAGAATTGTGCCAAGCGCGA | 14840.67 |
| 2 | TTCCACAGGGGAAAAATACCACATTCAACTGAGGCGCCAAAAGA | 13544.85 |
| 3 | ACACAGGAGCGGAACAACATTATTACAAAAGAGGAAATACGTA | 13327.76 |
| 4 | CCTCGTAACCATCAGGACGTTGGGAAGGACCTTCTGAGGACTA | 13252.61 |
| 5 | CGCCACCCTACTATGGTTGTGAATTACCTTATCAAATCAGCGAAAGA | 14390.39 |
| 6 | ATTACTCCCTCGGATAAGTGCCGTCGAAGGCCGACGGAATACCCAA | 14113.16 |
| 7 | CAGTCAGGAACAAACCGAGGAAACGCATTAGCAACATAGCCCCCTT | 14099.18 |
| 8 | AGAGGCTAGGCCACCTTTTTAAGAAAAGTAGAAACGCTGCCTTT | 13563.86 |
| 9 | CCCTGCTAGCAATTAAGAGCAAGAAACAAAGAAAATAAACCATCGAT | 14467.50 |
| 10 | ACGGGGTCAGAACTCCTAATATCAGAGAGATTCAACCGACCAGTAGCAC | 15076.82 |

| Index | Molecular weight [Da] (Bio-RP) | Molecular weight [Da] (PAGE) | Error [%] (Bio-RP) | Error [%] (PAGE) |
|---|---|---|---|---|
| 1 | 14863.0 | 14811.0 | 0.15 | 0.20 |
| 2 | 13559.0 | 13539.0 | 0.10 | 0.04 |
| 3 | 13339.0 | 13317.0 | 0.08 | 0.08 |
| 4 | 13285.0 | 13238.0 | 0.24 | 0.11 |
| 5 | 14406.0 | 14361.0 | 0.11 | 0.20 |
| 6 | 14139.0 | 14099.0 | 0.18 | 0.10 |
| 7 | 14116.0 | 14091.0 | 0.12 | 0.06 |
| 8 | 13595.0 | 13555.0 | 0.23 | 0.07 |
| 9 | 14488.0 | 14434.0 | 0.14 | 0.23 |
| 10 | 15097.0 | 15066.0 | 0.13 | 0.07 |

## 5.3. Twist control of DNA nanostructures by programming nick sequences

Our comprehensive and quantitative investigation on DNA nicks revealed that the major mechanical role of nicks in the stacked configuration is the sequence-dependent reduction of torsional rigidity. This torsion-softening effect of nicks is applicable particularly to twisted DNA origami bundle structures as multiple nicks scattered all over the section, and their locations can be easily adjusted. In order to experimentally demonstrate the usefulness of mechanical rigidities quantified for all regular and nicked BP steps in designing synthetic DNA nanostructure, we designed 6HB DNA origami structures whose ten twisting blocks controlled the global twist angle in the middle of the structure (Figure 5-11).

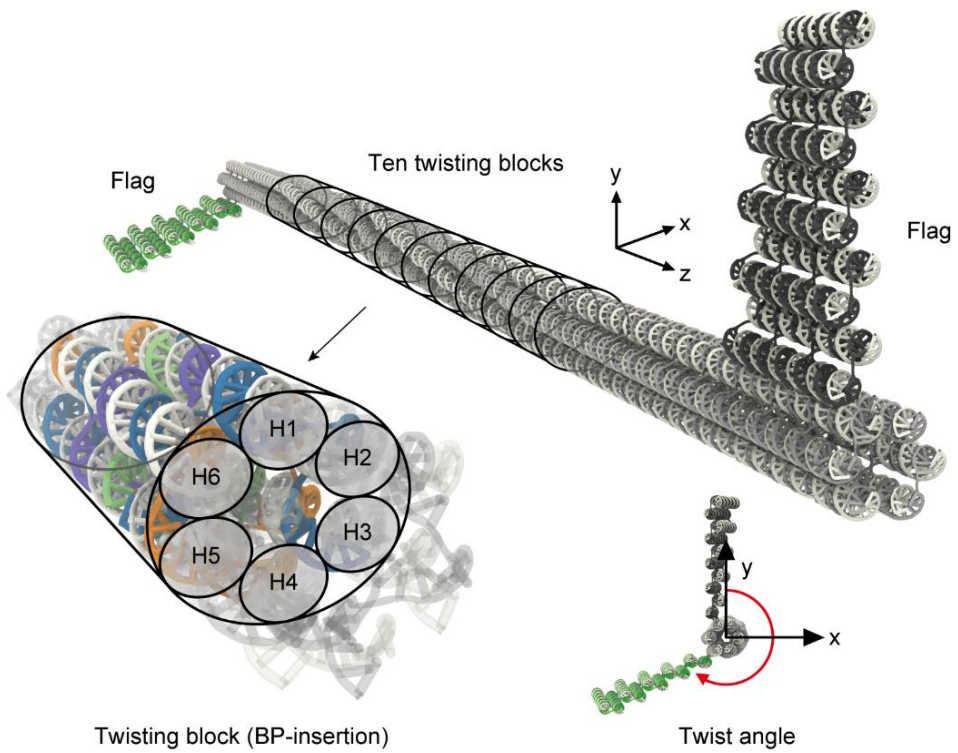


Figure 5-11. Schematic illustration of a 6HB structure. 6HB structures were designed to include ten twisting blocks composed of H1-H6 helices with BP-insertion. Two terminal flags showed the torsional deformation.

### 5.3.1. Sequences design to control the twist of DNA nanostructure

In a twisting block, each helix was 42-BP-long, the number of inserted BPs was adjusted, and six locations of nicks was selected by changing the length of the constituent staple strands (Figure 5-12). Inserted BPs to twisting blocks introduce the torsional mismatch of cross-linked DNA helices[7], consequently inducing the torsional strain energy by the geometric constraints. We modulated the twist deformation from induced torsional energy in twisting blocks by controlling the rigidities of nicks through sequence design based on our rigidity data, thereby regulating the globally twisted shape of the 6HB structure. We expected that only the twist angle of structures could be controlled by nicks inferred from a previous study that revealed almost no effect of nicks on the bending rigidity of DNA nanotubes[83].

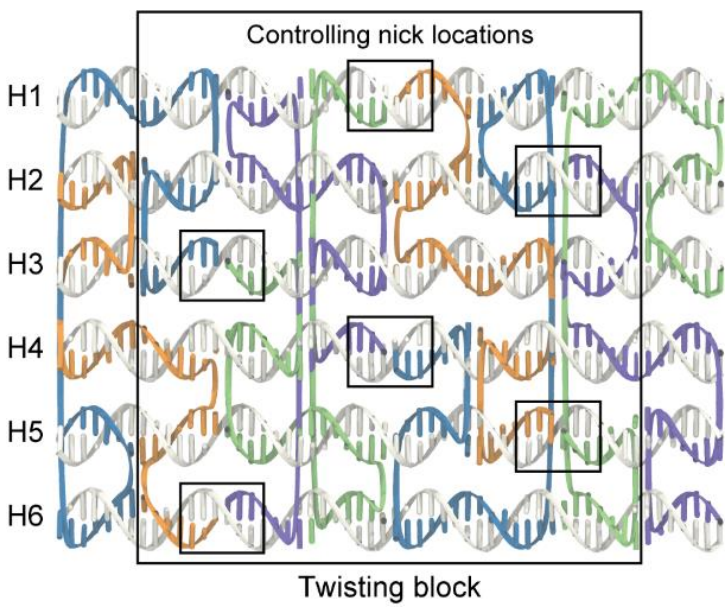


Figure 5-12. The development figure of a twisting block. 2-BPs were inserted into all 14-BP-long strands resulting in 16-BP-long strands. Any BP was not inserted into the other strands. In six regions where nicks exist, the locations of the nicks were programmed to control the sequence-dependent rigidities with at least 4-BPs away from Holliday-junctions.

Here, we might need to make the change in the equilibrium twist parameter by a nick into consideration. In the 6HB twisting block design with 2-BP-insertion, four BPs were totally inserted into each helix in order to increase the twist angle as a multiple of intrinsic helical rotation (Figure 5-3), which is approximately 138° assuming the mean twist parameter of 34.51° for regular BP steps (Table 2-2). However, only one nicked BP step exists in each helix whose highest change in the twist parameter is about 6° for AnC/GT step. This suggests that the twist change by a nick for a helix would be only 4% of that by BP-insertions at most (Table 2-2 and Table 2-3). Hence, we concluded that the change in the equilibrium twist at a nick site can be ignored.

According to our theoretical analysis, the C/B ratio dominates the twist angle of the bundle structure with BP-insertion. The C/B ratio is also certainly sequence-dependent and always smaller than one since the nick reduces the torsional rigidity while the bending rigidity does not considerably change. The C/B ratios for all nicked BP steps determined from our MD results range from 0.23 (AnA/TT step) to 0.81 (AG/CnT step) with the following order: AG/CnT > AA/TnT > GnG/CC > CG/CnG > AnG/CT > TnG/CA > GC/GnC > TG/CnA > GnA/TC > GA/TnC > AC/GnT > AnC/GT > AT/AnT > TA/TnA > GG/CnC > AnA/TT (Figure 5-13a and Table 5-1). Utilizing the C/B ratio data, we designed two pairs of stiff, moderate, and flexible structures with 2-BP-insertion by choosing the location of the nicks to control the C/B ratio. The stiff and flexible structures were designed by choosing nick sequences among the nine possible locations to maximize and minimize the C/B ratio, respectively (Figure 5-13b).

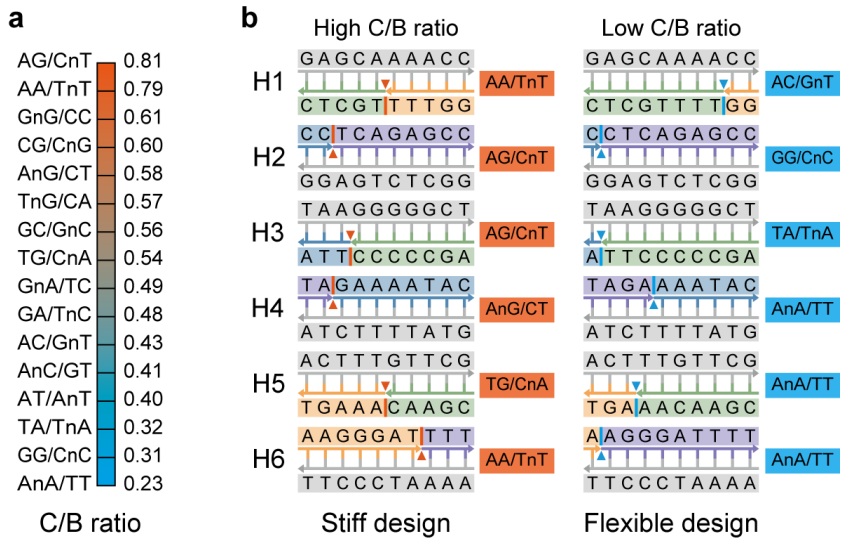


Figure 5-13. List of C/B ratio and an example design of a twisting block to design stiff and flexible structures. (**a**) C/B ratio of nicked BP steps was defined as the ratio of torsional rigidity to bending rigidity normalized by corresponding regular BP steps. The standard deviations of the C/B ratio were listed in Table 5-1. (**b**) White and colored strands represent scaffold and staple strands, respectively. The nicks were selected to induce the highest and lowest C/B ratio among possible nine positions of staple strands.

### 5.3.2. Prediction and experimental validation of the global twist angle

The location of nicks was adjusted to create two similar pairs of stiff and flexible structures, suggesting that the mean C/B ratios accounting for sixty nicked BP steps in ten twisting blocks ranged from 0.302 for the flexible design to 0.674 for the stiff design (Table 5-2). Two moderate structures were designed to have the middle C/B ratio of approximately 0.488 which is in the mean of C/B ratios used for stiff and flexible designs. The stiff design with the higher C/B ratio was expected to result in a larger twist angle than the flexible design since higher torsional strain energy was induced under the same torsional mismatch due to inserted BPs (Figure 5-14a).

The twist angle of self-assembled 6HB structures was characterized by AFM analysis. The results of agarose gel electrophoresis and AFM images indicated that monomeric structures were appropriately folded and the variations in nick position hardly affected the folding yield (Figure 5-8 and Figure 5-9). The structures took either the trans state (flags in the opposite sides) or the cis state (flags on the same side) in the AFM image (Figure 5-8 and Figure 5-14B). The number of monomeric structures in each state was reduced to the trans ratio and twist angle (Figure 5-14C and Table 5-4). Based on the MD results for a twisting block with 2-BP-insertion suggesting that the entire structures would be twisted by 550 ± 12° (Figure 5-3), the twist angles converted from the trans ratio were estimated as 614-624° for the stiff designs, 602-612° for the moderate designs, and 582-585° for the flexible designs on average. These experimental results confirmed our expectation based on theoretical analysis that the stiff design could be more twisted than the flexible design. Considering the wide controllable range of C/B ratio, even finer control on the twist angle was also available by using various sets of nicked BP steps for the same structure.

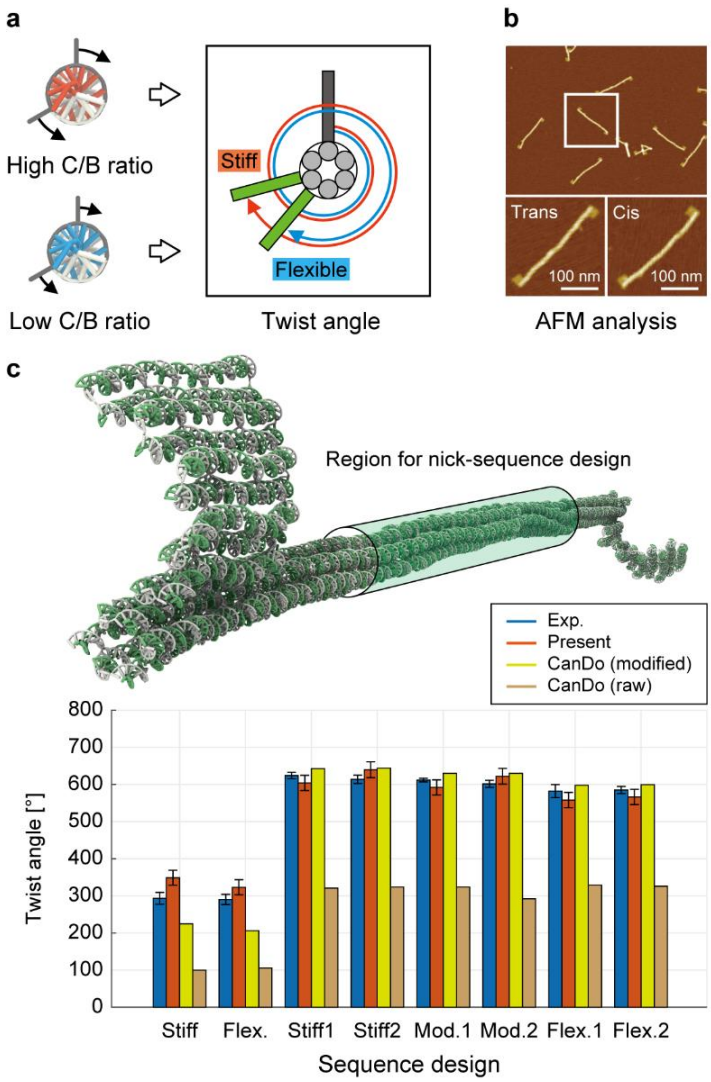


Figure 5-14. Experimental validation of twist control through controlling nick sequences. (**a**) Mechanical analysis of DNA nanostructures with BP-insertion. The twist angle is induced by the torsional energy due to the inserted BPs and controlled by C/B ratio. (**b**) AFM analysis of trans and cis monomers. (**c**) Results of trans ratio and twist angle from sequence design of nicks. Two pairs of stiff, moderate, and flexible structures are represented as descending order of mean C/B ratio in brackets. The trans ratio was calculated as dividing the number of trans monomers by the total number of monomers. The standard deviation of the trans ratio was calculated using the trans ratios of AFM images (Table 5-4 and Table 5-5).

We also performed the same experiments for stiff and flexible 1-BP-inserted structures (Figure 5-14). Results for 6HB structures with 1-BP-insertion, however, showed an indistinguishable difference between the stiff (293 ± 16°) and flexible (291 ± 14°) designs (Table 5-4). The trans ratios of stiff and flexible designs were not statistically different as the significance probability was 0.47. This might be because measuring a small difference in the twist angle for these 1-BP-inserted structures was hindered by the thermal fluctuation. Considering that the difference in the twist angle between the stiff and flexible structures with 2-BP-insertion was 35.4° on average (Table 5-4), the twist angle difference of 1-BP-inserted structures is expected to be approximately half of that (~17.7°) assuming that the twist angle is proportional to the number of BP-insertion. However, the standard deviations of the twist angle for 1-BP-inserted structures were measured in the range of 13.8-16.0° (Table 5-4) which amounts almost to the expected angle difference. Hence, it would be difficult to experimentally observe a significant difference in the 1-BP-inserted structures. The exceptional case in the 2-BP-inserted structures can be explained similarly. We, therefore, expect the proposed method for the twist control through the sequence design of nicks would be more effective for the design of highly twisted structures.

# 6. Dynamic characteristics of DNA nanostructures

## 6.1. Abstract

We present the characterizing procedure of dynamic properties for the DNA nanostructures and compare the results with ones from the atomic simulation. By performing the normal mode analysis, the eigenvalues and eigenmodes of the DNA nanostructure were calculated through the proposed multiscale approach. Eigenvalues and eigenmodes are the principal motions unique to the structure, and are necessary to understand the global dynamic behavior. Using the obtained eigensolution, we derived the root-mean-square-fluctuation of all base-pairs in the structure and the correlation coefficients between the two base-pairs. We confirmed a high agreement in the distribution map of the root-mean-square-fluctuation, and the Pearson and generalized correlation coefficients. Furthermore, the high computing efficiency of the multiscale approach was confirmed, in that the analysis was performed in minutes, compared to the molecular dynamics simulation that requires days.

## 6.2. Methods

### 6.2.1. Normal mode analysis

Normal mode analysis (or eigenvalue analysis) was performed for the final structures to derive eigenvalues and eigenvectors, providing the mode shape, the root-mean-square-fluctuation (RMSF), and correlation coefficients. Here, the generalized eigenproblem was considered[72] as

$$\mathbf{K}_G\mathbf{\Phi}=\mathbf{M}_G\mathbf{\Phi}\mathbf{\Lambda} \tag{6-1}$$

where $\mathbf{K}_G$ and $\mathbf{M}_G$ represent the global stiffness and mass matrices in finite element assemblage, $\mathbf{\Phi}$ indicates the eigenvector matrix, and $\mathbf{\Lambda}$ is the corresponding eigenvalue matrix.

The global stiffness matrix has already been constructed following the previous procedures, and the global mass matrix is computed as follows. The molar mass of each BP was sequence-dependently determined as the sum of the masses of two complementary bases from the values measured in the previous study[84]. The nodal mass in a structural element was then calculated by dividing the molar mass into the Avogadro's number. Accordingly, the local mass matrix ($\mathbf{M}^e$) for the structural element was constructed using the two nodal mass of BPs depending on sequences as

$$\mathbf{M}^e=\mathrm{diag}\left(\left[\vec{m}_1 \quad \vec{m}_2\right]\right), \quad \vec{m}_N=m_N\left[1 \;\; 1 \;\; 1 \;\; 0 \;\; 0 \;\; 0\right]^{\mathrm{T}} \tag{6-2}$$

where $m_N$ indicates the nodal mass of a BP calculated by the sum of two mass of the constituting bases, and $N$ represents the node index of the element ($N = 1,2$). The local mass matrices were assembled to provide global mass matrix based on the connectivity of elements as $\mathbf{M}_G = \mathbf{M}_G(\mathbf{M}^e)$.

The eigenvectors and eigenvalues were calculated by solving the eigenvalue problem of the matrices. An iterative method was used since there are no explicit formulas for the eigenproblem in general when the order of degrees of freedom is

larger than four. However, it requires expensive and unnecessary computation to find all eigensolution for the system with considerable degrees of freedom such as DNA nanostructures. In addition, for the observation of global motion, investigating low eigensolutions is significant in the biomolecule system.

Here, we employed the eigenproblem solver, *eigs* in MATLAB based on the Krylov-Schur algorithm[85] to obtain eigensolution from the lowest values, which provides the $n$-by-$p$ eigenvector and $p$-by-$p$ eigenvalue matrices for the lowest $p$ eigensolution and $n$ degree of freedom as

$$\mathbf{\Lambda} = \mathrm{diag}\left(\begin{bmatrix} \lambda_1 & \cdots & \lambda_k & \cdots & \lambda_p \end{bmatrix}\right), \quad \mathbf{\Phi} = \begin{bmatrix} \vec{\Phi}_1 \cdots \vec{\Phi}_k \cdots \vec{\Phi}_p \end{bmatrix} \tag{6-3}$$

where $\lambda_k$ and $\vec{\Phi}_k$ represent the $k^{\text{th}}$ eigenvalues and corresponding eigenvectors. The calculated eigenvectors indicate the mode shapes, and they are orthogonal and orthonormal to the stiffness and mass matrices, respectively, as below.

$$\mathbf{\Phi}_i^{\mathrm{T}} \mathbf{K} \mathbf{\Phi}_j = \lambda_i \delta_{ij}, \quad \mathbf{\Phi}_i^{\mathrm{T}} \mathbf{M} \mathbf{\Phi}_j = \delta_{ij} \tag{6-4}$$

where $\delta_{ij}$ is the Kronecker delta. Except for the first six values for the three-dimensional rigid-body motion, the eigenvalues were computed in ascending order as $\lambda_1 \leq \cdots \leq \lambda_k \leq \cdots \leq \lambda_p$.

### 6.2.2. Root-mean-square fluctuation and correlation coefficients

The root-mean-square fluctuation (RMSF) and the correlation coefficients are significant measures in the dynamic properties, which provide fundamental insights into equilibrium structural dynamics[86]. Both values are obtained from the trajectories of the molecular dynamics (MD) simulation and the eigensolution of the finite element system, respectively.

#### 6.2.2.1. Dynamic properties from MD simulation.

For MD trajectories, after aligning an entire structure, the average coordinate ( ${}^{t}\vec{r}_i$ ) of atoms constituting the $i^{\text{th}}$ BP in the trajectory time ($\tau$) provides the fluctuation vector as

$$ {}^{\tau}\Delta\vec{r}_i = {}^{\tau}\vec{r}_i - \langle \vec{r}_i \rangle \tag{6-5}$$

where the bracket represents the ensemble average for the total time step number ($T_N$) as

$$ \langle x \rangle = \frac{1}{T_N} \sum_{\tau=1}^{T_N} {}^{\tau}x \tag{6-6}$$

The RMSF value of the BP ( $\Delta r_i^{\text{MD}}$ ) is first computed by the definition as follows.

$$ \Delta r_i^{\text{MD}} = \sqrt{\langle \Delta\vec{r}_i^{\,\text{T}} \Delta\vec{r}_i \rangle} = \sqrt{\frac{1}{T_N} \sum_{\tau=1}^{T_N} {}^{\tau}\Delta\vec{r}_i^{\,\text{T}}\, {}^{\tau}\Delta\vec{r}_i} \tag{6-7}$$

The Pearson correlation coefficient between two BPs ( ${}^{\text{P}}C_{ij}^{\text{MD}}$ ) was calculated as

$$ {}^{\text{P}}C_{ij}^{\text{MD}} = \frac{\langle \Delta\vec{r}_i^{\,\text{T}} \Delta\vec{r}_j \rangle}{\sqrt{\langle \Delta\vec{r}_i^{\,\text{T}} \Delta\vec{r}_i \rangle \langle \Delta\vec{r}_j^{\,\text{T}} \Delta\vec{r}_j \rangle}} = \frac{\sum_{\tau=1}^{T_N} {}^{\tau}\Delta\vec{r}_i^{\,\text{T}}\, {}^{\tau}\Delta\vec{r}_j}{\sqrt{\left( \sum_{\tau=1}^{T_N} {}^{\tau}\Delta\vec{r}_i^{\,\text{T}}\, {}^{\tau}\Delta\vec{r}_i \right) \left( \sum_{\tau=1}^{T_N} {}^{\tau}\Delta\vec{r}_j^{\,\text{T}}\, {}^{\tau}\Delta\vec{r}_j \right)}} \tag{6-8}$$

The generalized correlation coefficients between two BPs ( ${}^{\text{G}}C_{ij}^{\text{MD}}$ ) is computed by

$$ {}^{\mathrm{G}}C_{ij}^{\mathrm{MD}} = \sqrt{1-\exp\left(-2L_{ij}/d\right)} \tag{6-9} $$

where $d$ represents dimensionality provided here as three, and the $L_{ij}$ indicates the linearized mutual information given by

$$ L_{ij} = \frac{1}{2}\left[\log\left\{\det\left(\mathbf{c}_i\right)\right\} + \log\left\{\det\left(\mathbf{c}_j\right)\right\} - \log\left\{\det\left(\mathbf{c}_{ij}\right)\right\}\right] \tag{6-10} $$

with

$$ \begin{aligned} \mathbf{c}_{ij} &= \left\langle \left[\Delta\vec{r}_i \quad \Delta\vec{r}_j\right]\left[\Delta\vec{r}_i \quad \Delta\vec{r}_j\right]^{\mathrm{T}} \right\rangle = \frac{1}{T_N}\sum_{\tau=1}^{T_N}\left[{}^{\tau}\Delta\vec{r}_i \quad {}^{\tau}\Delta\vec{r}_j\right]\left[{}^{\tau}\Delta\vec{r}_i \quad {}^{\tau}\Delta\vec{r}_j\right]^{\mathrm{T}} \\ \mathbf{c}_i &= \left\langle \Delta\vec{r}_i\Delta\vec{r}_i^{\mathrm{T}} \right\rangle = \frac{1}{T_N}\sum_{\tau=1}^{T_N} {}^{\tau}\Delta\vec{r}_i\,{}^{\tau}\Delta\vec{r}_i^{\mathrm{T}} \\ \mathbf{c}_j &= \left\langle \Delta\vec{r}_j\Delta\vec{r}_j^{\mathrm{T}} \right\rangle = \frac{1}{T_N}\sum_{\tau=1}^{T_N} {}^{\tau}\Delta\vec{r}_j\,{}^{\tau}\Delta\vec{r}_j^{\mathrm{T}} \end{aligned} \tag{6-11} $$

### 6.2.2.2. Dynamic properties from the finite element system.

For a finite element assemblage, the RMSF and correlation coefficient were estimated using the eigenvalues ($\lambda_k$) and eigenvectors ($\vec{\Phi}_k$) from the normal mode analysis. It was assumed that the elastic strain energy of each mode in the equilibrium equals to the half of $k_{\mathrm{B}}T$ in the previous studies[86-88], where $k_{\mathrm{B}}$ is the Boltzmann constant and $T$ is absolute temperature given by 300 K. The fluctuation vector was derived for the $i^{\mathrm{th}}$ node (BP) as below.

$$\Delta\vec{r}_i = \vec{r}_i - \langle \vec{r}_i \rangle = \sum_{k=1}^{\kappa} \sqrt{\frac{k_B T}{\lambda_k}} \vec{\Phi}_{ik} \tag{6-12}$$

where $k$ represents the mode number, and $\kappa$ is the total number of eigensolution from the lowest mode, which is generally set to 200. The RMSF value ($\Delta r_i^{\mathrm{FE}}$) was, therefore, calculated as follows.

$$\Delta r_i^{\mathrm{FE}} = \sqrt{\langle \Delta\vec{r}_i^{\mathrm{T}} \Delta\vec{r}_i \rangle} = \sqrt{k_B T \sum_{k=1}^{\kappa} \frac{\vec{\Phi}_{ik}^{\mathrm{T}} \vec{\Phi}_{ik}}{\lambda_k}} \tag{6-13}$$

where $\kappa$ is the calculated number of the lowest eigensolution, generally set to 200, which is enough number to examine the eigenproblem[86,87]. The Pearson correlation coefficient between two BPs ($^{\mathrm{P}}C_{ij}^{\mathrm{FE}}$) was calculated as

$$^{\mathrm{P}}C_{ij}^{\mathrm{FE}} = \frac{\langle \Delta\vec{r}_i^{\mathrm{T}} \Delta\vec{r}_j \rangle}{\sqrt{\langle \Delta\vec{r}_i^{\mathrm{T}} \Delta\vec{r}_i \rangle \langle \Delta\vec{r}_j^{\mathrm{T}} \Delta\vec{r}_j \rangle}} = \frac{\sum_{k=1}^{\kappa} \frac{\vec{\Phi}_{ik}^{\mathrm{T}} \vec{\Phi}_{jk}}{\lambda_k}}{\sqrt{\left( \sum_{k=1}^{\kappa} \frac{\vec{\Phi}_{ik}^{\mathrm{T}} \vec{\Phi}_{ik}}{\lambda_k} \right) \left( \sum_{k=1}^{\kappa} \frac{\vec{\Phi}_{jk}^{\mathrm{T}} \vec{\Phi}_{jk}}{\lambda_k} \right)}} \tag{6-14}$$

The generalized correlation coefficients[89] between two BPs ($^{\mathrm{G}}C_{ij}^{\mathrm{FE}}$) is computed by

$$^{\mathrm{G}}C_{ij}^{\mathrm{MD}} = \sqrt{1 - \exp\left(-2L_{ij}/d\right)} \tag{6-15}$$

where

$$L_{ij} = \frac{1}{2}\left[\log\left\{\det\left(\mathbf{c}_i\right)\right\} + \log\left\{\det\left(\mathbf{c}_j\right)\right\} - \log\left\{\det\left(\mathbf{c}_{ij}\right)\right\}\right] \tag{6-16}$$

with

$$\begin{aligned}
\mathbf{c}_{ij} &= \left\langle \left[\Delta\vec{r}_i \quad \Delta\vec{r}_j\right]\left[\Delta\vec{r}_i \quad \Delta\vec{r}_j\right]^{\mathrm{T}} \right\rangle = k_B T \sum_{k=1}^{\kappa} \frac{\left[\vec{\Phi}_{ik} \quad \vec{\Phi}_{jk}\right]\left[\vec{\Phi}_{ik} \quad \vec{\Phi}_{jk}\right]^{\mathrm{T}}}{\lambda_k} \\
\mathbf{c}_i &= \left\langle \Delta\vec{r}_i \Delta\vec{r}_i^{\mathrm{T}} \right\rangle = k_B T \sum_{k=1}^{\kappa} \frac{\vec{\Phi}_{ik}\vec{\Phi}_{ik}^{\mathrm{T}}}{\lambda_k} \\
\mathbf{c}_j &= \left\langle \Delta\vec{r}_j \Delta\vec{r}_j^{\mathrm{T}} \right\rangle = k_B T \sum_{k=1}^{\kappa} \frac{\vec{\Phi}_{jk}\vec{\Phi}_{jk}^{\mathrm{T}}}{\lambda_k}
\end{aligned} \tag{6-17}$$

## 6.3. Prediction of structural fluctuation

Once the three-dimensional shape of a structure is obtained, its equilibrium dynamic properties can be calculated as well by performing normal mode analysis[17,86-88,90]. In addition to the global stiffness matrix ($\mathbf{K}_G$), the mass matrix ($\mathbf{M}_G$) was constructed by assembling the element mass matrices of structural models for BP and CO steps, thereby setting and solving an eigenvalue problem, $\mathbf{K}_G\mathbf{\Phi} = \mathbf{M}_G\mathbf{\Phi}\mathbf{\Lambda}$, to obtain eigenvalues (in $\mathbf{\Lambda}$) and eigenvectors (in $\mathbf{\Phi}$) of the structure. Then, we examined two equilibrium dynamic properties: the root-mean-square-fluctuation (RMSF) magnitudes that measure the amplitude of thermal fluctuation of each BP and the correlation coefficients that indicate the correlated BPs according to the direction (the Pearson correlation) and the probability (the generalized correlation) of their molecular motions[86,87].

To illustrate, these dynamic properties for a 12HB structure (Figure 6-1a) were investigated. RMSF values predicted by our model using the lowest 200 normal modes showed a good agreement with those from equilibrated 50-ns-long MD trajectories[10] with the overlap coefficient of 0.97 (Figure 6-1b). They were the largest in helices 1 and 12 as crosslinked only to a single neighboring helix, unlike other helices. BPs at the ends of each helix showed the highest RMSF magnitudes as expected. A similar agreement between the proposed method and MD simulations was observed for other designs reported previously[31] (Figure 6-2).

Interestingly, while the previous models[17,86] could require the linear scaling factor to fit the RMSF, the multiscale approach provided RMSF values equivalent to MD by employing inherent properties of DNA, without adjustable parameters. For the pointer structure[80] whose three-dimensional structure was reconstructed from electron densities, the mean RMSF value was predicted as 39.1 nm similar to 36.5 nm estimated from experimentally determined Debye-Waller factors or B-factors[80].

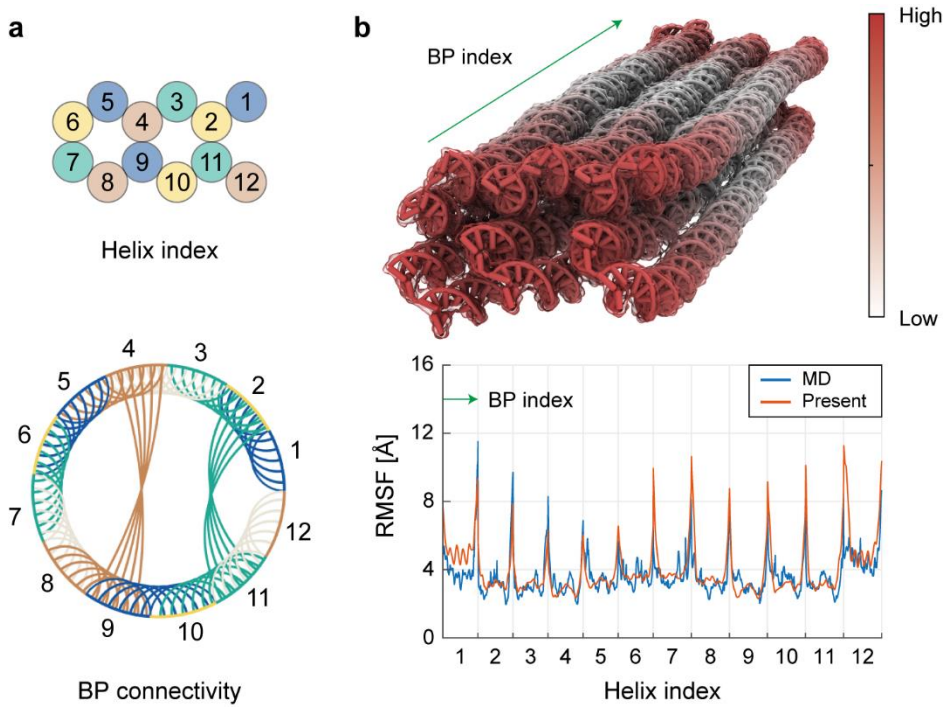


Figure 6-1. Prediction of RMSF. (**a**) Helix index and the BP connectivity diagram of the 12HB structure. Helix index represents constituent helices, and the connection diagram indicates the BP connection. (**b**) Comparison of RMSF values. BP index (Green arrow) represents the nodal positions of BPs along the longitudinal direction for each helix in the structure. The predicted RMSF showed a good agreement with those from MD simulation.

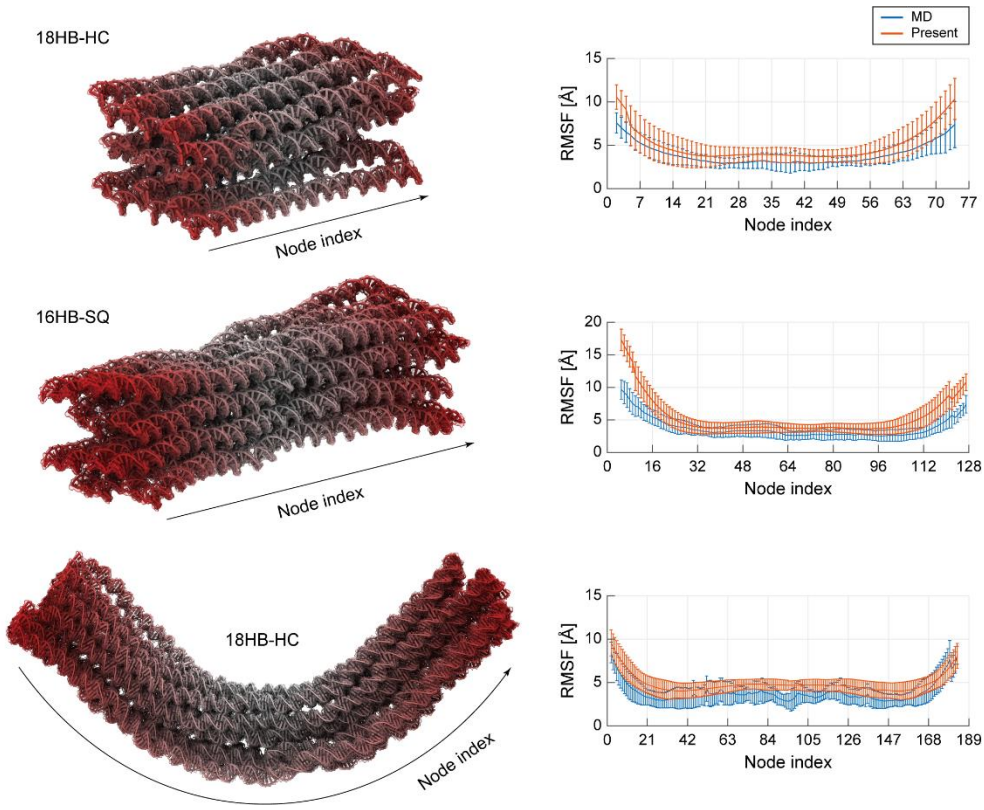


Figure 6-2. Comparison of the root-mean-square-fluctuation (RMSF). The RMSF values with respect to the nodal points in helices were obtained using normal mode analysis, and they were compared with the previous results.

## 6.4. Prediction of correlation coefficients

Correlation coefficients for the 12HB structure clearly showed a strong interaction among neighboring helices (Figure 6-3a). Particularly, they were the strongest between BPs connected by crossovers demonstrated by five points at crossover sites with the highest correlation values. According to Pearson correlation coefficients, BPs on the same side of the cross-section were positively correlated while those on the opposite sides were negatively correlated. For example, the first BP of helix 1 had positive correlation values with that of helices 2, 11, and 12, but negative ones with that of helices 5, 6, 7, and 8, suggesting a low-energy torsional mode might dominate the dynamic motion of the 12HB structure as helices in the opposite sides of the cross-section moved in the opposite directions in this mode.

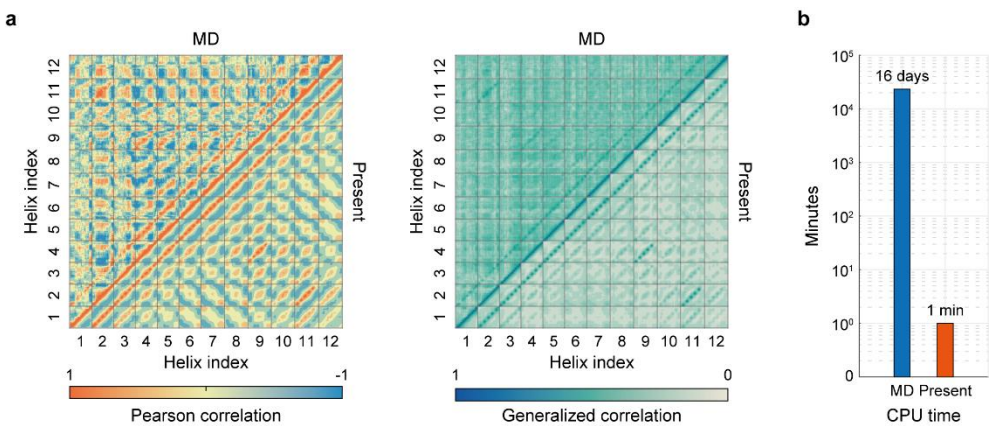


Figure 6-3. Prediction of correlation coefficients, and computation time. (**a**) The correlation coefficients indicate the correlated BPs according to the direction (Pearson correlation) and the probability (generalized correlation) of their molecular motions. The upper-left and lower-right triangles represent the correlation coefficients from MD simulations and the present framework, respectively. (**b**). CPU time for the analysis. The MD simulation required 16 days in a workstation with two Intel Xeon E5-2680 12-core CPUs and four Nvidia Tesla K80 GPUs, but in this framework, the analysis was completed in one minute using a PC with an Intel i7-4770 3.40 GHz CPU without a GPU.

Interestingly, the correlation coefficients calculated from the MD trajectories had higher values and spread more broadly overall than those obtained from the proposed method while strong correlations among adjacent helices could be observed similarly. It could be inferred therefore that unmodeled interactions of the proposed method such as random breakage of base-parings or explicit interaction with solvent might lead to more correlated, longer-range molecular motions.

The required analysis was just one minute using a personal computer, which is much faster than the MD simulation approximately requiring 16 days in a professional workstation with GPUs (Figure 6-3b). This demonstrates the effectiveness of the present approach.

# 7. Global mechanical rigidities of DNA nanostructures

## 7.1. Abstract

We introduced the approach to predicting the persistence length as the overall mechanical rigidity of DNA nanostructures. The natural frequency and mode shape of the DNA bundle structures were derived through the normal mode analysis. The bending and torsional rigidities of the entire structure were then derived through the continuum assumption. The bending and torsional rigidities were converted into the corresponding persistence lengths, which were compared with the experimentally measured ones, showing the good agreement. Furthermore, the persistence lengths of the bundle structure were theoretically predicted, and the bonding effect of crossovers, indicating the connection between inner helices in the bundle structure, was investigated. In particular, considering the bonding effect, the bending rigidity increased quadratically for the number of helices mechanically, but the torsional rigidity showed a linear increase, which was confirmed numerically, theoretically, and experimentally.

## 7.2. Methods

### 7.2.1. Estimation of persistence length from normal mode analysis

The persistence length of DNA bundle structures, which is a global structural characteristic, was estimated from the eigenvalues and eigenvectors in the lowest modes with an assumption of the structures as an equivalent continuum. Here, the bending and torsional persistence lengths were calculated for the various cross-sections. First, the contour length ($L_c$) was approximately computed by averaging the length of each helix as

$$L_c = \frac{1}{H}\sum_{h=1}^{H}\left|\vec{x}_1^h - \vec{x}_{\text{end}}^h\right| \tag{7-1}$$

where $\vec{x}_1^h$ and $\vec{x}_{\text{end}}^h$ represent the first and end nodal position of a helix ($h$), respectively, and the total number of helices is denoted as $H$.

#### 7.2.1.1. Bending persistence length.

The bending persistence length was derived in the assumption that the bundle structure is a homogeneous Euler-Bernoulli beam with the bending rigidity, $EI$. In this study, since the ratio of the thickness to the length of the bundle structures is smaller than 0.1, this assumption is valid. Then, when no external force was applied, by the separation of the spatial and temporal variables, the governing equation for the spatial term is given as

$$EI_y \frac{d^4 y}{dx^4} - \mu\omega^2 y = 0, \qquad y = y(x) \tag{7-2}$$

where $y$ denotes one of the transverse displacements as a function of the beam axis $x$, $EI_y$ represents the bending rigidity for the orthogonal direction of $y$, $\mu$ is the length density as $M/L_c$ of the contour length ($L_c$) and total mass ($M$) calculated as the summation of all nodal mass, and $\omega$ is the natural frequency satisfying the

relation with eigenvalue ($\lambda$) as $\omega^2 = \lambda$. The general solution of the spatial term is given by

$$y(x) = A\exp(-i\beta x) + B\exp(i\beta x) + C\exp(-\beta x) + D\exp(\beta x) \tag{7-3}$$

where the wavenumber, $\beta$ satisfies the characteristic equation as below.

$$EI_y\beta^4 = \mu\omega^2 \tag{7-4}$$

To determine $\beta$, the boundary condition of the free-free ends was applied as

$$\cosh(\beta L_c)\cos(\beta L_c) = 1 \tag{7-5}$$

This relation provides numerical solutions, $\beta_n L_c = 4.733,\ 7.853,\ 10.996,\ \cdots$ where $n$ is the mode number. Consequently, for the transverse direction, the bending rigidity was derived in terms of the natural frequency corresponding to bending mode shape as

$$EI_y = \frac{\mu\omega_n^2}{\beta_n^4} = \frac{M\omega_n^2 L_c^3}{(\beta_n L_c)^4} \tag{7-6}$$

Noting that, in three-dimensional structures, a certain bending mode shape (here, 1st bending mode) could appear in two directions of two different modes, the equivalent bending rigidity was estimated by the harmonic mean of the two bending rigidities obtained in the directions ( $EI_r$ and $EI_s$ )[18,67] as

$$EI = \frac{2}{EI_r^{-1} + EI_s^{-1}} = \frac{2EI_rEI_s}{EI_r + EI_s} \tag{7-7}$$

In summary, the bending persistence length of bundle structures ( $L_B^{\text{bundle}}$ ) is obtained as follows.

$$L_B^{\text{bundle}} = \frac{EI}{k_BT} = \frac{M\omega_n^2 L_c^3}{k_BT(\beta_n L_c)^4} \tag{7-8}$$

where $k_B$ is the Boltzmann constant and $T$ is the absolute temperature as 300 K.

### 7.2.1.2. Torsional persistence length.

The torsional persistence length of bundle structure was derived similarly in terms of natural frequency in the assumption of a continuum bar with the torsional rigidity ( $GJ$ ) as the product of shear modulus ( $G$ ) and torsion constant ( $J$ ). For the circular cross-section, the torsional constant is identical to the second moment of area ( $J_o$ ).

When no external force applied, the spatial term of the dynamic governing equation was given as

$$GJ\frac{\partial^2\theta}{\partial x^2}+\rho J_o\omega^2\theta=0, \qquad \theta=\theta(x) \tag{7-9}$$

where $\theta$ denotes the torsional angle as a function of the beam axis $x$, $\rho$ is the volume density as $M/(\mathrm{A}L_c)$, in which $M$ is the total mass and $A$ is the cross-section area of the bundle structures, and $\omega$ is the natural frequency.

The general solution of the spatial term was derived as

$$\theta(x)=C_1\exp(-i\beta x)+C_2\exp(i\beta x) \tag{7-10}$$

where the wavenumber ($\beta$) satisfies the characteristic equation

$$GJ\beta^2=\rho J_o\omega^2 \tag{7-11}$$

In free-free end boundary condition, the wavenumber satisfies a relation with the eigenmode number ($n$) as

$$\sin(\beta L_c)=0, \quad \beta_n L_c=n\pi \tag{7-12}$$

Accordingly, the torsional rigidity was derived in terms of the natural frequency from the characteristic equation.

$$GJ=\frac{\rho J_o}{\beta^2}\omega^2=\frac{M\omega_n^2 L}{n^2\pi^2}\left(\frac{J_o}{A}\right) \tag{7-13}$$

Here, the ratio of the polar moment of inertia to the area ( $J_o / A$) in a bundle structure should be determined earlier. First, the polar moment of inertia ( $J_o$ ) is the sum of the second moment of inertia in two orthogonal directions ( $I_y$ and $I_z$ ) as follows.

$$J_o = \int_A r^2 dA = \int_A \left(y^2 + z^2\right) dA = I_y + I_z \tag{7-14}$$

To determine $I_y$ and $I_z$, a helix as a cylindrical homogeneous bar was considered, and its area ( $A_h$ ) and second moment of inertia ( $I_h$ ) was defined as follows

$$A_h = \pi r_h^2, \quad I_h = \frac{\pi}{4} r_h^4 \tag{7-15}$$

where the radius was determined as $r_h = 1$.

Then, by the parallel axis theorem, the second moment of inertia of the helix for the axis of the bundle structure can be calculated as

$$I_{hy} = I_h + A_h y_h^2, \quad I_{hz} = I_h + A_h z_h^2 \tag{7-16}$$

where $x_h$ and $y_h$ are the displacement from the center, which was chosen as the geometric center due to the symmetrical shape. The polar moment of inertia and the area of the bundle structure was obtained as

$$J_o = I_y + I_z, \quad I_y = \sum_{h=1}^{H} I_{hy}, \quad I_z = \sum_{h=1}^{H} I_{hz}, \quad A = \sum_{h=1}^{H} A_h \tag{7-17}$$

This provides the ratio dependent on the cross-section of the bundle structure, $(J_o / A)_{\text{bundle}}$. In summary, the torsional persistence length of bundle structures ( $L_C^{\text{bundle}}$ ) is computed as follows.

$$L_C^{\text{bundle}} = \frac{GJ}{k_B T} = \frac{M \omega_n^2 L_c}{k_B T n^2 \pi^2} \left( \frac{J_o}{A} \right)_{\text{bundle}} \tag{7-18}$$

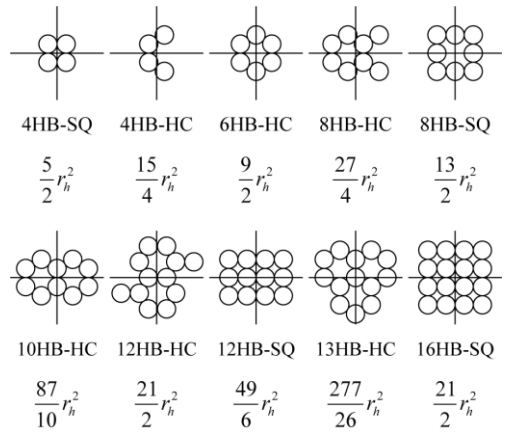


Figure 7-1. The ratio of the polar moment of inertia to the area for the bundle cross-sections.

### 7.2.2. Theoretical estimation of persistence lengths

Apart from the normal mode analysis, the persistence length of the bundle structure can also be theoretically predicted from the mechanical properties of a DNA helix. Symmetric bundle structures of square lattice were assumed, and the radius, area, and second moment of inertia in each helix were denoted as $r_h$, $A_h$, and $I_h$, respectively.

In the bundle structure of square lattice (Figure 7-2), the second moment of inertia ($I$) is the same with respect to the two axes toward the side direction ($I = I_y = I_z$) and can be expressed in terms of the total helix number ($H$) and the second moment of inertia of a helix ($I_h$) by parallel axis theorem as follows.

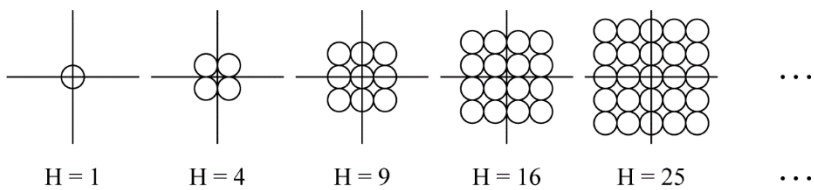


Figure 7-2. The cross-section of DNA bundle structures on square-lattice.

| $H$ | $\sqrt{H}$ | $I = I(I_h, H)$ |
|---|---|---|
| 1 | 1 | $I = I_h$<br>$= I_h H$ |
| 4 | 2 | $I = 4\left(I_h + r_h^2 A_h\right)$<br>$= I_h H + 2\sqrt{H} A_h \left[\left(r_h\right)^2\right]$ |
| 9 | 3 | $I = 3I_h + 6\left(I_h + \left(2r_h\right)^2 A_h\right)$<br>$= I_h H + 2\sqrt{H} A_h \left[\left(2r_h\right)^2\right]$ |
| 16 | 4 | $I = 8\left(I_h + r_h^2 A_h\right) + 8\left(I_h + \left(3r_h\right)^2 A_h\right)$<br>$= I_h H + 2\sqrt{H} A_h \left[\left(r_h\right)^2 + \left(3r_h\right)^2\right]$ |
| 25 | 5 | $I = 5I_h + 10\left(I_h + \left(2r_h\right)^2 A_h\right) + 10\left(I_h + \left(4r_h\right)^2 A_h\right)$<br>$= I_h H + 2\sqrt{H} A_h \left[\left(2r_h\right)^2 + \left(4r_h\right)^2\right]$ |

| | | |
|---|---|---|
| 36 | 6 | $I = 12\left(I_h + r_h^2 A_h\right) + 12\left(I_h + \left(3r_h\right)^2 A_h\right) + 12\left(I_h + \left(5r_h\right)^2 A_h\right)$ $= I_h H + 2\sqrt{H} A_h \left[\left(r_h\right)^2 + \left(3r_h\right)^2 + \left(5r_h\right)^2\right]$ |
| 49 | 7 | $I = 7I_h + 14\left(I_h + \left(2r_h\right)^2 A_h\right) + 14\left(I_h + \left(4r_h\right)^2 A_h\right) + 14\left(I_h + \left(6r_h\right)^2 A_h\right)$ $= I_h H + 2\sqrt{H} A_h \left[\left(2r_h\right)^2 + \left(4r_h\right)^2 + \left(6r_h\right)^2\right]$ |
| ⋮ | ⋮ | ⋮ |
| $H$ | $\sqrt{H}$ | $I = I_h H + 2\sqrt{H} A_h r_h^2 \zeta(H), \quad \zeta(H) = \begin{cases} \sum_{k=1}^{(\sqrt{H}-1)/2} (2k)^2 & \left(\sqrt{H} = \text{odd}\right) \\ \sum_{k=1}^{\sqrt{H}/2} (2k-1)^2 & \left(\sqrt{H} = \text{even}\right) \end{cases}$ |

Using the power series formula $\zeta(H)$ is simply expressed as

$$\zeta(H) = \frac{1}{6}\sqrt{H}(H-1) \tag{7-19}$$

Together, the second moment of inertia of the square lattice structure was derived as

$$I\left(I_h, H\right) = I_h H + \frac{1}{3} A_h r_h^2 H(H-1) \tag{7-20}$$

The first term $I_h H$ indicates the contribution of each helix itself to bundle structure, but the second term $A_h r_h^2 H(H-1)/3$ suggests the crosslinking effects of the inter-helix connection (Figure 7-3).

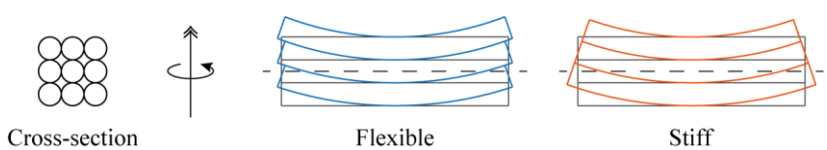


Figure 7-3. The crosslinking effects of helices in a bundle structure.

The minimum and maximum values of the second moment of inertia were obtained as below.

$$
\begin{aligned}
I|_{\min} &= I_h H \\
I|_{\max} &= \frac{1}{3} A_h r_h^2 H^2 + \left( I_h - \frac{1}{3} A_h r_h^2 \right) H
\end{aligned}
\tag{7-21}
$$

Consequently, the bending persistence length of the bundle structure ( $L_B^{\text{bundle}}$ ) was derived using the relation of $A_h r_h^2 = 4 I_h$ in assuming the circular cross-section of each helix as follows.

$$
\begin{aligned}
L_B^{\text{bundle}} &= \frac{EI}{k_B T} = L_B^{\text{helix}} H + \frac{4}{3} L_B^{\text{helix}} H (H-1) \\
L_B^{\text{bundle}}\Big|_{\min} &= L_B^{\text{helix}} H \\
L_B^{\text{bundle}}\Big|_{\max} &= \frac{4}{3} L_B^{\text{helix}} H^2 - \frac{1}{3} L_B^{\text{helix}} H
\end{aligned}
\tag{7-22}
$$

where $L_B^{\text{helix}}$ represents the persistence length of a helix as $L_B^{\text{helix}} = 46.5\,\text{nm}$ from the previous study[18].

Likewise, the torsional persistence length of the bundle structure ( $L_C^{\text{bundle}}$ ) was derived using the relation of $A_h r_h^2 = 2 J_h$ as follows.

$$
\begin{aligned}
L_C^{\text{bundle}} &= \frac{GJ}{k_B T} = L_C^{\text{helix}} H + \frac{4}{3} L_C^{\text{helix}} H (H-1) \\
L_C^{\text{bundle}}\Big|_{\min} &= L_C^{\text{helix}} H \\
L_C^{\text{bundle}}\Big|_{\max} &= \frac{4}{3} L_C^{\text{helix}} H^2 - \frac{1}{3} L_C^{\text{helix}} H
\end{aligned}
\tag{7-23}
$$

where $L_C^{\text{helix}}$ is the torsional length of a helix as $L_C^{\text{helix}} = 75.8\,\text{nm}$ from the previous study[18].

In summary, in good agreement with the previous studies[67,91,92], the persistence length can be controlled linearly by the number of helices and quadratically by the connections between the helixes. This suggests that controlling the density and arrangement of helix-connection could regulate the persistence length of the bundle structure.

## 7.3. Prediction of bending and torsional persistence length

We can derive the mechanical rigidities of a structure very efficiently using the proposed modeling approach. Here, we scrutinized the capability of our model in predicting the bending and torsional persistence lengths of DNA bundles with various numbers of comprising helices and cross-sectional shapes (Figure 7-4a). They were estimated from the natural frequencies of the lowest bending and torsional modes computed by normal mode analysis (Figure 7-4b and Figure 7-5).

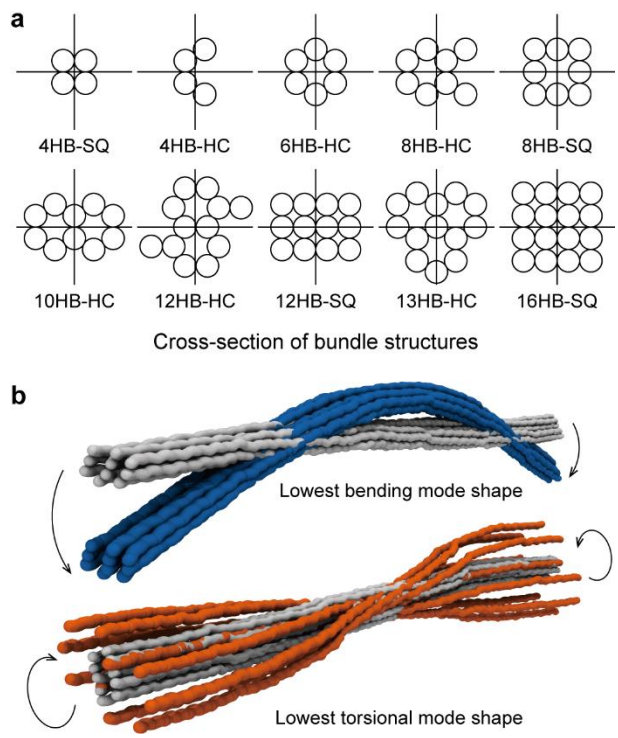


Figure 7-4. Prediction of global mode shapes. (**a**) Cross-sections of analyzed DNA bundle structures. To predict the persistence lengths, DNA bundle structures were designed with various numbers of comprising helices and cross-sectional shapes. (**b**) The lowest bending and torsional mode shapes of the structures. The eigenvalues and mode shapes for bending and torsional modes were derived by performing normal mode analysis for each structure. The lowest modes were used to calculate corresponding persistence lengths.

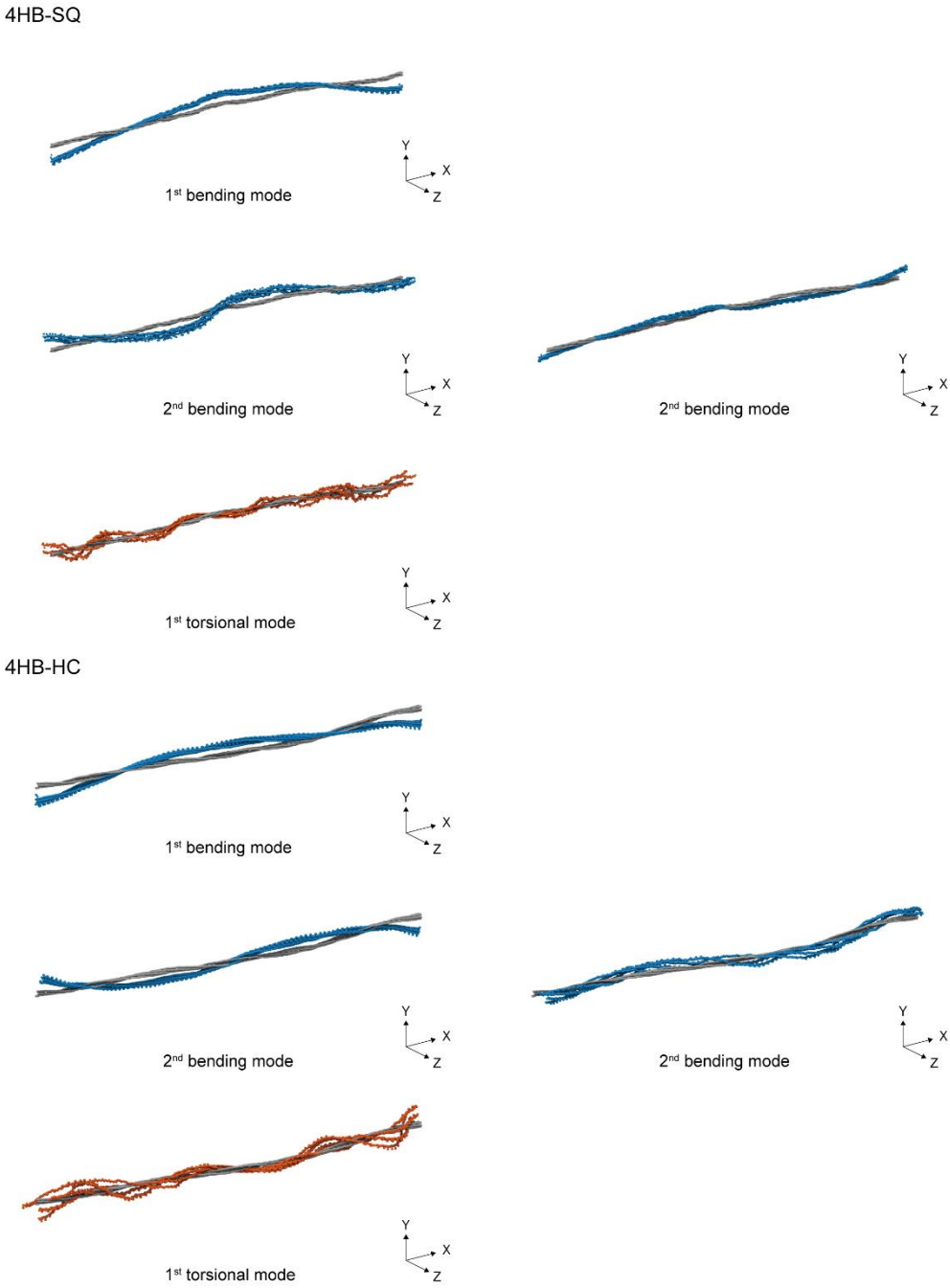


Figure 7-5. Mode shapes of bundle structures. The bending (blue) and torsional (orange) mode shapes of each bundle structure are shown along with the reference (grey) structure.

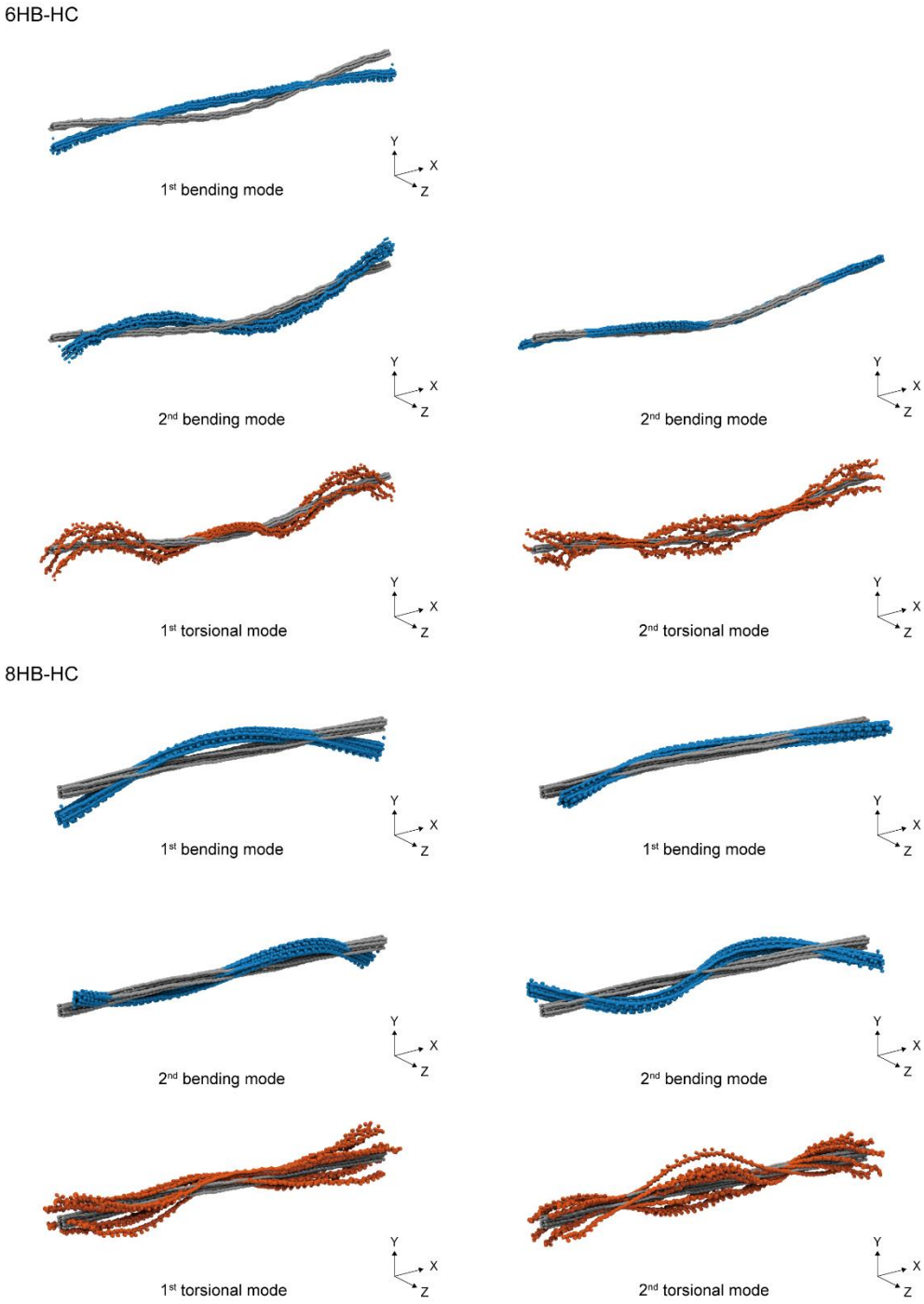


Figure 7-5 (Continued).

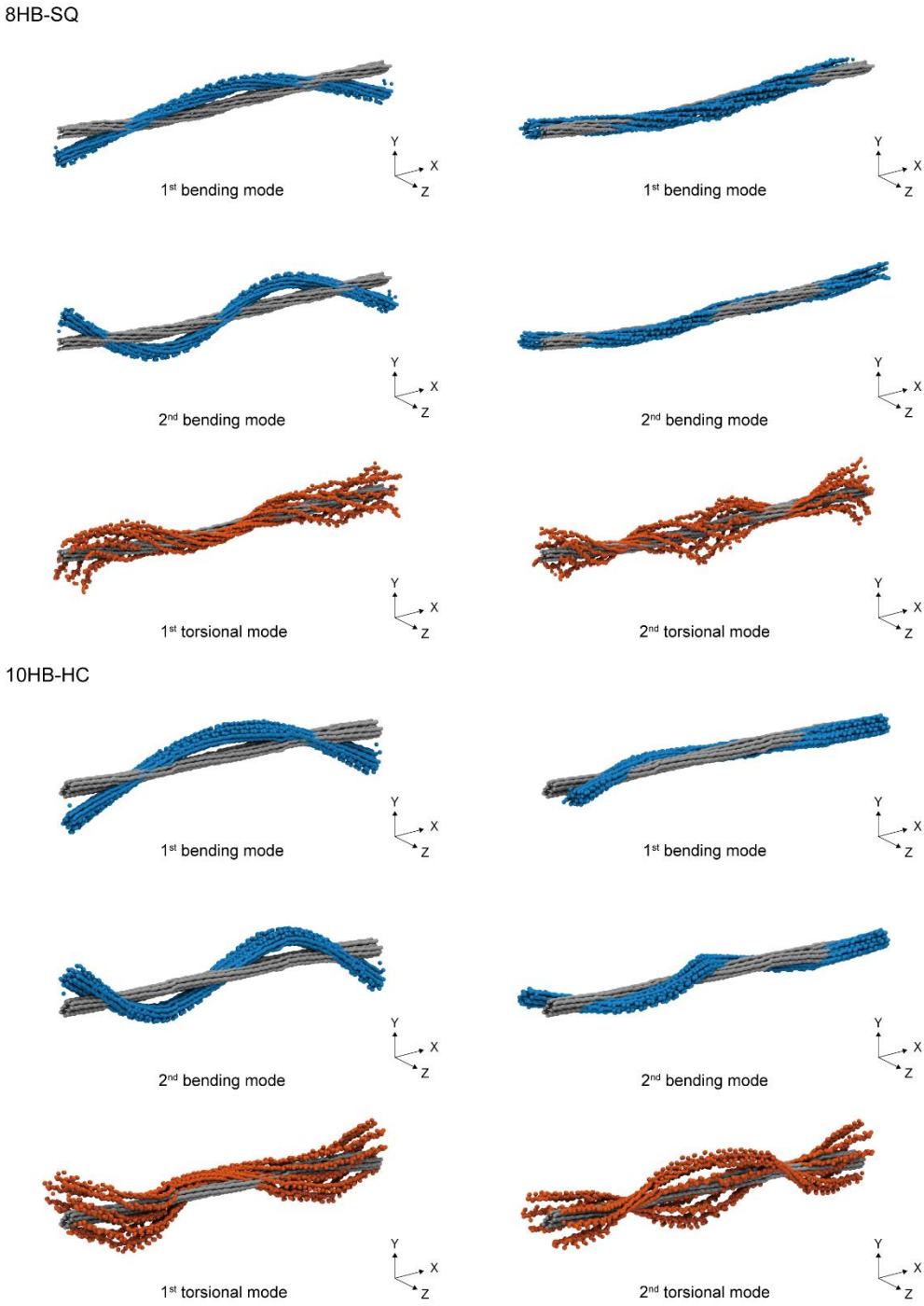


Figure 7-5 (Continued).

12HB-HC

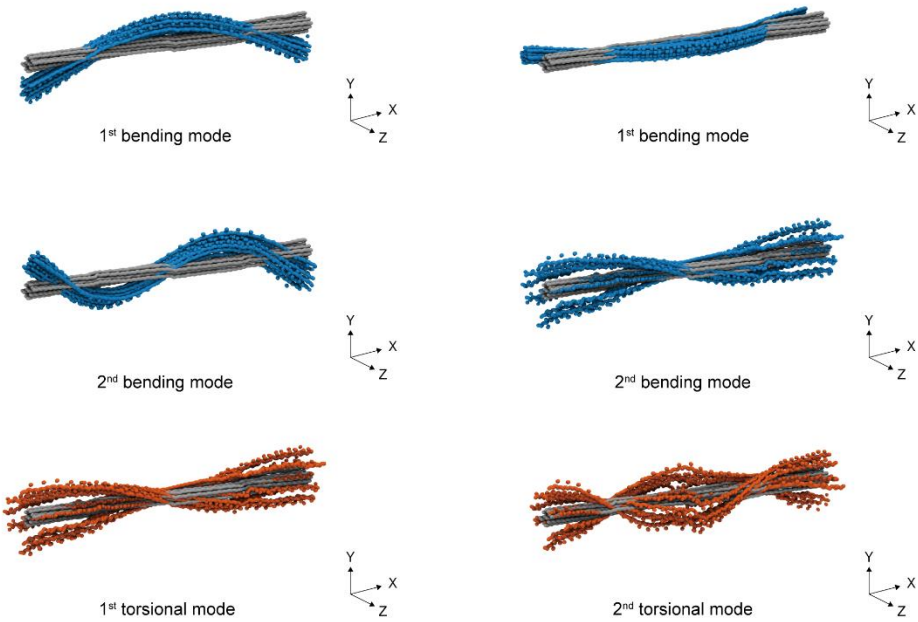


12HB-SQ

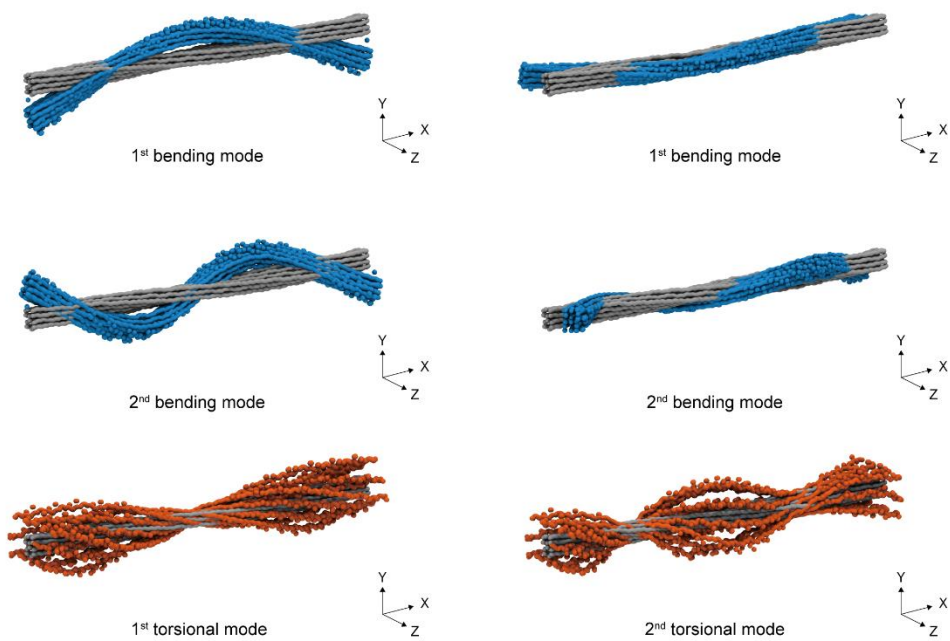


Figure 7-5 (Continued).

13HB-HC

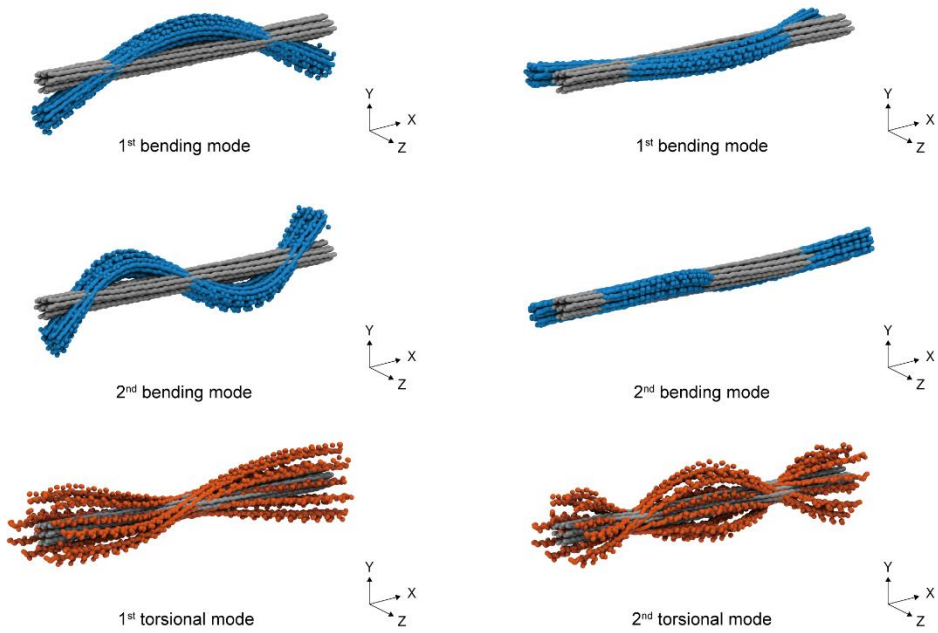


16HB-SQ

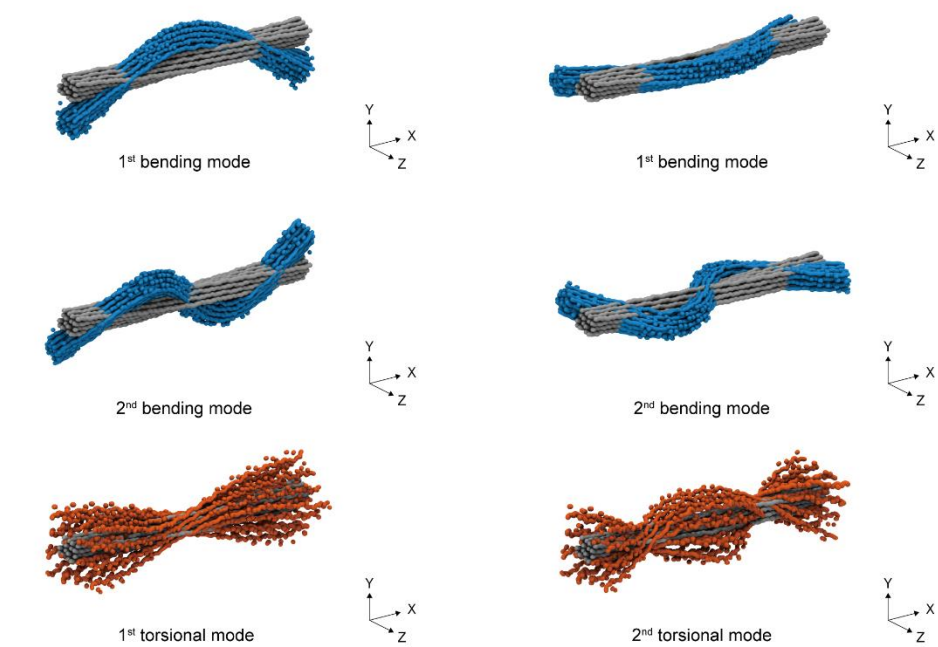


Figure 7-5 (Continued).

The bending persistence length ($L_B^{NMA}$) was derived as $L_B^{NMA} = M\omega^2 L_c^3 / [k_B T(\beta L_C)^4]$ based on the Euler-Bernoulli beam theory, where $M$ and $L_C$ are the total mass and contour length of the structure, respectively, $k_B T$ indicates the product of the Boltzmann constant and the absolute temperature of 300 K, $\beta$ represents the wavenumber of the lowest mode, and $\omega$ is the natural frequency computed by the square root of the lowest mode eigenvalue ($\omega = \sqrt{\lambda}$) (Table 7-1). The computed bending persistence lengths were well matched with the experimental values reported in literature[67,82,93] (Figure 7-6a and Table 7-2).

We theoretically formulated the range of the bending persistence length for bundles design on the square lattice assuming two extremely disconnected and perfectly bonded crosslink conditions between helices. Results confirmed that the predicted values followed the trend of the maximum bending persistence length, $L_{B,max}^{Th} = 4L_B^H N_H^2/3 - L_B^H N_H/3$, where $L_B^H$ is the bending persistence length of a single DNA double helix and $N_H$ is the number of comprising helices, in agreement with the reported quadratic increase[91,92] of $L_B$ with respect to $N_H$. This suggests that the inter-helical crossovers might tightly constrain the adjacent helices in bending and tensile deformation of structures.

Similarly, the torsional persistence length ($L_C^{NMA}$) was estimated from NMA results (Figure 7-6b and Table 7-2) using $L_C^{NMA} = M\omega^2 L_C(J_o/A)/(k_B T\pi^2)$ where $J_o/A$ is the ratio of the polar moment of inertia to the cross-sectional area that depends on the design. The range of the torsional persistence length was formulated theoretically as well. In contrast to bending, we observed that the measured torsional persistence length followed the minimum linear tendency, $L_{C,min}^{Th} = L_C^H N_H$, where the torsional persistence length of a single DNA double helix ($L_C^H$) was simply scaled by the number of helices, as shown in the previous result[82]. It could be, therefore, inferred that the torsional rigidity of a DNA bundle might not be significantly affected by the inter-helix connection by crossovers.

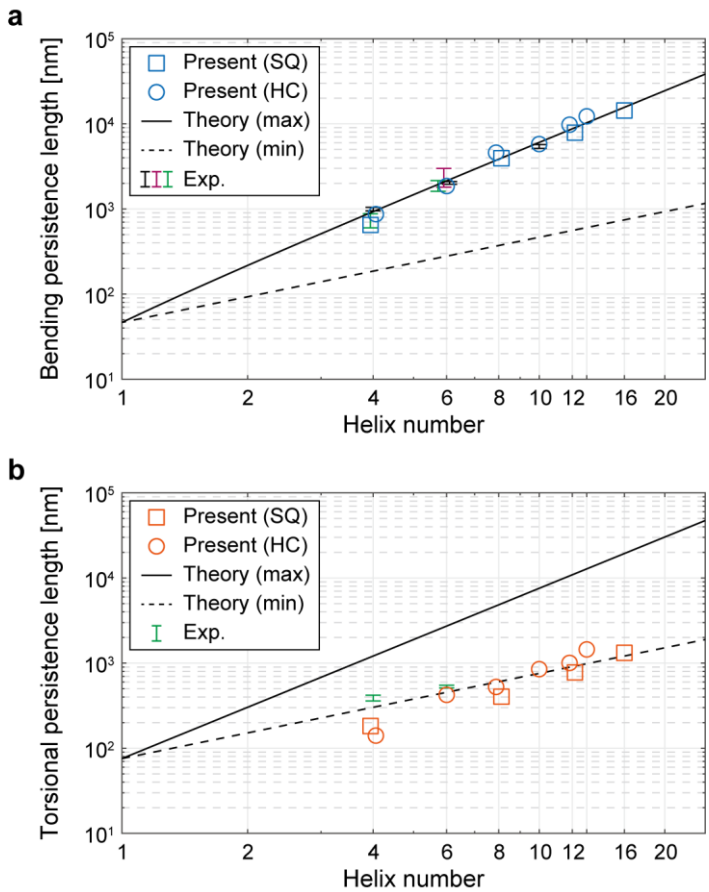


Figure 7-6. Prediction of persistence lengths. (**a**) Bending persistence length. The bending persistence length was derived based on the Euler-Bernoulli beam theory. The bending persistence lengths showed good agreement with the experimental results. The predicted values followed the trend of the maximum bending persistence length in the theoretically formulated range. (**b**) Torsional persistence length. The torsional persistence length was derived under the continuum assumption, showing similar values as previously reported. The measured torsional persistence length followed the minimum linear tendency in theoretical prediction, where the torsional persistence length of a single DNA double helix was simply scaled by the number of helices.

Table 7-1. The natural frequency of bundle structures.

| Mode # | 4HB SQ | 4HB HC | 6 HB HC | 8 HB HC | 8HB SQ | 10HB HC | 12HB HC | 12HB SQ | 13HB HC | 16HB SQ |
|---|---|---|---|---|---|---|---|---|---|---|
| 1 | 2.9E07 | 3.3E07 | 8.9E07 | 2.0E08 | 1.9E08 | 2.9E08 | 5.3E08 | 5.1E08 | 7.2E08 | 1.0E09 |
| 2 | 3.8E07 | 5.0E07 | 1.7E08 | 2.3E08 | 2.1E08 | 4.3E08 | 6.4E08 | 6.0E08 | 7.2E08 | 1.1E09 |
| 3 | 7.9E07 | 8.9E07 | 2.4E08 | 5.7E08 | 5.1E08 | 8.1E08 | 1.4E09 | 1.4E09 | 1.8E09 | 2.1E09 |
| 4 | 9.1E07 | 1.3E08 | 4.0E08 | 5.8E08 | 5.4E08 | 1.1E09 | 1.5E09 | 1.5E09 | 1.8E09 | 2.6E09 |
| 5 | 1.5E08 | 1.7E08 | 4.8E08 | 1.1E09 | 9.5E08 | 1.5E09 | 1.6E09 | 1.6E09 | 1.9E09 | 2.6E09 |
| 6 | 1.7E08 | 1.8E08 | 5.2E08 | 1.1E09 | 9.7E08 | 1.6E09 | 2.5E09 | 2.5E09 | 3.2E09 | 4.1E09 |
| 7 | 2.5E08 | 2.8E08 | 7.6E08 | 1.2E09 | 1.0E09 | 1.9E09 | 2.7E09 | 2.7E09 | 3.2E09 | 4.5E09 |
| 8 | 2.8E08 | 2.9E08 | 7.9E08 | 1.7E09 | 1.5E09 | 2.6E09 | 3.1E09 | 3.2E09 | 3.8E09 | 4.5E09 |
| 9 | 3.7E08 | 3.8E08 | 1.1E09 | 1.8E09 | 1.5E09 | 2.8E09 | 4.0E09 | 3.9E09 | 4.8E09 | 6.1E09 |
| 10 | 3.9E08 | 4.3E08 | 1.2E09 | 2.3E09 | 2.1E09 | 3.0E09 | 4.1E09 | 4.1E09 | 4.8E09 | 6.4E09 |
| 11 | 5.1E08 | 5.3E08 | 1.2E09 | 2.4E09 | 2.2E09 | 3.7E09 | 4.7E09 | 4.8E09 | 5.8E09 | 6.5E09 |
| 12 | 5.6E08 | 5.7E08 | 1.6E09 | 2.5E09 | 2.2E09 | 3.9E09 | 5.3E09 | 5.3E09 | 6.4E09 | 8.1E09 |
| 13 | 6.3E08 | 6.8E08 | 1.6E09 | 3.2E09 | 2.8E09 | 4.4E09 | 5.5E09 | 5.6E09 | 6.4E09 | 8.4E09 |
| 14 | 6.9E08 | 8.4E08 | 2.0E09 | 3.3E09 | 2.8E09 | 4.9E09 | 6.2E09 | 6.4E09 | 7.6E09 | 8.5E09 |
| 15 | 8.0E08 | 8.7E08 | 2.1E09 | 3.5E09 | 3.1E09 | 5.0E09 | 6.8E09 | 6.8E09 | 7.7E09 | 8.9E09 |

Table 7-2. The persistence length of bundle structures.

| Helix number | Bundle type | Contour Length [nm] | Bending persistence length [nm] | | | Torsional persistence length [nm] | | |
|---|---|---|---|---|---|---|---|---|
| $N_H$ | SQ/HC | $L_C$ | $L_{B,min}^{Th}$ | $L_{B,max}^{Th}$ | $L_B^{NMA}$ | $L_{C,min}^{Th}$ | $L_{C,max}^{Th}$ | $L_C^{NMA}$ |
| 4 | SQ | 593.23 | 186.0 | 930.0 | 648.7 | 303.0 | 1515.2 | 182.7 |
| 4 | HC | 599.39 | 186.0 | 930.0 | 869.0 | 303.0 | 1515.2 | 140.9 |
| 6 | HC | 394.06 | 279.0 | 2138.9 | 1857.3 | 454.6 | 3485.0 | 424.1 |
| 8 | HC | 298.01 | 372.0 | 3843.9 | 4584.4 | 606.1 | 6262.9 | 525.8 |
| 8 | SQ | 297.21 | 372.0 | 3843.9 | 3940.9 | 606.1 | 6262.9 | 404.6 |
| 10 | HC | 236.32 | 465.0 | 6044.8 | 5782.1 | 757.6 | 9849.0 | 850.4 |
| 12 | HC | 196.69 | 558.0 | 8741.7 | 9761.0 | 909.1 | 14243.1 | 1005.9 |
| 12 | SQ | 192.37 | 558.0 | 8741.7 | 7869.3 | 909.1 | 14243.1 | 777.9 |
| 13 | HC | 182.99 | 604.5 | 10276.1 | 12250.6 | 984.9 | 16743.3 | 1449.2 |
| 16 | SQ | 149.49 | 744.0 | 15623.4 | 14344.1 | 1212.2 | 25455.8 | 1321.5 |

# 8. Conclusion

We presented a multiscale framework that accurately predicts the structural shape and features of DNA assemblies. Since the proposed approach directly integrated the intrinsic properties of structural motifs obtained from the molecular dynamics simulation, it has the advantage of accurately predicting local and global structural features without modifying parameters. The consistency and efficiency of this framework were verified by addressing the previously reported comprehensive designs. Structural and dynamic characteristics were quantitatively predicted at base-level precision showing the general agreement. In addition, the reconstructed atomic information enables to apply various dynamic simulations from the structurally relaxed configuration. The proposed framework is also expected to be advanced by developing methods for constructing initial configurations from general design and embodying nonlinear mechanical properties. We, therefore, envision that the proposed framework provides detailed and accurate insights into the DNA assemblies. Furthermore, our approach not only supports the wide applicability in structural DNA nanotechnology but also suggests further development for other biomolecules, indicating the possibility of generalization.

# A. SNUPI (Structured NUcleic acids Programming Interface)

The proposed multiscale modeling approach is provided for anyone to use, in a freely available standalone package: SNUPI (Structured Nucleic Acids Programming Interface). The SNUPI is intended for operation in a general personal computing environment. A graphical user interface (GUI) was also developed for easy use by first-time users. The following sections describe the system requirement, general procedure, practical examples, and analysis options in SNUPI.

## A.1. System requirement

○ The implementation of SNUPI was targeted at the personal PC or laptop (GPU card is not required).

○ The pretested computing environment: Windows 10 64 bit, i7-4770 3.4GHz CPU.

○ SNUPI was created using the Standalone Application Compiler in MATLAB.

○ To execute SNUPI, MATLAB Runtime version R2019a (9.6) for windows should be installed.

- If the runtime version is different, it may not run properly. Please check the version.
- Installer site: http://www.mathworks.com/products/compiler/mcr/index.html

○ Mac and Linux OS are not supported currently.

## A.2. Preparation for the analysis

○ Download the SNUPI file.

- SNUPI site: https://github.com/SSDL-SNU/SNUPI

○ The following files are included.

- SNUPI_GUI.exe — SNUPI with a graphical user interface.
- EXAMPLE\<Ex_files> — Example design files.
- FILES\snupi.exe — Solver file.
- FILES\Default.snp — Default analysis options file.
- FILES\Input.txt — The temporary location of an input design.
- INPUT\<input_files> — Input files will be temporarily located in this folder.
- OUTPUT\<output_files> — Output files will be located in this folder.

○ To prepare or modify design files, the caDNAno program should be installed.

- caDNAno site: https://cadnano.org/

○ Notes on design.

- The scaffold strand should be linear, not circular when generating a ‘pdb’ file.
- BP-deletion should not be placed on the BPs of crossover and nick.
- The double-strand break is not considered in the analysis.
- Both ends of the single-strand should be connected to the structure.

○ To visualize the results, the VMD program is recommended.

- VMD site: https://www.ks.uiuc.edu/Research/vmd/

## A.3. General procedure

- Step 1. Run SNUPI.
- Step 2. Select a design file.
    - Design file (.json) should be assigned but sequence file (.csv) is optional.
- Step 3. Select the options.
- Step 4. Perform the analysis.
    - Design and option files are temporarily saved in the INPUT folder.
    - The result files are saved in the OUTPUT folder.
- Step 5. Post-process the results.

## A.4. Examples

### A.4.1. Example 1: Simple structural analysis using the default option

○ This example describes how to analyze a design file using the default option.

● Step 1. Run SNUPI.

• Execute ‘SNUPI_GUI.exe’.

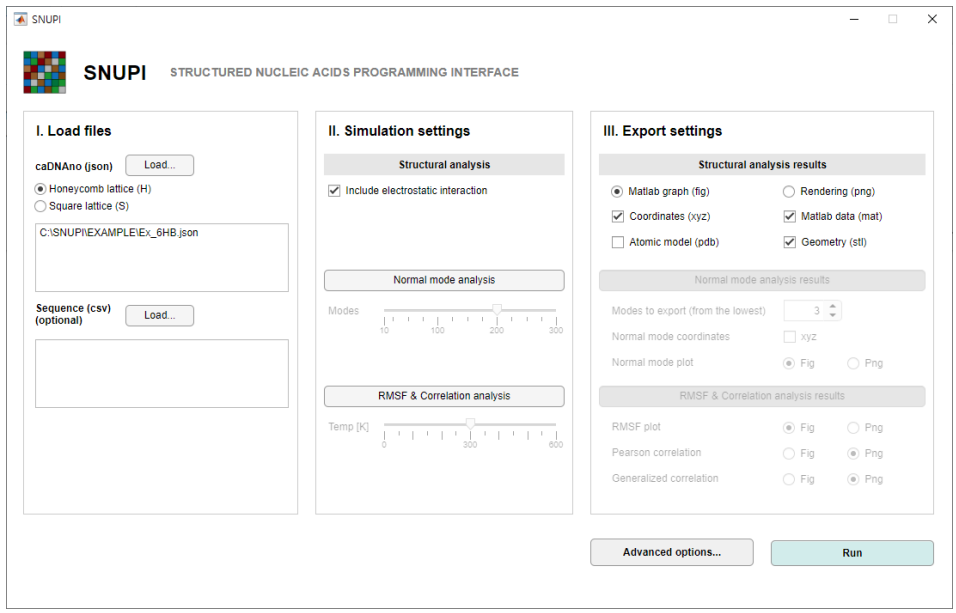


Figure A-1. SNUPI graphical user interface (GUI) window.

• Description of the GUI window.

[I. Load files]

- caDNAno (json): select a design file and its lattice type.
- Sequence (csv): select the corresponding sequence file (optional).

[II. Simulation options]

- Structural analysis: select if applying electrostatic interaction.
- Normal mode analysis: select (1) whether performing the analysis and (2) the lowest mode number to calculate.
- RMSF & Correlation analysis: select (1) whether performing the analysis and (2) temperature.

[III. Export options]

- Structural analysis results: select the exporting file type of the final configuration.
- Normal mode analysis results: select (1) the modes to export, (2) whether exporting 'xyz' files, and (3) plot type of each mode shape.
- RMSF & Correlation analysis results: select the plot type of (1) RMSF, (2) Pearson correlation, and (3) Generalized correlation.

● Step 2. Select a design file.

- Load the design file (EXAMPLE\Ex_6HB.json),
- Specify the 'Honeycomb lattice'.
- Sequence file (.csv) is not necessary.

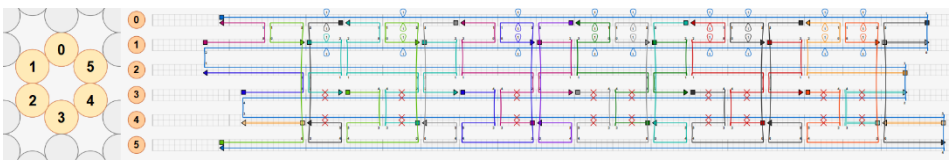


Figure A-2. Example 6-helix-bundle design.

● Step 3. Select options.

- To use the default options, any modification in GUI is not necessary.
- In 'Advanced options...', the analysis parameters can be modified in more detail.
- Advanced options are described in the independent section (*SNUPI options*).
- To use the default options, press the 'Save and Close' button.

● Step 4. Perform analysis.

- Press the 'Run' button.
  - The selected option (.snp) and design (.json) files are saved in the 'INPUT' folder.
  - The analysis procedure is displayed in the command prompts as below.
  - The log file of the analysis procedure is saved as an 'Ex_6HB.log' file in the 'OUTPUT' folder.

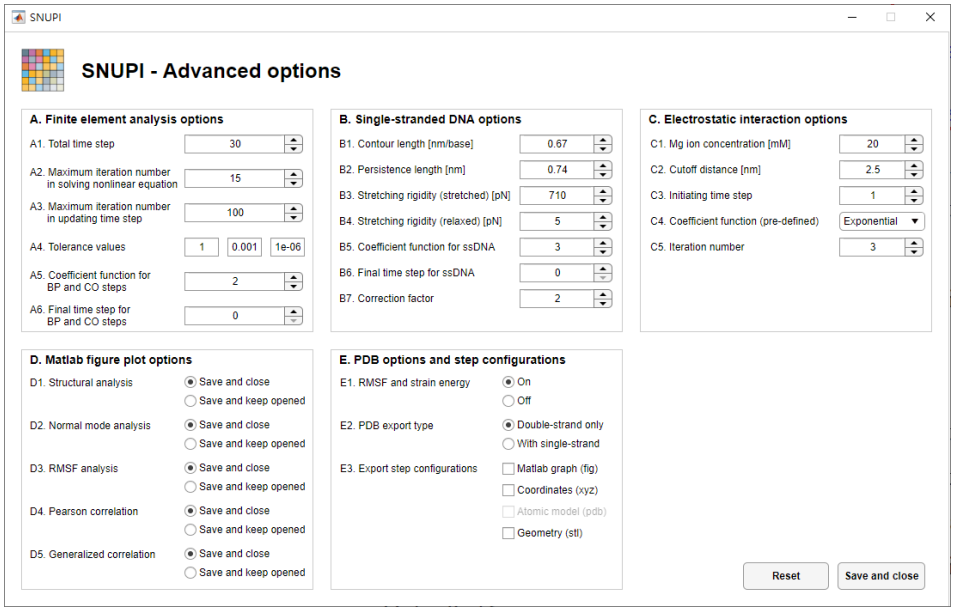


Figure A-3. Advanced options window.

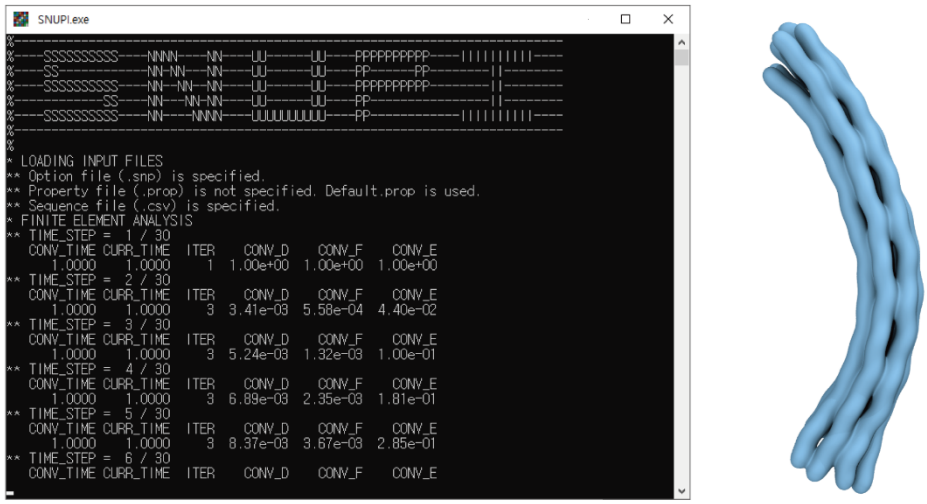


Figure A-4. Analysis procedure and the predicted shape.

- Step 5: Post-process the results
  - The output files are saved in the directory, ‘OUTPUT\Ex_6HB_<time>’.
    - The design file is saved as the ‘Ex_6HB.json’ file.
    - Since sequence (csv) was not specified, mean properties were used.
  - The employed options for the analysis were saved as ‘OUTPUT\Ex_6HB.snp’.

- Since any option was not modified, the default options were used.
- The default file is provided as 'DEFAULT\Default.snp'.

• The final shape is saved as 'Ex_6HB_FINAL.fig', 'Ex_6HB_FINAL.xyz', 'Ex_6HB_FINAL.stl' files.

• The 'Ex_6HB.xyz' file can be rendered using the VMD program with the graphical options as above.
- The topology ('psf' file) should be first generated.
- Material: AOChalky
- Drawing Methods: QuickSurf
- Radius Scale: 3.8
- Renderer: Tachyon

• Results are saved in 'Ex_6HB.mat' file (MATLAB).
- FE_DATA: Structural element connectivity (E_CONN), Mass matrix (M_G)
- NLA_DATA: Initial nodal configuration for each time step (INIT_NODE), Final nodal configuration for each time step (FINL_NODE), Initial element triads for each time step (INIT_TR), Final element triads for each time step (FINL_TR), Stiffness matrix for each time step (K_G)
- NA_HELIX: Helix data
- NA_CROSS: Crossover data
- The unit of values is [pN] or [nm].

### A.4.2. Example 2: Prediction of structural and dynamic properties

○ This example describes how to predict structural shape, normal modes, and dynamic properties.

● Step 1. Run SNUPI.

• Execute 'SNUPI_GUI.exe'.

● Step 2. Select a design file.

• Load the design file (EXAMPLE\Ex_8HB.json),

• Specify the 'Square lattice'.

• Load sequence file (EXAMPLE\Ex_8HB.csv).

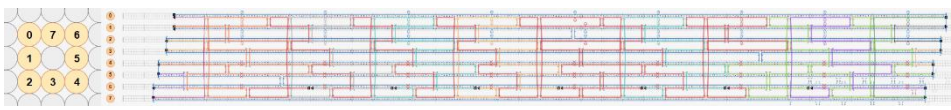


Figure A-5. Example 8-helix-bundle design.

● Step 3. Select options.

• To export atomic representation, select the 'atomic model (pdb)'.

• To perform normal mode analysis, select 'Normal mode analysis'.

- The number of the lowest normal modes to calculate was set to 200 in default.

- The number of the lowest normal modes to export was set to 3 in default.

• To additionally export 'xyz' files for mode shapes, select 'Normal mode coordinates'.

• To calculate dynamic properties, select 'RMSF & Correlation analysis'.

- The root-mean-square-fluctuation (RMSF) and correlation coefficients are calculated.

- The default absolute temperature was set to 300 K in default.

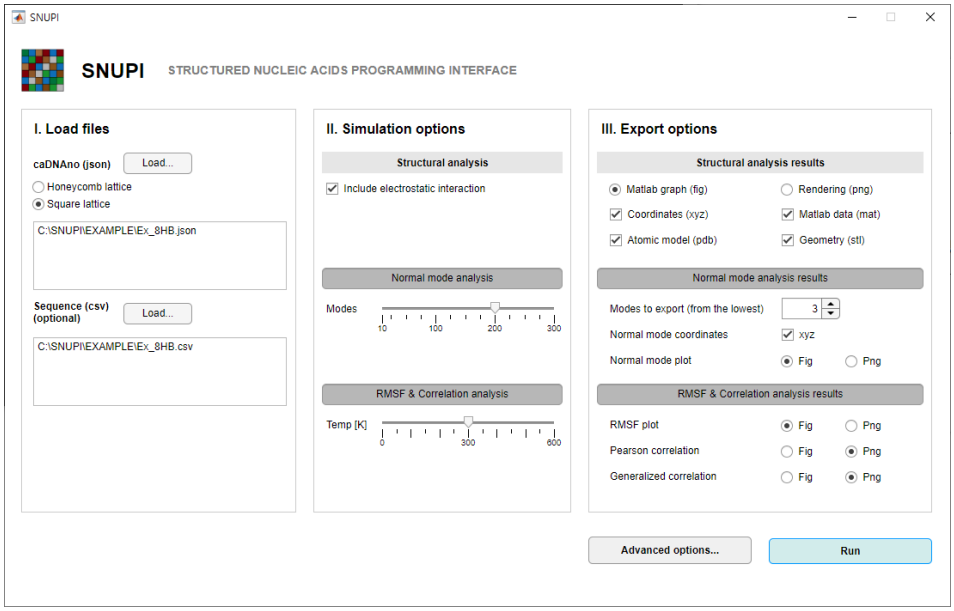


Figure A-6. SNUPI graphical user interface window.

- Step 4. Perform analysis.
  - Press the 'Run' button.
    - The selected option (.snp) and design (.json) files are saved in the 'INPUT' folder.
    - The analysis procedure is displayed in the command prompts as below.
    - The log file of the analysis procedure is saved as the 'Ex_8HB.log' file in the 'OUTPUT' folder.

- Step 5: Post-process the results
  - The output files are saved in the directory, 'OUTPUT\Ex_8HB_<time>'.
    - The design file is saved as the 'Ex_8HB.json' file.
    - The sequence file is saved as the 'Ex_8HB.csv' file.
    - Since sequence (csv) was specified, sequence-dependent properties were used.
  - The employed options for the analysis were saved as 'OUTPUT\Ex_8HB.snp'.
  - The final shape is saved as files with different formats (fig, xyz, stl, and pdb).

• The ‘Ex_8HB.pdb’ file can be rendered using the VMD program with the graphical options as below.

- Material: AOChalky
- Drawing Methods: NewCartoon
- Renderer: Tachyon

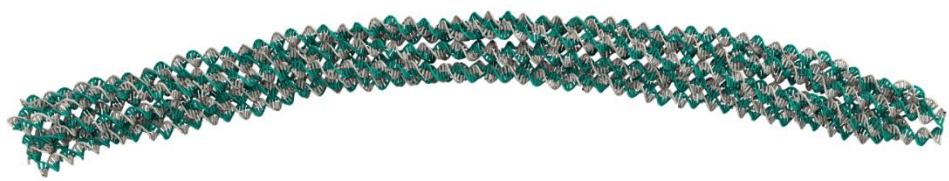

Figure A-7. Predicted structural shape.

• Results of the structural analysis were saved in ‘Ex_8HB.mat’ file (MATLAB)

- FE_DATA: Structural element connectivity (E_CONN), Mass matrix (M_G), Total strain energy (TOTAL_SE)
- NLA_DATA: Initial nodal configuration for each time step (INIT_NODE), Final nodal configuration for each time step (FINL_NODE), Initial element triads for each time step (INIT_TR), Final element triads for each time step (FINL_TR), Stiffness matrix for each time step (K_G)
- The unit of values is [pN] or [nm].

• The total strain energy values were saved in the Beta column of the ‘Ex_8HB.pdb’ file.

- The values are normalized in the range of 0 to 1.

• The total strain energy map in the ‘Ex_8HB.pdb’ file can be rendered using the VMD program as below.

- Material: AOChalky
- Coloring Methods: Beta
- Drawing Methods: QuickSurf
- Renderer: Tachyon
- Color: Low strain energy (white), High strain energy (blue)

Figure A-8. The total strain energy map of the structure.

• By performing normal mode analysis, the eigensolutions were saved in 'Ex_8HB.mat' file.

  - NMA_DATA: Eigenvalues (EIG_VAL), Eigenvectors (EIG_VEC)

• The bending mode shape was obtained as the lowest (first) mode.

  - The reference (final) shape is saved as 'Ex_8HB_MODE_0_REF.xyz' or 'fig' files.

  - The $k^{th}$ mode shape is saved as 'Ex_8HB_MODE_k.xyz' or 'fig' files.

• The 'xyz' files of mode shapes can be rendered using the VMD program with the graphical options as below.

  - Material: AOChalky

  - Drawing Method: Beads

  - Color: Reference shape (gray), the lowest mode shape (blue)

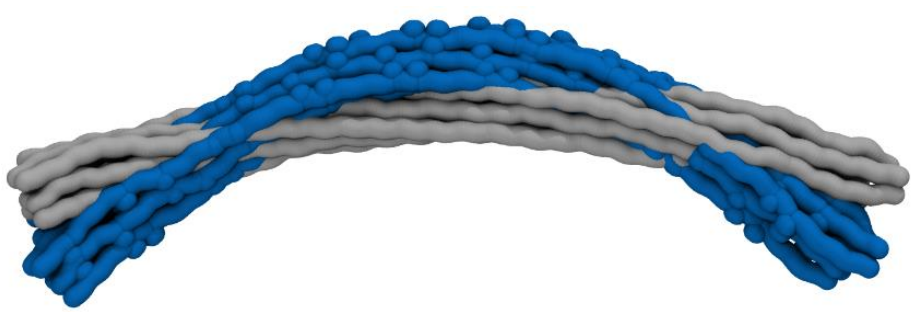

Figure A-9. The lowest mode shape of the structure.

• The dynamic properties were saved in 'Ex_8HB.mat' file.

  - NMA_DATA: RMSF values (RMSF), Pearson correlation coefficient (CORR_P_MAT), Generalized correlation coefficient (CORR_G_MAT)

• The RMSF values were saved in the Occupancy column of the 'Ex_8HB.pdb' file.

- The values are normalized in the range of 0 to 1.

• The RMSF map in the 'Ex_8HB.pdb' file can be rendered using the VMD program as below.

- Material: AOChalky
- Coloring Methods: Occupancy
- Drawing Methods: QuickSurf
- Renderer: Tachyon
- Color: Low fluctuation (white), High fluctuation (red)

Figure A-10. The RMSF map of the structure.

• Correlation coefficients are saved in the 'Ex_8HB_CORR' files.

- Pearson correlation coefficient: 'Ex_8HB_CORR_P.png'
- Generalized correlation coefficient: 'Ex_8HB_CORR_G.png'

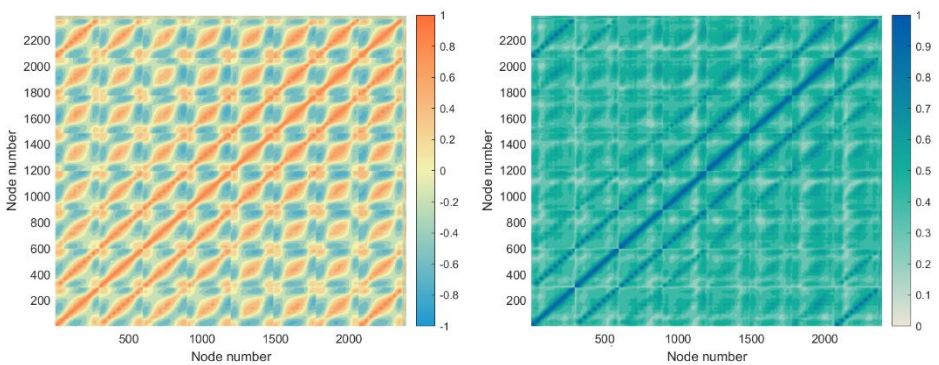


Figure A-11. Pearson (left) and generalized (right) correlation coefficients.

# A.5. Analysis options

## A.5.1. Finite element analysis option

○ TIME_STEP Total time step ($T$).

This represents the total time step for structural analysis. The larger the time step is, the finer the properties change from the initial to the final structure. In general, the total time step between 20 and 40 is appropriate.

Default: 30

○ ITER_NL_NUM Maximum iteration number in each time step.

This represents the maximum iteration number for finding a solution in a time step. If no solution is found in each step, the properties are adjusted.

Default: 15

○ ITER_TIME_NUM Maximum iteration number in updating the time step.

This represents the maximum number of adjustments of properties in each time step.

Default: 100

○ TOL Tolerance value for displacement, force, and energy criteria.

Two of the three tolerance values are generally specified lower than 1.

Default: 1 1E-3 1E-6

## A.5.2. Base-pair and crossover steps options

○ BP_CF_IND Coefficient function for BP and CO steps (${}^{t}\alpha_{\mathrm{BP}}^{k}$).

This represents the degree of adjusting properties from the initial ($t = 1$) to the final time step ($t = t_f$). The order of the prebuilt coefficient function is specified. For example, if 1 is specified, the property values are linearly modified. When using the electrostatic Interaction option (DO_ES), it could be appropriate to specify 2 since it is efficient to first build the structural shape and then gradually increase the electrostatic elements. The coefficient function has a value between 0 and 1 in time steps from 0 to $t_f$.

[1] Order 1: ${}^{t}\alpha_{\mathrm{BP}}^{1} = 1 - (t - t_f)/(1 - t_f)$

[2] Order 2: ${}^{t}\alpha_{\mathrm{BP}}^{2} = 1 - (t - t_f)^2/(1 - t_f)^2$

[k] Order $k$: ${}^{t}\alpha_{\mathrm{BP}}^{k} = 1 - (t - t_f)^k/(1 - t_f)^k$

Default: 2

○ BP_TIME_FINL Final time step for BP and CO steps ($t_f$).

This represents the final time step at which each structural element of BP and CO steps has the final properties. After $t_f$, the coefficient function has the value 1. $t_f$ should have the value the same or smaller than the total time step ($T$). If $t_f$ is assigned to 0 or $t_f > T$, $t_f$ is automatically set to $T$. This option can be used to first converge the mechanical properties and later generate the electrostatic force. For example, setting as $T = 30$, $t_f = 15$, and $t_{\mathrm{ES}} = 10$ represents that the properties of structural elements of BP and CO steps are adjusted for 0-15 time steps, and electrostatic elements are generated for 10-30 time steps.

Default: 0

### A.5.3. Single-stranded DNA options

○ SS_LC1 Contour length per nucleotide ($L_{C1}$).

This value represents the length of each nucleotide (nt) of a single-stranded DNA.

The total contour length ($L_C$) is obtained by multiplying this value by the number of nucleotides. Unit = [nm/nt]

Default: 0.67

○ SS_LB Persistence length ($L_B$).

This value represents the bending persistence length of a single-strand DNA. Unit = [nm]

Default: 0.74

○ SS_EA_H Stretching rigidity when stretched ($EA^H$).

This value represents the stretching rigidity in the high force region. Unit = [pN]

Default: 710

○ SS_EA_L Stretching rigidity when relaxed ($EA^L$).

This value represents the stretching rigidity in the low force region. Unit = [pN]

Default: 5

○ SS_CF_IND Coefficient function for ssDNA (${}^t\alpha_{ss}^k$).

This represents the degree of adjusting properties from the initial ($t = 1$) to the final time step ($t = t_f$). The order of the prebuilt coefficient function is specified.

[1] Order 1: ${}^t\alpha_{ss}^1 = 1 - (t - t_f)/(1 - t_f)$

[2] Order 2: ${}^t\alpha_{ss}^2 = 1 - (t - t_f)^2/(1 - t_f)^2$

[k] Order *k*: ${}^t\alpha_{ss}^k = 1 - (t - t_f)^k/(1 - t_f)^k$

Default: 3

○ SS_TIME_FINL Final time step for single-stranded DNA ($t_f$).

This represents the final time step at which each structural element of ssDNA has the final properties. $t_f$ should have the value the same or smaller than the total time step ($T$). If $t_f$ is assigned to 0 or $t_f > T$, $t_f$ is automatically set to $T$. After $t_f$, the coefficient function has the value 1. This option can be used to first converge the mechanical properties and later generate the electrostatic force. For example, setting as $T = 30$, $t_f = 15$, and $t_{\mathrm{ES}} = 10$ represents that the properties of ssDNA elements are adjusted for 0-15 time steps, and electrostatic elements are generated for 10-30 time steps.

Default: 0

○ SS_CORR Correction factor of single-stranded DNA ($\gamma_{ss}$).

This index controls the ratio of ssDNA (end-to-end length/contour length). The ratio could be larger than the default value (1) in the structure.

Default: 2

## A.5.4. Electrostatic interaction options

○ DO_ES Electrostatic interaction.

If this option was used, electrostatic elements were generated between two nodes in the cut-off distance.

[0] Not use

[1] Use

Default: 1

○ ES_TEMP Temperature ($T$).

This represents the temperature used to determine the Debye screening length.

Unit = [K]

Default: 300

○ ES_MG Mg concentration ($C_{\mathrm{Mg}}$).

This option represents the Mg condition used to calculate electrostatic forces. Unit = [mM]

Default: 20

○ ES_R_CUT Cutoff distance ($r_{\mathrm{cut}}$).

The cutoff distance was used as a criterion whether electrostatic elements are generated or not by measuring the distance between nodes in a nonlinear solution procedure. Unit = [nm]

This option corresponds to [C2] in the 'Advanced options' window.

Default: 2.5

○ ES_TIME_INIT Initiating time step of electrostatic interaction ($t_{\mathrm{ES}}$).

For this effective generation of electrostatic elements, $t_{\mathrm{ES}}$ can be used as the initiating time step of the electrostatic interaction, which was excluded when the time step was smaller than $t_{\mathrm{ES}}$.

This option corresponds to [C3] in the 'Advanced options' window.

Default: 1

○ ES_CF_IND Coefficient function for electrostatic elements (${}^{t}\beta_{\mathrm{ES}}^{k}$).

This represents the degree of the number of electrostatic elements from the initial ($t = t_{\mathrm{ES}}$) to the final time step ($t = t_f$).

This option corresponds to [C4] in the 'Advanced options' window.

If the structural deformation is expected to be small or large, invoking exponential [1] or linear [3] increase is appropriate, respectively. It is generally sufficient to increase the number of electrostatic elements in a quadratic manner [2].

[1] Exponential: ${}^{t}\beta_{\mathrm{ES}} = (0.5^{T-t} - 0.5^{T-t_{\mathrm{ES}}}))/(1 - 0.5^{T-t_{\mathrm{ES}}})$

[2] Quadratic: ${}^{t}\beta_{\mathrm{ES}}^{2} = (t - t_{\mathrm{ES}})^2/(t_f - t_{\mathrm{ES}})^2$

[3] Linear: ${}^{t}\beta_{\mathrm{ES}}^{1} = (t - t_{\mathrm{ES}})/(t_f - t_{\mathrm{ES}})$

[4] Constant: ${}^{t}\beta_{\mathrm{ES}}^{0} = 1$

Default: 1

○ ES_ITER_NUM Iteration number for electrostatic interaction.

This represents the iteration number to generate electrostatic elements in each time step. Electrostatic elements were generated uniformly by the number determined by the coefficient function. To avoid the divergence, different configurations were analyzed by this iteration number for the same number of electrostatic elements.

This option corresponds to [C5] in the 'Advanced options' window.

Default: 3

○ ES_QEFF_USER User-defined effective charge.

Effective charge ($q$) values were used as 0.7 and 1.5 for 20 and 100 mM Mg concentration, respectively. In default, for other conditions, the effective charge is determined in terms of Mg concentration ($C_{\mathrm{Mg}}$) by a linear function ($q = 0.01C_{\mathrm{Mg}} + 0.5$). This option allows specifying a different effective charge regardless of the Mg concentration.

Not to use this option, set 0.

Default: 0

○ ES_CF_USER User-defined coefficient function for electrostatic elements.

The electrostatic interaction can be controlled by the user-defining coefficient function. Input values should have the same dimension of total time step ($T$), and each value should be in the range of [0, 1]. For example, for the total time step 10, ES_CF_USER can be set as 0 0.1 0.2 0.4 0.6 0.8 0.9 0.95 0.99 1

Not to use this option, set 0.

Default: 0

### A.5.5. Normal mode analysis options

○ DO_NMA Normal mode analysis (NMA).

If this option was used, NMA was performed after the solution converged.

[0] Not perform NMA

[1] Perform NMA

Default: 0

○ NMA_MODE_NUM The lowest mode number to be calculated.

Eigenmodes will be calculated from the smallest eigenvalue to this value. This mode number should be smaller than the total degrees of freedom.

Default: 200

○ PLOT_NMA_MODE Plot or save mode shapes.

[0] Not save and not plot

[1] Save and closed (.fig)

[2] Save and opened (.fig)

[3] Save and closed (.png)

[4] Save and opened (.png)

Default: 1

○ PLOT_MODE_NUM Mode number to be plotted from the lowest mode.

This represents the number of eigenmodes to plot and save from the first mode.

Default: 0

○ XYZ_MODE_NUM Mode number to save in the XYZ format.

This option indicates the number of eigenmodes from the lowest mode to save as an XYZ file.

[0] Not save

[k] Save 1 to k modes to XYZ files

Default: 0

### A.5.6. RMSF and correlation options

○ DO_RMSF_CORR RMSF and correlation coefficients.

This option indicates whether to calculate the root-mean-square-fluctuation (RMSF) and the correlation coefficients. This only works when the NMA option is turned on (DO_NMA = 1).

[0] Not perform

[1] Perform

Default: 0

○ RMSF_CORR_TEMP Temperature.

This represents the absolute temperature used in the equipartition theorem.

Unit = [K]

Default: 300

○ PLOT_RMSF Plot or save the RMSF distribution.

[0] Not save and not plot

[1] Save and closed (.fig)

[2] Save and opened (.fig)

[3] Save and closed (.png)

[4] Save and opened (.png)

Default: 3

○ PLOT_CORR_P Plot or save the Pearson correlation map.

[0] Not save and not plot

[1] Save and closed (.fig)

[2] Save and opened (.fig)

[3] Save and closed (.png)

[4] Save and opened (.png)

Default: 3

○ PLOT_CORR_G Plot or save the generalized correlation map.

[0] Not save and not plot

[1] Save and closed (.fig)

[2] Save and opened (.fig)

[3] Save and closed (.png)

[4] Save and opened (.png)

Default: 3

### A.5.7. Configuration plot options

○ PLOT_FINL_CONF Plot or save the configuration at the final time step.

[0] Not save and not plot

[1] Save and closed (.fig)

[2] Save and opened (.fig)

[3] Save and closed (.png)

[4] Save and opened (.png)

Default: 1

○ PLOT_STEP_CONF Plot or save the configurations at the given time steps.

The configurations are saved as fig files. The maximum time step should be less than or equal to the total time step ( $T$ ). The values are given in row values. For example, PLOT_STEP_CONF 10 15 20

Not to use this option, set 0.

Default: 0

## A.5.8. Output file options

○ GEN_FINL_XYZ Generation of the xyz file of the final configuration.

[0] Not generation

[1] Generation

Default: 1

○ GEN_STEP_XYZ Generation of the xyz file for given time steps.

The configurations are saved as the xyz files. The maximum time step should be less than or equal to the total time step ($T$). The values are given in row values. For example, GEN_STEP_XYZ 10 15 20

Not to use this option, set 0

Default: 0

○ GEN_FINL_STL Generation of the stl file of the final configuration.

[0] Not generation

[1] Generation

Default: 1

○ GEN_STEP_STL Generation of the stl file for given time steps.

The configurations are saved as the stl files. The maximum time step should be less than or equal to the total time step ($T$). The values are given in row values.

Not to use this option, set 0

Default: 0

○ GEN_FINL_PDB Generation of the pdb file of the final configuration.

The pdb file is generated only when the input CSV file is assigned.

[0] Not generation

[1] Generation

Default: 0

○ GEN_STEP_PDB Generation of the pdb file for given time steps.

The configurations are saved as the pdb files. The maximum time step should be less than or equal to the total time step ( $T$ ). The values are given in row values. For example, GEN_STEP_PDB 10 15 20

Not to use this option, set 0

Default: 0

○ PDB_OB_IND Save occupancy and beta as RMSF and strain energy in the pdb file.

This option is used to save the RMSF (occupancy) and residual strain energy (beta) values into the PDB file for visualization. Each value is normalized.

[0] Not save

[1] Save

Default: 1

○ PDB_EX_IND Export format of the pdb file.

Since the position of central nucleotides of ssDNA does not be determined, they are generated evenly based on the configuration of terminal BPs. The configuration of the generated ssDNA may not be appropriate.

[1] Generation of PDB file except for ssDNA configuration

[2] Generation of PDB file including ssDNA configuration

Default: 1

○ SAVE_MAT_IND Save of the mat file.

[0] Not save

[1] Save initial and final step data

[2] Save all step data

Default: 1

# Bibliography


1 Pinheiro, A. V., Han, D., Shih, W. M. & Yan, H. Challenges and opportunities for structural DNA nanotechnology. *Nat. Nanotechnol.* **6**, 763 (2011).

2 Jones, M. R., Seeman, N. C. & Mirkin, C. A. Programmable materials and the nature of the DNA bond. *Science* **347**, 1260901 (2015).

3 Winfree, E., Liu, F., Wenzler, L. A. & Seeman, N. C. Design and self-assembly of two-dimensional DNA crystals. *Nature* **394**, 539-544 (1998).

4 Ke, Y., Ong, L. L., Shih, W. M. & Yin, P. Three-dimensional structures self-assembled from DNA bricks. *Science* **338**, 1177-1183 (2012).

5 Rothemund, P. W. Folding DNA to create nanoscale shapes and patterns. *Nature* **440**, 297-302 (2006).

6 Zhang, F. et al. Complex wireframe DNA origami nanostructures with multi-arm junction vertices. *Nat. Nanotechnol.* **10**, 779 (2015).

7 Dietz, H., Douglas, S. M. & Shih, W. M. Folding DNA into twisted and curved nanoscale shapes. *Science* **325**, 725-730 (2009).

8 Douglas, S. M. et al. Self-assembly of DNA into nanoscale three-dimensional shapes. *Nature* **459**, 414 (2009).

9 Han, D. et al. DNA origami with complex curvatures in three-dimensional space. *Science* **332**, 342-346 (2011).

10 Lee, C., Lee, J. Y. & Kim, D.-N. Polymorphic design of DNA origami structures through mechanical control of modular components. *Nat. Commun.* **8**, 2067 (2017).

11 Wagenbauer, K. F., Sigl, C. & Dietz, H. Gigadalton-scale shape-programmable DNA assemblies. *Nature* **552**, 78 (2017).

12 Tikhomirov, G., Petersen, P. & Qian, L. Fractal assembly of micrometre-scale DNA origami arrays with arbitrary patterns. *Nature* **552**, 67-71 (2017).

13 Snodin, B. E. et al. Introducing improved structural properties and salt dependence into a coarse-grained model of DNA. *J. Chem. Phys.* **142**, 06B613_611 (2015).

14 Reshetnikov, R. V. et al. A coarse-grained model for DNA origami. *Nucleic Acids Res.* **46**, 1102-1112 (2018).

15 Snodin, B. E., Schreck, J. S., Romano, F., Louis, A. A. & Doye, J. P. Coarse-grained modelling of the structural properties of DNA origami. *Nucleic Acids Res.* **47**, 1585-1597 (2019).

16 Castro, C. E. et al. A primer to scaffolded DNA origami. *Nat. Methods* **8**, 221 (2011).

17 Kim, D.-N., Kilchherr, F., Dietz, H. & Bathe, M. Quantitative prediction of 3D solution shape and flexibility of nucleic acid nanostructures. *Nucleic Acids Res.* **40**, 2862-2868 (2012).

18 Lee, J. Y. et al. Investigating the sequence-dependent mechanical properties of DNA nicks for applications in twisted DNA nanostructure design. *Nucleic Acids Res.* **47**, 93-102 (2019).

19 Brooks, B. R., Janežič, D. & Karplus, M. Harmonic analysis of large systems. I. Methodology. *J. Comput. Chem.* **16**, 1522-1542 (1995).

20 Battini, J.-M. & Pacoste, C. Co-rotational beam elements with warping effects in instability problems. *Comput. Methods. Appl. Mech. Eng.* **191**, 1755-1789 (2002).

21 Bosco, A., Camunas-Soler, J. & Ritort, F. Elastic properties and secondary structure formation of single-stranded DNA at monovalent and divalent salt conditions. *Nucleic Acids Res.* **42**, 2064-2074 (2013).

22 Yoo, J. & Aksimentiev, A. The structure and intermolecular forces of DNA condensates. *Nucleic Acids Res.* **44**, 2036-2046 (2016).

23 Zhang, Z.-L., Wu, Y.-Y., Xi, K., Sang, J.-P. & Tan, Z.-J. Divalent ion-mediated DNA-DNA interactions: a comparative study of triplex and duplex. *Biophys. J.* **113**, 517-528 (2017).

24 Pasi, M. et al. μABC: a systematic microsecond molecular dynamics study of tetranucleotide sequence effects in B-DNA. *Nucleic Acids Res.* **42**, 12272-12283 (2014).

25 Lavery, R. et al. A systematic molecular dynamics study of nearest-neighbor effects on base pair and base pair step conformations and fluctuations in B-DNA. *Nucleic Acids Res.* **38**, 299-313 (2010).

26 Lu, X. J. & Olson, W. K. 3DNA: a software package for the analysis, rebuilding and visualization of three-dimensional nucleic acid structures. *Nucleic Acids Res.* **31**, 5108-5121 (2003).

27 Häse, F. & Zacharias, M. Free energy analysis and mechanism of base pair stacking in nicked DNA. *Nucleic Acids Res.* **44**, 7100-7108 (2016).

28 Yakovchuk, P., Protozanova, E. & Frank-Kamenetskii, M. D. Base-stacking and base-pairing contributions into thermal stability of the DNA double helix. *Nucleic Acids Res.* **34**, 564-574 (2006).

29 Phillips, J. C. et al. Scalable molecular dynamics with NAMD. *J. Comput. Chem.* **26**, 1781-1802 (2005).

30 Hart, K. et al. Optimization of the CHARMM additive force field for DNA: Improved treatment of the BI/BII conformational equilibrium. *J. Chem. Theory. Comput.* **8**, 348-362 (2012).

31 Yoo, J. & Aksimentiev, A. In situ structure and dynamics of DNA origami determined through molecular dynamics simulations. *Proc. Natl. Acad. Sci. U.S.A.* **110**, 20099-20104 (2013).

32 Maffeo, C., Yoo, J. & Aksimentiev, A. De novo reconstruction of DNA origami structures through atomistic molecular dynamics simulation. *Nucleic Acids Res.* **44**, 3013-3019 (2016).

33 Pan, K. et al. Lattice-free prediction of three-dimensional structure of programmed DNA assemblies. *Nat. Commun.* **5**, 5578 (2014).

34 Pan, K., Bricker, W. P., Ratanalert, S. & Bathe, M. Structure and conformational dynamics of scaffolded DNA origami nanoparticles. *Nucleic Acids Res.* **45**, 6284-6298 (2017).

35 Jorgensen, W. L., Chandrasekhar, J., Madura, J. D., Impey, R. W. & Klein, M. L. Comparison of simple potential functions for simulating liquid water. *J. Chem. Phys.* **79**, 926-935 (1983).

36 Essmann, U. et al. A smooth particle mesh Ewald method. *J. Chem. Phys.* **103**, 8577-8593 (1995).

37 Feller, S. E., Zhang, Y., Pastor, R. W. & Brooks, B. R. Constant pressure molecular dynamics simulation: the Langevin piston method. *J. Chem. Phys.* **103**, 4613-4621 (1995).

38 Fujii, S., Kono, H., Takenaka, S., Go, N. & Sarai, A. Sequence-dependent DNA deformability studied using molecular dynamics simulations. *Nucleic Acids Res.* **35**, 6063-6074 (2007).

39 Lankaš, F., Šponer, J., Langowski, J. & Cheatham III, T. E. DNA basepair step deformability inferred from molecular dynamics simulations. *Biophys. J.* **85**, 2872-2883 (2003).

40 Liebl, K., Drsata, T., Lankas, F., Lipfert, J. & Zacharias, M. Explaining the striking difference in twist-stretch coupling between DNA and RNA: A comparative molecular dynamics analysis. *Nucleic Acids Res.* **43**, 10143-10156 (2015).

41 Gore, J. et al. DNA overwinds when stretched. *Nature* **442**, 836-839 (2006).

42 Gross, P. et al. Quantifying how DNA stretches, melts and changes twist under tension. *Nat. Phys.* **7**, 731-736 (2011).

43 Smith, S. B., Cui, Y. & Bustamante, C. Overstretching B-DNA: the elastic response of individual double-stranded and single-stranded DNA molecules. *Science* **271**, 795-799 (1996).

44 Wang, M. D., Yin, H., Landick, R., Gelles, J. & Block, S. M. Stretching DNA with optical tweezers. *Biophys. J.* **72**, 1335 (1997).

45 Baumann, C. G., Smith, S. B., Bloomfield, V. A. & Bustamante, C. J. P. o. t. N. A. o. S. Ionic effects on the elasticity of single DNA molecules. *Proc. Natl. Acad. Sci. U.S.A.* **94**, 6185-6190 (1997).

46 Moroz, J. D. & Nelson, P. Torsional directed walks, entropic elasticity, and DNA twist stiffness. *Proc. Natl. Acad. Sci. U.S.A.* **94**, 14418-14422 (1997).

47 Bustamante, C., Smith, S. B., Liphardt, J. & Smith, D. Single-molecule studies of DNA mechanics. *Curr. Opin. Struct. Biol.* **10**, 279-285 (2000).

48 Bryant, Z. et al. Structural transitions and elasticity from torque measurements on DNA. *Nature* **424**, 338-341 (2003).

49 Lipfert, J., Kerssemakers, J. W., Jager, T. & Dekker, N. H. Magnetic torque tweezers: measuring torsional stiffness in DNA and RecA-DNA filaments. *Nat. Methods* **7**, 977 (2010).

50 Lipfert, J., Wiggin, M., Kerssemakers, J. W., Pedaci, F. & Dekker, N. H. Freely orbiting magnetic tweezers to directly monitor changes in the twist of nucleic acids. *Nat. Commun.* **2**, 1-10 (2011).

51 Herrero-Galán, E. et al. Mechanical identities of RNA and DNA double helices unveiled at the single-molecule level. *J. Am. Chem. Soc.* **135**, 122-131 (2013).

52 Perez, A., Lankas, F., Luque, F. J. & Orozco, M. Towards a molecular dynamics consensus view of B-DNA flexibility. *Nucleic Acids Res.* **36**, 2379-2394 (2008).

53 Noy, A., Perez, A., Lankas, F., Luque, F. J. & Orozco, M. Relative flexibility of DNA and RNA: a molecular dynamics study. *J. Mol. Biol.* **343**, 627-638 (2004).

54 Marin-Gonzalez, A., Vilhena, J., Perez, R. & Moreno-Herrero, F. Understanding the mechanical response of double-stranded DNA and RNA under constant stretching forces using all-atom molecular dynamics. *Proc. Natl. Acad. Sci. U.S.A.* **114**, 7049-7054 (2017).

55 Olson, W. K., Gorin, A. A., Lu, X.-J., Hock, L. M. & Zhurkin, V. B. DNA sequence-dependent deformability deduced from protein–DNA crystal complexes. *Proc. Natl. Acad. Sci. U.S.A.* **95**, 11163-11168 (1998).

56 Kannan, S., Kohlhoff, K. & Zacharias, M. B-DNA under stress: over-and untwisting of DNA during molecular dynamics simulations. *Biophys. J.* **91**, 2956-2965 (2006).

57 Norberg, J. & Nilsson, L. Stacking free energy profiles for all 16 natural ribodinucleoside monophosphates in aqueous solution. *J. Am. Chem. Soc.* **117**, 10832-10840 (1995).

58 Brown, R. F., Andrews, C. T. & Elcock, A. H. Stacking free energies of all DNA and RNA nucleoside pairs and dinucleoside-monophosphates computed using recently revised AMBER parameters and compared with experiment. *J. Chem. Theory. Comput.* **11**, 2315-2328 (2015).

59 Hunter, C. A. & Lu, X.-J. DNA base-stacking interactions: a comparison of theoretical calculations with oligonucleotide X-ray crystal structures. *J. Mol. Biol.* **265**, 603-619 (1997).

60 Packer, M. J. & Hunter, C. A. Sequence-dependent DNA structure: the role of the sugar-phosphate backbone. *J. Mol. Biol.* **280**, 407-420 (1998).

61 Kim, Y.-J. & Kim, D.-N. Structural basis for elastic mechanical properties of the DNA double helix. *PloS One* **11**, e0153228 (2016).

62 Protozanova, E., Yakovchuk, P. & Frank-Kamenetskii, M. D. Stacked–unstacked equilibrium at the nick site of DNA. *J. Mol. Biol.* **342**, 775-785 (2004).

63 Ma, N. & van der Vaart, A. Anisotropy of B-DNA groove bending. *J. Am. Chem. Soc.* **138**, 9951-9958 (2016).

64 Ivani, I. et al. Parmbsc1: a refined force field for DNA simulations. *Nat. Methods* **13**, 55 (2016).

65 Cardoso, J. R. & Leite, F. S. Exponentials of skew-symmetric matrices and logarithms of orthogonal matrices. *J. Comput. Appl. Math.* **233**, 2867-2875 (2010).

66 Gruttmann, F., Sauer, R. & Wagner, W. Theory and numerics of three-dimensional beams with elastoplastic material behaviour. *Int. J. Numer. Methods. Eng.* **48**, 1675-1702 (2000).

67 Lee, C., Kim, K. S., Kim, Y.-J., Lee, J. Y. & Kim, D.-N. Tailoring the Mechanical Stiffness of DNA Nanostructures Using Engineered Defects. *ACS Nano* **13**, 8329-8336 (2019).

68 Zhang, X., Bao, L., Wu, Y.-Y., Zhu, X.-L. & Tan, Z.-J. Radial distribution function of semiflexible oligomers with stretching flexibility. *J. Chem. Phys.* **147**, 054901 (2017).

69 Roth, E., Glick Azaria, A., Girshevitz, O., Bitler, A. & Garini, Y. Measuring the Conformation and Persistence Length of Single-Stranded DNA Using a DNA Origami Structure. *Nano Lett.* **18**, 6703-6709 (2018).

70 Yagyu, H., Lee, J.-Y., Kim, D.-N. & Tabata, O. Coarse-Grained Molecular Dynamics Model of Double-Stranded DNA for DNA Nanostructure Design. *J. Phys. Chem. B* **121**, 5033-5039 (2017).

71 Arbona, J. M., Aimé, J.-P. & Elezgaray, J. Modeling the mechanical properties of DNA nanostructures. *Phys. Rev. E* **86**, 051912 (2012).

72 Bathe, K.-J. *Finite Element Procedures*. (2006).

73 Rau, D., Lee, B. & Parsegian, V. Measurement of the repulsive force between polyelectrolyte molecules in ionic solution: hydration forces between parallel DNA double helices. *Proc. Natl. Acad. Sci. U.S.A.* **81**, 2621-2625 (1984).

74 Douglas, S. M. et al. Rapid prototyping of 3D DNA-origami shapes with caDNAno. *Nucleic Acids Res.* **37**, 5001-5006 (2009).

75 Moakher, M. Means and averaging in the group of rotations. *SIAM J. Matrix Anal. Appl.* **24**, 1-16 (2002).

76 Kim, Y.-J., Lee, C., Lee, J. G. & Kim, D.-N. Configurational Design of Mechanical Perturbation for Fine Control of Twisted DNA Origami Structures. *ACS Nano* **13**, 6348-6355 (2019).

77 Ke, Y. et al. Multilayer DNA origami packed on a square lattice. *J. Am. Chem. Soc.* **131**, 15903-15908 (2009).

78 Woo, S. & Rothemund, P. W. Programmable molecular recognition based on the geometry of DNA nanostructures. *Nat. Chem.* **3**, 620 (2011).

79 Franquelim, H. G., Khmelinskaia, A., Sobczak, J.-P., Dietz, H. & Schwille, P. Membrane sculpting by curved DNA origami scaffolds. *Nat. Commun.* **9**, 811 (2018).

80 Bai, X.-c., Martin, T. G., Scheres, S. H. & Dietz, H. Cryo-EM structure of a 3D DNA-origami object. *Proc. Natl. Acad. Sci. U.S.A.* **109**, 20012-20017 (2012).

81 Chen, H. et al. Dynamic and progressive control of DNA origami conformation by modulating DNA helicity with chemical adducts. *ACS Nano* **10**, 4989-4996 (2016).

82 Kauert, D. J., Kurth, T., Liedl, T. & Seidel, R. Direct mechanical measurements reveal the material properties of three-dimensional DNA origami. *Nano Lett.* **11**, 5558-5563 (2011).

83 O'Neill, P., Rothemund, P. W., Kumar, A. & Fygenson, D. K. Sturdier DNA nanotubes via ligation. *Nano Lett.* **6**, 1379-1383 (2006).

84 Muddiman, D. C., Anderson, G. A., Hofstadler, S. A. & Smith, R. D. Length and base composition of PCR-amplified nucleic acids using mass

measurements from electrospray ionization mass spectrometry. *Anal. Chem.* **69**, 1543-1549 (1997).

85 Stewart, G. W. A Krylov--Schur algorithm for large eigenproblems. *SIAM J. Matrix Anal. Appl.* **23**, 601-614 (2002).

86 Kim, D.-N., Nguyen, C.-T. & Bathe, M. Conformational dynamics of supramolecular protein assemblies. *J. Struct. Biol.* **173**, 261-270 (2011).

87 Kim, J., Kim, J.-G., Yun, G., Lee, P.-S. & Kim, D.-N. Toward modular analysis of supramolecular protein assemblies. *J. Chem. Theory. Comput.* **11**, 4260-4272 (2015).

88 Yun, G., Kim, J. & Kim, D.-N. A critical assessment of finite element modeling approach for protein dynamics. *J. Comput. Aided Mol. Des.* **31**, 609-624 (2017).

89 Lange, O. F. & Grubmüller, H. Generalized correlation for biomolecular dynamics. *Proteins* **62**, 1053-1061 (2006).

90 Kim, D.-N., Altschuler, J., Strong, C., McGill, G. & Bathe, M. Conformational dynamics data bank: a database for conformational dynamics of proteins and supramolecular protein assemblies. *Nucleic Acids Res.* **39**, D451-D455 (2011).

91 Claessens, M. M., Bathe, M., Frey, E. & Bausch, A. R. Actin-binding proteins sensitively mediate F-actin bundle stiffness. *Nat. Mater.* **5**, 748 (2006).

92 Castro, C. E., Su, H.-J., Marras, A. E., Zhou, L. & Johnson, J. Mechanical design of DNA nanostructures. *Nanoscale* **7**, 5913-5921 (2015).

93 Liedl, T., Högberg, B., Tytell, J., Ingber, D. E. & Shih, W. M. Self-assembly of three-dimensional prestressed tensegrity structures from DNA. *Nat. Nanotechnol.* **5**, 520 (2010).

# Abstract in Korean

DNA 나노기술은 DNA의 자가조립원리를 이용해 나노 해상도의 정밀한 구조체를 설계 및 제작, 해석하는 분야로, DNA 나노구조체를 이용한 수많은 응용 연구가 지속적으로 제시되고 있다. DNA 나노구조체는 기본 염기(A, T, G, C) 간의 연결체로서, 이에 따른 국소적인 역학적 물성은 염기를 구성하는 원자 간의 상호작용에 의해 발현된다. 따라서 DNA 나노구조체의 역학적 거동을 온전히 이해하기 위해서는 나노 스케일의 전원자 시뮬레이션이 필요하다. 그러나 일반적으로 DNA 나노구조체는 염이 포함된 수용액 환경에서 수천 개의 염기가 연결되어 구성되므로, 이를 원자 스케일에서 해석하기 위해서는 억 단위의 원자 자유도 문제를 수치적으로 해결해야 하여, 시스템 전체의 전원자 시뮬레이션은 거의 불가능하다. 이에 자유도를 줄여 DNA 나노구조체를 해석하기 위한 여러 축소모델이 개발되고 있으나, 해석의 높은 효율성과 정확성을 모두 달성하려면 여전히 난제가 많다. 이에 본 연구에서는 멀티스케일 모델링을 통해 염기 스케일의 정확도로 DNA 나노구조체를 효율적으로 해석하는 방법을 제시한다. 먼저 염기 간의 다양한 연결 방식을 분류하고, 이를 포함한 작은 시스템의 분자동역학 시뮬레이션을 통해, 염기에 따른 역학적 특성을 정량화하고 물성 라이브러리를 구축하였다. 다음으로 염기 간의 연결에 따른 고유한 역학적 물성과 수용액 환경에서 DNA의 음전하로 인해 발생하는 구조체 내부의 정전기적 반발력을 완전히 반영하는 유한요소 모델을 개발하여, DNA 나노구조체를 구성하는 모든 염기 간의 연결과 구조체 내부의 상호작용을 유한요소 연결체로 변환하였다. 구성된 유한요소 연결체는 염기 스케일의 해상도로 DNA 나노구조체의 역학적 특성을 모두 내포하고 있어, 비선형 수치해석과 고유모드 분석을 통해 DNA 나노구조체의 염기서열에 따른 평형 형상과 동적 특성을 정확하고 빠르게 예측할 수 있다. 본 연구에서 제시하는 기법은 핵산 기반의 구조체 해석에 쉽게 적용할 수 있으며, 다양한 바이오 재료의 멀티스케일 모델링 기술로 확장될 수 있다.

주요어: DNA 나노기술, DNA 나노구조체, 역학적 물성, 멀티스케일 모델링, 분자동역학 시뮬레이션, 유한요소해석

학 번: 2014-21861